國 立 交 通 大 學

光 電 工 程 研 究 所

博士論文

超高速 60GHz 光載微波無線訊號系統

Extremely High-Capacity 60 GHz Radio-over-Fiber Systems

研 究 生：江 文 智

指 導 教 授：陳 智 弘 博士

指 導 教 授：林 俊 廷 博士

中 華 民 國 一 零 一 年 七 月

超高速 60GHz 光載微波無線訊號系統

Extremely High-Capacity 60 GHz Radio-over-Fiber Systems

研 究 生 :江文智　　Student : Wen-Jr Jiang

指導教授 :陳智弘 博士　　Advisor : Dr. Jyehong Chen

:林俊廷 博士　　: Dr. Chun-Ting Lin

A Dissertation

Submitted in Partial Fulfillment of the Requirements

For the Degree of PhD in

Department of Photonics

College of Electrical and Computer Engineering

National Chiao-Tung University

HsinChu, Taiwan 300, R.O.C.

中 華 民 國 一 零 一 年 七 月

Extremely High-capacity 60 GHz Radio-over-Fiber Systems

Student: Wen-Jr Jiang

Advisor: Dr. Jyehong Chen
Dr. Chun-Ting Lin

Department of Photonics
National Chiao Tung University

ABSTRACT

The increasing demand for wireless video-based interactive and multimedia data services explains why 60-GHz wireless system is a promising candidate to provide multi-gigabit-per-second services. While attempting to generate and transmit 60-GHz signals in a wireless system cost effectively and increase the spectral efficiency to facilitate multi-gigabit-per-second services, this work presents four novel RoF systems based on optical frequency multiplication to reduce the bandwidth requirement of optical transmitters. In this thesis, the performances of RoF systems are investigated by theoretical analysis, VPI WDM-TransmissionMaker simulation, and experimental demonstration. Additionally, we employ RoF systems with OFDM modulation, single carrier modulation, adaptive bit-loading algorithm, I/Q imbalance compensation algorithm, and pre-coded method to successfully circumvent multiple system impairments resulting in significant system performance improvement.

Optical I/Q up-conversion system with frequency quadrupling technique for 60-GHz RoF system are proposed. The advantage of the proposed transmitter is that no electrical mixer is needed to generate RF signal. Therefore, I/Q data of RF signals are processed at baseband at the transmitter, which is independent

of the carrier frequency of the generated RF signal. Negligible power penalty following 25-km standard single-mode fiber transmission is observed, capable of significantly extending the service range to various applications within a building or campus.

Electrical I/Q up-conversion RoF system which is a simple architecture for 60-GHz application are proposed. This system can achieve fiber transmission distances exceeding 3-km and 10-m wireless transmission distance without any chromatic dispersion compensation. Fiber links of 3km are sufficient for most short-range RoF applications such as in-building systems, where low system complexity is very critical. This work also demonstrates the 2×2 MIMO technique for capacity improvement of the proposed system. Both SISO and MIMO systems are achieved record data-rate within 7-GHz license-free band at 60 GHz and BER measurement results are below the FEC limit of $1x10^{-3}$.

Hybrid access network which support both 60-GHz RoF and FTTx systems using a frequency multiplication technique are presented. One of architectures uses single-electrode MZM with frequency doubling technology. The other architecture uses dual parallel MZM with frequency quadrupling technology. Furthermore, wavelength reuse for uplink data transmission via a RSOA is also demonstrated. Two proposed hybrid access network systems exhibit no RF fading, no narrow-band optical filter is required at the remote node to separate the RF and BB signals, and vector signals are carried. Therefore, the proposed systems are compatible with the current PON system.

ACKNOWLEDGEMENT

在博士班這四年，首先感謝我的指導老師 陳智弘教授與 林俊廷教授，提供良好的實驗環境以及無私的指導與照顧，並教導我實驗方法以及報告技巧，讓我在博士生涯中成長許多，也更認識自己的長處與短處。還要感謝 祁甦教授提供給我許多寶貴的意見及資源，使我提升不少的研究能力以及對事情的看法，另外要特別感謝 Anthony Ng'oma 博士、Hejie Yang 博士、Rakesh Sambaraju 博士，讓我在 Corning 公司的實習期間，獲益良多。

這些年來，感謝與我一起奮鬥，一起成長的實驗室伙伴們：非常感謝 Kate 在研究生涯上的幫忙，感謝 Boris 學長、達儒、芳銘同學、俊宏、奕誠、星宇、立穎、彥霖、明義、維元、宜閔、上詠、冠穎學弟，讓我博士生涯不孤單。還有許許多多的學弟妹們在我實驗忙碌時，熱心地幫忙處理瑣事，謝謝你們陪我度過這段日子。

另外我要感謝高中到研究所的同學朋友們，謝謝你們的加油與鼓勵，並感謝交大給予我許多的資源與溫暖，讓我成長與茁壯。最後要感謝我的家人，爸爸的支持與媽媽的擔心，親戚的加油及照顧，因為你們我才能勇敢地克服困難，完成博士學位。帶著歡笑與淚水編織而成的回憶，邁向下個新奇的旅程，再會了交大。

江文智 于 風城 交大 民國一零一年七月

TABLE OF CONTENTS

LIST OF FIGURES

LIST OF TABLES

Chapter 1

INTRODUCTION

1.1 Review of Wireless Communication Systems

Instantaneous information exchanges, which drive wireless communications to be more and more important in the past 20 years, have become an important part of daily life for many people today. The general idea of wireless communications is transferring signals by electro-magnetic waves which provide mobility to the end users. The first-generation (1G) wireless communication system is the narrowband analog system which was launched in Japan by Nippon telegraph and telephone (NTT) in 1979. With the disadvantages of low spectral efficiency, incompatible with digital data services, and poor security, the second-generation (2G) which are narrowband digital systems was proposed in the 1991. Mobile devices, such as smart phones, tablet, ultrabooks, and e-readers, growth rapidly these days and provide conveniences of internet accesses for various kind of services, including social networking sites, online gaming, video calls, video streaming, cloud computing, and cloud storages. To support the tremendous amount of data transmission, broad-band wireless communications, including 3G, 4G (LTE, WiMAX), and WiFi, were proposed [1-7].

Today, these wireless technologies have become a part of daily life and continue developing to provide better quality of experience. On the other hand, the better quality of experience means the wireless systems need to provide higher data rates. However, data rates of current microwave wireless systems are still limited to several tens of Mbps which are hampered by congestion and

limited spectrum in their current frequency bands of operation. Since the key to achieve higher data rate is bandwidth, the most promising path to multi-Gbps wireless communication is the use of mm-wave frequencies where very large bands of frequency spectra are available [8]. Thanks for the advances in process technologies and low cost integration solutions over the past few years. The mm-wave technology has attracted great interest of the standards groups and industry alliances. For instance, the US Federal Communications Commission (FCC) released a number of unlicensed bandwidth at 60GHz (57-64 GHz), 70GHz (71-76 GHz), 80GHz (81-86GHz), and 90GHz (92-94GHz and 94.1-95GHz) [9, 10].

Since the 60 GHz technology enables many new applications which are difficult to be offered by wireless systems at lower frequencies, the 60 GHz band has attracted many standardization bodies based on the huge continuous unlicensed bandwidth. As show in Fig. 1-1, many countries define different unlicensed bandwidth at 60GHz. For example, 9-GHz bandwidth is available in Europe and 7GHz bandwidth is available in USA, Canada, Japan and Korea [11-38].

The huge unlicensed bandwidth represents great potential for gigabit wireless applications. Furthermore, the standers for 60GHz application allow much higher transmit power that could provide high signal quality than other frequency bands. For example, the equivalent isotropic radiated power (EIRP) for 60GHz band is 35dBm and the EIRP for 802.11n is 25dBm. The reason for the higher EIRP limitation at 60GHz is crowded applications in lower frequency band [12]. Because of the combination of high EIRP limit and huge unlicensed bandwidth, the 60GHz system could provide services, such as

uncompressed HD video streaming with high speed data transfer, which ensure high quality performance and low latency for exceptional use experience.

However, 60-GHz wireless networking brings many technical challenges owing to the high carrier frequencies and the wide channel bandwidths. The challenges include the significantly higher air-link loss, and reduced device performance and lower power efficiency. Figure 1-2 shows the propagation losses comparison between the 2.4-GHz WiFi and the 60-GHz wireless signals. The propagation loss of the 60-GHz wireless signals is about 30 dB higher than 2.4 GHz WiFi signal [12]. In addition, the wide channel bandwidth means higher noise power and reduced signal-to-noise ratio (SNR).

Because of the high path loss and high attenuation through building walls, in-building radio cells at 60 GHz are confined to a single room [36]. This reduces user interference resulting in very high wireless data capacity per user [37]. All of these factors make wireless networking at 60-GHz "pico-cellular" in nature with the radio cells typically smaller than 10 m. Consequently, multi-gigabit-per-second wireless networking at 60 GHz requires an extensive high-capacity feeder network to interconnect the large number of radio access points.

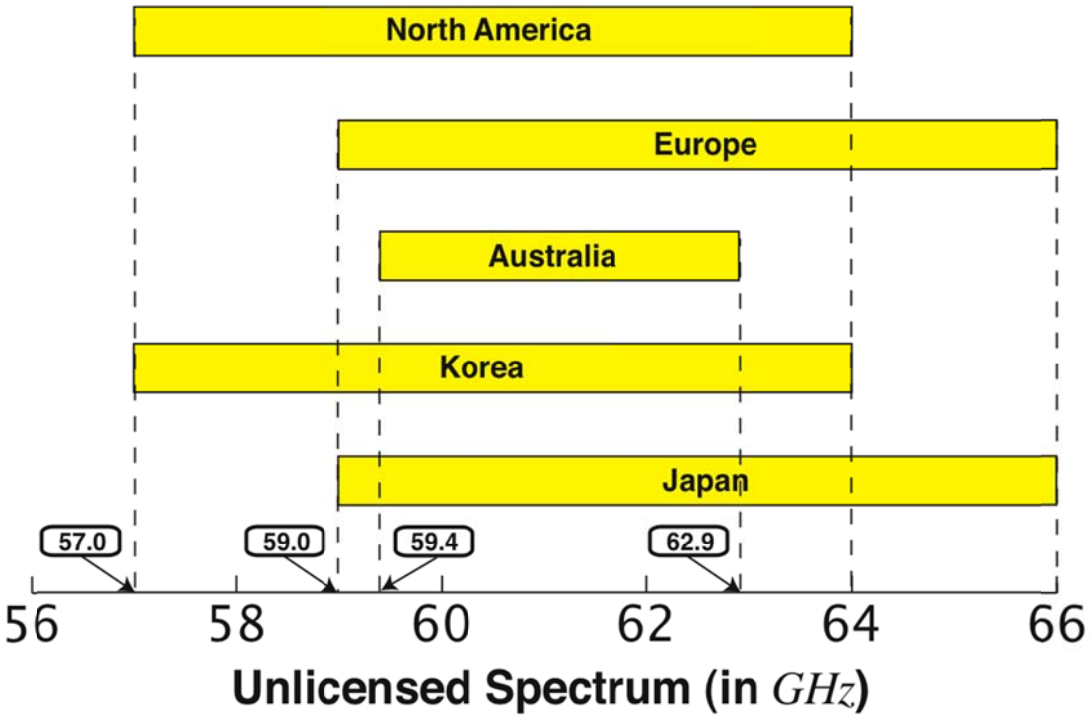

Figure 1-1 Worldwide unlicensed band for 60 GHz.

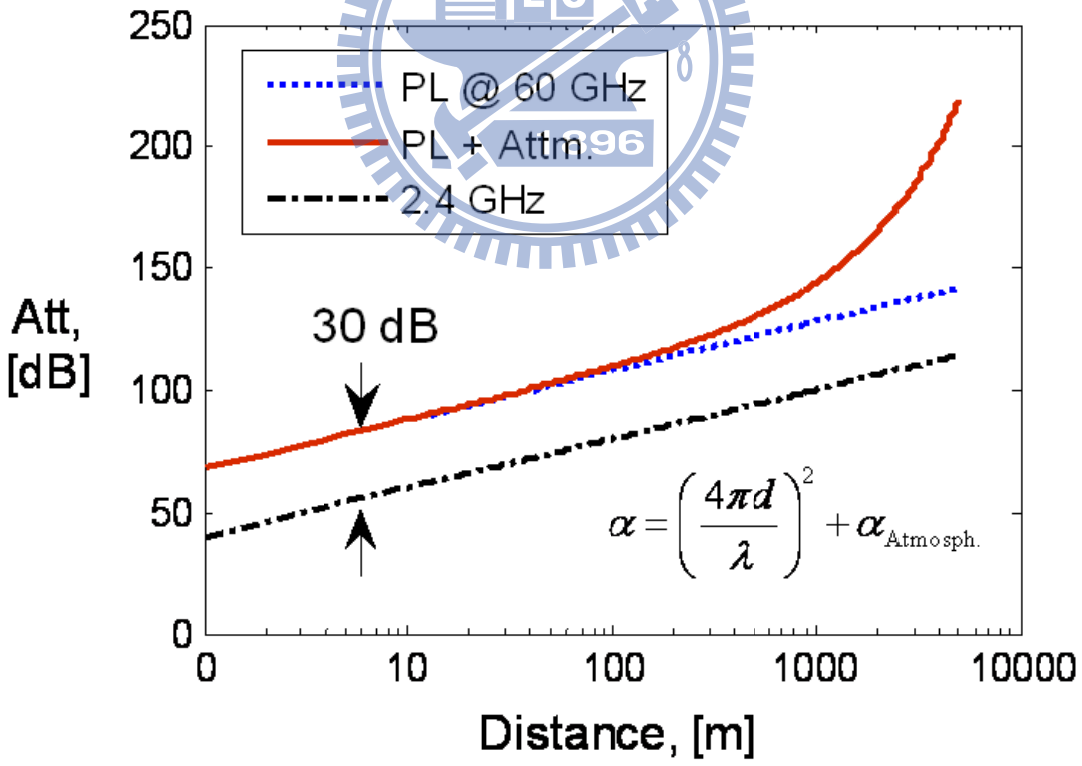

Figure 1-2 Propagation losses at 2.4 GHz and 60 GHz.

1.2 Radio-over-Fiber Technologies

Figure 1-3 shows the basic structure of traditional wireless communication systems. The traditional wireless access points receive baseband on-off keying signal from the central office using Ethernet cables. The access points convert the wirelind baseband signal to wireless RF signal. Since the bandwidth of wireless channel is limited, the wireless systems need modulation formats with higher spectral efficiencies than wireline systems. After digital signal processing, the digital signal transfer to the analog signal by using digital to analog converter. The baseband analog signals up-convert to desire carrier frequency using electrical I/Q mixer. The generated RF signal is amplified using RF amplifiers and transmitted using wireless antennas.

Because of the high wireless path loss and high attenuation through building walls for the 60-GHz wireless signal, the signal coverage per cell is much smaller than the WiFi system. More antenna units are required for the 60-GHz wireless system to provide the same signal coverage as the WiFi system. However, more antenna units also increase the system complexity and cost. Complex antenna units are not practical solutions for the 60GHz applications. Therefore, the system needs to simplify the antenna units.

Recently, radio-over-fiber (RoF) systems have attracted considerable interest because of their potential implementation in future broadband wireless communications. Since RoF technology reduces the cost of the access points and shifts the system complexity to central office, it can provide the required feeder network as it is best suited to deal with the demands of small-cell networks [38].

Figure 1-4 illustrates a cartoon for future 60-GHz wireless home network

based on RoF technology. The central office receives the data from the core network first. Then the central office generates the electrical RF signal. The electrical RF signal transfer to RoF signal by using optical modulator. After the optical fiber transmission, the RoF signal is sent into photodiode and converted to electrical RF signal at access point. For the RoF system, the access point does not need digital to analog converts, digital signal processing, electrical mixers, and RF local oscillators. Consequently, the advantages of RoF technologies have made them attractive options for 60 GHz wireless applications [18-35].

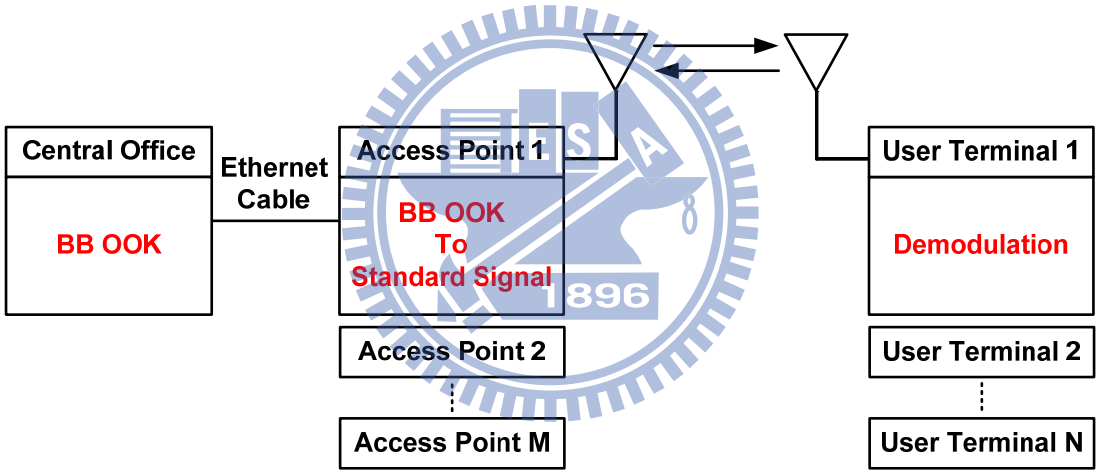

Figure 1-3 Basic structure of wireless system.

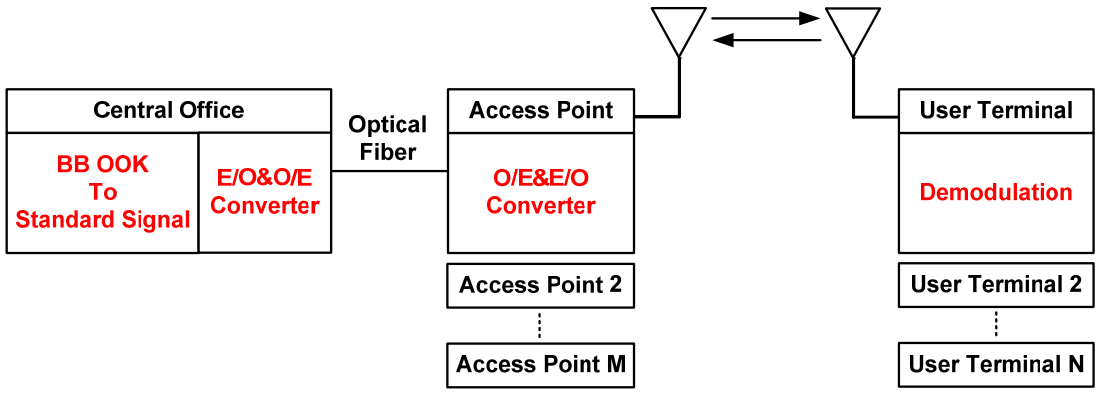

Figure 1-4 Basic structure of Radio-over-Fiber system.

1.3 Digital Signal Processing

Since the capacity requirement for wireless communications continues to increase, high spectral efficiency modulation formats and a high carrier frequency are required for the next generation of ultra-high capacity wireless systems. Many standards have been proposed concerning the delivery of multi-gigabit-per-second services for 60-GHz wireless system in the 7-GHz license-free band, including IEEE 802.15.3c, ECMA 387, WirelessHD, IEEE 802.11.ad and Wireless Gigabit Alliance (WiGig). These standards utilize many data formats, such as phase-shift keying (PSK), minimum-shift keying (MSK), quadrature amplitude modulation (QAM), amplitude-shift keying (ASK), differential phase-shift keying (DPSK), single-carrier frequency-domain-equalization (SC-FDE), and orthogonal frequency-division multiplexing (OFDM). Moreover, these standards not only have different data formats but also have different data throughput. For example, the IEEE 802.15.3c supports data rate from 25.3Mbps to 5.67Gbps. The WirelessHD specification can support data rates up to 28 Gbps for 4K resolution and 3D TV support [12].

In order to achieve multi-standard operation, 60-GHz RoF systems must be able to handle wireless signals with different requirements. These standards may impose different system performance requirements on the 60-GHz RoF systems. For instance channel uniformity is very critical for single-carrier systems [29, 39]. On the other hand, the presence of multiple carrier transmission in the OFDM signal format makes linearity and the ability to handle a high peak-to-average power ratio (PAPR) very critical system parameters. Therefore, the properties of modulation format are very important

for the system design [33-35, 40].

Furthermore, the system requirements are rendered even more critical for the very wide-band (>1 GHz) channels being considered at 60 GHz and other mm-wave bands. The consequence of these requirements is that they lead to the use of digital signal processing (e.g. I/Q imbalance compensation and adaptive bit-loading algorithm) for signal demodulation.

1.4 Current State of 60 GHz RoF System

Although the feasibility of the 60-GHz RoF system has been demonstrated using electro-absorption-modulator (EAM) [18-22], 60-GHz equipment and components are required, subsequently increasing overall system costs significantly. Moreover, the EAM modulation generates a double sideband (DSB) signal, which suffers from dispersion-induced performance fading. Therefore, the maximum data throughput has been demonstrated is 21 Gbps by using OFDM modulation format [22].

Generating a 60-GHz millimeter-wave signal with frequency doubling and overcome the dispersion-induced performance fading warrants the development of a double sideband with carrier suppression (DSB-CS) modulation scheme using Mach-Zehnder modulator (MZM), and can support only an on-off-keying (OOK) modulation format [23, 24]. However, OOK format cannot fulfill next generation wireless multimedia services with a target bit rate reaching 10 Gb/s within the 7-GHz license-free band at 60 GHz.

Recently, some of complex RoF system architectures for radio-frequency OFDM signal transmission are proposed with a target bit rate reaching 14 Gbps [33, 34]. However, it is imperative that the employed RoF links are as simple as possible to reduce cost, while providing the needed performance. This is

especially true for certain applications such as in-building systems, where certain performance attributes offered by complex RoF systems are not even required. Therefore, the 60 GHz RoF system that has simple architecture and support vector signals is very important for future applications.

1.5 Objective and Outlines of the Thesis

In this thesis, four novel RoF systems were proposed for transporting and generating wideband signals at 60 GHz, and the performances were investigated both theoretically and experimentally. The first architecture demonstrates the feasibility of the generation of an RF direct-detection vector signal using optical I/Q up-conversion. The second system demonstrates a short-range RoF system employing a single-electrode Mach-Zehnder modulator (MZM). Both systems transmit single-carrier and multi-carrier signal, and employ several digital signal processing techniques. The third and fourth systems present two simple hybrid access network architectures for generating and transmitting a 60GHz radio frequency (RF) phase-shift keying (PSK) signal with a baseband (BB) on-off keying (OOK) signal simultaneously.

This thesis is organized as the following. Chapter 1 provides the review of wireless systems and the advantages of 60 GHz technology. The challenges of the transmission of the 60 GHz signal are also discussed. Therefore, the 60 GHz RoF systems with digital signal processing attract great interests for future applications. Chapter 2 describes the basic ideas of 60 GHz RoF systems using external modulator. RoF system can be separated into an optical system and a wireless system. Optical system includes the optical transmitter, the optical channel and the optical receiver. The optical double-sideband (DSB) and

double-sideband with carrier suppression (DSB-CS) modulation schemes will be discussed. The properties of 60 GHz components and 60 GHz wireless channel will be discussed. The impairments of 60 GHz RoF systems will also been investigated in Chapter 2. The properties of digital signal modulation formats and digital signal processing will be discussed in Chapter 3. The signal carrier, OFDM, SC-FDE, single-carrier frequency-division multiple access (SC-FDMA), and single-carrier frequency-division multiplexing (SC-FDM) modulation formats will be discussed. The digital signal processing for system impairments and concept of multiple-input multiple-output (MIMO) will also been discussed.

A novel optical I/Q up-conversion RoF system for 60 GHz wireless applications will be proposed in Chapter 4. The advantage of the proposed transmitter is that no electrical mixer is needed to generate RF signals. Therefore, I/Q data of RF signals are processed at baseband at the transmitter, which is independent of the carrier frequency of the generated RF signal. Theoretical analysis and experimental demonstration of this system will be performed. The impacts of the I/Q imbalance will also been discussed. In order to achieve multi-standard operation, signal carrier and OFDM signals are utilized in the proposed system. The I/Q imbalance correction and adaptive loading algorithm are used to improve system performance. In Chapter 5, a simple 60GHz RoF system employing a single-electrode MZM are demonstrated. This system uses only one single-electrode MZM with bandwidth less than 35.5 GHz. The impacts of fiber chromatic dispersion and beat-noise on the performance of the RoF system are investigated by theoretical analysis and experimental demonstration. OFDM, SC-FDE and

SC-FDM signal generation and modulation techniques will be developed. 2 x 2 MIMO technologies also investigated to increase the data throughput within the 7 GHz band.

In Chapter 6, two novel multi-service hybrid access network systems for 60GHz wireless and wireline applications using frequency multiplication techniques will be presented. One of architecture uses a single-electrode MZM with frequency doubling technology. The other architecture uses a dual-parallel MZM with frequency quadrupling technology. These two schemes employ a novel pre-coded method that is based on the digital signal processing. The proposed systems does not suffer from RF fading and needs no narrow-band optical filter at the remote node to separate the RF and baseband signals. A frequency multiplication method for RoF link is realized to reduce the bandwidth requirement of the transmitter. Finally, Chapter 7 reviews the main conclusion of the thesis.

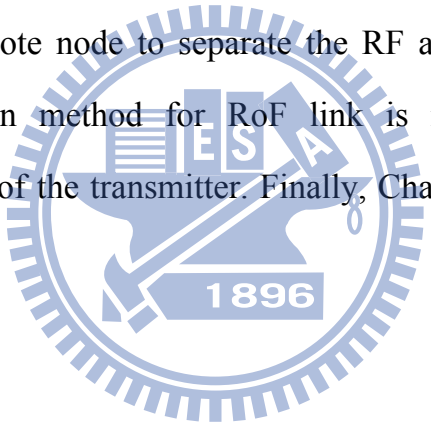

Chapter 2

RADIO-OVER-FIBER SYSTEMS USING EXTERNAL MODULATOR

2.1 The Architecture of 60 GHz Radio-over-Fiber Systems

There are two parts in radio-over-fiber (RoF) system: optical system and wireless system [38]. The optical system includes optical transmitter, optical channel, and optical receiver. The wireless system includes wireless transmitter, wireless channel, and wireless receiver. Optical transmitter converts an electrical input signal into the corresponding optical signal and then launches it into the optical fiber serving as a communication channel. Since the optical signal transfer in the optical fiber, the signal would suffer fiber dispersion that would induce frequency-selective fading. This phenomenon would introduce in 2.2.2. The role of an optical receiver is to convert the optical signal back into electrical form using photodiode. The generated electrical signal is at radio frequency and then launches it into the antenna serving as wireless transmitter.

For the wireless transmitter, the electrical amplifier amplified radio frequency signal and then broadcast the signal into the air by using antenna. The signal transfers the energy using electro-magnetic waves without wires. At wireless receiver side, the radio frequency signal down-converted to lower frequency and demodulated the signal. In this chapter, we will do an introduction about the radio-over-fiber systems using external Mach-Zehnder Modulator (MZM), and investigate its impairments of theoretically and experimentally in 2.3.

2.2 Optical System

2.2.1 Optical Transmitter

The traditional optical transmitter concludes RF driving signal, optical source, and optical modulator. The RF driving signal with high spectral efficiency modulation is required to provide higher data-rate transmission because the bandwidth of a wireless channel is limited. Therefore, high order quadrature amplitude modulation (QAM) is a good candidate [41]. The corresponding system requires I/Q mixer to up-convert the in-phase (I) and quadrature phase (Q) signals.

Presently, most RoF systems are using laser as optical source. The advantages of laser are compact size, high efficiency, good reliability small emissive area compatible with fiber core dimensions, and possibility of direct modulation at relatively high frequency.

For the optical modulator, direct modulation and external modulation are two modulations of generated optical signal. When the bandwidth of direct modulation signal is above 10 GHz, the frequency chirp imposed on signal becomes large enough. Hence, it is difficult to apply direct modulation to generate microwave/mm-wave signal. However, the bandwidth of signal generated by external modulator can exceed 10 GHz easily. Presently, most RoF systems are using external modulation with MZM or electro-absorption modulator (EAM) [18-22]. The most commonly used MZM are based on $LiNbO_3$ (lithium niobate) technology. According to number of electrode, there are two types of $LiNbO_3$ device: dual-drive Mach-Zehnder modulator (DD-MZM) and single-drive Mach-Zehnder modulator (SD-MZM) [42, 43].

The SD-MZM has two arms and an electrode. The optical phase in each arm can be controlled by changing the voltage applied on the electrode. When the lightwaves are in phase, the modulator is in “on” state. On the other hand, when the lightwaves are in opposite phase, the modulator is in “off ” state, and the lightwave cannot propagate by waveguide for output.

The modulator is used for converting electrical signal into optical form. Because the external dual-parallel modulator was composed of MZMs, we select MZM as modulator to build the architecture of optical transmitter. Figure 2-1 shows the schematic model of the MZM. The incident optical filed E_{in} is divided into two optical fields by optical coupler. The two optical fields send into two isolated paths, which are called upper arm and lower arm. The applied electrical signal modifies the velocities of the optical fields by the Pockels-Effect [43]. The velocity variation corresponds to the phase modulation of the optical field. The output optical filed for upper arm is

$$E_{upper} = E_{in} \cdot \sqrt{a} \cdot e^{j\Delta\varphi_1} \tag{2-1}$$

Where a is the power splitting ratio of power coupler. $\Delta\varphi_1$ is the optical carrier phase difference that is induced by driving voltage for upper arm. The power splitting ratio is defined as the ratio of the transmission power to the coupling power. A coupler always has non-ideal power splitting ratios due to manufacturing limitations, e.g. $a \neq 1/2$. Therefore, the output optical filed for lower arm is

$$E_{lower} = E_{in} \cdot \sqrt{1-a} \cdot e^{j\Delta\varphi_2} \tag{2-2}$$

$\Delta\varphi_2$ is the optical carrier phase difference that is induced by driving voltage for lower arm. The output optical filed for MZM is

$$E_{out} = E_{in} \cdot \left\{\sqrt{a} \cdot \sqrt{b} \cdot e^{j\Delta\varphi_1} + \sqrt{1-a} \cdot \sqrt{1-b} \cdot e^{j\Delta\varphi_2}\right\} \tag{2-3}$$

b is the power splitting ratio of second power coupler in MZM. The power splitting ratio of two couplers of a balanced MZM is 0.5. The output optical filed of the balanced MZM is given by

$$E_{out} = \frac{1}{2} \cdot E_{in} \cdot \{e^{j\Delta\varphi_1} + e^{j\Delta\varphi_2}\} \tag{2-4}$$

$$E_{out} = E_{in} \cdot \cos\left(\frac{\Delta\varphi}{2}\right) \cdot \exp\left(j\frac{\Delta\varphi_1 + \Delta\varphi_2}{2}\right) \tag{2-5}$$

$\Delta\varphi$ is the combined phase shift and can be calculated as the difference between $\Delta\varphi_1$ and $\Delta\varphi_2$ ($\Delta\varphi = \Delta\varphi_1 - \Delta\varphi_2$). For single electro x-cut MZM, the driving voltage for lower arm is the opposite of driving voltage for upper arm ($\Delta\varphi_1 = -\Delta\varphi_2$) [44]. Therefore, the output optical field for single electro x-cut MZM can be simplify as

$$E_{out} = E_{in} \cdot \cos\left(\frac{\Delta\varphi}{2}\right) \tag{2-6}$$

$$\Delta\varphi \triangleq \frac{v}{v_\pi} \cdot \pi \tag{2-7}$$

The v_π is called half-wave voltage that can induce π combined phase shift if the half-wave voltage is applied to the driving voltage [45]. If driving voltage equals to v_π, the modulator output power has its minimum value. The optical field E_0 of the laser can be expressed by

$$E_{in}(t) = E_0 \cos(\omega_0 t) \tag{2-8}$$

Where E_0 and ω_0 denote the amplitude and angular frequency of input optical field, respectively. After add time component, the optical field will become as

$$E_{out}(t) = E_{in}(t) \cdot \cos\left(\frac{\Delta\varphi}{2}\right) \cdot \cos(\omega_0 t) \tag{2-9}$$

The loss of MZM is neglected in previous equations. $V(t)$ consisting of an electrical sinusoidal signal and a dc biased voltage can be written as,

$$V(t) = V_{bias} + V_m \cos(\omega_{RF} t) \tag{2-10}$$

where V_{bias} is the dc biased voltage, V_m and ω_{RF} are the amplitude and the angular frequency of the electrical driving signal, respectively. The optical carrier phase difference induced by $V(t)$ is given by

$$\frac{\Delta\varphi}{2} = V(t) \cdot \frac{\pi}{2V_\pi} = \frac{V_{bias}+V_m \cos(\omega_{RF}t)}{2V_\pi} \cdot \pi \tag{2-11}$$

Equation (2-10) can be written as:

$$\begin{aligned} E_{out}(t) &= E_{in}(t) \cdot \cos\left[\frac{V_{bias}+V_m \cos(\omega_{RF}t)}{2V_\pi} \cdot \pi\right] \cdot \cos(\omega_0 t) \\ &= E_0 \cdot \cos[b + m \cdot \cos(\omega_{RF}t)] \cdot \cos(\omega_0 t) \\ &= E_0 \cdot \cos(\omega_0 t) \cdot \{\cos(b) \cdot \cos[m \cdot \cos(\omega_{RF}t)] \\ &\quad -\sin(b) \cdot \sin[m \cdot \cos(\omega_{RF}t)]\} \end{aligned} \tag{2-12}$$

where $b \triangleq \frac{V_{bias}}{2V_\pi}\pi$ is a constant phase shift that is induced by the dc biased voltage, and $m \triangleq \frac{V_m}{2V_\pi}\pi$ is the MZM modulation index (MI). The time dependent terms in Eq. (2-12) can be substituted with $\cos(x\cos\theta)$ and $\sin(x\cos\theta)$. The $\cos(x\cos\theta)$ and $\sin(x\cos\theta)$ terms can be expanded applying Bessel functions. The expansion results can be summarized as follows [46]

$$\begin{cases} \cos(x\cos\theta) = J_0(x) + 2\sum_{n=1}^{\infty}(-1)^n J_{2n}(x)\cos(2n\theta) \\ \sin(x\cos\theta) = 2\sum_{n=1}^{\infty}(-1)^n J_{2n-1}(x)\cos[(2n-1)\theta] \end{cases} \tag{2-13}$$

Expanding Equation (2-12) using Bessel functions, as detailed in Equation (2-13). The optical field at the output of the MZM can be written as:

$$E_{out}(t) = E_0(t) \cdot \cos(\omega_0 t) \cdot$$

$$\{\cos(b) \cdot [J_0(m) + 2 \cdot \sum_{i=1}^{\infty}(-1)^n \cdot J_{2n}(m) \cdot \cos(2n\omega_{RF}t)]$$

$$-\sin(b)\cdot[2\cdot\sum_{i=1}^{\infty}(-1)^n\cdot J_{2n-1}(m)\cdot\cos[(2n-1)\omega_{RF}t]]\}$$

(2-14)

where J_n is the Bessel function of the first kind of order n. the optical field of the mm-wave signal can be written as

$$\begin{aligned}\mathrm{E_{out}} &= \mathrm{E_0}\cdot\cos(b)\cdot J_0(m)\cdot\cos(\omega_0 t)\\ &+\mathrm{E_0}\cdot\cos(b)\cdot\sum_{i=1}^{\infty}J_{2n}(m)\cdot\cos[\,(\omega_0\pm 2n\omega_{RF})t+n\pi]\\ &-\mathrm{E_0}\cdot\sin(b)\cdot\sum_{i=1}^{\infty}J_{2n-1}(m)\cdot\cos[\,\omega_0\pm(2n-1)\omega_{RF})t+n\pi]\end{aligned}$$

(2-15)

When the MZM is biased at the maximum transmission point, the bias voltage is set at $V_{bias}=0$, and $\cos b = 1$ and $\sin b = 0$. Consequently, the optical field of the mm-wave driving signal can be written as

$$\begin{aligned}\mathrm{E_{out}}(t) &= \mathrm{E_0}\cdot J_0(m)\cdot\cos(\omega_0 t)\\ &+\mathrm{E_0}\cdot\sum_{n=1}^{\infty}J_{2n}(m)\cdot\cos[\,(\omega_0\pm 2n\omega_{RF})t+n\pi]\end{aligned}$$

(2-16)

The amplitudes of the generated optical sidebands are proportional to those of the corresponding Bessel functions associated with the phase modulation index m. With the amplitude of the electrical driving signal V_m equal to V_π, the m is $\pi/2$. Due to the properties of Bessel function of the first kind, the value of $J_n(m)$ would increase as order n decrease when $0<m<\frac{\pi}{2}$ and $n\geq 1$. As shown in Fig. 2-2, $J_1\left(\frac{\pi}{2}\right)$, $J_2\left(\frac{\pi}{2}\right)$, $J_3\left(\frac{\pi}{2}\right)$, and $J_4\left(\frac{\pi}{2}\right)$ are

0.5668, 0.2497, 0.069, and 0.014, respectively. Therefore, the optical sidebands with the Bessel function of first kind of high order term can be ignored, and Eq. (2-16) can be further simplified to

$$\mathrm{E_{OUT}} = \mathrm{E_0} \cdot J_0(m) \cdot \cos(\omega_0 t) + \mathrm{E_0} \cdot J_2(m) \cdot \cos[(\omega_0 \pm 2\omega_{RF})t + \pi] \quad (2\text{-}17)$$

When the MZM is biased at the middle point, the bias voltage is set at $\mathrm{V_{bias}} = \frac{\mathrm{V_\pi}}{2}$, and $\cos \mathrm{b} = \frac{\sqrt{2}}{2}$ and $\sin \mathrm{b} = \frac{\sqrt{2}}{2}$. Consequently, the optical field of the mm-wave signal using double sideband (DSB) can be written as

$$\mathrm{E_{out}} = \frac{1}{\sqrt{2}} \cdot \mathrm{E_0} \cdot J_0(m) \cdot \cos(\omega_0 \mathrm{t}) + \frac{1}{\sqrt{2}} \cdot \mathrm{E_0} \cdot J_1(m) \cdot \cos[(\omega_0 \pm \omega_{RF})t] \quad (2\text{-}18)$$

When the MZM is biased at the null point, the bias voltage is set at $V_{bias} = \mathrm{V_\pi}$, and $\cos b = 0$ and $\sin b = 1$. Consequently, the optical field of the mm-wave signal using DSB with carrier suppression (DSBCS) modulation can be written as

$$\mathrm{E_{out}} = \mathrm{E_0} \cdot J_1(m) \cdot \cos[(\omega_0 \pm \omega_{RF})t] \quad (2\text{-}19)$$

The generated optical spectrums of DSB and DSBCS signal are shown in Fig. 2-3 (a) and (b), respectively.

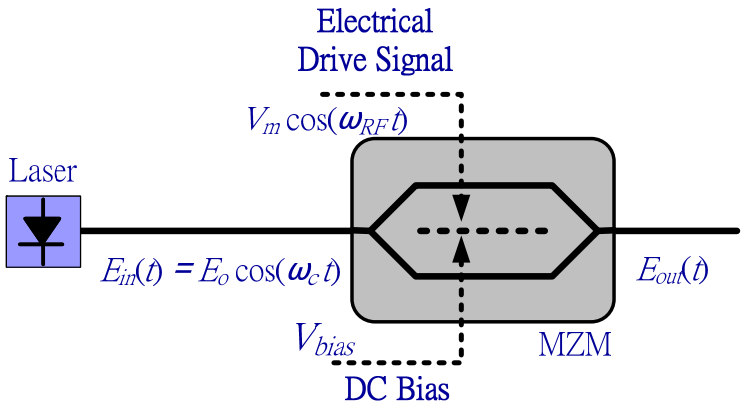

Figure 2-1 The principle diagram of the optical mm-wave generation using MZM.

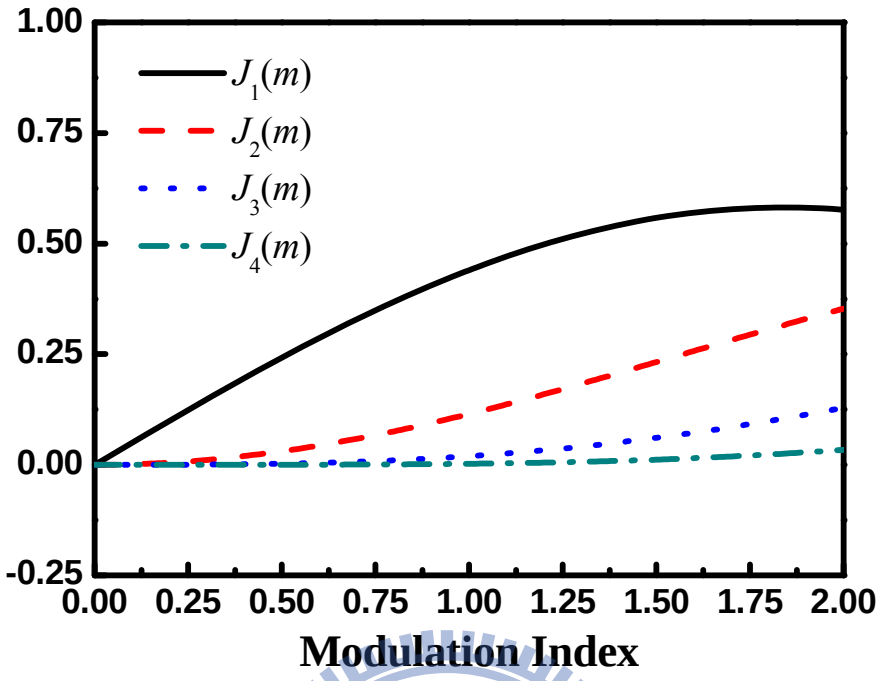

Figure 2-2 The magnitude of Bessel functions versus different RF modulation index.

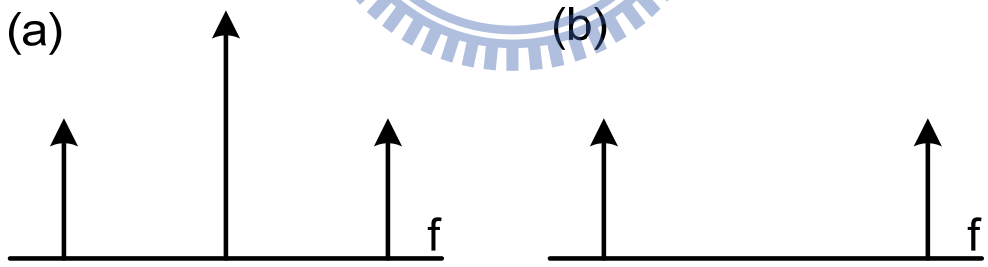

Figure 2-3 The generated optical spectrum: (a) DSB signal; (b) DSBCS signal.

2.2.2 Optical Channel

Communication channel concludes fiber, optical amplifier, etc.. Presently, most RoF systems are using standard single-mode fiber or dispersion compensated fiber (DCF) as the transmission medium. When the optical signal transmits in optical fiber, dispersion will be happened. DCF is use to

compensate dispersion. The transmission distance of any fiber-optic communication system is eventually limited by fiber losses. For long-haul systems, the loss limitation has traditionally been overcome using regenerator witch the optical signal is first converted into an electric current and then regenerated using a transmitter. Such regenerators become quite complex and expensive for WDM lightwave systems. An alternative approach to loss management makes use of optical amplifiers, which amplify the optical signal directly without requiring its conversion to the electric domain. Presently, most RoF systems are using erbium-doped fiber amplifier (EDFA). An optical band-pass filter (OBPF) is necessary to filter out the amplified spontaneous emission (ASE) noise. The model of communication channel is shown in Fig. 2-4.

When optical RF signals are transmitted over a standard single-mode fiber with dispersion, a phase shift to each optical sideband relative to optical carrier is induced. The propagation constant of the dispersion fiber $\beta(\omega)$ can be expressed as [47]

$$\beta(\omega) = n(\omega)\frac{\omega}{c}$$

$$= \beta_0 + \beta_1(\omega - \omega_0) + \frac{1}{2}\beta_2(\omega - \omega_0)^2 + \cdots \qquad (2\text{-}20)$$

where $\beta_m = \left.\frac{d^m\beta}{d\omega^m}\right|_{\omega=\omega_c}$ is the derivative of the propagation constant evaluated at $\omega = \omega_c$. The effect of high order fiber dispersion at 1550-nm band is neglected. For carrier tones with central frequency at $\omega = \omega_c \pm n\omega_{RF}$, the eq. (2-20) can be expressed as

$$\beta(\omega_0 \pm n\omega_{RF}) \cong \beta_0 \pm n\beta_1(\omega_0)\omega_{RF} + \frac{1}{2}n^2\beta_2(\omega_0)\omega_{RF}^2 \qquad (2\text{-}21)$$

$$\beta_2(\omega_c) = -\frac{c}{2\pi {f_c}^2} \cdot \mathrm{D}(\omega_0) \tag{2-22}$$

where c is light speed in free space and D is the chromatic dispersion parameter. For a standard single-mode fiber, D is 17-ps/(nm.km) [43]. The fiber loss is ignored. Therefore, after transmission over a standard single-mode fiber of length z, the optical field for the DSB modulation scheme can be written as

$$\mathrm{E}_{\mathrm{out}}(t) = \frac{1}{\sqrt{2}}\mathrm{E}_0 \cdot \{J_0(m)\cos(\omega_c t - \beta_0 z) + J_1(m)\cos[(\omega_c \pm \omega_{\mathrm{RF}})t - \beta_0 z \mp \beta_1 \omega_{\mathrm{RF}} z - \frac{1}{2}\beta_2 \omega_{\mathrm{RF}}^2 z] \tag{2-23}$$

The optical field for the DSBCS modulation scheme can be written as

$$\mathrm{E}_{\mathrm{out}}(t) = \mathrm{E}_0 \cdot J_1(m)\cos[(\omega_c \pm \omega_{\mathrm{RF}})t - \beta_0 z \mp \beta_1 \omega_{\mathrm{RF}} z - \frac{1}{2}\beta_2 \omega_{\mathrm{RF}}^2 z] \tag{2-24}$$

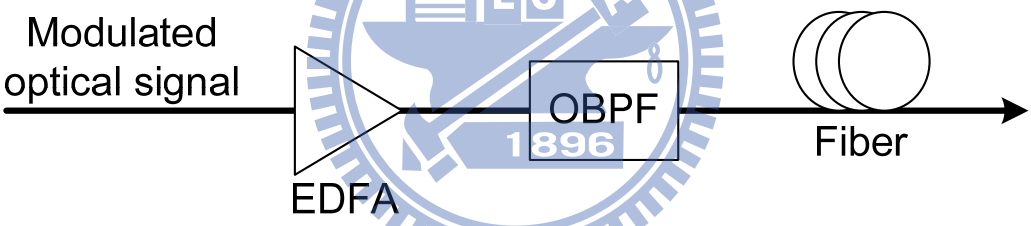

Figure 2-4 The model of optical channel in a RoF system. (OBPF: optical bandpass filter; EDFA: erbium doped fiber amplifier.)

2.2.3 Optical Receiver

Optical receiver usually consists of the photodiode and the trans-impedance amplifier (TIA). The function of photodiode is to convert optical signal to electrical current. The function of TIA is to convert current to output voltage. The generated electrical signal is proportional to the square of the optical filed.

$$i(t) = R \cdot E^2(t) \tag{2-25}$$

where R is the responsivity of photodiode [47]. The optical field for the DSB modulation scheme will generate the electrical signal after photodiode. The photocurrent for the DSB modulation scheme without optical fiber transmission at different frequency can be expressed as

$$i_0 = \frac{1}{4} \cdot R \cdot E_0^2 [J_0^2(m) + 2 \cdot J_1^2(m)]$$

$$i_{\omega_{\mathrm{RF}}} = \frac{1}{2} \cdot R \cdot E_0^2 \cdot J_0(m) \cdot J_1(m)$$

$$i_{2\omega_{\mathrm{RF}}} = \frac{1}{4} \cdot R \cdot E_0^2 \cdot J_1^2(m) \qquad (2\text{-}26)$$

For the RoF application, the frequency of desired mm-wave signal is ω_{RF}. The reason is that the photocurrent at ω_{RF} is proportional to driving signal v without significant distortion for small modulation index. Therefore, the DSB modulation scheme is one of RoF schemes for vector signal generation. In order to investigate the impairment of fiber dispersion, the he photocurrent with optical fiber transmission at ω_{RF} can be expressed as

$$i_{\omega_{\mathrm{RF}}} = \frac{1}{2} \cdot R \cdot E_0^2 \cdot J_0(m) \cdot J_1(m) \cdot \cos[\frac{1}{2}\beta_2 z \omega_{RF}^2] \qquad (2\text{-}27)$$

Due to fiber dispersion effect, the RF fading issue would be observed. The RF signal power is related to $\cos[\frac{1}{2}\beta_2 z \omega_{RF}^2]$. Therefore, the RF fading issue would become serious when the magnitude of frequency ω_{RF} become large. As shown in the Fig. 2-5, when the frequency ω_{RF} increases, the RF power will drop off rapidly. For 60-GHz applications, the frequency f_{RF} is fixed at 60.5 GHz. The first deep appears following 1-km fiber transmission.

The photocurrent for the DSBCS modulation scheme without optical fiber transmission at different frequency can be expressed as

$$i_0 = R \cdot E_0^2 \cdot J_1^2(m)$$

$$i_{2\omega_{RF}} = \frac{1}{2} \cdot R \cdot E_0^2 \cdot J_1^2(m) \quad (2\text{-}28)$$

The frequency of desired RoF signal is $2\omega_{RF}$. DSBCS modulation scheme has effective in the millimeter-wave range with excellent spectral efficiency, a low bandwidth requirement for electrical components. However, the photocurrent at $2\omega_{RF}$ is proportional to the square of driving signal. Therefore, DSBCS schemes can only support on-off keying (OOK) format, and none can transmit vector modulation formats, such as phase-shift keying (PSK), QAM, or OFDM signals, which are of utmost importance for wireless applications. In order to investigate the impairment of fiber dispersion, the photocurrent with optical fiber transmission at $2\omega_{RF}$ is the same with the optical signal without optical fiber transmission. The reason is that the desired RoF signal comes from one copy of the optical signal at photodiode. In order to combine with wireless system, the electrical bandpass filter will be used to reject out-of-band signals in wireless transmitter.

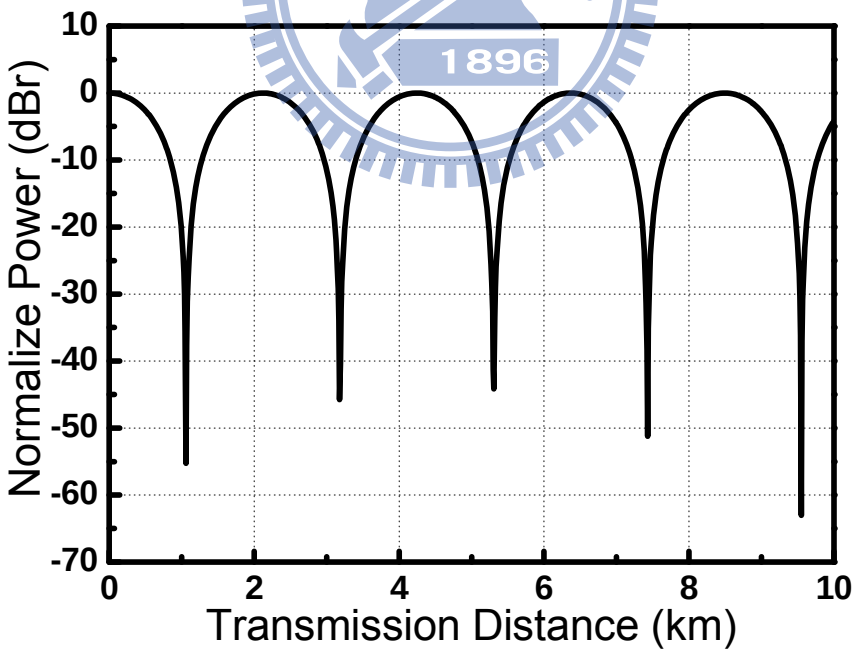

Figure 2-5 Simulated RF power of the generated mm-wave signal versus standard single-mode fiber length.

2.3 Wireless System

2.3.1 Wireless Transmitter

Thanks to the RoF technology, the wireless transmitter does not need electrical mixer and local oscillator to up-convert signal to wanted carrier frequency. Therefore, the wireless transmitter only consists of electrical bandpass filter, electrical amplifier and, antennas, as shown in Fig. 2-6. Since the high transmit power is necessary to overcome the higher path loss at 60 GHz, FCC allocated the 60 GHz license-free band in US from 57 to 64 GHz with a maximum equivalent isotropically radiated power (EIRP) of 40 dBm average and 43 dBm peak [12]. However, the output power for 60 GHz amplifier is typically limited to 10 dBm because the implementation of efficient power amplifiers at 60 GHz is challenging. Thanks for the huge antenna gain can be used to increase EIRP. The huge antenna gain at 60 GHz has significantly boosted the allowable EIRP limits.

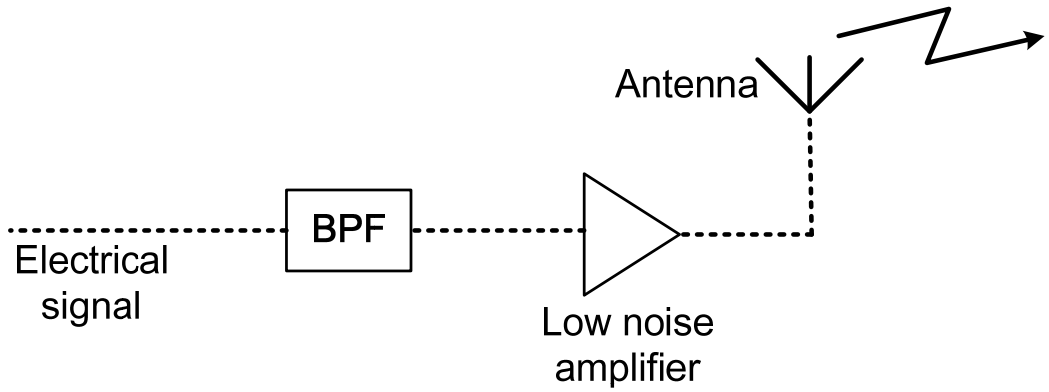

Figure 2-6 The model of wireless transmitter of RoF system.

2.3.2 Wireless channel

In order to improve the quality of 60GHz communications, understand the characteristics of 60GHz wireless channel is very important. The path loss is an important parameter for the wireless application. The Friis free space propagation formula could be express as

$$P_R = P_T G_T G_R \frac{\lambda^2}{16\pi^2 d^2} \quad (2\text{-}29)$$

where P_R and P_T are the transmitted and received power, respectively. λ is the signal wavelength, d is the transmission dictation between transmitter antenna and receiver antenna, G_T and G_R are transmit and receiver antenna gain, respectively. From this equation, the higher carrier frequency signals have lower wavelength and high path loss. Compared with signal propagation in 2.4 GHz, the path loss in 60 GHz is 20-30dB attenuation.

The other phenomenon of wireless communication is multipath fading. The wireless signals at low frequency suffer serious frequency-selective fading because of the scattering effect which comes from objects that are roughness compared to the wavelength. Things change in 60 GHz signal, the signal wavelength is much smaller than low frequency signal. The reflection effect which comes from objects that are smooth compared to the wavelength. Therefore, the 60-GHz signal does not suffer too much scattering effect, but reflection effect. Because of the reflection loss for the 60-GHz signal is about 10dB, the main propagation phenomenon for 60-GHz signal consists line-of-sight (LoS), first, and second order reflections [12].

2.3.3 Wireless Receiver

The wireless signal is received by receiver antenna. After receiver antenna,

RF bandpass filter is used to reject out-of-band signals. In order to keep the SNR of signal as high as possible, the in-band RF signals are then amplified by a low-noise amplifier (LNA). After the LNA, there have three methods for the RF front-end architecture [12].

In first method, the RF signal split into two signals, two RF signals are down-converted to baseband with two mixers and the quadrature local oscillators. Two baseband signals are transferred to digital signals by using analog to digital converters, as shown in Fig. 2-7 (a). Since this direct down-convert system is very challenging in 60 GHz circuit, the system has multiple down-converter stage is more practical. In second method (see Fig. 2-7 (b)), the RF signal is down-converted to intermediate frequency (IF) by a local oscillator and electrical mixer. And then the IF signal split into two signals, two IF signals are down-converted to baseband with two mixers and the quadrature local oscillators. Two baseband signals are transferred to digital signals by using analog to digital converters. In third method, the system is almost the same with second method. As Fig. 2-7 (c) shows, These IF signals are not directly down-converted into baseband but send the IF signal into analog-to-digital converter (ADC). The IF signals are digitalized by ADC. Then, the function of I/Q mixer is done in the digital domain.

Because of the I/Q mixer in digital domain is more accurate than analog I/Q mixer and high sampled scope is not difficult for experiment, this thesis use third method for experimental demonstration.

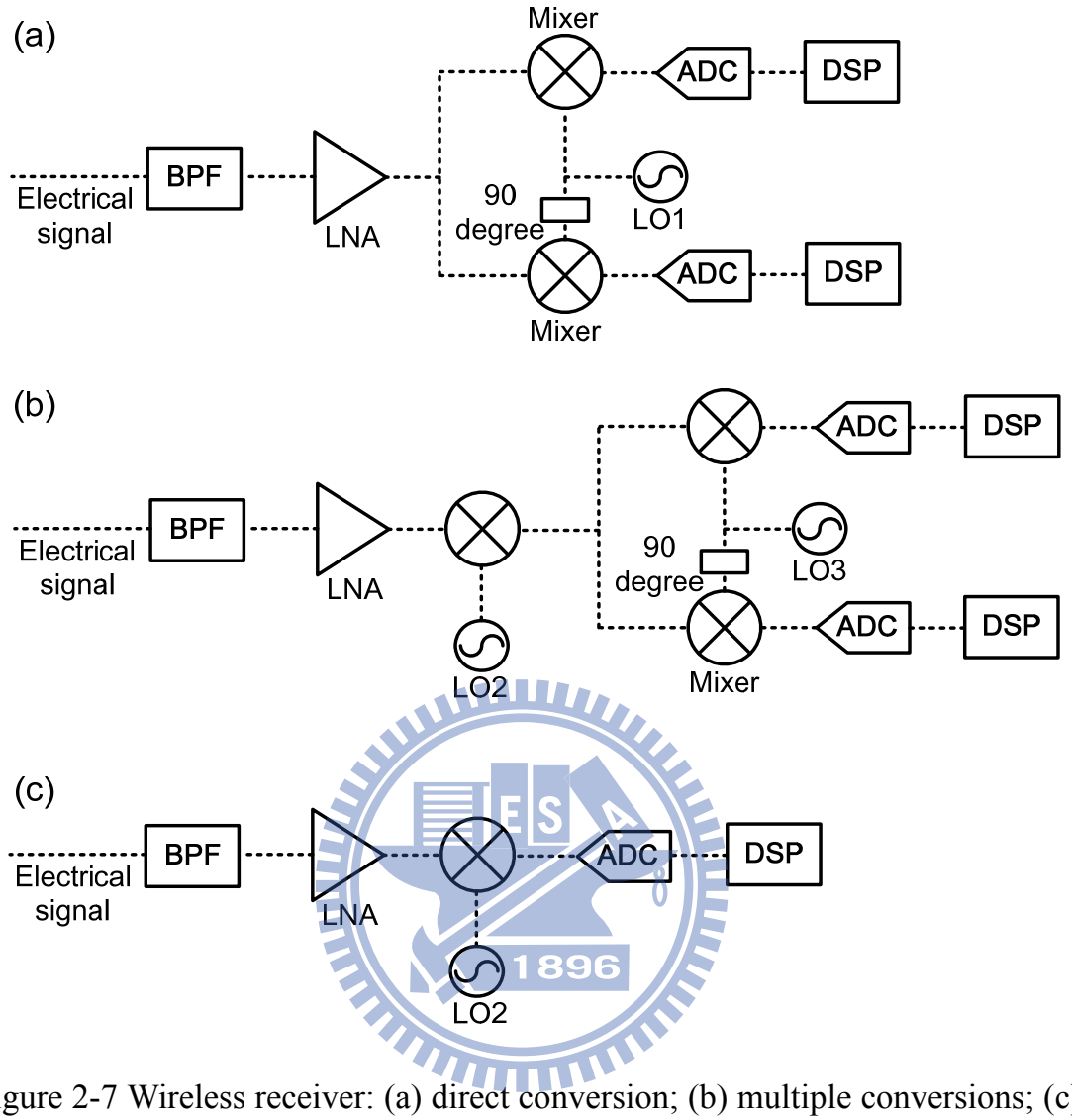

Figure 2-7 Wireless receiver: (a) direct conversion; (b) multiple conversions; (c) digital conversion. (BPF: bandpass filter; LO: local oscillator; DSP: digital signal processing.)

2.4 The Impairments of 60 GHz Radio-over-Fiber Systems

2.4.1 Inter-Symbol Interference

One of impairment of 60 GHz RoF system is inter-symbol interference (ISI), which causes a transmitted symbol to be interfered by other transmitted symbols. ISI is usually caused by multipath propagation and non-ideal channel

impulse response. Multipath propagation means that the signal from transmitter to receiver has many different paths. The causes of this include reflection, refraction and atmospheric effects. This effect always occurs in the wireless signal transmission and the connections between components that do not match. Non-ideal channel impulse response means that the channel impulse response is not impulse. The receiver signal equals to the convolution of transmitter signal and channel impulse response. Since the channel impulse response is not impulse, a transmitted symbol would be interfered by other transmitted symbols, as shown in Fig. 2-8. This effect always happens at components which have uneven impulse response and fiber induced fiber dispersion [23, 29].

Figure 2-8 The schematic diagram of inter-symbol interference.

2.4.2 Frequency-Selective Fading

Fading means that the single has large attenuation at some of frequencies. This effect caused by partial cancellation of a signal by itself. The signal arrives at the receiver by two different paths. These two paths have same amplitude response and 180 degree difference phase response. At receiver side, the combination signal would disappear due to disruptive interference. In 60 GHz RoF systems, fading always may be due to multipath propagation or due to fiber dispersion. A good example is shown in Fig. 2-5, where a carrier frequency of 60.5 GHz is chosen, resulting in the huge deep occurs after 1 km fiber transmission [26].

2.4.3 I/Q Imbalance

For the vector signal generation, the generator needs I/Q modulator to up-convert the in-phase (I) and quadrature phase (Q) signals. Since the I and Q data go through different paths, the amplitude and phase imbalance would contribute an additional interfering component at image frequency and induce signal performance degradation, as shown in Fig. 2-9. Due to the 7-GHz wide signal at 60 GHz band, different frequency has different imbalance coefficient. Therefore, it is difficult to maintain the I/Q balance at every frequency by using time domain compensation algorithm. Therefore, an adaptive I/Q imbalance correction scheme in frequency domain is needed to compensate the wideband signal.

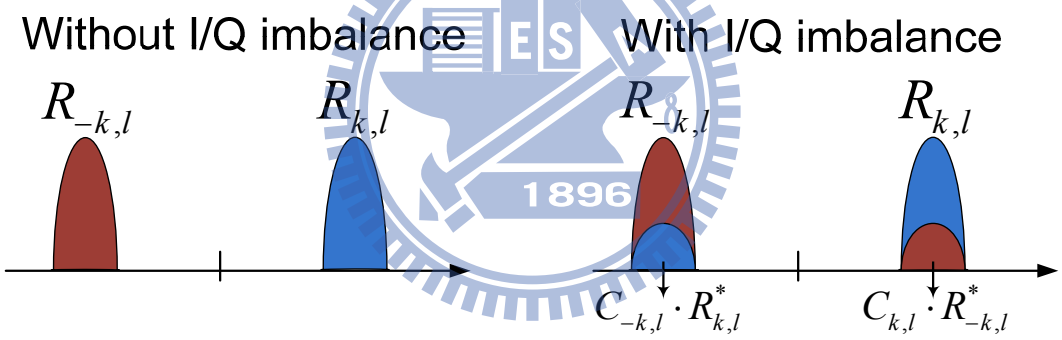

Figure 2-9 The schematic diagram of I/Q imbalance.

2.4.4 Peak-to-Average Power Ratio

Peak-to-Average Power Ratio (PAPR) is calculated from the peak amplitude of the waveform divided by the average power of the waveform [48]. If waveforms have same average power, high PAPR waveforms which have high peak power compared with low PAPR waveforms, as shown in Fig. 2-10. Since the linear region of system is limited, the high PAPR signals are easily distorted. Due to the large power variation for high PAPR signals, these signals

also induce high quantization noise for the digital-to-analog converter (DAC) and ADC. Since some of components have limited input peak power, the output power for the high PAPR signals is limited. Therefore, the high PAPR signals would degrade system performance.

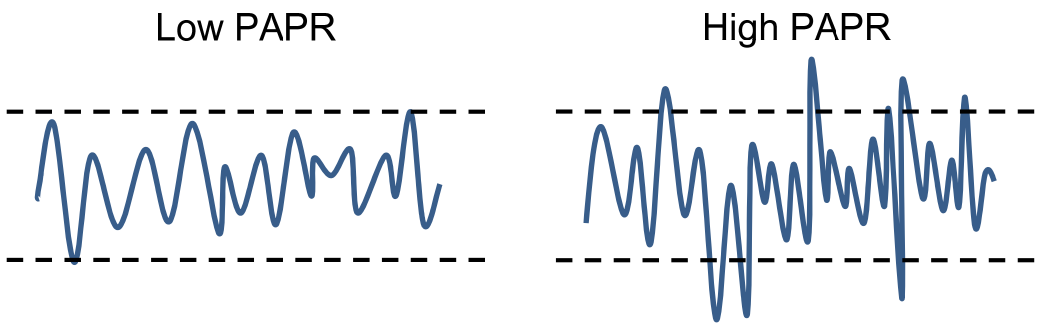

Figure 2-10 The schematic diagram of PAPR.

2.5 Summary

Optical RF signal generations using an external MZM based on DSB and DSBCS modulation schemes are reliable techniques. The DSB modulation signal undergoes performance fading that restricts the fiber transmission distance due to fiber dispersion. Although DSBCS modulation has been demonstrated to be effective in the millimeter-wave range, it cannot generate vector modulation formats which are of utmost importance in wireless applications. The transmission distance of the 60-GHz wireless signal is dramatically restricted in a small range due to the high path losses. The main propagation phenomenon for 60-GHz signal consists LoS, first and second order reflections. Wireless transmitter and receiver were discussed in this chapter. The impairments of 60-GHz RoF systems are also investigated in this chapter. They include inter-symbol interference, fading, I/Q imbalance, and PAPR.

Chapter 3

DIGITAL MODULATION TECHNIQUES

3.1 Preface

In this chapter, we will give the brief overviews for digital signal techniques. The digital modulation formats including 1: single carrier, 2: orthogonal frequency-division multiplexing (OFDM), 3: single-carrier frequency-domain-equalization (SC-FDE), 4: single-carrier frequency-division multiple access (SC-FDMA), 5: single-carrier frequency-division multiplexing (SC-FDM). The digital signal processing for system impairments including: 1. Adaptive bit-loading algorithm, 2: I/Q imbalance compensation algorithm. This chapter also introduces multiple-input multiple-output (MIMO) technique in 3.4.

3.2 Digital Modulation Formats

3.2.1 Single Carrier

The single carrier modulation is a popular modulation format in digital communication systems. A single carrier system modulates a sequence of digital symbols into a high frequency sinusoidal signal called carrier. The modulated signal has three parameters: frequency, phase, and amplitude. Figure 3-1 shows two basic single carrier modulations with one bit per symbol. They are amplitude-shift keying (ASK) and phase-shift keying (PSK) [41]. The ASK signal with one bit per symbol is also called on-off keying (OOK). The PSK signal with one bit per symbol is also called binary PSK (BPSK). For the BPSK signal, the signal has 180 degree phase different between 1 and 0. The

BPSK signal can be expressed as

$$s_1(t) = A\cos 2\pi f_{RF}t \text{ , for 1}$$

$$s_0(t) = A\cos(2\pi f_{RF}t + \pi) = -A\cos 2\pi f_{RF}t \text{ , for 0} \quad (3\text{-}1)$$

where A and f_{RF} are the amplitude and frequency of carrier signal, respectively. The BPSK signals can be graphically represented by a constellation diagram. The constellation diagrams only consider the amplitude and phase information of transmitted signal.

The BPSK signal contains only one bit per symbol which is very low spectral efficiency. Modulation format with high spectral efficiency is very important for wireless communication systems. Figure 3-2 shows the constellation diagrams for the PSK, quadrature PSK (QPSK), and 8PSK signals. The QPSK and 8PSK signal have 2 and 3 bits per symbol, respectively. Based on amplitude and phase modulations, a variety of modulation schemes can be derived from their combinations. For example, by modulating both amplitude and phase of the carrier, we can obtain a scheme called quadrature amplitude modulation (QAM). Figure 3-3 shows the constellation diagrams for the 8QAM, 16QAM, and 32QAM signals. The transmitted $s(t)$ can be express as

$$s(t) = I(t)\cos(2\pi f_0 t) - Q(t)\sin(2\pi f_0 t) \quad (3\text{-}2)$$

where $I(t)$ and Q(t) are the in-phase and quadrature component, respectively. At the receiver, the $I(t)$ and Q(t) can be obtained by multiplying the received signal with cosine and sine signals, respectively.

While transmitting through the channel, the signal suffers distortions, interferences, and noises which may introduce error after demodulation. Therefore, bit-error rate (BER) is the preferred measurement to verify system performance. When the real-time BER measurement is impossible in some of

digital receiver, the BER estimation from the demodulated constellation is very important. The BER of square QAM signal can be related to the signal to noise ratio (SNR):

$$\text{BER} = \frac{2}{\log_2 M} \cdot \left(1 - \frac{1}{\sqrt{M}}\right) \cdot erfc\left(\sqrt{\frac{3 \cdot SNR}{2 \cdot (M-1)}}\right) \quad (3\text{-}3)$$

The SNR can be derived from error vector magnitude (EVM):

$$\text{SNR} = -20 \log (\text{EVM}/100\%) \quad (3\text{-}4)$$

The EVM is defined as the noise power from constellation over the signal power from constellation, as shown in Fig. 3-4. The importance of the above equation is that it relates EVM to BER through the SNR. These equations assume that the noise is Additive White Gaussian Noise (AWGN) [41, 49].

By the way, the channel also induces inter-symbol interference (ISI). The single carrier modulation signal could use feed-forward equalizer or feedback equalizer to improve system performance. The principles of these time domain equalizers are that the equalizers capture a sequence symbols and using adaptive signal processing to find the best weight coefficients for the reduction of impairment of ISI [50-52].

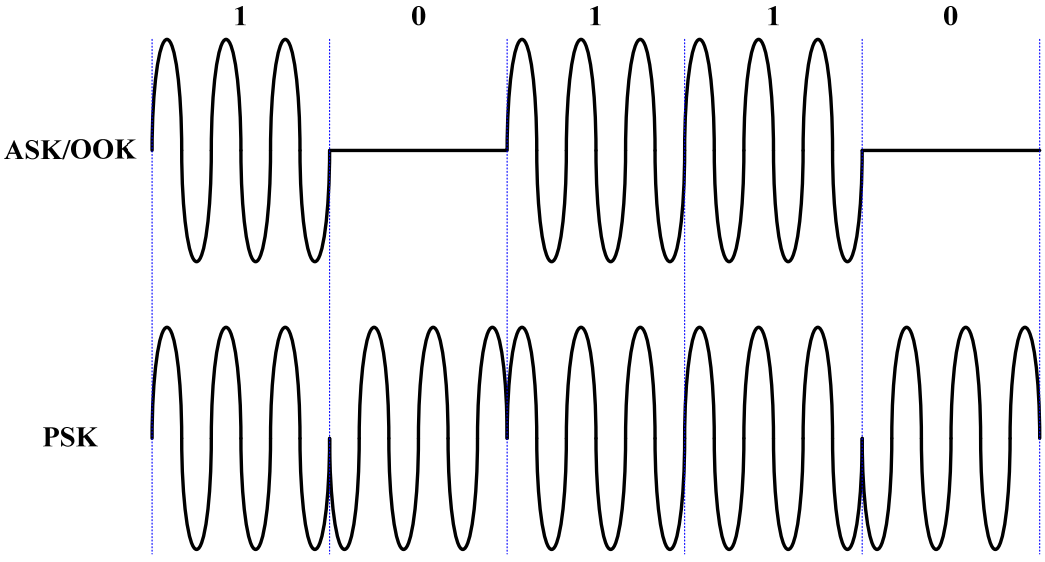

Figure 3-1 The waveform of bandpass modulation signals.

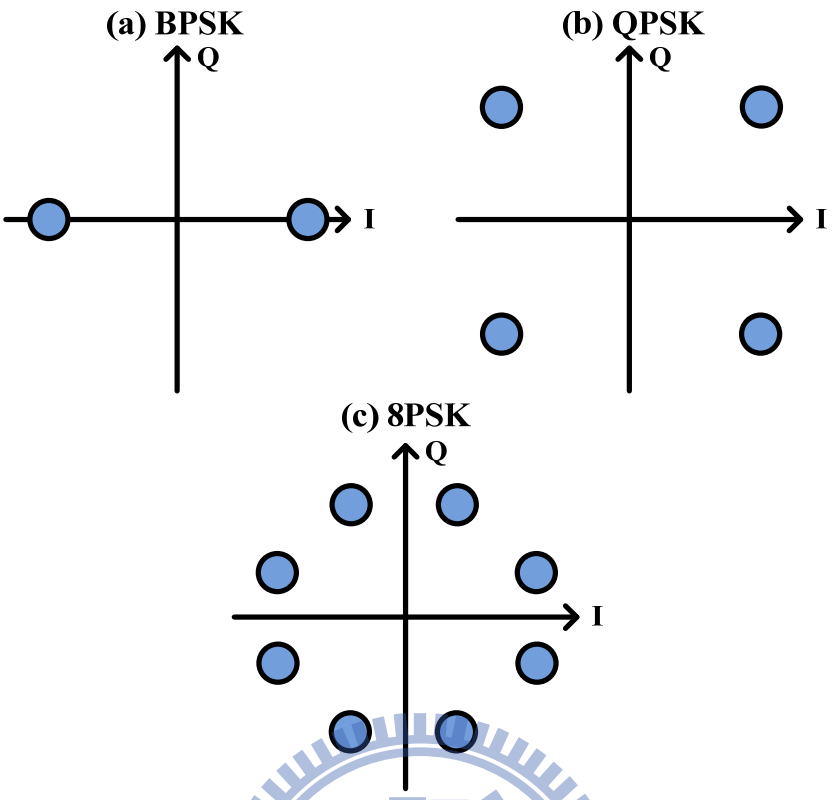

Figure 3-2 Signal constellation: (a) BPSK, (b) QPSK, (c) 8-PSK.

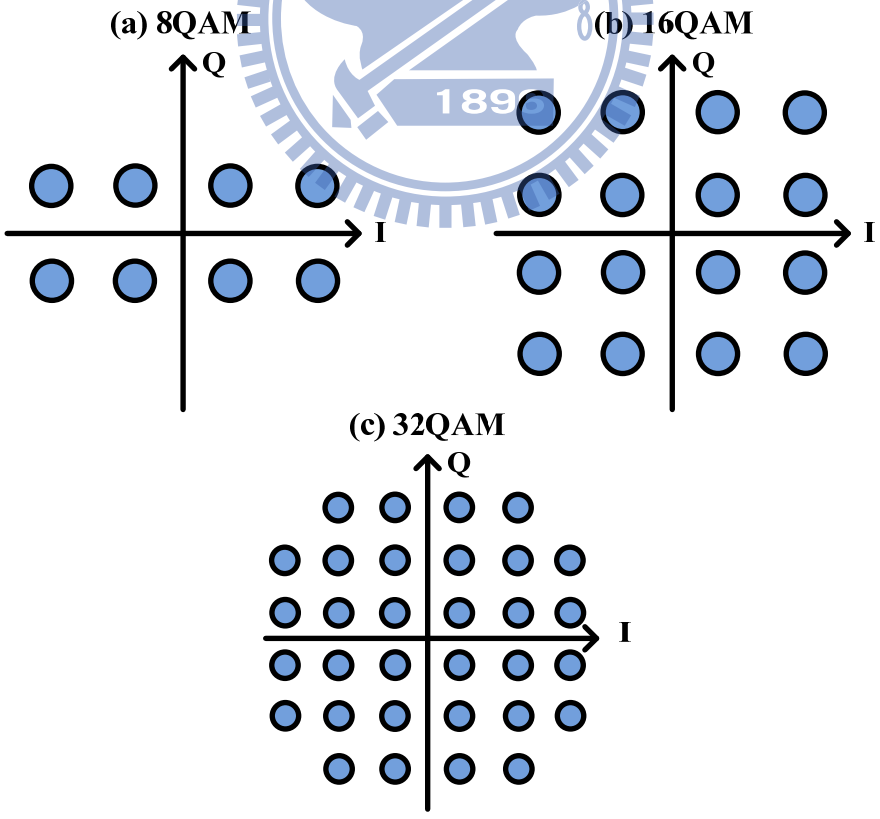

Figure 3-3 Signal constellation: (a) 8-QAM, (b) 16-QAM, (c) 32-QAM.

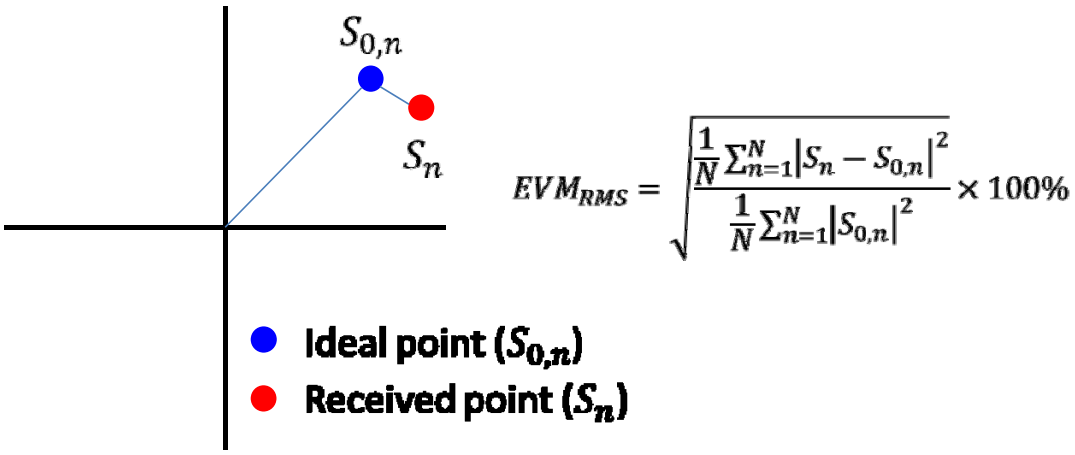

Figure 3-4 The principle diagram of error vector magnitude (EVM).

3.2.2 Orthogonal Frequency-Division Multiplexing

Recently, the multicarrier modulations have attracted significant interest because of many advantages [53-56]. One of advantages is that the symbol rate of multicarrier modulations is much lower than single carrier modulations. Thus the effect of ISI will be reduced and the equalization in the demodulation will be easier than single carrier modulation system with high symbol rate. In order to increase data throughput within limited bandwidth, the frequency spacing between subcarriers is set as low as possible. The minimum frequency spacing between subcarriers is equal to the symbol rate, so that all subcarriers are orthogonal to each other and can be separated without using filter in the receiver. This modulation format is called OFDM.

The block diagram of the OFDM transmitter consists of serial-to-parallel conversion, modulation mapping, inverse fast Fourier transform (IFFT), cyclic prefix (CP) insertion, and digital-to-analog converter (DAC), as shown in Fig. 3-5 (a). The serial binary data sequence is firstly transfer to parallel sequence for each subcarrier. The binary data is mapped onto high order modulation symbols that can enhance spectral efficiency. The symbols are

transferred into time domain waveform through an IFFT. After the IFFT operator, the symbols at different subcarriers are assigned to suitable frequencies which are orthogonal each other. Then, a generated single inserts a waveform referred to as a CP. The CP that is a copy of the last part of the block could provide a guard time to prevent ISI.

The block diagram of the typical OFDM receiver is shown in Fig. 3-5 (b). This demodulation process includes synchronization, fast Fourier transform (FFT), equalization, and symbol decoding. After timing synchronization by using training symbols, the FFT operator is used to transfer time domain signal to frequency domain. The channel information can be found from received training symbols. Due to the bandwidth of one subcarrier is fairly narrow for OFDM signals, the equalization can be implemented by just multiplying a value for each subcarrier. This equalization is called one-tap equalization or frequency domain equalization.

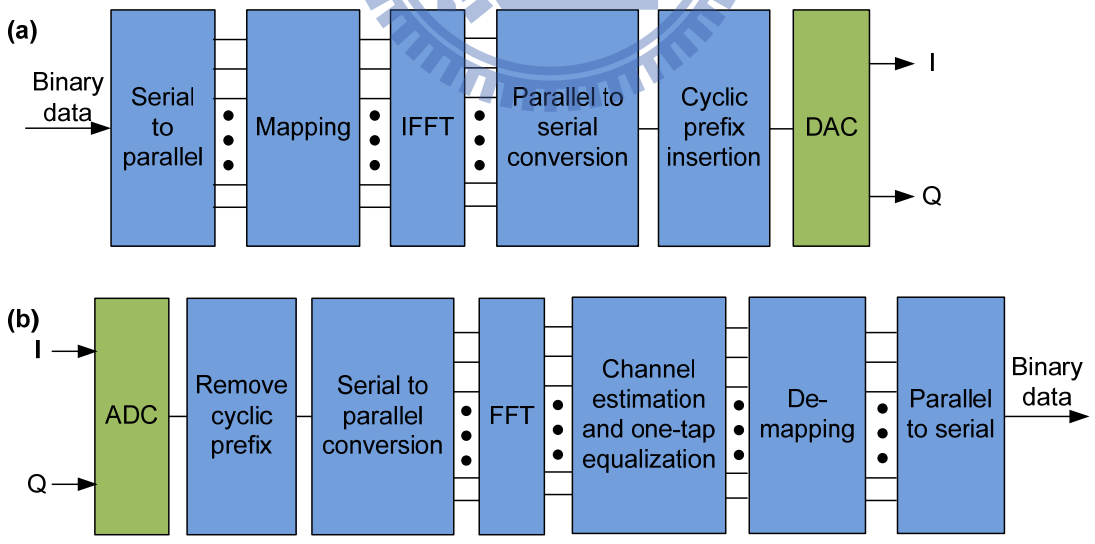

Figure 3-5 Block diagrams of OFDM transmitter (a) and receiver (b). (IFFT: inverse fast Fourier transform, DAC: digital-to-analog converter, ADC: analog-to-digital converter, FFT: fast Fourier transform)

3.2.3 Single-Carrier Frequency-Domain-Equalization

The drawback of OFDM signals is the high peak-to-average power ratio (PAPR). The OFDM signal is the sum of all the subcarriers. If many subcarriers are in phase for some input data, the signal would have high peak power. There are some issues for high PAPR signal. Because the system is not completely linear, the high peak power of a signal would be clipped by the system. Therefore, the high PAPR signals are easily distorted and cause performance degradation. On the other hand, since the high PAPR signals have large power distribution, the signal would suffer more quantization noise and also induce performance degradation. Moreover, some of components limit the peak power of the signal. The system would have less power budget that would limit the transmission length. Due to these reasons, high PAPR become a big issue for the OFDM signal.

The equalizer is needed to compensate ISI that is introduced by the multipath propagation channel. The traditional single carrier signal use conventional time domain equalizers that are not practical for the broadband signal because of the long channel impulse response in the time domain. Therefore, the FDE is more practical for the 60 GHZ systems with broadband channels. The transitional single carrier signal has low PAPR, but without using frequency domain equalization (FDE). If we can combine the advantage of OFDM and single carrier signal, this SC-FDE signal would have higher quality than the OFDM and traditional signal carrier signal. Therefore, the SC-FDE is used in this research [57, 58].

Figure 3-6 shows the basic idea of the time domain equalizer and the FDE. The input signal and channel impulse response are x and h, respectively. The

received signal y is the convolution of the input signal x and channel response h in time domain. For the linear time invariant system, the convolution operation between the time-domain signal and channel response is equal to a multiplication operation in frequency domain.

However, the Fourier transform of the entire data sequence is not a practical solution. Thus, the signal is separated to several blocks which are equal to the defined FFT size. As the FFT is the implementation of a circular convolution, adding CP to the signal maintains the continuity of the signal. Therefore, the principle of SC-FDE is almost the same with OFDM signal. The advantage of frequency domain equalizer is only a one-tap equalizer is needed. When the broadband signal suffers a serious ISI, the time domain equalizer needs more taps to compensate for system performance which increase the computation requirement of the algorithm. On the other hand, the FDE only needs to increase the length of CP and FFT size. Although, larger FFT size also increase the computation requirement but increase the number of processing symbols. Different CP size only increase overhead of signal but does not increase processing complexity.

Figure 3-7 shows the block diagram of SC-FDE transmitter and receiver. The transmitter is almost the same with traditional single carrier modulation. The only difference is the SC-FDE needs additional overhead that is CP for FDE. At the receiver side, the CP is removed from the signal and then transfer to the frequency domain using FFT operator. The FDE is used to compensate for ISI. Due to the original signal is in time domain, the IFFT operator is used to transfer the frequency domain signal to time domain after equalization.

There are some similarities and differences between OFDM and SC-FDE.

The similarities are the FFT based implementations with CP and FDE. The difference are: the SC-FDE has FFT and IFFT at the receiver, whereas OFDM has the IFFT at the transmitter and the FFT at the receiver. SC-FDE has lower PAPR than OFDM. SC-FDE has lower sensitivity to the carrier frequency offset than OFDM. SC-FDE could not use adaptive bit and power loading, whereas OFDM could use adaptive bit and power loading. Because the SC-FDE has lower complexity at the transmitter, the SC-FDE is very suitable for the uplink of communication system.

By the way, equalizer coefficients play important roles in FDE to compensate for ISI. The OFDM signal uses train symbol to find equalizer coefficients. Therefore, the SC-FDE signal also needs train symbol. However, the SC-FDE signal has different power for different frequency subcarriers. Due to this reason, some subcarriers easily suffer noise interference and hard to find correct equalizer coefficients. One solution is that the SC-FDE systems use the OFDM train symbol. Nevertheless, the OFDM train symbol have high PAPR problem. Consequently, the Zadoff-Chu sequence is used to solve this problem. A Zadoff-Chu sequence is a complex-valued sequence which has constant power in time domain and frequency domain [59]. Therefore, this sequence provides low PAPR train symbols in time domain and without power variation in frequency domain.

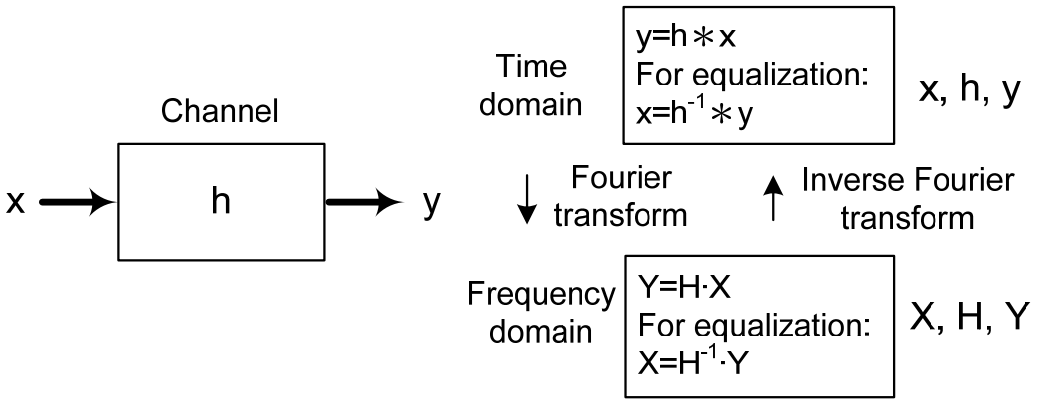

Figure 3-6 Basic idea for frequency domain equalization.

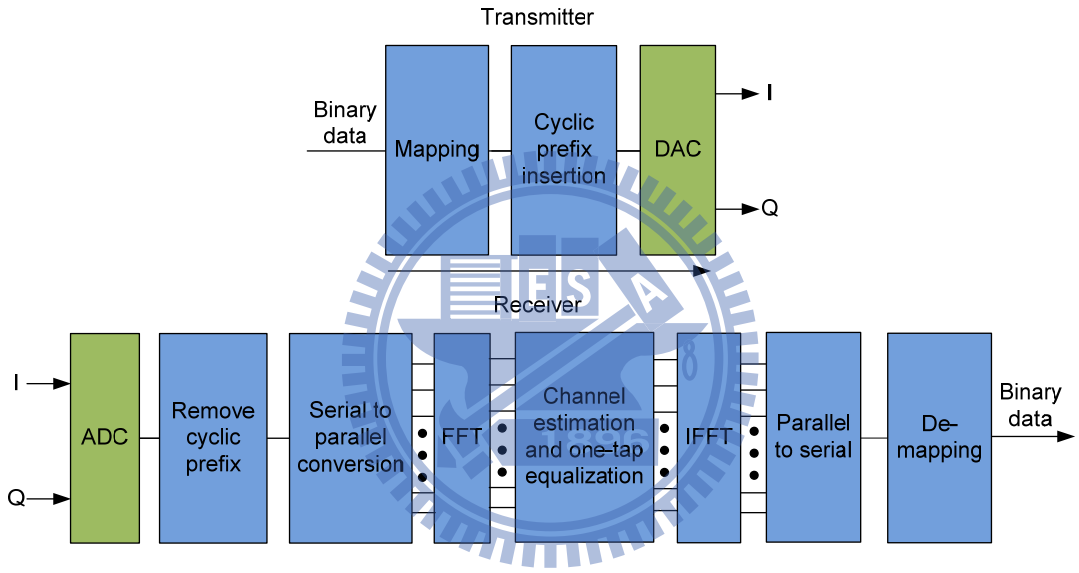

Figure 3-7 Block diagrams of SC-FDE transmitter and receiver.

3.2.4 Single-Carrier Frequency-Division Multiple Access

Before start with SC-FDMA modulation format, we introduce orthogonal frequency-division multiple access (OFDMA) modulation format first. The OFDMA modulation format is a multi-user version of OFDM modulation scheme [60, 61]. Different users have different channel. The OFDMA could assign suitable subcarriers for different users. However, the OFDMA has the same problem, which is high PAPR issue, with the OFDM signal. Signal with a high PAPR require high linearity components to avoid inter-modulation

distortion. Therefore, the SC-FDMA signal is proposed to provide better system performance for multi-user system. The OFDMA modulation format is a multi-carrier signal whereas SC-FDMA modulation format is a single carrier signal. Because of this reason, the SC-FDMA modulation format has lower PAPA than OFDMA modulation format.

Figure 3-8 shows the concept of SC-FDMA generation and demodulation system for uplink [48, 62]. Therefore, the system has several transmitters. The principle of SC-FDMA comes from SC-FDE system. Due to the IFFT is the inverse operator of a FFT, the block diagram of SC-FDE transmitter could be change as Figure 3-9. The original binary data sequence is sent into a vector signal modulator to map the original data onto a constellation. Then, a serial data sequence transfer to a parallel data sequence by using serial to parallel converter. In order to provide multi-user version, the FFT length need to be reduced. The FFT length of system depends on user bandwidth. The N-points modulation symbols X_n provide N-points output symbols in frequency domain by using N-points DFT operator. The SC-FDMA generator then maps several set of N-points output symbols to M orthogonal subcarriers. Then, an IFFT convert the frequency domain signal into a time domain signal. Then, CP, which is a copy of the end of the block and provides a guard time to prevent ISI, is inserted to the start of the generated time domain signal.

Two mapping methods will be introduced in this thesis. Figure 3-10 shows a distributed subcarrier mapping and a localized subcarrier mapping. In the distributed subcarrier mapping the N-points output symbols are distributed within the entire channel bandwidth that has M subcarriers. In the localized subcarrier mapping, the N-points output symbols are assigned to adjacent

frequency subcarriers. The SC-FDMA signal with distributed subcarrier mapping is named DFDMA. The LFDMA is the SC-FDMA signal with localized subcarrier mapping. The other M-N subcarriers, which are not occupied by data symbols, are assigned to be zero. If the occupied subcarriers are with equal frequency spacing in distributed mapping method, this mapping method is also named interleaved subcarrier mapping. The interleaved subcarrier mapping of SC-FDMA is interleaved FDMA (IFDMA) which is a special case of DFDMA [63, 64].

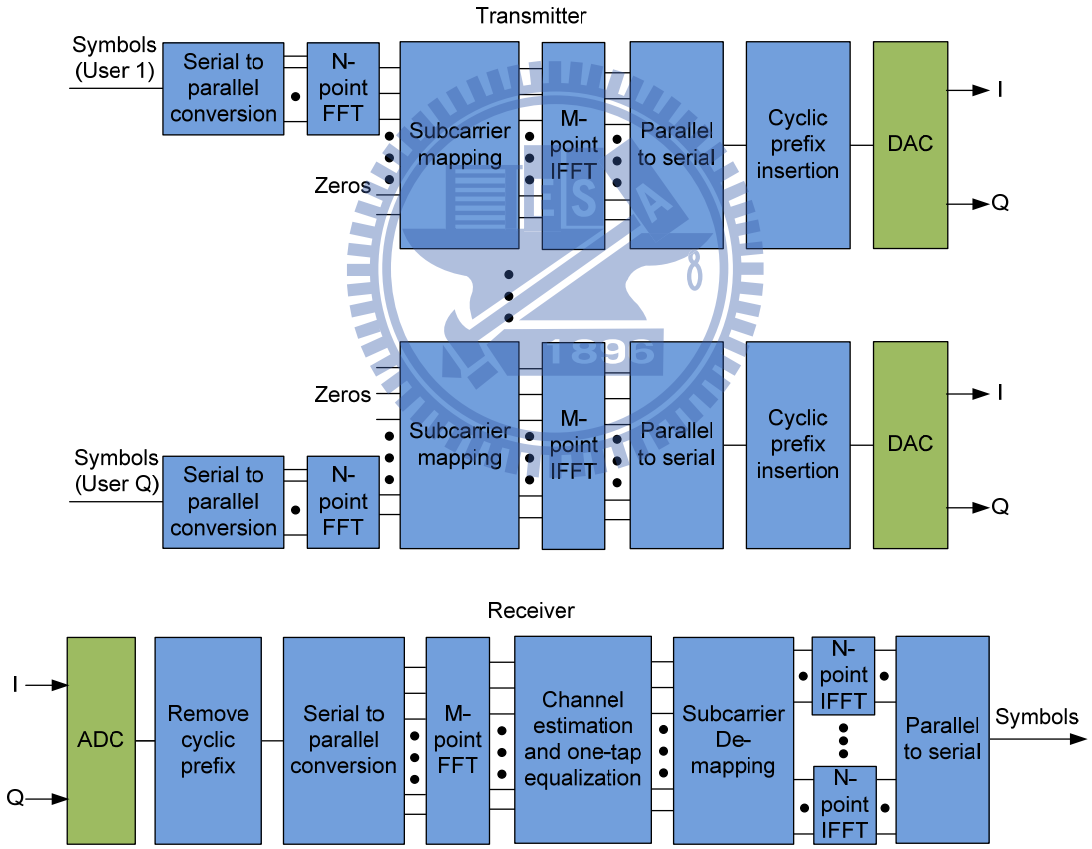

Figure 3-8 Block diagrams of SC-FDMA transmitter and receiver.

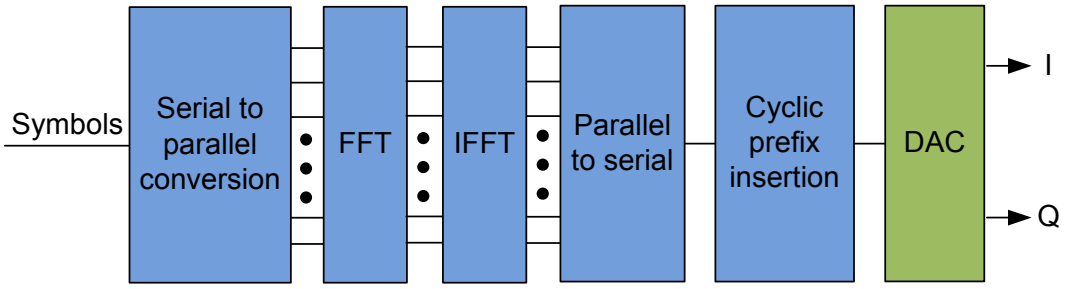

Figure 3-9 Block diagrams of SC-FDE transmitter.

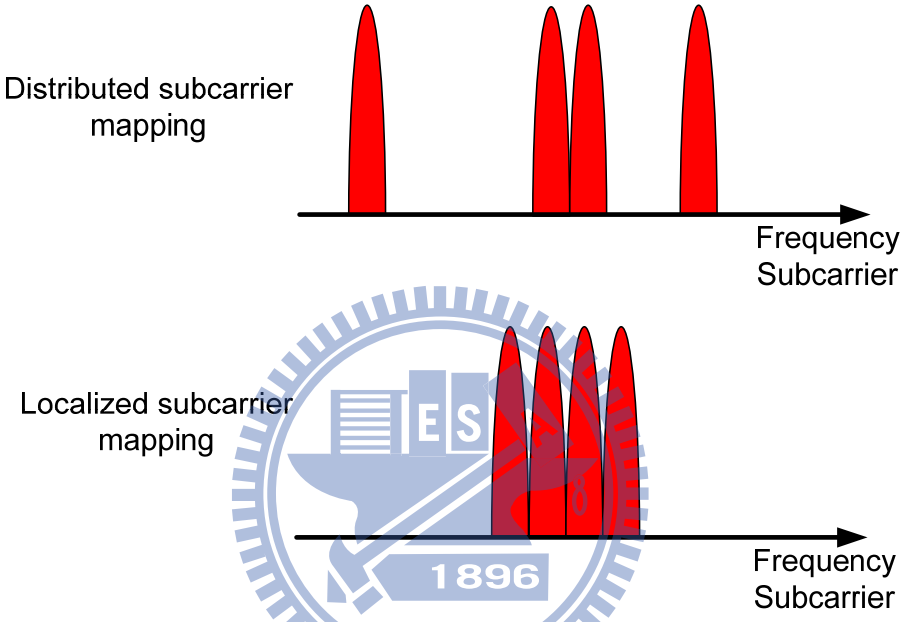

Figure 3-10 The distributed and localized subcarrier mapping modes for one user of SC-FDMA signal.

3.2.5 Single-Carrier Frequency-Division Multiplexing

From previous description, different user uses different subcarriers. However, this thesis focuses on 60-GHz RoF system with only one transmitter which could provide high data throughput. Therefore, this thesis proposed a novel modulation format that looks like SC-FDMA signal as shown in Fig. 3-11. The proposed modulation format is named single-carrier frequency-division multiplexing (SC-FDM). The concept of SC-FDM combines the signal processing for different users. The difference between

SC-FDM and SC-FDMA modulation formats are the serial to parallel converter, FFT, and IFFT operator. Since the proposed modulation format wants to occupy the full channel bandwidth, the serial to parallel converter needs to provide M symbols from M/N N-points FFT operators. Because the IFFT is a linear operator, the generator only needs one IDFT operator to convert the signal which is the combination of M symbols from frequency domain to time domain. Since the SC-FDMA receiver demodulate the signal from all users at the same time, the SC-FDM modulation scheme has the same receiver.

Figure 3-12 shows the conceptual diagrams of SC-FDM with interleaved subcarrier mapping and localized subcarrier mapping. The figures show that the signals consist of three groups. The SC-FDM signal with interleaved subcarrier mapping is named SC-IFDM. The SC-LFDM is the SC-FDM signal with localized subcarrier mapping. When there is only one group in the signal, the signal is the SC-FDE modulation format. When the number of groups equals to IFFT size, the signal is very similar to OFDM modulation format.

Compared with OFDM signal, the advantage of the proposed modulation format is the low PAPR. This thesis use numerical analysis to investigate the PAPR properties for SC-FDE and OFDM signals. Using Monte Carlo simulation, this thesis calculates the complementary cumulative distribution function (CCDF) of PAPR. The $\Pr(\text{PAPR}>\text{PAPR}_o)$ is the probability that PAPR is higher than PAPR_o [65, 66]. Figure 3-13 shows the CCDF curves of PAPR for SC-FDE, SC-IFDM, SC-LFDM, and OFDM. The SC-FDM transmitter uses square-root-raised-cosine filter with 0.05 roll-off factor. The results show that the SC-FDM signals have lower PAPR than OFDM signal.

Since different modulation formats could be assigned to different group,

adaptive bit-loading technology can be also utilized in SC-FDM signals. Table 3-1 shows the performance of different modulation formats. The property of SC-FDM signal that depend on the number of groups is between OFDM and single carrier signal. Compared with OFDM and single carrier, SC-FDM can adapt to different environments. If the system has serious uneven frequency response and good linearity, the system needs more groups. Otherwise, the system needs fewer groups.

Different mapping methods also induce different system performances. Localized subcarrier mapping and interleave subcarrier mapping are used in this experiment. For the SC-LFDM signal, the modulation symbols for a single group are assigned to adjacent subcarriers. In the interleaved subcarrier mapping, the modulation symbols for a single group are separated evenly within the entire channel bandwidth. Because of the single group of SC-LFDM signal is centralized in frequency domain, the signal will get more benefit from adaptive bit-loading algorithm. For the SC-IFDM signal, a single group of signal is separated into the used bandwidth. Therefore, the SC-IFDM signal does not get much benefit after bit-loading algorithm. However, the advantage of the SC-IFDM signal is the lower PAPR compared with the SC-LFDM signal.

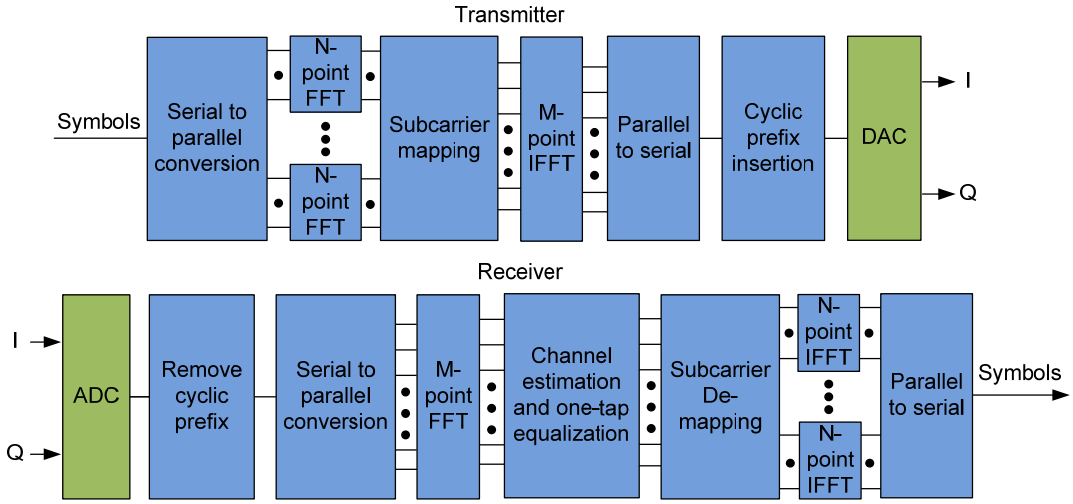

Figure 3-11 Block diagrams of proposed SC-FDM transmitter and receiver.

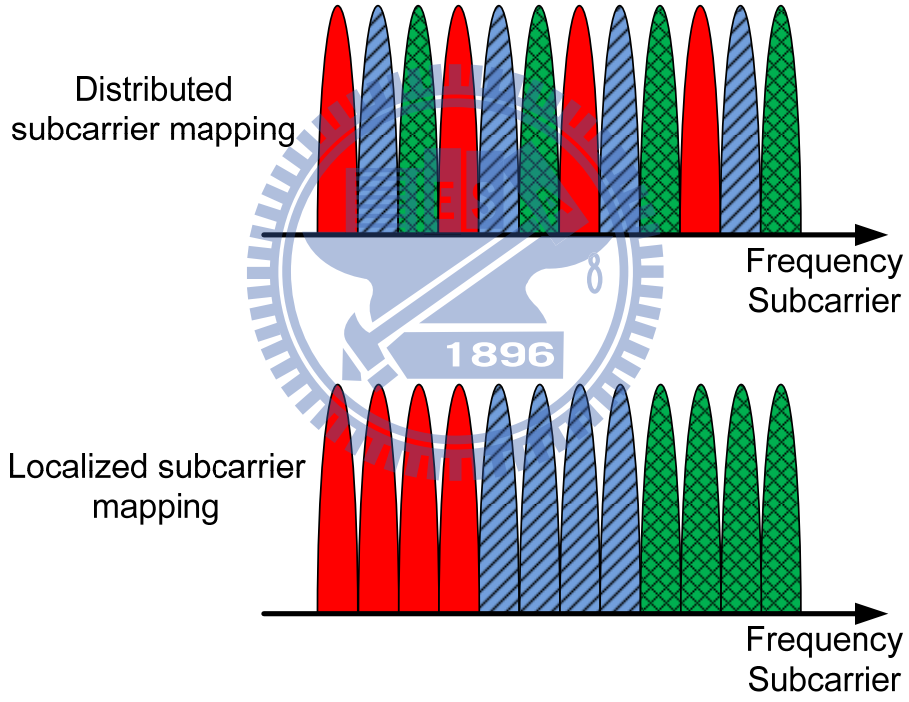

Figure 3-12 The distributed and localized subcarrier mapping modes for SC-FDM signal with 3 groups.

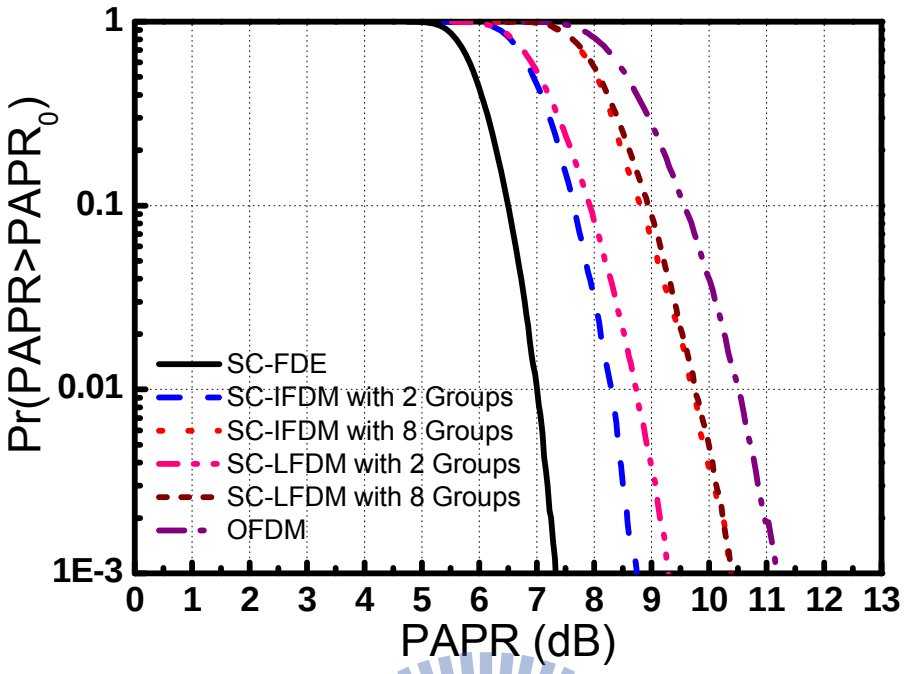

Figure 3-13 Comparison of CCDF of PAPR for SC-FDE, SC-IFDM, SC-LFDM, and OFDM with 512 subcarriers.

Table 3-1 The properties of different modulation format.

Properties\Modulation	Single Carrier	OFDM	SC-FDE	SC-FDM
PAPR	Low	High	Low	Middle
Equalizer	Complex	Simple	Simple	Simple
Transmitter	Simple	Middle	Simple	Complex
Receiver	Complex	Simple	Middle	Middle
Bit-loading	No	Yes	No	Yes
I/Q Imbalance	Time	Frequency	Frequency	Frequency

3.3 Digital Signal Processing for System Impairments

3.3.1 Adaptive Bit-loading Algorithm

Since the 60-GHz communication systems suffers from uneven channel frequency response [26, 29], the system performance is dominated by the

subcarrier/group with poorest error performance. The adaptive power and bit loading for each subcarrier/group is a good solution to increase the overall system performance and total data-capacity with the same communication system [67-69]. The adaptive bit-loading algorithm could maximize total data throughput within a target BER. Due to the BER for each subcarrier is the function of SNR and modulation format, a suitable modulation format can be decided dependent on the SNR and target BER for different subcarrier/group. For example, the BER for a square M-ary QAM signal is shown in eq. (3-3). This equation could be rewritten as

$$\boldsymbol{SNR_{norm}} = \frac{[erfc^{-1}(\frac{2\cdot \mathrm{BER\_target}}{4})\cdot\sqrt{2}]^2}{3} > \frac{\boldsymbol{SNR}}{\boldsymbol{M-1}}. \tag{3-5}$$

From this equation, the BER for a M-ary QAM single with SNR lower than the target BER can be obtained. Therefore, the total data throughput could be expressed as

$$\boldsymbol{b} = \sum_{n=1}^{N} \mathbf{log_2}(\boldsymbol{M}) = \sum_{n=1}^{N} \mathbf{log_2}(\mathbf{1} + \frac{\boldsymbol{P_n \cdot SNR_n}}{\boldsymbol{SNR_{norm}}}) \tag{3-6}$$

where b is bits per symbol, n is the subcarrier/group index, N is total subcarriers/groups, $\boldsymbol{P_n}$ is the power for each subcarrier/group, and the $\boldsymbol{SNR_{norm}}$ is the function of target BER. Then, the water-filling algorithm is used to find the optimal corresponding power weighting factor for each subcarrier to maximize data throughput. Because total power of a signal is fixed, this algorithm will provide more power for high SNR subcarrier/group to maximize data throughput as shown in Fig. 3-14. However, this algorithm may produce non-integer bit number per symbol. Therefore, the program will find rounding of integer bit number for this experiment. Finally, the optimized

signal is generated using the optimal results of the power weighting factor and modulation formats as shown in Fig. 3-15.

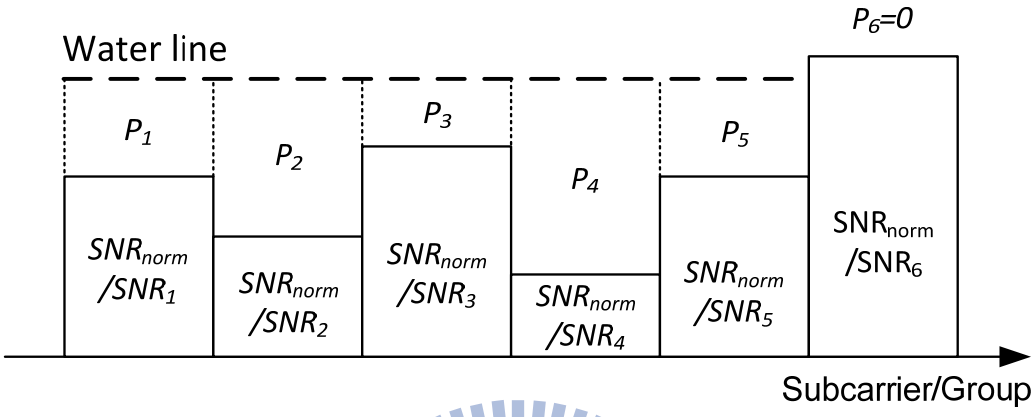

Figure 3-14 The principle diagram of water filling algorithm.

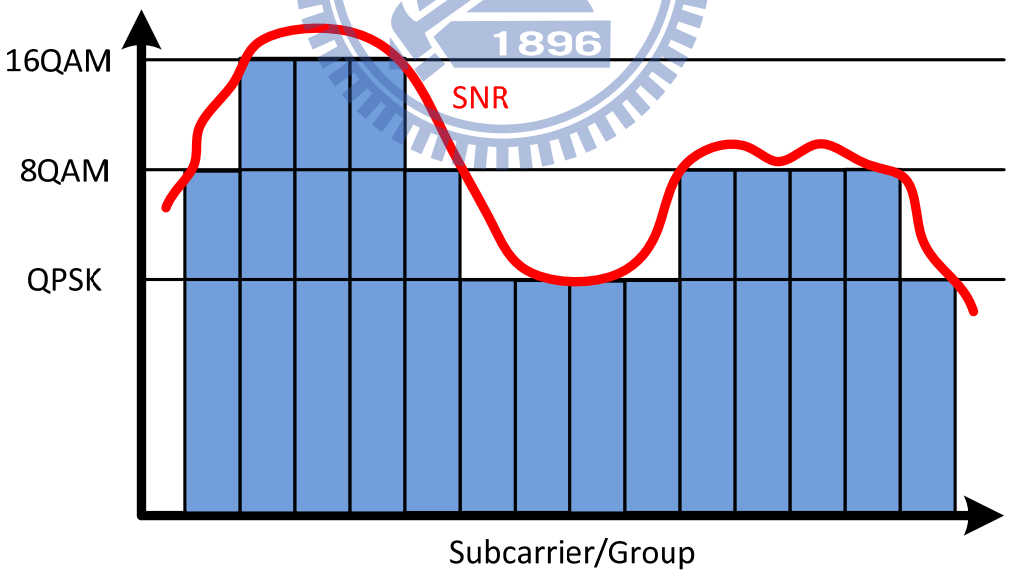

Figure 3-15 The principle diagram of adaptive bit-loading algorithm.

3.3.2 I/Q Imbalance Compensation Algorithm

The I/Q data transmit over different paths to the mixer, resulting in amplitude mismatch and conjugate misalignment. These mismatches will significantly degrade the system performance. The possible origins of the amplitude mismatch can be the difference between the input powers of the I/Q signals, the different conversion loss of mixer of I/Q paths, and the imperfect splitting ratio of local oscillator (LO) between I/Q paths. Furthermore, conjugate misalignment arises from that the LO does not provide an exact 90^{o} phase shift between the I and Q. The amplitude mismatch can cause signal distortion, and the conjugate misalignment causes interference between I and Q signals. These effects can be expressed analytically:

$$s(t) = a \cdot I(t)\cos(2\pi f_0 t) - Q(t)\sin(2\pi f_0 t + \theta) \tag{3-7}$$

where a and θ are the amplitude mismatch and the conjugate misalignment parameter, respectively. Figure 3-16 presents the concept of amplitude mismatch and conjugate misalignment. While Fig. 3-16 (a) exhibits the ideal constellation of a square 16-QAM signal, the amplitude mismatch results in unequal powers of the I/Q signals shown in Fig. 3-16 (b). Moreover, the conjugate misalignment leads an oblique constellation depicted in Fig. 3-16 (c). To solve the issue of I/Q imbalance, the Gram–Schmidt orthogonalization procedure (GSOP) is proposed [70], and the procedure consists of three key steps:

$$I(t) = \frac{r_I(t)}{\sqrt{P_I}} \tag{3-8}$$

$$Q'(t) = r_Q(t) - \frac{\rho r_I(t)}{P_I} \tag{3-9}$$

$$Q(t) = \frac{Q'(t)}{\sqrt{P_Q}} \tag{3-10}$$

where $r_I(t)$ and $r_Q(t)$ are I/Q components of the received signal, and $I(t)$ and $Q(t)$ are the I/Q signals after GSOP processing. The other parameters are $\rho = \mathrm{E}\{r_I(t) \cdot r_Q(t)\}$, $P_1 = \mathrm{E}\{r_I^2(t)\}$, and $P_1 = \mathrm{E}\{Q'^2(t)\}$, where $\mathrm{E}\{\cdot\}$ denotes the expected value operator. Firstly, Eq. (3-8) indicates the normalization of the I signal. Then, minimizing the interference between the I/Q signals and normalizing the Q signal described by Eqs. (3-9) and (3-10) are adopted to obtain the balanced I/Q signals. These I/Q imbalance compensation algorithm in time domain can be used to reduce the imbalance effect.

However, each subcarrier has different imbalance coefficient especially for wideband signals. Therefore, it is difficult to maintain the I/Q balance at total subcarriers by using time domain compensation algorithm. Therefore, an adaptive I/Q imbalance compensation algorithm in frequency domain is needed to compensate the wideband signal [71-75]. As shown in Fig. 3-17, the amplitude and phase imbalance would contribute an additional interfering component at image frequency and induce signal performance degradation. The center frequency of the subcarrier at index $-k$ exactly coincides with the image at the center frequency of the subcarrier at index k. The interfering components at image frequency will severely worsen the performance of the system. An adaptive I/Q imbalance compensating in frequency domain is proposed to remove I/Q imbalance for each subcarrier. While compensating the desired subcarrier, the influences on the image subcarrier should be eliminated.

$$\begin{bmatrix} y(k) \\ y^*(-k) \end{bmatrix} = \begin{bmatrix} C(k) & C(k') \\ C^*(-k') & C^*(-k) \end{bmatrix} \cdot \begin{bmatrix} x(k) \\ x^*(-k) \end{bmatrix} \tag{3-11}$$

This equation shows the I/Q imbalance effect in frequency domain, where x is input vector, C is imbalance coefficient vector, y is output vector with imbalance issue, and k denotes k-th frequency subcarrier. Since the I/Q imbalance is time invariant, the imbalance matrix is easy to be optimized by using training symbols. Compared with the input and output of training symbols, the imbalance matrix could be obtained. The inverse of imbalance matrix could be used to remove I/Q imbalance from received data. The recovered signal could be express as this equation,

$$\begin{bmatrix} \hat{x}(k) \\ \hat{x}^*(-k) \end{bmatrix} = \begin{bmatrix} C(k) & C(k') \\ C^*(-k') & C^*(-k) \end{bmatrix}^{-1} \cdot \begin{bmatrix} y(k) \\ y^*(-k) \end{bmatrix} \quad (3\text{-}12)$$

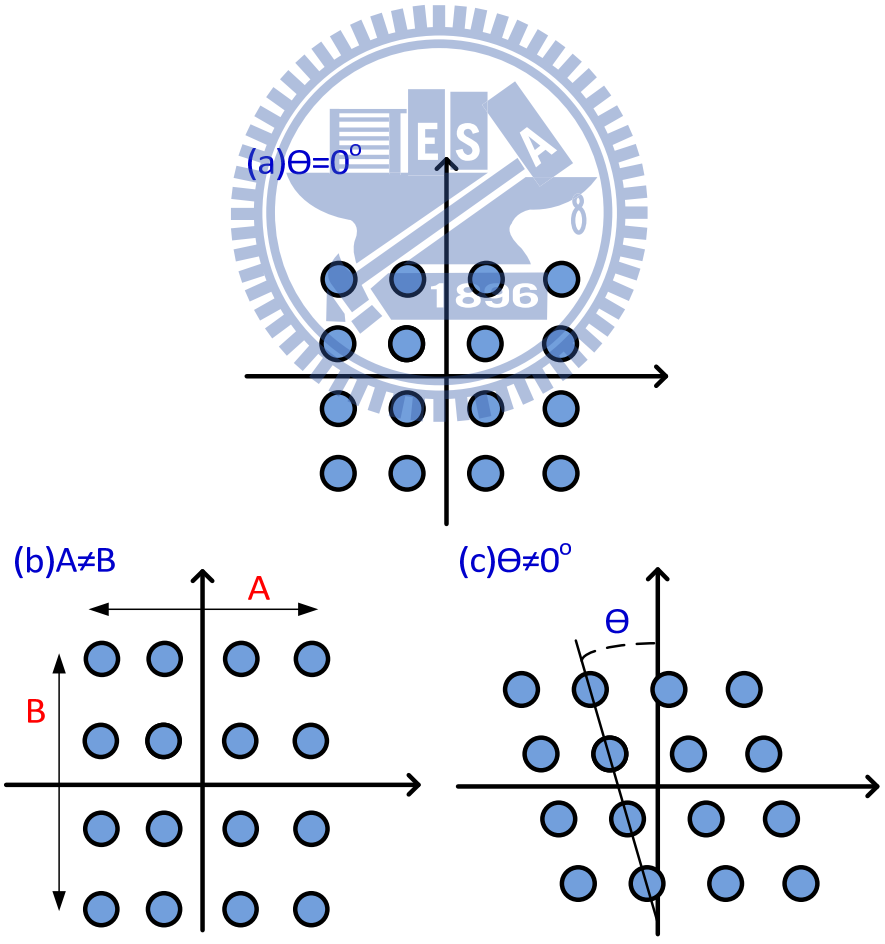

Figure 3-16 The principle diagram of Gram–Schmidt orthogonalization procedure (GSOP).

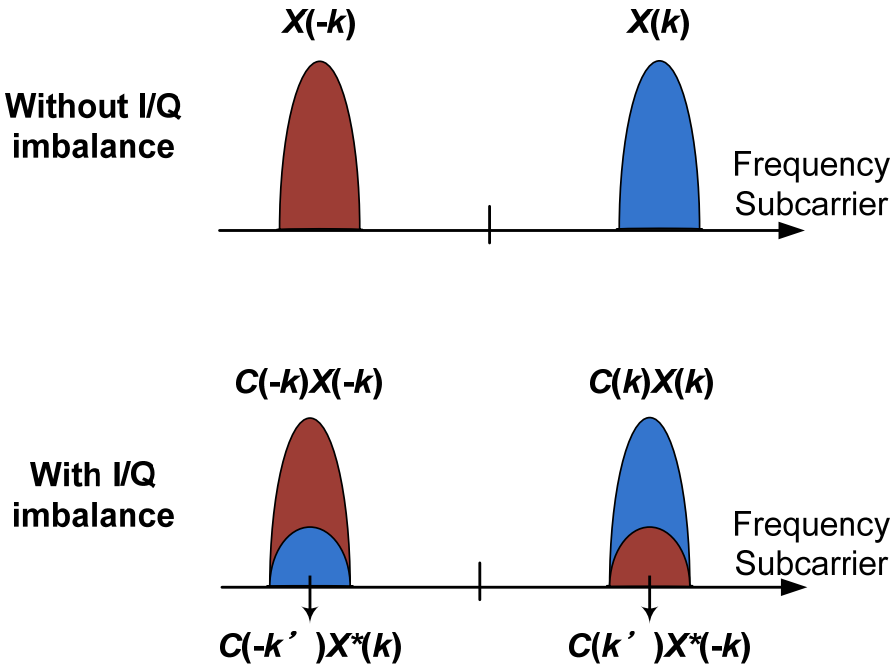

Figure 3-17 The effect of I/Q imbalance in frequency domain.

3.4 Multiple-Input Multiple-Output

The data throughput of communication system proportions to the bandwidth of wireless and the SNR. However, the bandwidth of wireless system is limited and it is hard to increase the SNR of a system. One of powerful techniques to improve data throughput is the MIMO technology. For the wireless communication system, the MIMO use multiple antennas at both the transmitter and receiver to improve system performance.

Figure 3-18 shows the principle of a MIMO technology [76, 77]. There are M transmitter antennas, and N receiving antennas. The x_i is the transmit signal from transmitter antenna i and the y_j is the receive signal from receiver antenna j. The H is the channel matrix. The h_{ij} is the channel response from transmitter antenna i to receiver antennal j. The signals from different transmitter antennas go through different path and are received by different receiver antennas. The received signal Y is written as

$$Y = \begin{bmatrix} y_1 \\ y_2 \\ \vdots \\ y_N \end{bmatrix} = \begin{bmatrix} h_{11}\, h_{21} \cdots h_{M1} \\ h_{12}\, h_{22} \cdots h_{M2} \\ \vdots \quad \vdots \quad \ddots \quad \vdots \\ h_{1N} h_{2N} \cdots h_{MN} \end{bmatrix} \begin{bmatrix} x_1 \\ x_2 \\ \vdots \\ x_M \end{bmatrix} + \begin{bmatrix} n_1 \\ n_2 \\ \vdots \\ n_M \end{bmatrix} = HX + N \qquad (3\text{-}13)$$

Where H is the N by M channel matrix and N is the AWGN vector.

The advantages of MIMO communication can be divided into three categories, beam-forming, spatial diversity and spatial multiplexing. The beam-forming technology is like a spatial filter. Based on control the phase and gain of each antenna which transmits identical waveform, the direction of antenna beam would change because of constructive or destructive interferences in different directions. Therefore, this technology could increase the gain of transmitter and receiver antenna and reduce the multipath fading effect from channel.

The purpose of spatial diversity is to enhance the quality of signal [77]. Since the signal may be reflected, scattered, refracted and even blocked on the way to the receiver, the signal suffered different fading effect at different frequency and time. Because each transmitter antenna locates in different position, the signal transmission path from each antenna is also different. Since multiple transmitter antennas will create different channels, the signal from different antenna has different channel response. If different transmitter antennas send relational signal, the signal can be recovered when one path is blocked.

One of the powerful techniques is spatial multiplexing [76]. The spatial multiplexing means that different transmitter antenna send different signal at the same frequency in the same time. The signals transmit over the wireless channel and received by the receiver antenna array. If multiple transmit signals can be recover in the receiver side after demodulation, the system capacity can

be improved by this technique. This thesis focuses on the spatial multiplexing. For the 2x2 MIMO scheme, the system could be express as this equation,

$$\begin{bmatrix} y_1 \\ y_2 \end{bmatrix} = \begin{bmatrix} h_{11} h_{21} \\ h_{12} h_{22} \end{bmatrix} \begin{bmatrix} x_1 \\ x_2 \end{bmatrix} + \begin{bmatrix} n_1 \\ n_2 \end{bmatrix} \tag{3-14}$$

The transmitted signals could be recovered from received signals by multiply suitable matrix W. The target of W is to have highest quality of recovered signals. The recovered signal could be express as this equation,

$$\begin{bmatrix} \hat{x}_1 \\ \hat{x}_2 \end{bmatrix} = W \begin{bmatrix} y_1 \\ y_2 \end{bmatrix} \tag{3-15}$$

The recover matrix W could be calculate form receiver signals and train signals and express as this equation,

$$W = \begin{bmatrix} x_1 \\ x_2 \end{bmatrix} \begin{bmatrix} y_1 \\ y_2 \end{bmatrix}^{-1} \tag{3-16}$$

The channel matrix is very important in the MIMO system. From mathematics, the condition number of the matrix is a good parameter for analyzing system the performance. The condition number is:

$$c = \frac{\lambda_{max}}{\lambda_{min}} \tag{3-17}$$

Where λ_{max} and λ_{min} are maximal and minimal singular value of matrix, respectively. The higher condition number means the recovery signal is susceptible to noise. The maximal condition number and minimal condition number are infinity and one, respectively.

If channel matrix H equals to $\begin{bmatrix} 10 \\ 01 \end{bmatrix}$, the system could be separated to two independent SISO system. If the signal power from each transmitter antenna is the same, the system have double data throughput. The condition number equals to one in this matrix. On the other case, the channel matrix H equals to $\begin{bmatrix} 10 \\ 10 \end{bmatrix}$. The condition number is infinity. The system could not find the recovery

matrix W and the data throughput equals zero.

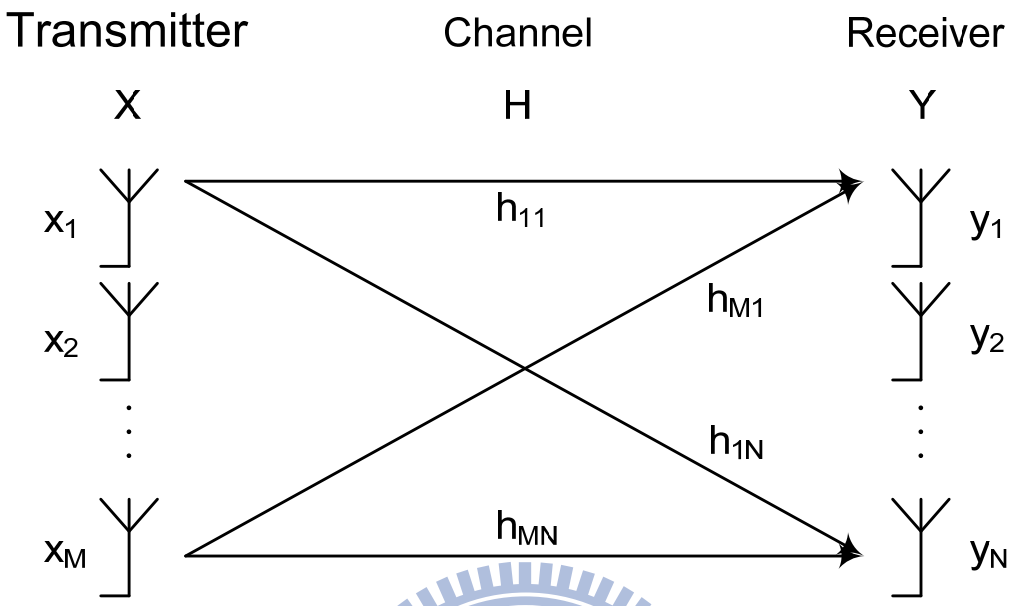

Figure 3-18 MxN MIMO channel model with M transmitter antennas and N receiver antennas.

3.5 Summary

This chapter introduces four digital modulation formats. The properties of these formats are shown in table 3-1. Single carrier signal has low PAPR, but easily suffer ISI. The OFDM signal robust to ISI, but has high PAPR issue. Therefore, the SC-FDE is proposed to provide easily equalization in frequency domain and reduce ISI by adding CP. However, the complex receiver is needed to demodulate signals. Moreover, the SC-FDE could not provide bit-loading for signal generation. Therefore, the SC-FDM is proposed to solve these problems. However, the SC-FDM system has complex transmitter and receiver. The adaptive bit-loading algorithm and I/Q imbalance compensation algorithm were investigated. The bit-loading algorithm could increase the total data-capacity with the same communication system by adjusting power and bits per symbol

for each subcarrier/group. The I/Q imbalance compensation algorithm could reduce the impairment of I/Q imbalance effect from non-ideal I/Q mixer. This chapter also introduces MIMO technology that could increase total data throughput by adding transmitter and receiver antennas.

Chapter 4

OPTICAL I/Q UP-CONVERSION RADIO-OVER-FIBER SYSTEM

4.1 Preface

In the previous chapter, we have introduced RoF systems, digital modulation format, and digital signal processing. The generation of optical RF vector signals, using an external Mach–Zehnder modulator (MZM) based on double-sideband (DSB) modulation scheme have been demonstrated [42]. However, the DSB signal undergoes performance fading due to the fiber dispersion. Furthermore, to generate an RF vector signal in a high frequency band, an electrical mixer with a typical conversion loss of more than 8 dB is required to up-convert vector signals to an inter-medium or radio frequency, which degrades the performance of the up-converted RF vector signals, especially at the higher frequency. Recently, the generation of optical RF signals by all optical up-conversion has been extensively investigated [78-83]. However, the corresponding system requires at least two modulators to up-convert the in-phase (I) and quadrature phase (Q) signals, and occupies much more optical bandwidth than traditional DSB modulation schemes [80-83].

This investigation proposes a novel optical RF vector signal generation approach using optical up-conversion and studies its performance both numerically and experimentally. The advantage of this architecture is that it requires no electrical mixer with a typical conversion loss of more than 8 dB to generate the electrical vector RF signal. Furthermore, since the proposed

system generates only one un-modulated optical subcarrier and one modulated optical subcarrier, i.e. optical single sideband (SSB) format, the system does not suffer from RF fading. Since the generated optical signal has one modulated subcarrier and one un-modulated subcarrier, the proposed system can generate not only OOK signals but also PSK, QAM and OFDM signals. Additionally, the relative powers of un-modulated and modulated subcarriers can be easily tuned by adjusting the individual intensities of the electrical sinusoidal waves and data signals to optimize the performance of the RoF system.

However, an important factor that significantly affects system performance is the precision of controlling the amplitude and phase of the input I/Q signals. Therefore, the I/Q imbalance compensation algorithm that compensates for the I/Q imbalance is proposed and demonstrated numerically and experimentally. With I/Q imbalance compensation, both simulation and experimental results verify a significant increase in the tolerance of both amplitude mismatching and conjugate misalignment. In this experiment, a 32.65-Gb/s bit-loading OFDM signal with I/Q imbalance compensation in frequency domain is generated, and the power penalty is negligible after 25km standard single-mode fiber transmission.

4.2 The Concept of Proposed System

Figure 4-1 schematically depicts the proposed frequency quadrupling system employing all-optical up-conversion. The proposed 60-GHz RoF transmitter consists of two dual-parallel MZMs for optical up-conversion and frequency quadrupling, respectively. For all-optical up-conversion, OFDM I and Q signals are sent to MZ-a and MZ-b of the first dual-parallel MZM,

respectively. Next, both MZ-a and MZ-b are biased at the null point to achieve high optical modulation depth and operate in the optical field linear region of MZM. Additionally, direct-detection vector signals are realized by inserting an optical subcarrier as a remote heterodyne scheme through the use of optical single side band modulation with carrier suppression [84]. The electrical sinusoidal signals which have 90^{o} phase difference are sent to MZ-a and MZ-b of the first dual-parallel MZM, respectively. When MZ-c of the first dual-parallel MZM is biased at the quadrature point, the optical phase of LSB would be opposite between the output of MZ-a and MZ-b. The LSB will be cancelled and the USB is still obtained. Therefore, according to inset (a) of Fig. 4-1, the generated optical vector signal consisting of an un-modulated subcarrier and an modulated subcarrier, which can be converted into electrical RF vector signals by square-law photo-diode (PD) detection, can be produced. Unfortunately, the bandwidth of typical dual-parallel MZM is less than 25GHz. The second dual-parallel MZM is needed to provide high frequency application.

Next, the generated optical vector signal is up-converted by using the frequency quadrupling method [85] (inset (b) of Fig. 4-1). When the MZ-a and MZ-b of the second dual-parallel MZM are biased at full point, the optical phase of the odd order sidebands are suppressed. The electrical sinusoidal signals which have 90^{o} phase difference are sent to MZ-a and MZ-b of the second dual-parallel MZM, respectively. When MZ-c of the second dual-parallel MZM is biased at the null point, the optical phase of the zero, fourth, etc order sidebands are opposite between the output of MZ-a and MZ-b. The pure second order sidebands could be obtained.

Following an interleaver to filter out the unwanted sideband, the proposed optical SSB signal is generated, as shown in inset (c) of Fig. 4-1. Notably, the relative intensity between the un-modulated and modulated subcarriers can be modifying by varying the individual power of the electrical sinusoidal and vector signals to optimize the performance of the optical RF signals [86].

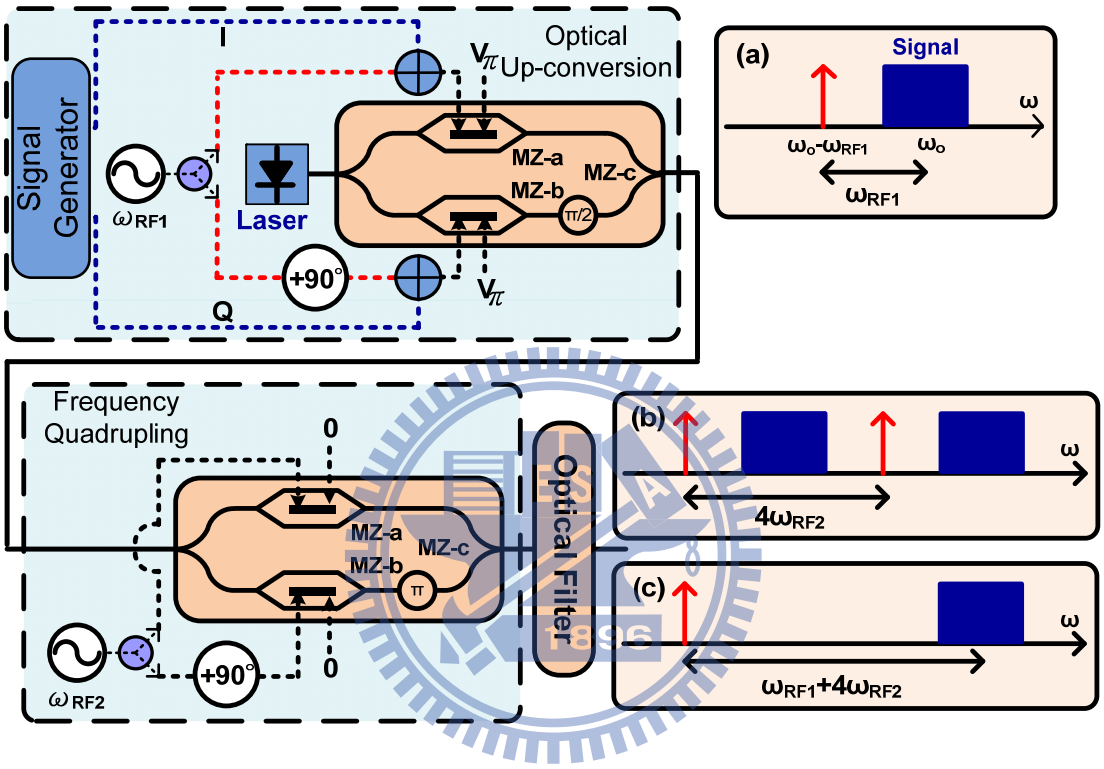

Figure 4-1 Conceptual diagram of the 60-GHz RoF system using all-optical up-conversion.

4.3 Theoretical Calculations and Simulation Results

4.3.1 The Generated Optical Signal

Figure 4-1 presents the proposed optical transmitter to generate a direct-detection wideband optical vector signal. For optical up-conversion, the optical field is modulated by an dual-parallel MZM, which consists of three sub-modulators: two sub-modulators for in-phase modulation (MZ-a) and quadrature-phase modulation (MZ-b), and another sub-modulator (MZ-c) for

controlling the phase difference between MZ-a and MZ-b. The optical field at the input of the dual-parallel modulator is given by $E_{\text{in}}(t) = E_0 \cos(\omega_0 t)$, where E_0 and ω_0 are the amplitude and angular frequency of the optical field, respectively. MZ-a and MZ-b are both biased at the null point, and MZ-c maintains a 90° phase shift between the output signals of MZ-a and MZ-b. The optical field at the output of the transmitter is given by

$$E_{\text{out1}}(t) = -E_{\text{o}} \sin\frac{\pi I(t)}{2V_\pi}\cos\omega_{\text{o}}t + E_{\text{o}} \sin\frac{\pi Q(t)}{2V_\pi}\sin\omega_{\text{o}}t \qquad (4\text{-}1)$$

where $I(t)$ and $Q(t)$ are the in-phase and quadrature-phase data of the vector signal, respectively.

To realize the direct-detection optical vector signals, an un-modulated optical subcarrier is generated at $\omega_0 + \omega_{RF1}$, as shown in Fig. 4-1. Two sinusoidal waves with the same RF frequency (ω_{RF1}) but a 90° phase difference are sent to the MZ-a and MZ-b after being combined with the electrical I/Q signals. Since the bias points of MZ-a and MZ-b are set at the null point, one un-modulated optical subcarrier with carrier suppression is generated at the angular frequency of $\omega_0 + \omega_{RF1}$. The high-order terms and the interference between the un-modulated and modulated subcarriers caused by the nonlinear transfer function of an MZM can be neglected when the modulation depth is small. Accordingly, the optical field at the output of the transmitter can be approximated as,

$$E_{\text{out1}}(t) \cong E_{\text{o}}\{-J_0(m)\sin\frac{\pi I(t)}{2V_\pi}\cos\omega_{\text{o}}t + J_0(m)\sin\frac{\pi Q(t)}{2V_\pi}\sin\omega_{\text{o}}t$$
$$-2J_1(m)\cos[(\omega_{\text{o}} + \omega_{\text{RF1}})\,t]\} \qquad (4\text{-}2)$$

where m is $(V/2V_\pi)\pi$ and V is the amplitude of electrical sinusoidal driving signal. From equation (4-2), the un-modulated subcarrier at $\omega_{\text{o}} + \omega_{\text{RF1}}$ and modulated subcarrier at ω_{o} will be obtained after first dual-parallel modulator.

For frequency quadrupling, the optical field at the input of the second modulator is $E_{\text{in}}(t) = E_0 \cos(\omega_0 t)$. MZ-a and MZ-b are both biased at the maximum transmission point, and MZ-c maintains a 180° phase shift between the output signals of MZ-a and MZ-b. Two sinusoidal waves with the same RF frequency (ω_{RF2}) but a 90° phase difference are sent to the MZ-a and MZ-b. The optical field at the output of the MZ-a and MZ-b of second dual-parallel modulator are given by

$$E_{\text{MZ-a2}}(t) = \frac{E_0}{\sqrt{2}} \cdot \{J_0(m) \cdot \cos(\omega_0 t) + \sum_{n=1}^{\infty} J_{2n}(m) \cdot \cos[(\omega_0 \pm 2n\omega_{RF2})t + n\pi]\} \quad (4\text{-}3)$$

$$E_{\text{MZ-b2}}(t) = \frac{E_0}{\sqrt{2}} \cdot \{J_0(m) \cdot \cos(\omega_0 t) + \sum_{n=1}^{\infty} J_{2n}(m) \cdot \cos[(\omega_0 \pm 2n\omega_{RF2})t]\} \quad (4\text{-}4)$$

The high-order terms caused by the nonlinear transfer function of an MZM can be neglected when the modulation depth is small. Accordingly, the optical field at the output of the second dual-parallel modulator can be approximated as,

$$E_{\text{out2}}(t) = \frac{E_{\text{MZ-a2}}(t)}{\sqrt{2}} - \frac{E_{\text{MZ-b2}}(t)}{\sqrt{2}} \cong -E_0 \cdot J_2(m)\cos[(\omega_0 \pm 2\omega_{RF2})t] \quad (4\text{-}5)$$

If the optical field at the input of the second modulator is $E_{\text{out1}}(t)$, the optical field at the output of the second dual-parallel modulator can be express as

$$E_{\text{out2}}(t) = E_0 \cdot J_0(m_1) \cdot J_2(m_2) \cdot \sin\frac{\pi I(t)}{2V_\pi}\cos[(\omega_0 \pm 2\omega_{RF2})t] - E_0 \cdot J_0(m_1) \cdot J_2(m_2) \cdot \sin\frac{\pi Q(t)}{2V_\pi}\sin[(\omega_0 \pm 2\omega_{RF2})t] - 2E_0 \cdot J_1(m_1) \cdot J_2(m_2) \cdot \cos[(\omega_0 + \omega_{\text{RF1}} \pm 2\omega_{RF2})t] \quad (4\text{-}6)$$

where m_1 and m_2 are the modulation index of first and second MZM,

respectively. From equation (4-2), Four subcarriers will be obtained after second dual-parallel modulator as shown inset (b) of Fig. 4-1.

4.3.2 The Generated Electrical Signal

First, we calculated generated electrical RF signal from equation (4-2). As determined by square-law photo-detection, the beating terms of the modulated and un-modulated signals generate the desired RF vector electrical signal at the frequency of ω_{RF1}, and can be expressed as,

$$I_{\text{out1}}(t) = RJ_0(m)J_1(m)E_o^2[\sin\frac{\pi I(t)}{2V_\pi}\cos\omega_{\text{RF1}}t - \sin\frac{\pi Q(t)}{2V_\pi}\sin\omega_{\text{RF1}}t] \quad (4\text{-}7)$$

where R is the responsivity of the photodiode. Since the modulation depth is small, the equation can be further simplified as

$$I_{\text{out1}}(t) = \frac{\pi}{2V_\pi}RJ_0(m)J_1(m)E_o^2[I(t)\cos\omega_{\text{RF1}}t - Q(t)\sin\omega_{\text{RF1}}t] \quad (4\text{-}8)$$

However, the I/Q data transmit over different paths to the modulator, resulting in amplitude mismatch and conjugate misalignment. These mismatches will significantly degrade the system performance. The possible origins of the amplitude mismatch can be the difference between the powers of the I/Q signals, the different V_π of MZ-a and MZ-b, and the imperfect splitting ratio between MZ-a and MZ-b. Furthermore, conjugate misalignment arises from that the MZ-c does not provide an exact 90^o phase shift between the output signals of MZ-a and MZ-b. The amplitude mismatch can cause signal distortion, and the conjugate misalignment causes interference between the I/Q signals as shown in Fig. 4-2. These effects can be expressed analytically:

$$I_{\text{out1}}(t) = \frac{\pi}{2V_\pi}RJ_0(m)J_1(m)E_o^2[aI(t)\cos\omega_{\text{RF1}}t - Q(t)\sin(\omega_{\text{RF1}}t + \theta) \quad (4\text{-}9)$$

where a and θ are the amplitude mismatch and the conjugate misalignment parameter, respectively. The GSOP algorithm which is based in time domain

can be used to reduce the imbalance effect [70], and it will be revealed by both the simulation and the experimental results.

The VPI WDM-TransmissionMaker™ is used to simulate the effects of I/Q imbalance and the compensation using the GSOP. Figures 4-3 (a) and (b) present the simulation results concerning a QPSK signal. In our simulation, 3 dB amplitude mismatch and 15° conjugate misalignment result in 3.2 dB and 2.3 dB SNR degradation, respectively. The SNR is defined by

$$\text{SNR} = -20 \log (\text{EVM}/100\%) \tag{4-10}$$

where EVM is defined as the noise power from constellation over the signal power from constellation. The SNR degradations of ~0.6 dB and ~0.4 dB corresponding to 3 dB amplitude mismatch and 15° conjugate misalignment, respectively, are achieved by the GSOP compensation. Figures 4-4 (a) and (b) present the cases of 16-QAM signals. While 3 dB amplitude mismatch and 15° conjugate misalignment result in 8 dB and 6.4 dB SNR degradation, the degradation is suppressed to 0.6 dB and 0.9 dB by using the GSOP compensation, respectively. The results clearly reveal the criticality of the I/Q imbalance for the QPSK format and the 16-QAM format and the great performance improvement by the GSOP. The simulation results reveal that the GSOP can remove most penalties caused by the I/Q imbalance for different modulation formats.

Second, we calculated generated electrical RF signal from equation (4-6). The individual square term of this equation will generate the baseband signal, and the cross terms will generate the RF signal. Since the modulation depth is small, these signals can be expressed as

$$I_{\omega_{\mathrm{RF1}}} = -\frac{\pi}{2V_\pi} R J_0(m_1) J_1(m_1) J_2^2(m_2) E_o^2 [I(t) \cos \omega_{\mathrm{RF1}} t - Q(t) \sin \omega_{\mathrm{RF1}} t]$$

$$I_{4\omega_{\mathrm{RF2}}-\omega_{\mathrm{RF1}}} = -\frac{\pi}{2V_\pi} R J_0(m_1) J_1(m_1) J_2^2(m_2)$$
$$\cdot E_o^2\{I(t)\cos[(4\omega_{\mathrm{RF2}}-\omega_{\mathrm{RF1}})t] - Q(t)\sin[(4\omega_{\mathrm{RF2}}-\omega_{\mathrm{RF1}})t]\}$$
$$I_{4\omega_{\mathrm{RF2}}+\omega_{\mathrm{RF1}}} = -\frac{\pi}{2V_\pi} R J_0(m_1) J_1(m_1) J_2^2(m_2)$$
$$\cdot E_o^2\{I(t)\cos[(4\omega_{\mathrm{RF2}}+\omega_{\mathrm{RF1}})t] - Q(t)\sin[(4\omega_{\mathrm{RF2}}+\omega_{\mathrm{RF1}})t]\} \quad (4\text{-}11)$$

The RF signal will generate at ω_{RF1}, $4\omega_{\mathrm{RF2}}-\omega_{\mathrm{RF1}}$, and $4\omega_{\mathrm{RF2}}+\omega_{\mathrm{RF1}}$. Since the RoF want to use low frequency components to generate high frequency RF signal, the desire frequency of generated RF signal is $4\omega_{\mathrm{RF2}}+\omega_{\mathrm{RF1}}$. Moreover, the optical filter can be used to remove some of subcarriers that do not contribute for RoF system. Therefore, the filter will use to filter out optical subcarriers at $\omega_0+\omega_{\mathrm{RF1}}-2\omega_{RF2}$ and $\omega_0+2\omega_{RF2}$ in experiment. The optical filed after filter can be expressed as

$$E_{\mathrm{out2}}(t) = E_{\mathrm{o}}\cdot J_0(m_1)\cdot J_2(m_2)\cdot \sin\frac{\pi I(t)}{2V_\pi}\cos[(\omega_0-2\omega_{RF2})t]$$
$$-E_{\mathrm{o}}\cdot J_0(m_1)\cdot J_2(m_2)\cdot \sin\frac{\pi Q(t)}{2V_\pi}\sin[(\omega_0-2\omega_{RF2})t]$$
$$-2E_{\mathrm{o}}\cdot J_1(m_1)\cdot J_2(m_2)\cdot \cos[(\omega_0+\omega_{\mathrm{RF1}}+2\omega_{RF2})t] \quad (4\text{-}12)$$

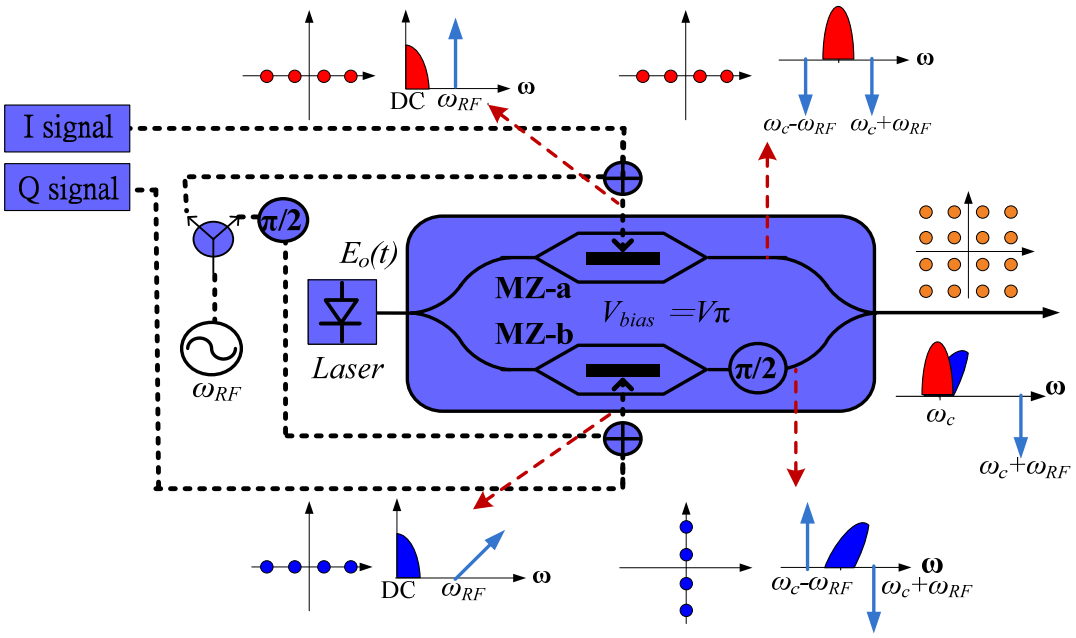

Figure 4-2 Concept of proposed optical I/Q up-conversion system.

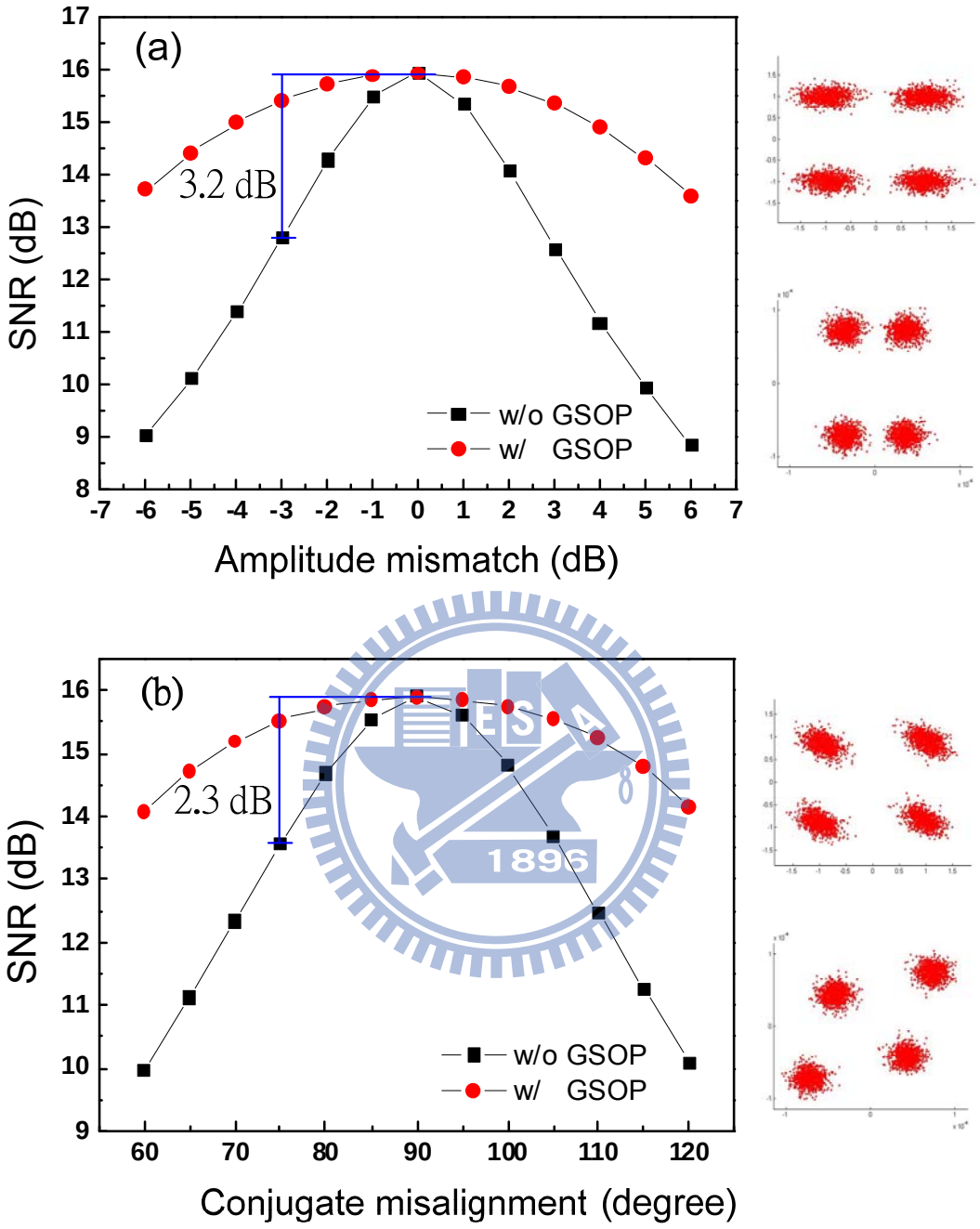

Figure 4-3 Simulation results of QPSK signal of amplitude mismatch and conjugate misalignment.

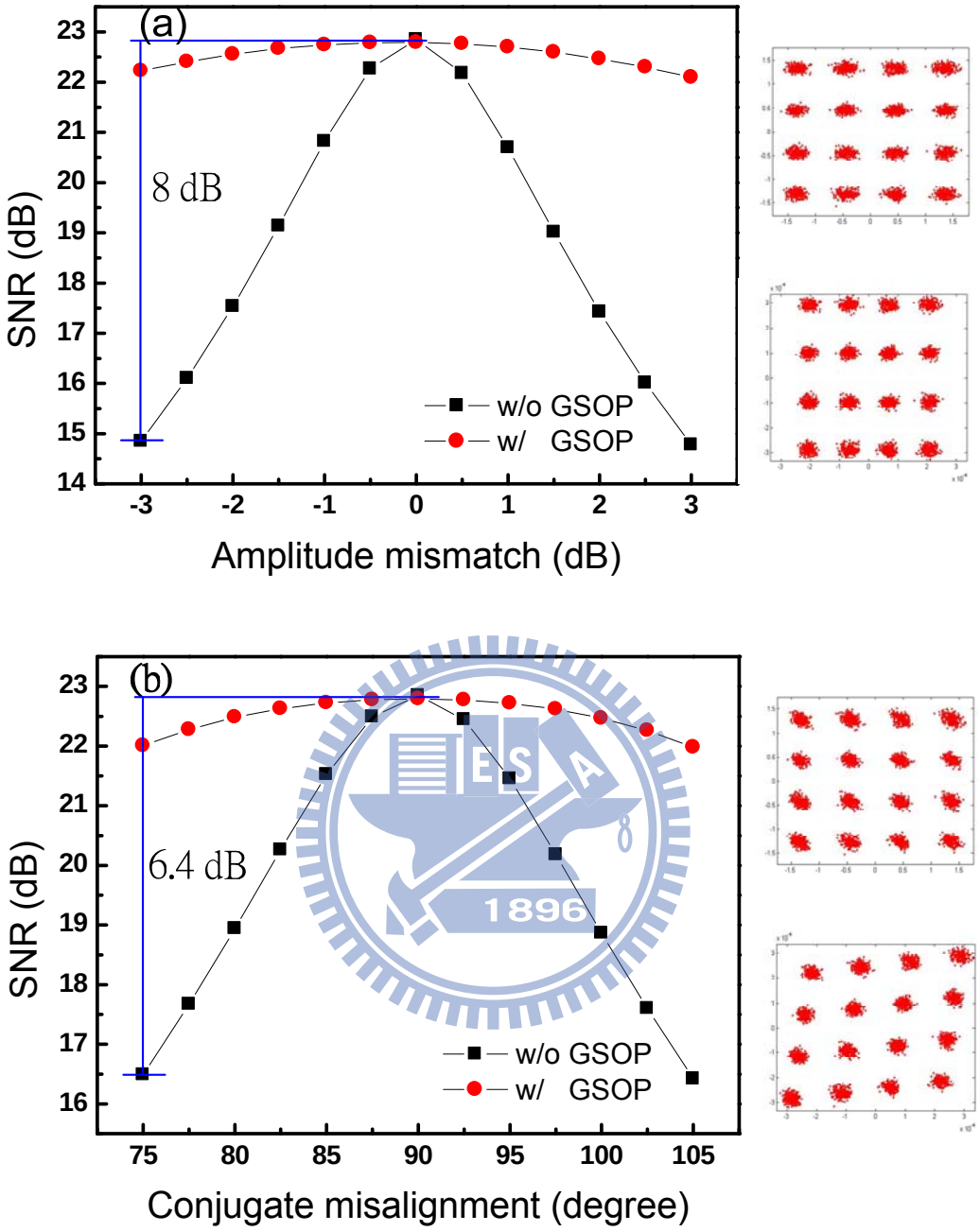

Figure 4-4 Simulation results of 16-QAM signal of amplitude mismatch and conjugate misalignment.

4.3.3 Consider Dispersion Effect

The dispersion will contribute different phase delay for different subcarriers. For optical I/Q up-conversion RoF system, the generation of only

one copy of the desired RF signal after photodiode could eliminate the possibility for fading. Therefore, dispersion does not induce RF fading problem in the proposed RoF system.

4.4 Experimental Demonstration without Frequency Quadrupling

4.4.1 Experiment Setup

Figure 4-5 presents the experimental setup of the proposed system. Since the baseband QPSK and 16-QAM signals are complex, the real and imaginary parts are sent from channel one and channel two of a Tektronix® AWG7102 arbitrary waveform generator (AWG). The sampling rate and the digital-to-analogue converter resolution of the AWG are 10 GHz and 8 bits, respectively. The QPSK and 16-QAM signal symbol rates are 2.5 GSymbol/s, as shown in inset (i) of Fig. 4-5. The data rate is 5 Gb/s for the QPSK signal and 10 Gb/s for the 16-QAM signal. To realize optical direct-detection, a new optical subcarrier is generated in one sideband at the frequency of 8 GHz higher than the original optical carrier. The generated photonic vector signal is then amplified using an EDFA and filtered through a 0.4 nm optical filter to suppress the ASE noise, as shown in inset (ii) of Fig. 4-5. An optical attenuator is used to set the optical launching power to be 0 dBm before transmission to prevent fiber nonlinearity. A 50km standard single-mode fiber is used to evaluate the transmission penalty of the system. Following square-law detection, an electrical 2.5GSymbol/s signal at 8 GHz is generated and captured by a Tektronix® DPO 71254 with a 50Gb/s sampling rate and a 3dB bandwidth of 12.5 GHz, as shown in the inset (ii) in Fig. 4-5. The off-line DSP program is used to demodulate the vector signal. The bit error rate (BER)

performance is calculated from the measured SNR.

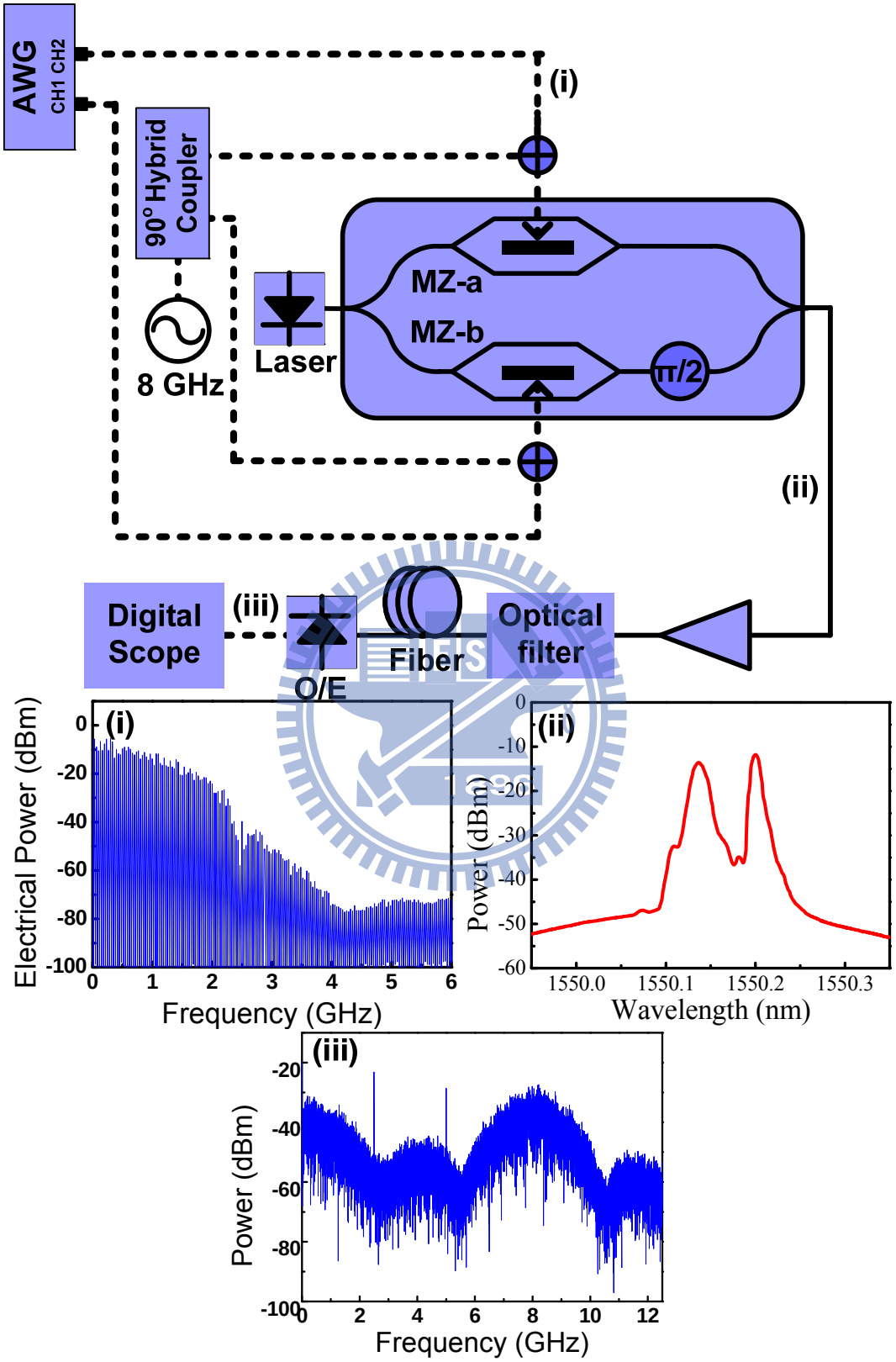

Figure 4-5 Experimental setup of the proposed optical I/Q up-conversion system.

4.4.2 Results and Discussions

Figure 4-6 and Fig. 4-7 present the experimental results obtained using GSOP compensation. Since the frequency response of AWG is uneven, the feedforward equalizer is used to reduce the ISI effect. The experimental results in Figs. 4-6 (a) and (b) reveal that 3 dB amplitude mismatch and 15° conjugate misalignment correspond to ~5.9 dB and ~3.6 dB SNR degradation, respectively. However, the GSOP greatly improves performance, such that SNR degradation becomes only 0.6 dB and 0.2 dB, respectively. Figures 4-7 (a) and (b) present experimental results concerning the 16-QAM signal, and the GSOP compensation can decrease the SNR degradation from 8.3 dB to 0.6 dB (from 6.6 dB to 0.6 dB) due to 3 dB amplitude mismatch (15° conjugate misalignment). The results also verify the criticality of the I/Q imbalance for both the QPSK format and the 16-QAM format. Because the spacing of 16-QAM constellation points is closer than that of QPSK, the 16-QAM signal has more penalty than the QPSK signal with the same I/Q imbalance. Furthermore, the experimental results agree with the simulation results well. Figures 4-8 (a) and (b) plot the transmission BER curves of the QPSK and 16-QAM signals with the GSOP compensation. For the QPSK signal, a receiver sensitivity of -17.2 dBm is achieved at a BER of 10^{-9} in the BTB case, and for the 16-QAM signal, the receiver sensitivity is -11.7 dBm in the BTB case. For both signals, the penalty at the BER of 10^{-9} is negligible following 50km standard single-mode fiber transmission. The inserts in Fig. 4-8 present the constellation diagrams, and no obvious distortion is observed after fiber transmission.

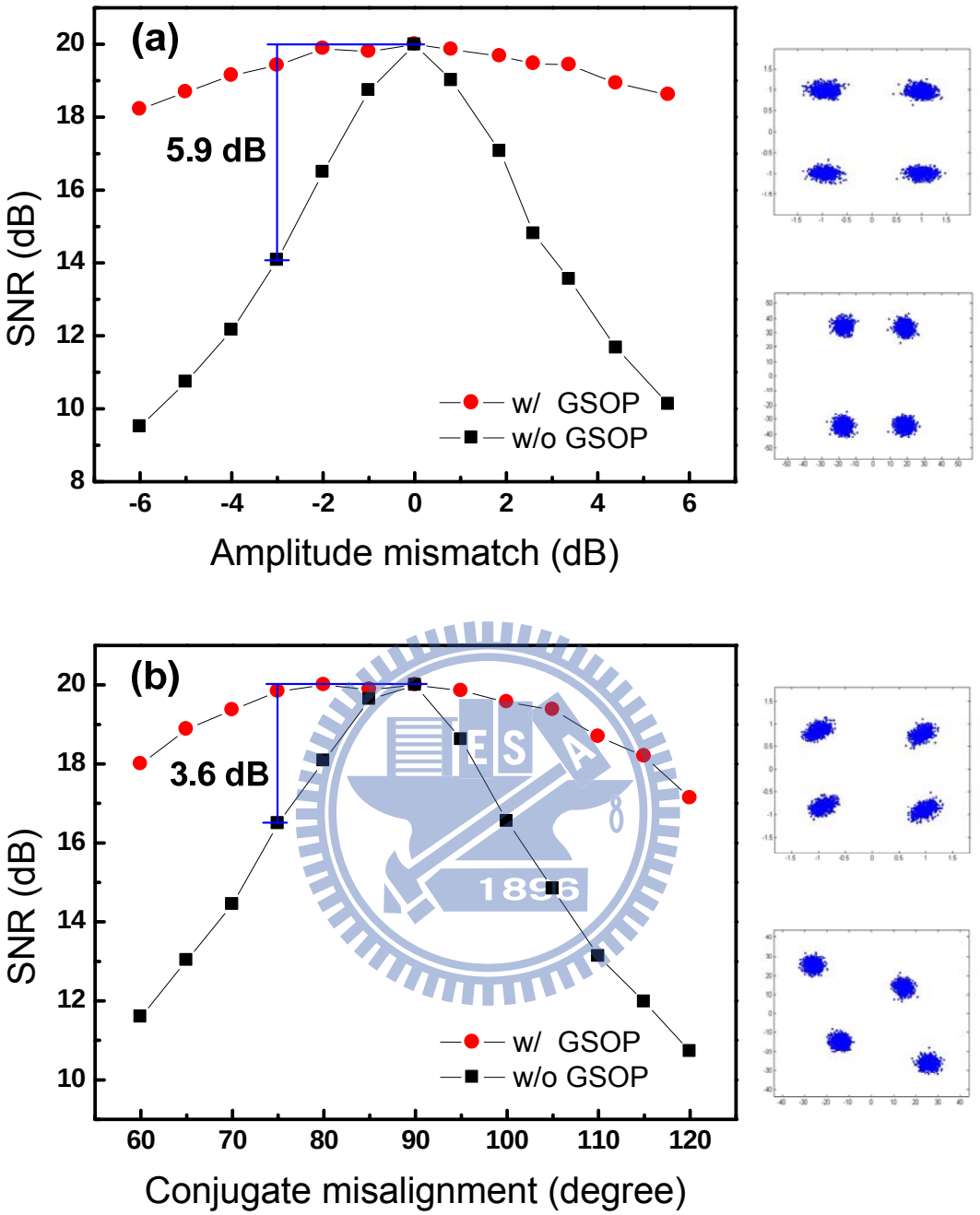

Figure 4-6 Experimental results of QPSK signal of amplitude mismatch and conjugate misalignment.

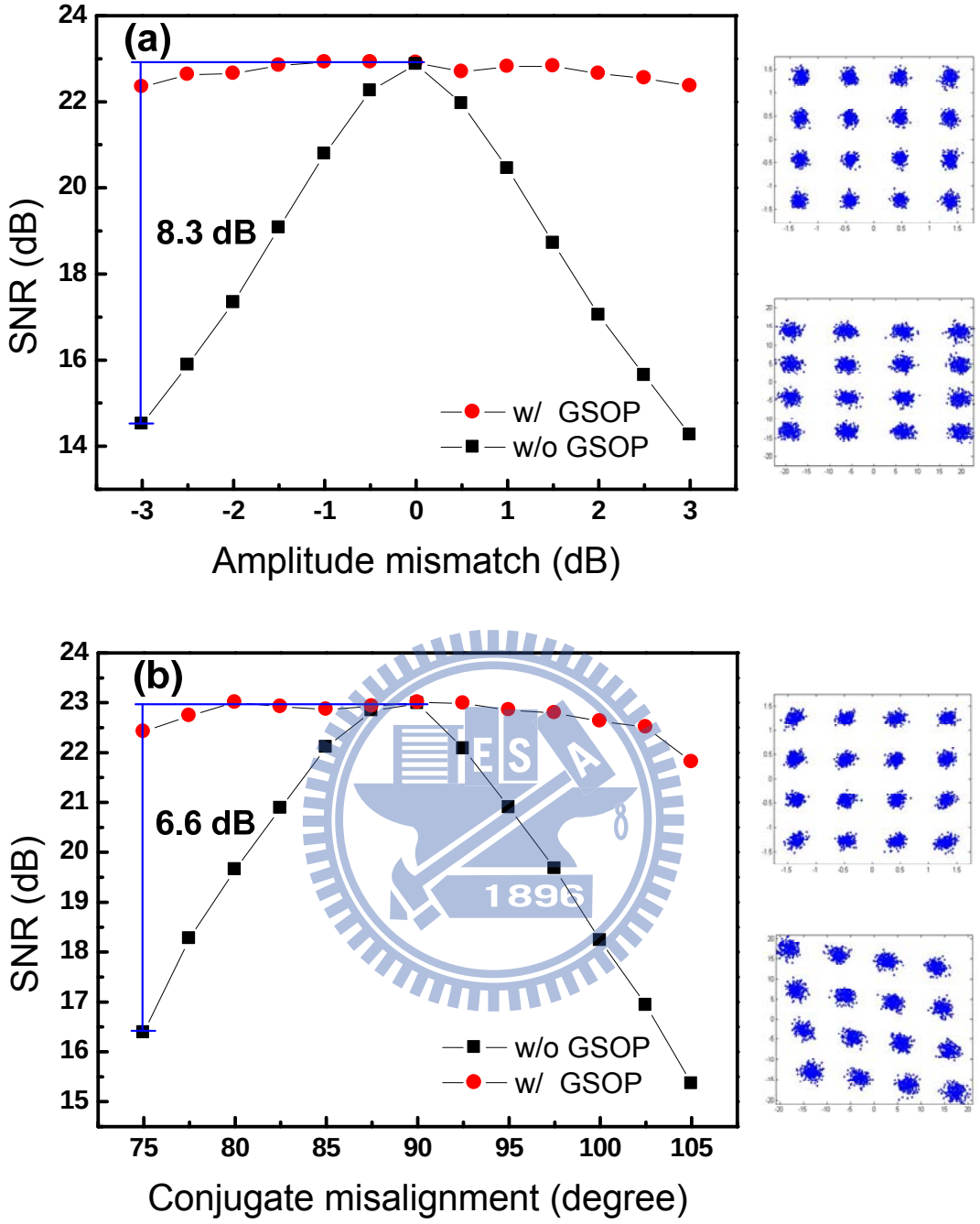

Figure 4-7 Experimental results of 16-QAM signal of amplitude mismatch and conjugate misalignment.

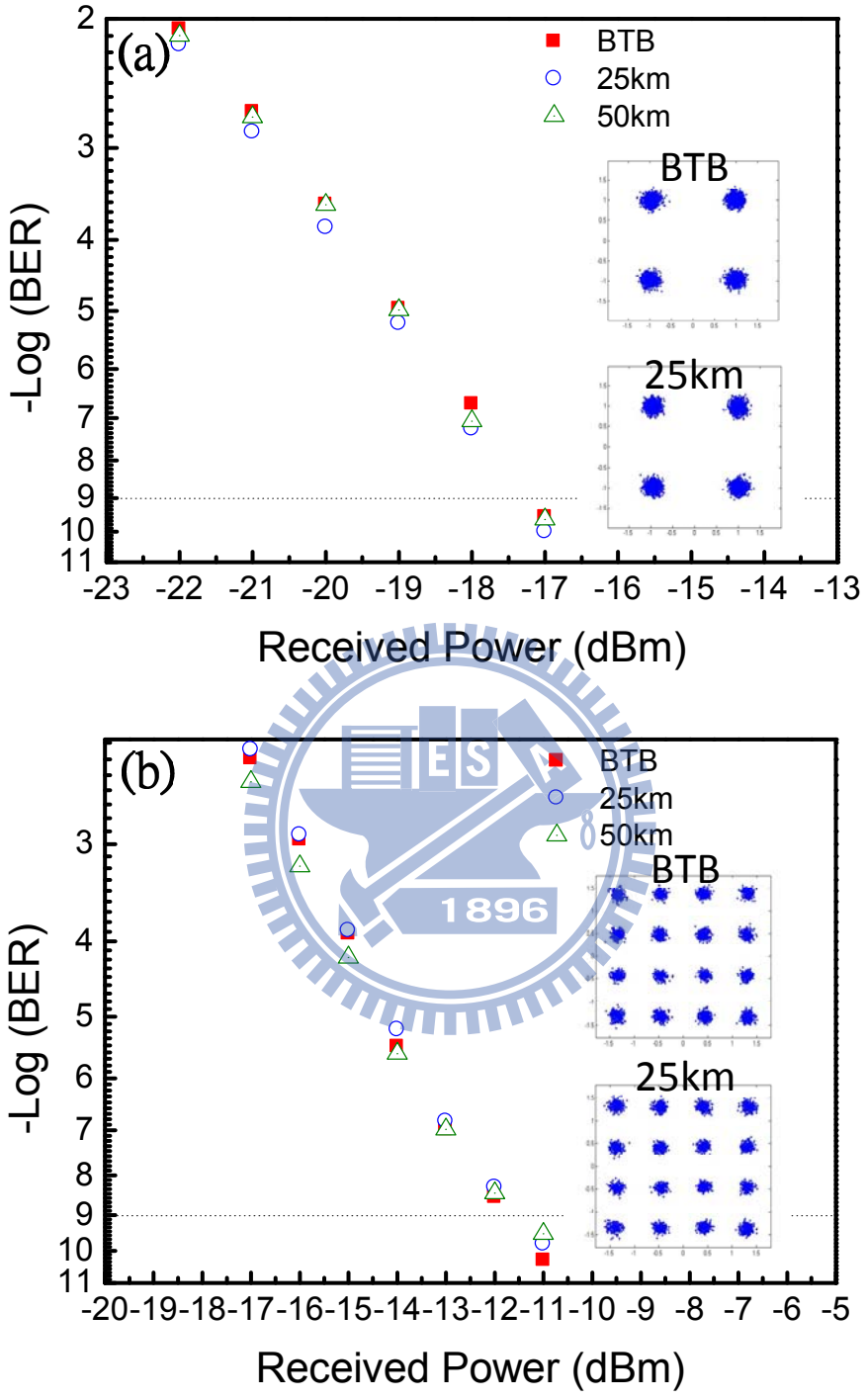

Figure 4-8 BER curves of (a) 5-Gb/s QPSK and (b) 10-Gb/s 16-QAM signals.

4.5 Experimental Demonstration with Frequency Quadrupling

4.5.1 Experiment Setup

Figure 4-9 shows the experimental setup of the 60-GHz OFDM RoF system employing all-optical up-conversion and frequency quadrupling technique. The light source is generated by a continue wave tunable laser. The optical power and wavelength of light source are 4dBm and 1550nm, respectively. The OFDM signals are generated by an AWG (Tektronix® AWG7122B) using a Matlab® software program. The sample rate and digital-to-analog converter resolution of AWG are 12 GHz and 8 bits, respectively. The IFFT length and CP of OFDM signal are 256 and 16, respectively. A 39.0625-MSym/s QAM symbol is encoded at 176 channels, with the remaining 80 channels set to zero. Therefore, an OFDM signal that occupies 7GHz bandwidth is generated. The real part and image part of OFDM signal are sent into MZ-a and MZ-b of first modulator, respectively. To realize the optical direct-detection OFDM signal, a new optical subcarrier is generated at the lower sideband of the original carrier by 12 GHz (inset (b) of Fig. 4-9). Notably, the undesired sideband suppress ratio is greater than 28 dB, which only slightly influences the performance of the generated OFDM signals. The generated optical direct detection OFDM signal is up-converted by using optical frequency quadrupling method. Then two copies of optical direct detection OFDM signal are generated with 48GHz separation. After a 50/100 GHz optical interleaver, OFDM signal at 60 GHz with frequency quintupling is generated (inset (c) of Fig. 4-9). Notably, the transmission penalty of the system is evaluated using a 25-km standard single-mode fiber.

At the remote antenna unit, square-law detection in a 70 GHz photodiode

was used to convert the optical signal into an electrical signal. The beating product of two subcarriers resulted in the desired 7 GHz-wide (57 – 64 GHz) OFDM signal centered at 60.5 GHz. After amplification in a low noise amplifier (LNA), the 60 GHz signal was fed into a standard gain horn antenna (gain ~ 23dBi) and radiated. After transmission over 3m wireless distances, the 60 GHz signal was received by a second standard gain horn antenna and fed into a 60 GHz receiver where it was down-converted to an IF frequency of 5 GHz as shown in insert (d) of Fig 4-9. The IF signal was captured by a real-time oscilloscope sampling at 50 GSamples/s (Tektronix® DPO71254) for offline signal processing and analysis. In addition to the standard OFDM signal decoding functions, the signal processing included adaptive bit-loading algorithm and I/Q imbalance compensation. The results were performed to compensate for the imbalance between I and Q signals in the I/Q mixer used at the RAU, owing to the large signal bandwidth (3.5 GHz at baseband) used.

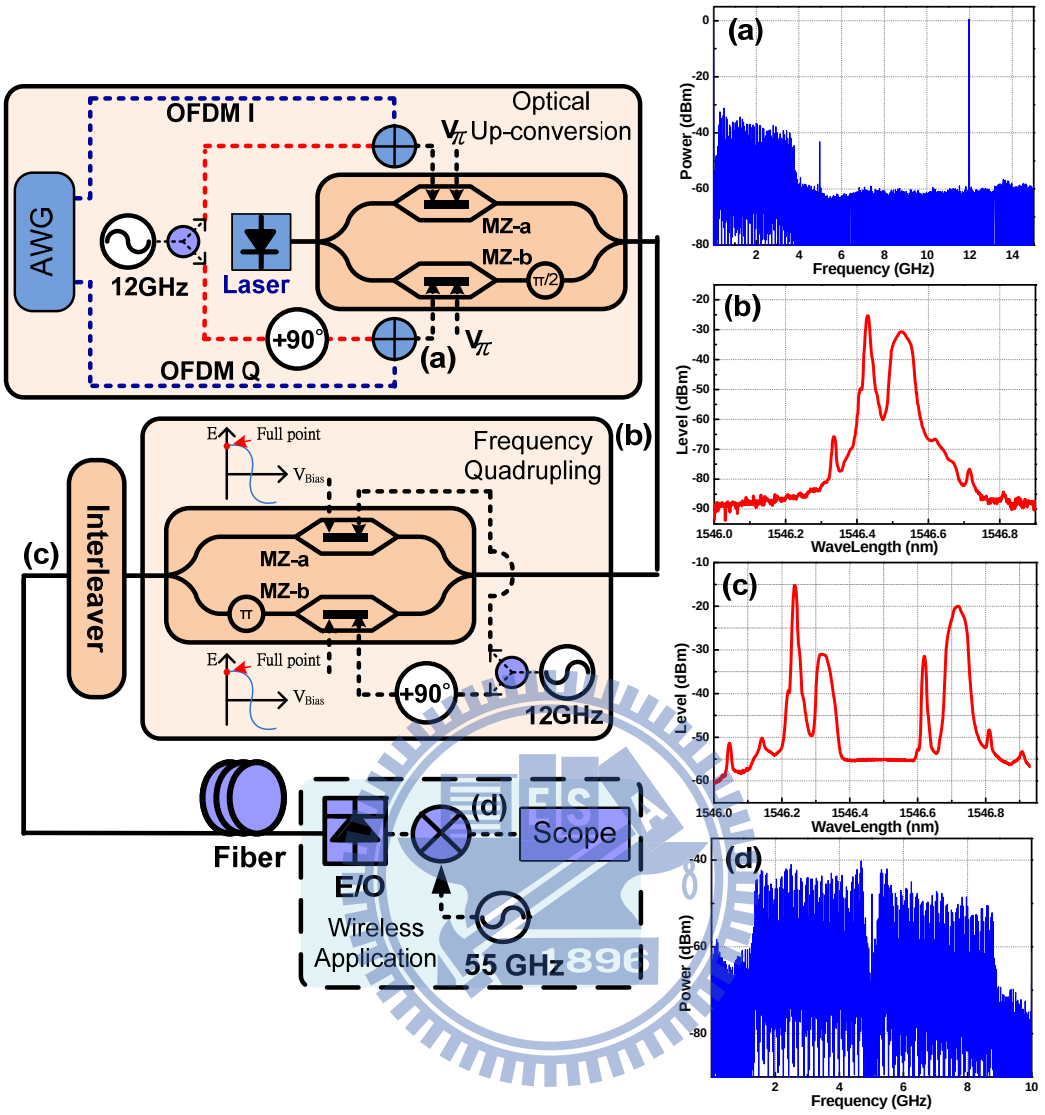

Figure 4-9 Experimental setup of the 60-GHz RoF system using all-optical up-conversion.

4.5.2 Results and Discussions

Figure 4-10 shows the 16-QAM OFMD constellation diagrams before and after the one-tap equalizer in back-to-back (BTB) and following standard single-mode fiber transmission cases. Both the frequency response of various millimeter-wave components at 60 GHz and fiber dispersion are combated using the equalizer in OFDM transceiver. Since the proposed OFDM

transmitter can generate high-purity two-tone lightwave, the generated OFDM signals do not incur periodic fading due to fiber dispersion. Only in-band distortion of the OFDM-encoded subcarrier induced by fiber dispersion is considered. Since the symbol rate of each subcarrier is only 39.0625 MSym/s, the fiber chromatic penalty can be ignored. Figure 4-11 displays the BER curves of the 27.5-Gb/s 16-QAM OFDM signals using optimal OPRs after transmission exceeds 25-km standard single-mode fiber. The optimal OPR is 4 dB, where the power of the un-modulated sideband is 4 dB higher than that that of the OFDM-modulated sideband. The sensitivity penalties due to the fiber transmission are negligible. The received optical power of −9 dBm was enough to achieve the forward error correction (FEC) error-free transmission. The output BER could be achieved 10^{-15} with $1x10^{-3}$ input BER by using FEC coding with 7% overhead and a net coding gain (NCG) of ~8.1dB [96].

Fig. 4-12 (a) and (b) illustrates the SNR and BER of 16-QAM OFDM signals versus different ratio of V_{PP} between I and Q respectively. It is obvious that the performance of OFDM signals deteriorate as the amplitude ratio between I and Q increases. The I/Q imbalance compensation algorithm could reduce impairment of amplitude imbalance. Figure 4-13 shows the SNR versus subcarrier without and with I/Q imbalance compensation when the amplitude ratio between I and Q is 1.3. The lower subcarrier numbers have better performance. This is because amplifiers and MZMs at transmitter have worse performance at high frequency. Figure 4-14 (a) and (b) show the constellation diagrams at -6dBm optical received power without compensation and with compensation, respectively.

Figure 4-15 (a) and (b) illustrates the SNR and BER of 16-QAM OFDM

signals versus phase difference between I and Q respectively. The performance of OFDM signals worsens as the difference phase between I and Q increases. With I/Q imbalance compensation in frequency domain, experimental results verify a significant increase in the tolerance of both amplitude mismatching and conjugate misalignment. Figure 4-16 shows the SNR curve versus subcarrier without and with compensation when the ratio of phase difference between I and Q is 9 degrees. Figure 4-17 (a) and (b) show the constellation diagrams at -6dBm optical received power without compensation and with compensation, respectively. After compensation, clearer constellations are obtained. Figure 4-18 illustrates the BER curves of 16-QAM OFDM signal without and with I/Q imbalance compensation. The BER has a little improvement after imbalance compensation.

The electrical spectrum of the OFDM signal is shown in insert (d) of Fig 4-9. This spectrum exhibits about 10-dB power deviation between the subcarriers caused by irregular frequency response of the system, and therefore, it resulted in high SNR deviation of 6 dB as shown in Fig. 4-16. To achieve higher data rate, the adaptive bit-loading algorithm was used to adjust the power and the format of each subcarrier. The adaptive bit-loading signals are generated according to the 16QAM OFDM signal at -6dBm optical received power without fiber transmission. One is generated before imbalance compensation and the other is generated after compensation.

Figure 4-19 shows BER curves of bit-loading OFDM signal. This bit-loading OFDM single is generated before imbalance compensation. The total data rate is 31.37Gbps. The sensitivity penalties due to the fiber transmission are negligible. Figure 4-20 shows BER curves of bit-loading

OFDM signal that is generated after imbalance compensation. The total data rate is 32.38Gbps. The sensitivity penalties due to the fiber transmission are negligible. The total data throughput is increased 1 Gbps after I/Q imbalance compensation. Figure 4-21 shows the SNR versus subcarrier for the 32.38 Gb/s adaptive bit-loading OFDM signal with -6dBm optical received power. The performance of each subcarrier has improved. Figure 4-22 (a) and (b) show the constellation diagrams of 32.38Gbps bit-loading OFDM signal at -6dBm optical received power without compensation and with compensation, respectively. Since the adaptive bit-loading is used in this experiment, different subcarrier has different modulation format. The modulation format is depended on SNR of each subcarrier. After I/Q imbalance compensation, clear separation of constellation points confirms excellent signal transmission quality.

(a) BTB w/o equalizer

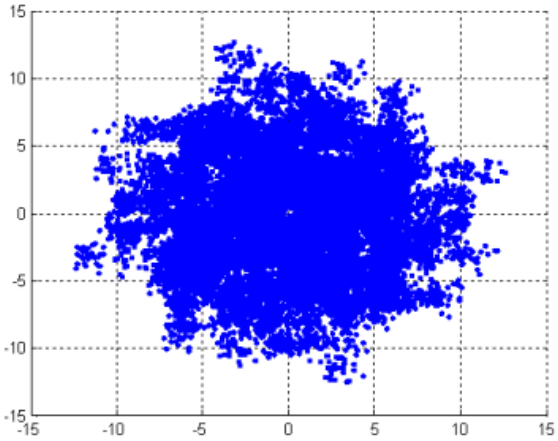

(b) BTB w/ equalizer

(c) 25km w/ equalizer

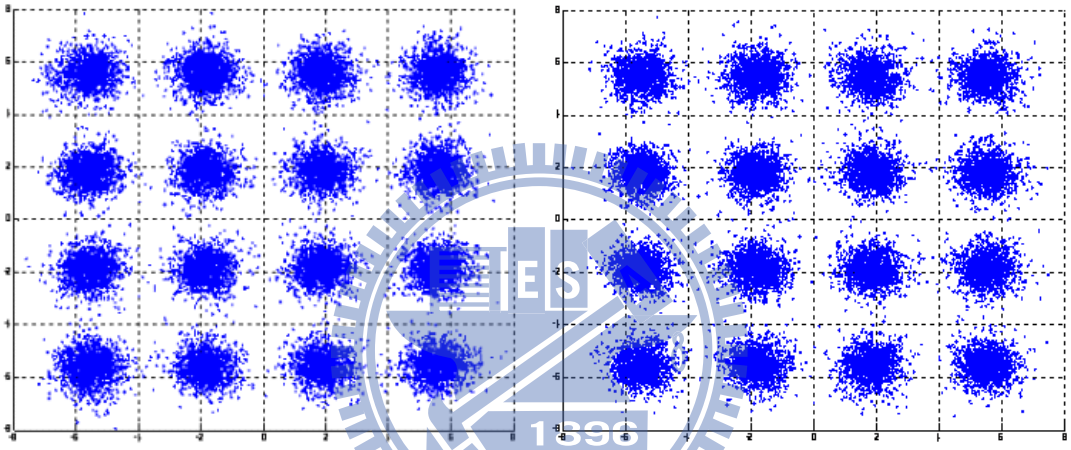

Figure 4-10 Constellations of the 16-QAM OFDM signals.

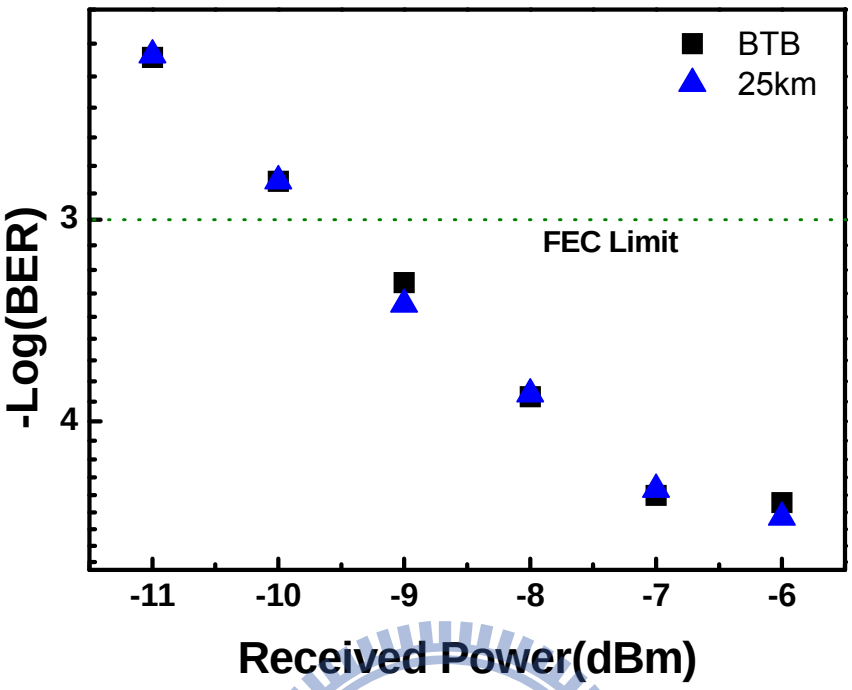

Figure 4-11 BER curves of the 16-QAM OFDM signals.

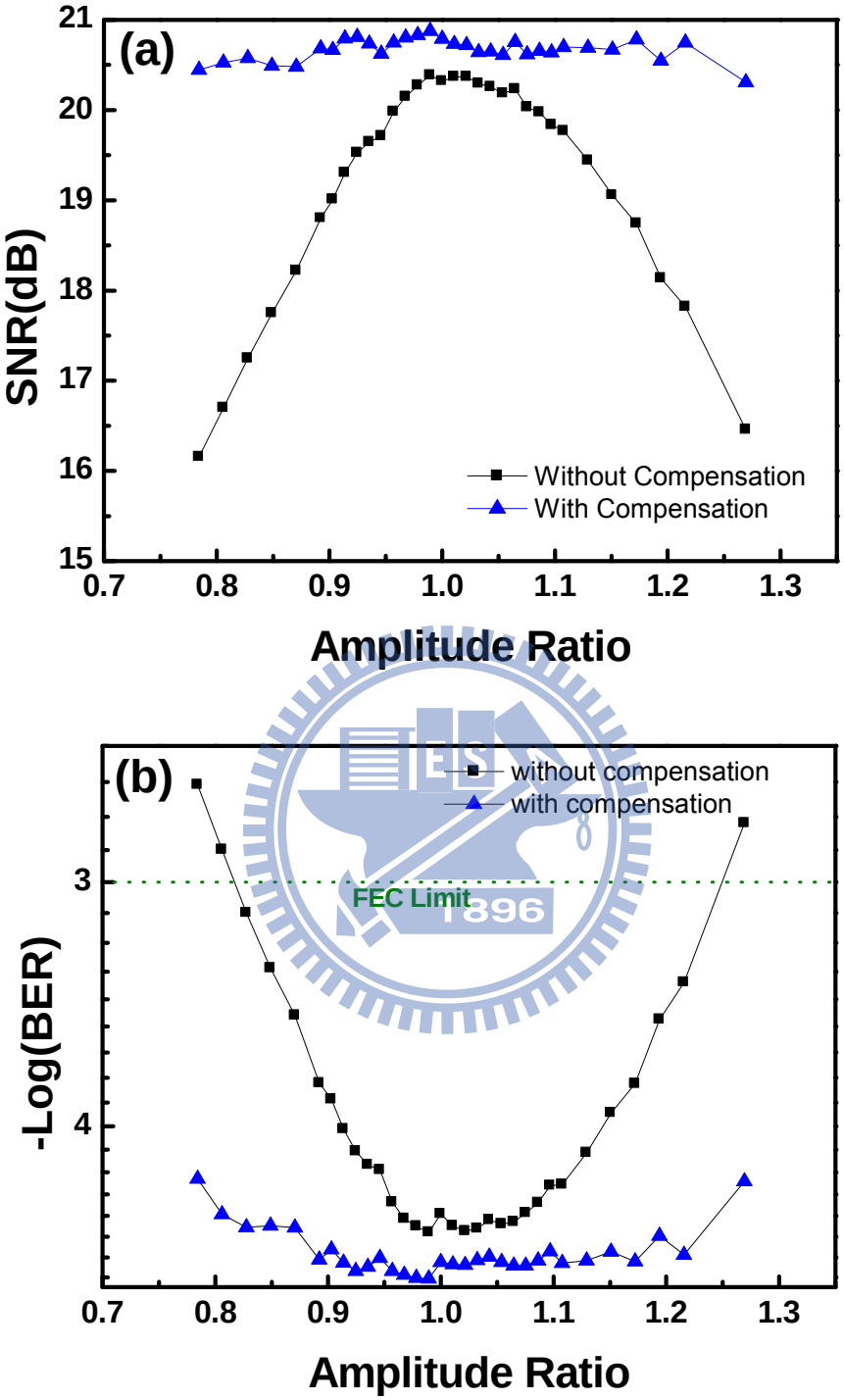

Figure 4-12 The SNR and BER versus amplitude ratio between I and Q without and with I/Q imbalance compensation.

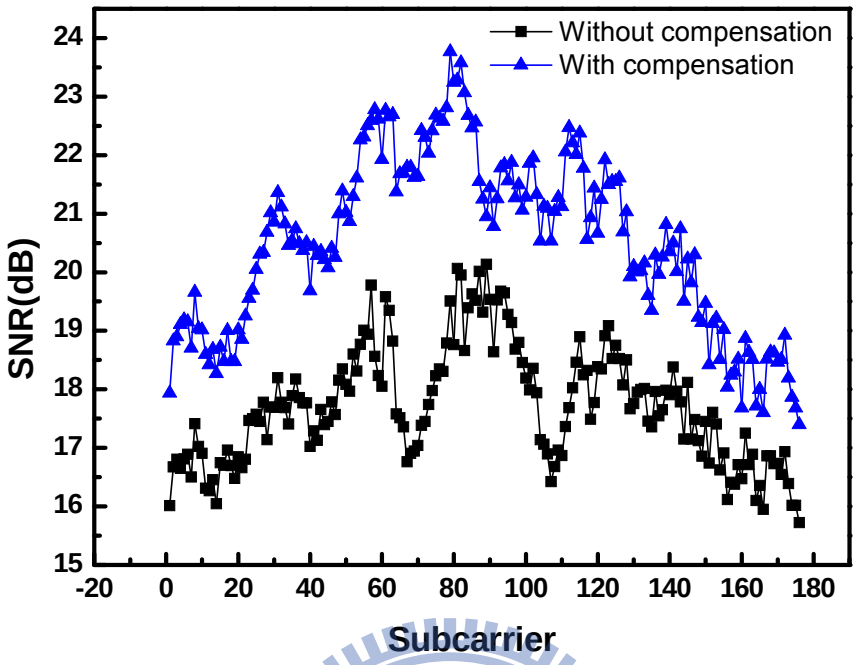

Figure 4-13 The SNR curves versus subcarrier number for OFDM signal with 1.2 amplitude ratios.

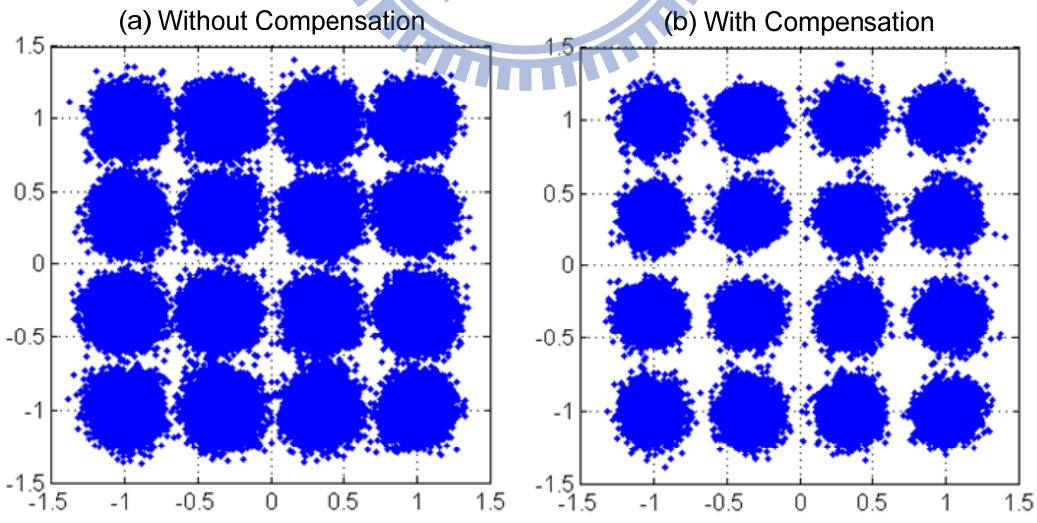

Figure 4-14 Constellations of the 16-QAM OFDM signals with 1.2 amplitude ratios.

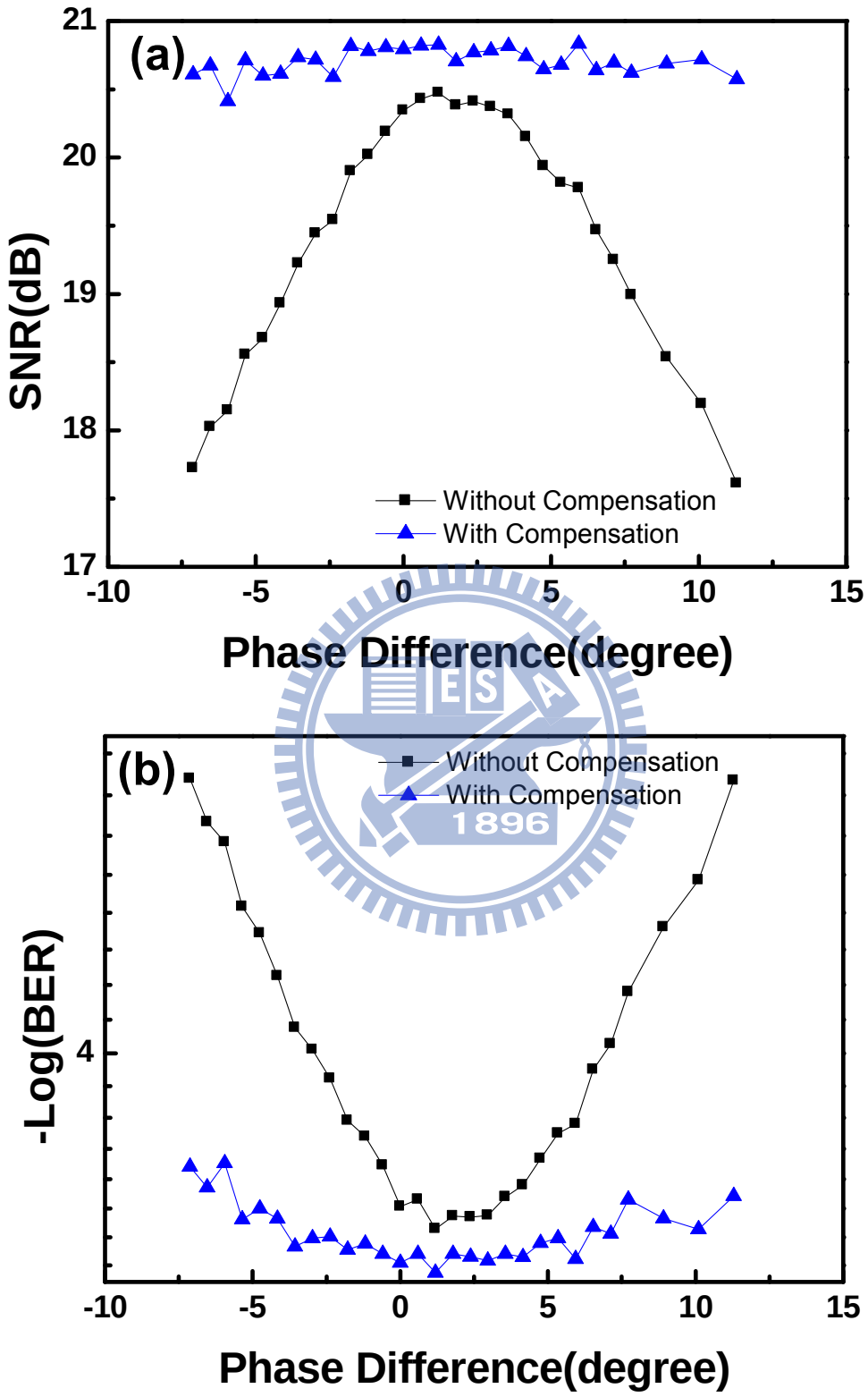

Figure 4-15 The SNR and BER versus phase difference between I and Q without and with I/Q imbalance compensation.

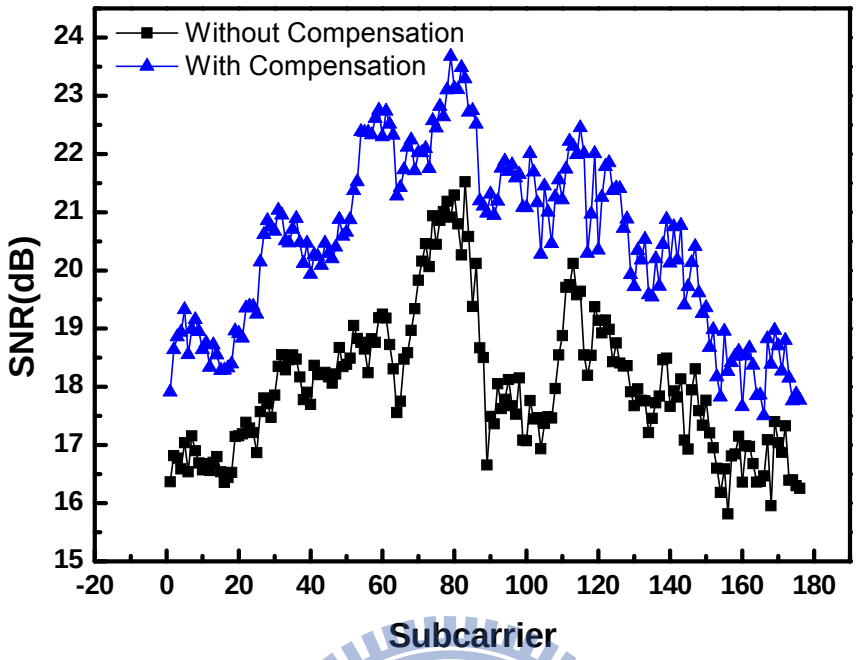

Figure 4-16 The SNR curves versus subcarrier number for OFDM signal with 9 degree phase difference.

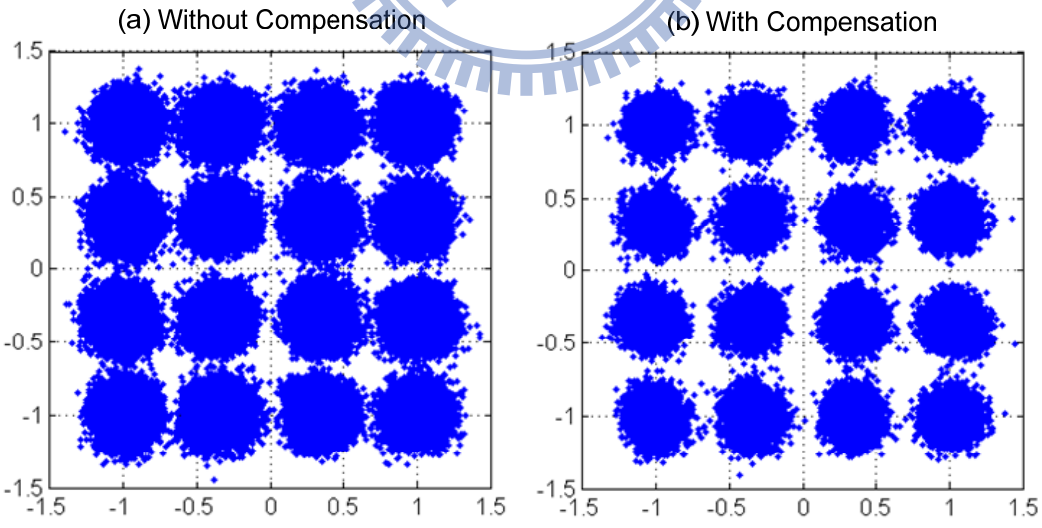

Figure 4-17 Constellations of the 16-QAM OFDM signals with 9 degree phase difference.

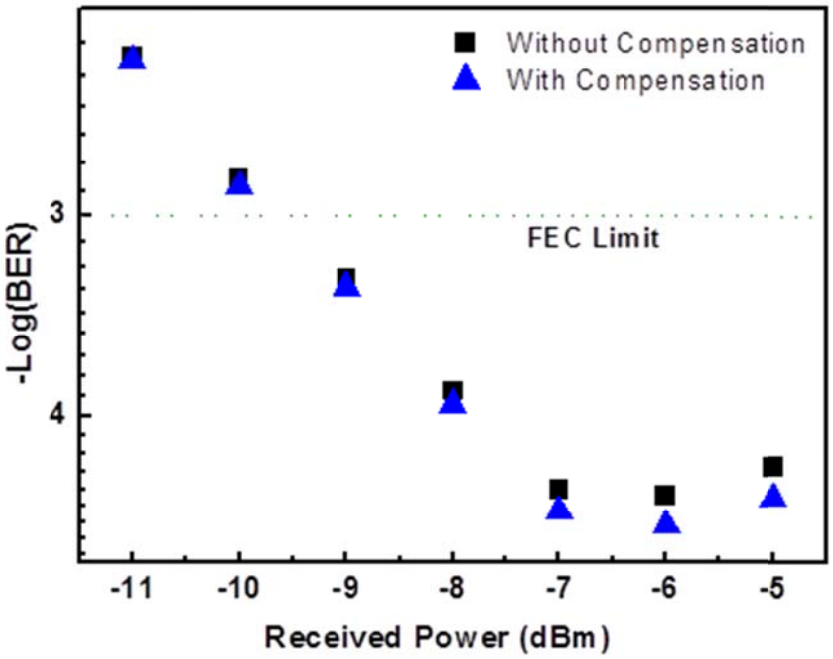

Figure 4-18 The BER curves of 16QAM OFDM signal without and with I/Q imbalance compensation.

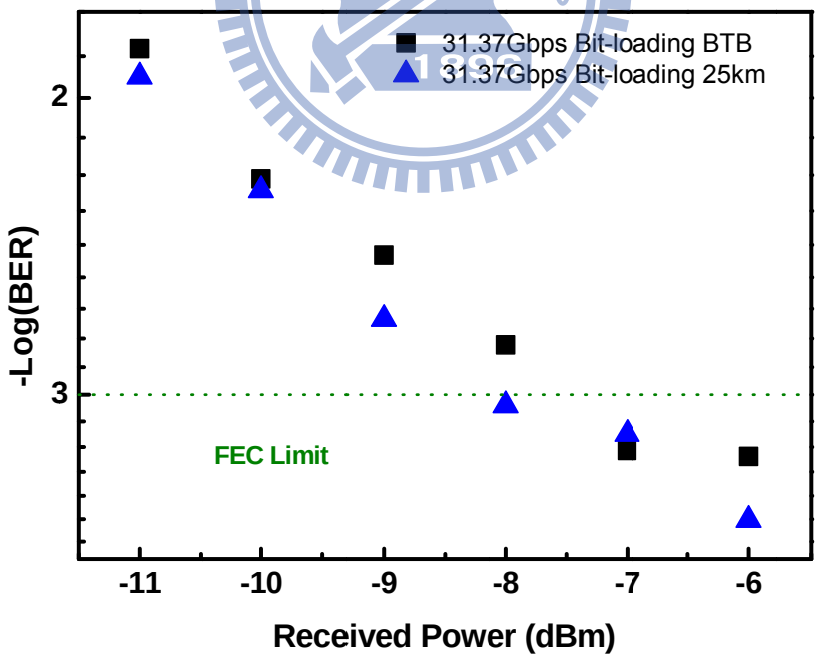

Figure 4-19 The BER curves of 31.37Gbps bit-loading OFDM signal without I/Q imbalance compensation.

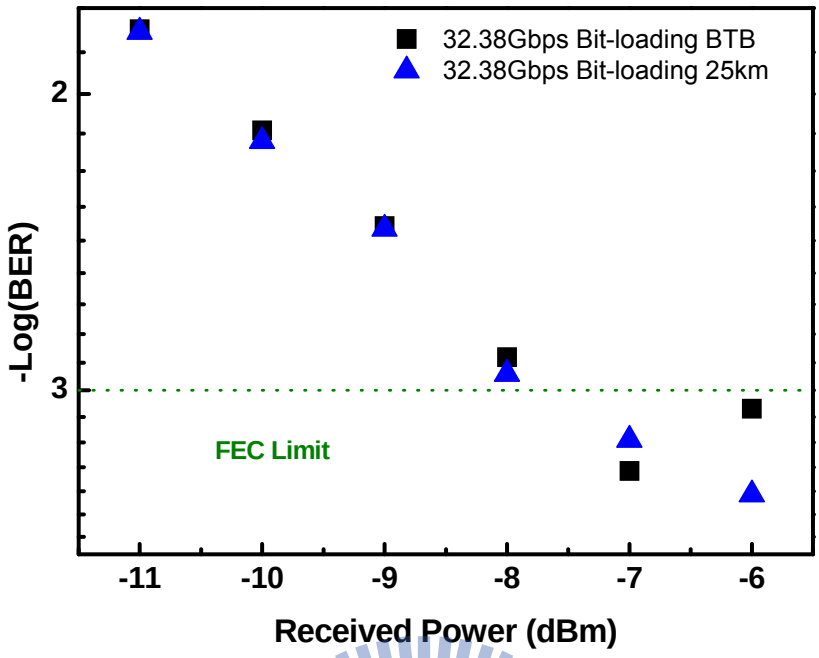

Figure 4-20 The BER curves of 32.38Gbps bit-loading OFDM signal with I/Q imbalance compensation.

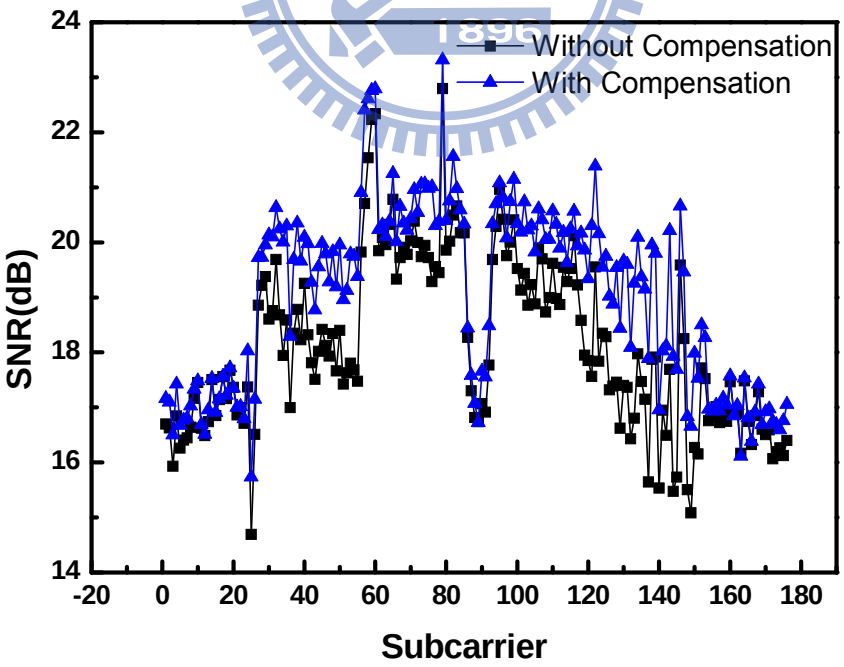

Figure 4-21 The SNR curves versus subcarrier number for 32.38Gbps bit-loading OFDM signal.

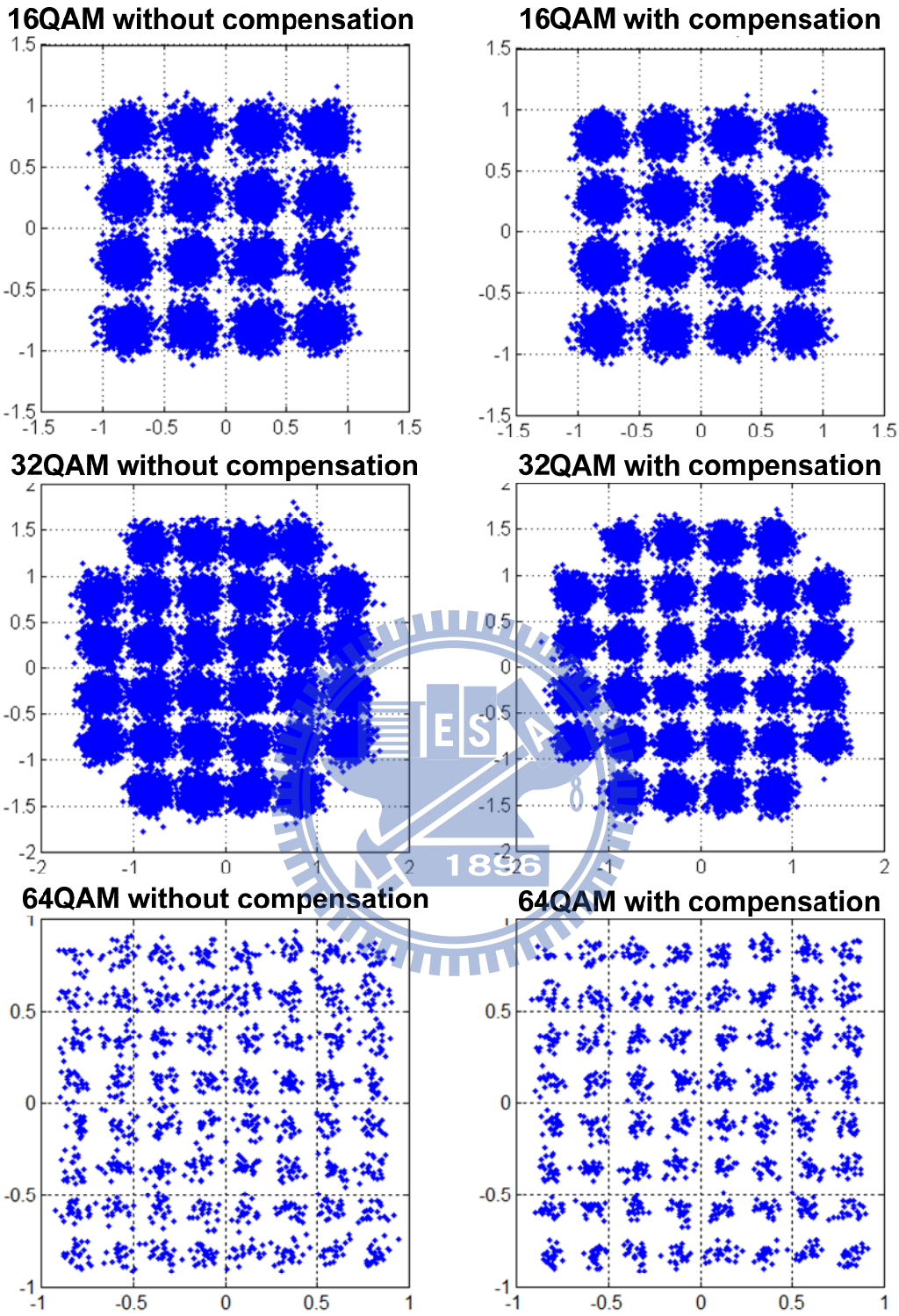

Figure 4-22 Constellations of the 32.38Gbps bit-loading OFDM signal with -6dBm optical received power.

4.6 Summary

This study proposes the generation of an RF vector signal using all optical I/Q up-conversion for direct detection. To eliminate the I/Q imbalance, the I/Q imbalance compensation algorithm in time domain approach is used to compensate for the amplitude mismatch and conjugate misalignment. 5 Gb/s QPSK and 10 Gb/s 16-QAM signals at 8 GHz are demonstrated in both the numerical simulation and the experiment. By applying GSOP, the SNR degradation of less than 2 dB (1 dB) is achieved for the QPSK (16-QAM) signals, as 3 dB amplitude mismatch or 15° conjugate misalignment is applied. Moreover, after transmission over 50-km standard single-mode fiber, a negligible power penalty is observed.

By using all-optical up-conversion and frequency quintupling, we demonstrate 16-QAM OFDM signal generation and transmission with a 27.5 Gb/s within 7-GHz license-free spectrum at 60 GHz band. Transmission over 25-km standard single-mode fiber transmission with negligible penalty is achieved without any dispersion compensation. In order to resolve I/Q imbalance in 7-GHz band, the I/Q imbalance compensation in frequency domain is applied to compensate the amplitude and conjugate imbalance. After employing correction, a 32.38 Gb/s RoF signal at 60 GHz band signal is demonstrated. The total data throughput of OFDM signal with adaptive bit-loading algorithm is improved from 31.37Gbps to 32.38Gbps. After transmission over 25-km standard single-mode fiber, negligible penalty is achieved without any dispersion compensation.

Chapter 5

ELECTRICAL I/Q UP-CONVERSION RADIO-OVER-FIBER SYSTEM

5.1 Preface

Complex RoF system architectures for radio-frequency (RF) signal generation and transmission are proposed in the last chapter. However, it is imperative that the employed RoF links are as simple as possible to reduce costs, while providing the needed performance. This is especially true for certain applications such as in-building systems, where certain performance offered by complex RoF systems are not even required. For example fiber spans in most in-building applications are typically less than 500 m [87]. Therefore, in-building RoF systems for 60 GHz do not need the fiber chromatic dispersion tolerance for tens of kilometers that complex systems boast of. In this chapter we propose a simple RoF system architecture for transporting and generating wideband signals at 60 GHz, and investigate its performance theoretically and experimentally. This RoF system uses only one single-electrode Mach-Zehnder modulator (MZM) which is the same as the one used in DSB and DSBCS modulation schemes with bandwidth no more than 35.5-GHz. This work presents a novel method for optical RF signal generation using the DSBCS modulation scheme that can carry vector signals. A frequency multiplication scheme is adopted to reduce the bandwidth requirements of electrical components, which is an important issue for ROF systems at millimeter-wave range.

We experimentally demonstrate the successful use of the simple RoF

system to deliver a 40-Gb/s wireless signal at 60 GHz. The signal occupied the full 7-GHz license-free spectrum at the 60-GHz band. Remote frequency up-conversion from the intermediate frequency (IF) to 60 GHz was achieved by employing a system configuration that used a 35.5-GHz local oscillator (LO) signal, which was transported alongside the signal. This enabled high-quality signal transmission over extended fiber lengths exceeding 3 km without any fiber dispersion compensation. The RoF link included a wireless transmission distance of 10 m.

5.2 The Concept of Proposed System

Figure 5-1 schematically depicts the concept of the proposed RoF system. The MZM driving signal consists of an vector signal at a frequency of f_1 and a sinusoidal LO signal with a frequency of f_2, as indicated in insets (i)-(iii) of Fig. 5-1. The frequency, f_1+f_2 of the LO signal is half the desired mm-wave frequency of operation. To achieve the double sideband with carrier suppression (DSBCS) modulation scheme, the MZM is biased at the null point to suppress the optical carrier. Inset (iv) of Fig. 5-1 shows the generated optical vector signal and LO spectrum that has two upper-wavelength sidebands (USB1 and USB2) and two lower-wavelength sidebands (LSB1 and LSB2) with carrier suppression at the output of the MZM. After square-law photo detection, the generated photocurrent can be written as

$$\mathrm{I_{photo}} \propto (\mathrm{USB1} + \mathrm{USB2} + \mathrm{LSB1} + \mathrm{LSB2})^2 \tag{5.1}$$

Expanding the above equation produces the following terms:

$$\mathrm{BaseBand} \propto \mathrm{USB1}^2 + \mathrm{USB2}^2 + \mathrm{LSB1}^2 + \mathrm{LSB2}^2 \tag{5.2}$$

Signal at the sum frequency $\propto$

$$\mathrm{USB1} \times \mathrm{LSB2} + \mathrm{USB2} \times \mathrm{LSB1} \tag{5.3}$$

Signal at the frequency difference $\propto$

$$\mathrm{USB1} \times \mathrm{USB2} + \mathrm{LSB1} \times \mathrm{LSB2} \tag{5.4}$$

Beat noise $\propto$

$$\mathrm{USB1} \times \mathrm{LSB1} + \mathrm{USB2} \times \mathrm{LSB2} \tag{5.5}$$

The beating terms of USB1 × LSB2 and USB2 × LSB1 generate the desired electrical vector signals at the sum frequency (f_2+f_1). The beating terms of USB1 × USB2 and LSB1 × LSB2 generate electrical vector signals at the frequency difference (f_2-f_1), which are well below the desired mm-wave frequency band and are filtered off prior to wireless transmission. Notably, a frequency multiplication can be achieved by properly choosing frequencies f_1 and f_2. This reduces the bandwidth requirements of the RoF transmitter allowing for the use of low-frequency electrical and optical components, including the MZM (< 40 GHz), which are readily available and have very good performance (e.g. flat frequency response).

In this chapter, the target sum frequency is 60 GHz. Two main issues will be crucial to the system performance and will be explained in details in following sections. First, the RF fading issue, as shown in the equation (5.12), comes from the interaction between the two copies of the desired signals, which are generated at the photodiode, namely USB1 × LSB2 and USB2 × LSB1. After fiber transmission, the relative phase between the two generated RF signals will change with transmitted distance owing to the slight difference in the propagation speeds of the two sideband pairs induced by fiber chromatic dispersion. As the relative phase reaches 180°, the electrical RF signal will vanish. This is the RF fading problem. The second issue comes from the beat noise of two vector signals USB1 × LSB1. If the center frequency of vector

signals is not properly chosen, the beat noise will fall into the signal band and severely degrade the system performance.

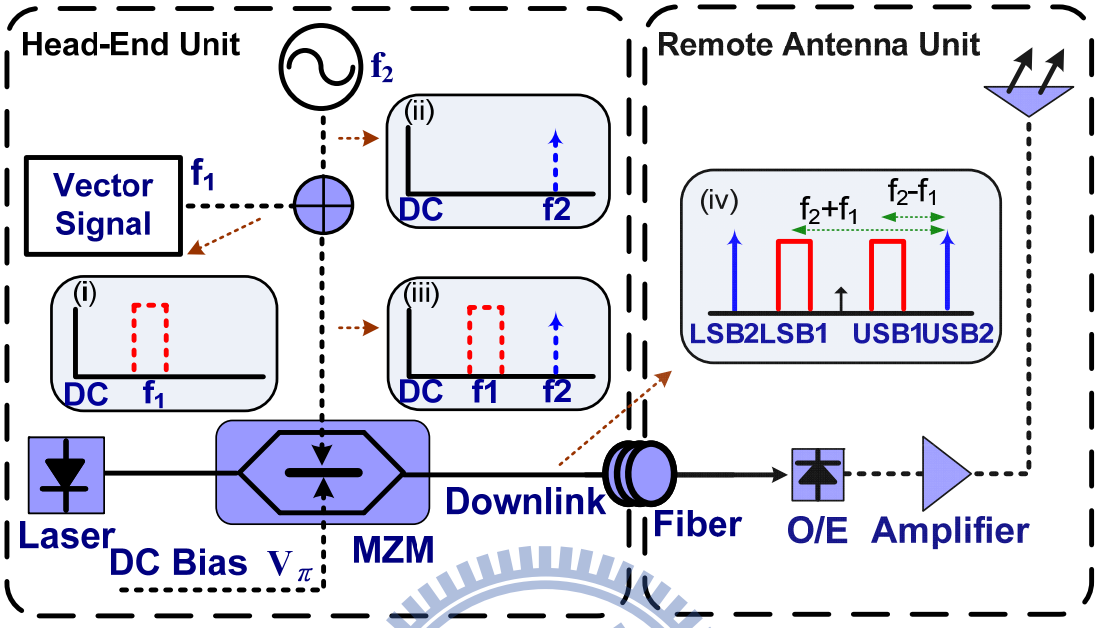

Figure 5-1 The proposed RoF system based on a single-electrode MZM.

5.3 Theoretical Calculations and Simulation Results

5.3.1 The Generated Optical Signal

In this section, we present a theoretical basis of the proposed mm-wave generation and transmission system. The concept behind the generation of the 60-GHz wireless signal is shown in Fig. 5-1, where only one single-electrode MZM is utilized. The optical field at the input of the single-electrode MZM is given by $E_{in}(t) = E_0\cos(\omega_c t)$, where E_0 and ω_c are the amplitude and angular frequency of the optical field, respectively. The driving RF signal $V(t)$ consisting of two signals at different frequencies MZM is $V(t) = V_1\cos(\omega_1 t) + V_2\cos(\omega_2 t)$, where V_1 and V_2 are the signal amplitudes at frequency ω_1 and ω_2, respectively. To simplify the analysis, the power

splitting ratio of the MZM is set as 0.5. In order to suppress the undesired optical carrier, the single-electrode MZM is biased at the null point. The optical field at the output of the MZM is then given by

$$E_{OUT}(t) = \mathrm{E_o} \cdot \cos\omega_c t \cdot \cos\left[\left(\frac{\pi}{2V_\pi}\right) \cdot (V_\pi + V_1 \cdot \cos\omega_1 t + V_2 \cdot \cos\omega_2 t)\right] \quad (5.6)$$

Using Bessel function expansion, the output optical field at the output of the MZM can be rewritten as

$$\begin{aligned} E_{out}(t) = E_o \cdot \{ & J_0(m_2)J_1(m_1)\cdot\cos[(\omega_c \pm \omega_1)t] \\ & - J_0(m_2)J_3(m_1)\cdot\cos[(\omega_c \pm 3\omega_1)t] \\ & - J_1(m_1)J_2(m_2)\cdot\cos[(\omega_c + \omega_1 \pm 2\omega_2)t] \\ & - J_1(m_1)J_2(m_2)\cdot\cos[(\omega_c - \omega_1 \pm 2\omega_2)t] \\ & + J_0(m_1)J_1(m_2)\cdot\cos[(\omega_c \pm \omega_2)t] \\ & - J_0(m_1)J_3(m_2)\cdot\cos[(\omega_c \pm 3\omega_2)t] \\ & - J_1(m_2)J_2(m_1)\cdot\cos[(\omega_c + \omega_2 \pm 2\omega_1)t] \\ & - J_1(m_2)J_2(m_1)\cdot\cos[(\omega_c - \omega_2 \pm 2\omega_1)t] + \ldots\}, \end{aligned} \quad (5.7)$$

where m_1 and m_2 are the modulation indices defined as $\frac{V_1\pi}{2V_\pi}$ and $\frac{V_2\pi}{2V_\pi}$, respectively. $J_n()$ is the n_{th} order Bessel function of the first kind. For a small modulation index the magnitude of Bessel function of the first kind is proportional to the order of the function. As shown in the Fig. 5-2, when the modulation index is small, the output optical field can be further simplified to

$$\begin{aligned} E_{out}(t) = E_o \cdot \{ & J_0(m_2)J_1(m_1)\cdot\cos[(\omega_c \pm \omega_1)t] \\ & + J_0(m_1)J_1(m_2)\cdot\cos[(\omega_c \pm \omega_2)t]\}. \end{aligned} \quad (5.8)$$

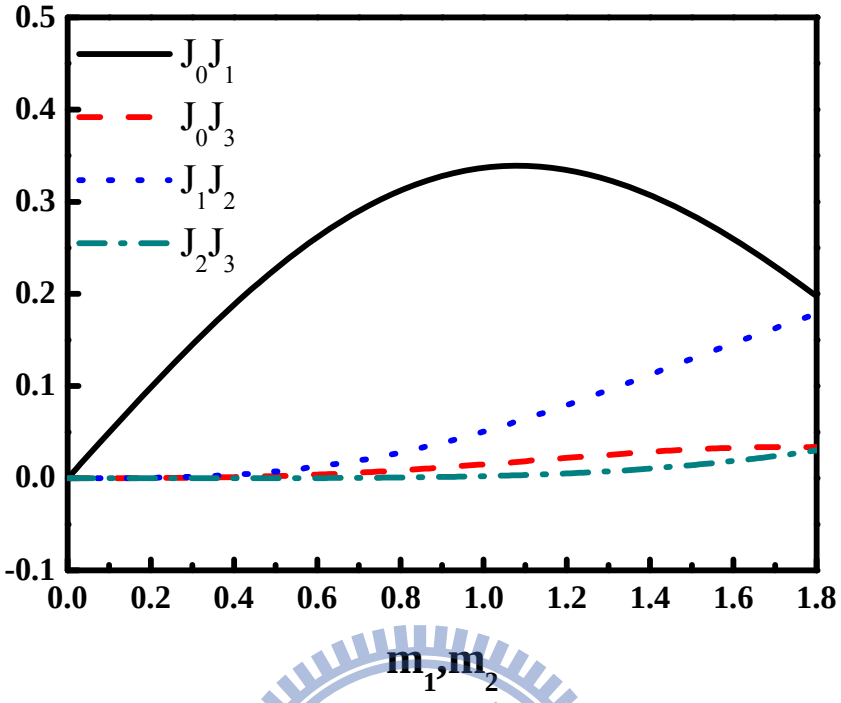

Figure 5-2 The magnitude of Bessel functions versus different RF modulation index.

5.3.2 The Generated Electrical Signal

After square-law photo detection the photocurrent of the mm-wave at frequency of $\omega_1 + \omega_2$ can be expressed as

$$i_{\omega_1+\omega_2} = R \cdot E_o^2 J_0(m_1) J_0(m_2) J_1(m_1) J_1(m_2), \tag{5.9}$$

where R is the responsivity of photodiode.

When optical RF signals are transmitted over a standard single-mode fiber with dispersion, a phase shift to each optical sideband relative to optical carrier is induced by fiber dispersion. The propagation constant of fiber can be expressed as [47]

$$\beta(\omega) = n(\omega)\frac{\omega}{c} = \beta_0 + \beta_1(\omega - \omega_c) + \frac{1}{2}\beta_2(\omega - \omega_c)^2 + \cdots, \tag{5.10}$$

where $\beta_m = (d^m \beta / d\omega^m)\big|_{\omega=\omega_c}$ is the derivative of the propagation constant evaluated at $\omega = \omega_c$. To simplify the analysis, the effect of high order fiber dispersion (i.e. 3rd order and higher) at 1550-nm band is neglected. For carrier tones with central frequency at $\omega = \omega_c \pm n\omega_{RF}$, we have $\beta(\omega_c \pm n\omega_{RF}) \cong \beta_0 \pm n\beta_1(\omega_c)\omega_{RF} + \frac{1}{2}n^2\beta_2(\omega_c)\omega_{RF}{}^2$ and, $\beta_2(\omega_c) = -(c/2\pi f_c^2)\cdot \mathrm{D}(\omega_c)$ where c is light speed in free space, D is the chromatic dispersion parameter, and f_c is the frequency of the optical carrier. For a standard single-mode fiber, D is 17-ps/(nm.km). Therefore, after transmission over a standard single-mode fiber of length z, the electrical field can be written as

$$\begin{aligned} E_{OUT}(t) = E_o \cdot \{ & J_0(m_2)J_1(m_1) \\ & \cdot \cos[(\omega_c \pm \omega_1)t - \beta_0 z \mp \beta_1\omega_1 z - \tfrac{1}{2}\beta_2\omega_1^2 z] \\ & + J_0(m_1)J_1(m_2) \\ & \cdot \cos[(\omega_c \pm \omega_2)t - \beta_0 z \mp \beta_1\omega_2 z - \tfrac{1}{2}\beta_2\omega_2^2 z]\}. \end{aligned} \tag{5.11}$$

After square-law photo detection, the photocurrent at the frequency of can be expressed as

$$\begin{aligned} i_{\omega_1+\omega_2}(t) = & R \cdot E_o^2 J_0(m_1)J_0(m_2)J_1(m_1)J_1(m_2) \\ & \cdot \cos[\frac{1}{2}\beta_2 z(\omega_2^2 - \omega_1^2)]. \end{aligned} \tag{5.12}$$

Due to fiber dispersion effect, the RF fading issue would be observed. The RF signal power is related to $\cos[\frac{1}{2}\beta_2 z(\omega_2^2 - \omega_1^2)]$. Therefore, the RF fading issue would become serious when the magnitude of sum frequency (f_2+f_1) and frequency difference (f_2-f_1) become large.

For 60-GHz applications, the sum frequency (f_2+f_1) is fixed at 60.5 GHz,

and the frequency difference (f_2-f_1) will dictate the performance of RF fading. As shown in the Fig. 5-3, when the frequency difference increases, the RF power will drop off rapidly due to the fading effect. For frequency differences of 10 GHz and 40 GHz, the first deep appears following 6 and 1.6-km fiber transmission, respectively. The smaller frequency difference not only results in a longer fiber transmission distance, but it also reduces the bandwidth requirements of the transmitter.

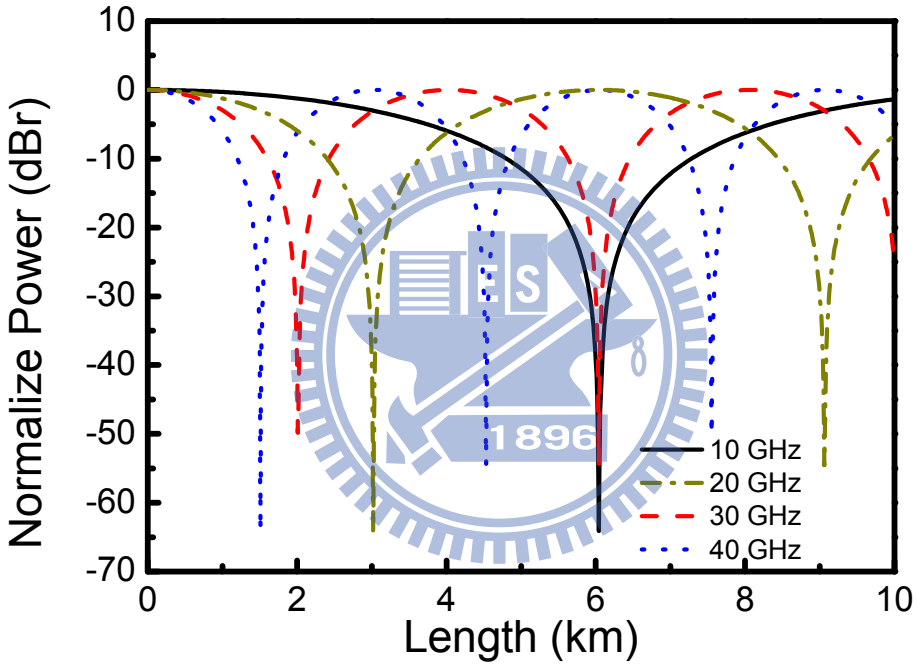

Figure 5-3 Simulated RF power of the generated mm-wave signal versus standard single-mode fiber length for various input frequency differences (i.e. f_2 - f_1).

5.3.3 Beat Noise in Proposed System

The smaller frequency difference would bring many benefits to the proposed system. However, the drawback of a small frequency difference is the risk of having beat noise interference. For example, if we choose 5.5 GHz as

the frequency difference, and set the input frequencies at ω_2 = 33 GHz and ω_1 = 27.5 GHz, then with 7-GHz signal bandwidth, the driving data will occupy frequencies from 24 to 31 GHz. As a result the beat noise (i.e. USB1 × LSB1) will fill the band from 48 to 62 GHz. Since the generated vector signal will fill the band from 57 to 64 GHz, the beat noise will fall in-band as shown in Fig. 5-4 (a), resulting in the possibility for severe system performance degradation. It is therefore necessary to choose proper frequencies of the input signals in the design process in order to avoid beat-noise induced system performance degradation. A good example is shown in Fig. 5-4 (b), where a frequency difference of 15.5 GHz is chosen, resulting in the beat noise occupying the band from 38 to 52 GHz and causing no interference.

Therefore, there are tradeoffs between RF fading and beat noise interference. In the following analysis, we will choose the lowest possible frequency difference without causing any beat noise interference. With a target signal bandwidth of 7 GHz and center frequency of 60.5 GHz, we have

$$\begin{cases} f_1 + f_2 = 60.5 \text{ GHz} \\ 2(f_1 + 3.5) = 60.5 - 3.5 = 57 \text{ GHz} \end{cases} \tag{5.13}$$

This leads to a frequency difference equal to 10.5 GHz and input signal frequencies f_1 = 25 GHz and f_2 = 35.5 GHz, respectively. In this case the beat noise falls just outside the desired signal band, as shown in Fig. 5-4 (c). With the chosen frequency parameters, we can calculate the RF fading performance.

Figure 5-5 (a) shows the RF power of the mm-wave signals generated between 57-64 GHz plotted against frequency. The line and circle represent theoretical results obtained using the model in equation (5.12) and VPI WDM-TransmissionMaker simulation results, respectively. It can be seen that

RF fading is negligible over the whole 7-GHz spectrum for fiber spans up to 1 km. Beyond 1 km, frequencies in the lower part of the spectrum begin to experience increasing attenuation because they are generated from larger frequency differences. After 4 km of fiber transmission, the attenuation increases to 14 dB at 57 GHz and only 3 dB at 64 GHz. Nonetheless, for typical indoor applications, 2 to 3 km is more than enough. On the other hand, if longer fiber transmission distances are needed, then any one of the four optical sidebands (see Fig. 5-1) may be filtered off to eliminate fading. To compare the fading length of the proposed system to that of a DSB intensity-modulation direct detection (IMDD) transmission system, we plot the calculated and the simulated (VPI WDM-TransmissionMaker) fading (signal power) as a function of frequency. As Fig. 5-5 (b) shows, the first deep (total fading) at 60.5 GHz occurs after just 1 km of standard single-mode fiber transmission in the case of the DSB IMDD RoF system. Therefore, compared with the DSB IMDD RoF system, the proposed system offers superior transmission performance and more flexible system design.

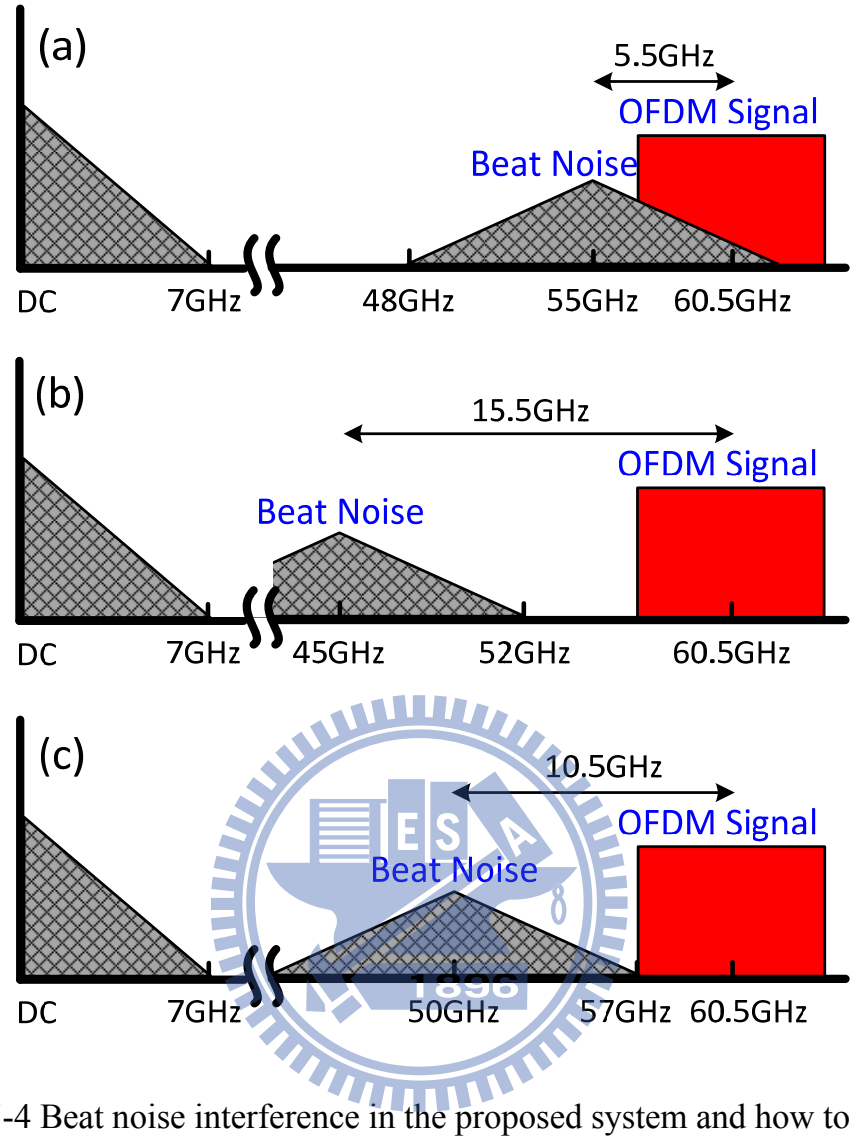

Figure 5-4 Beat noise interference in the proposed system and how to keep it from degrading system performance: (a) beat signal falls inside the desired band, (b) beat signal is far away from desired band, and (c) beat noise is just outside the desired frequency band.

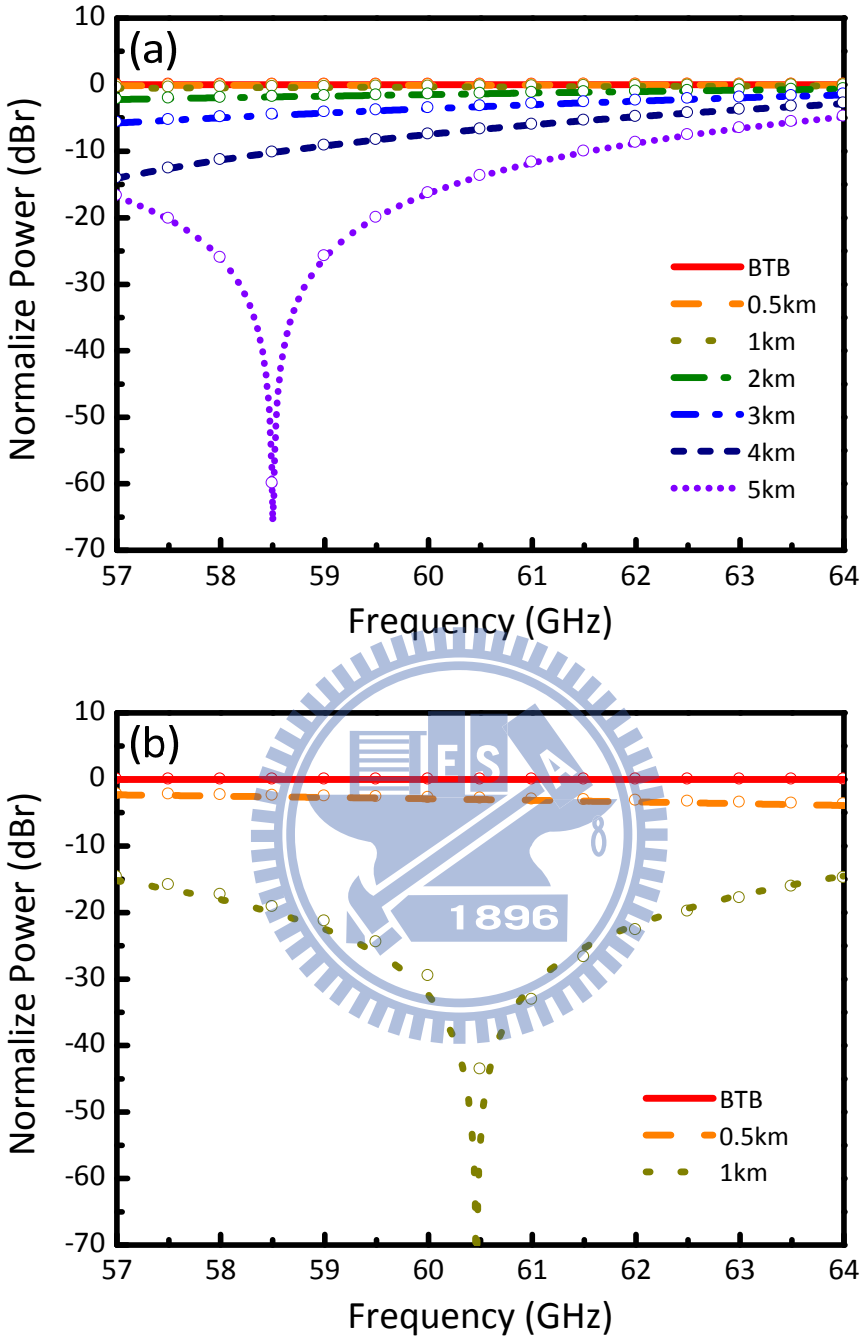

Figure 5-5 Simulations results of RF fading at 60 GHZ band versus different transmission length, (a) proposed system, (b) double side band modulation format.

5.4 Experimental Demonstration of Proposed System

In 5.4, the experimental demonstration could separate into two parts. One is the SISO system, the other is MIMO system. Two modulation formats are demonstrated in the SISO system, including the OFDM (5.4.1-5.4.2) and the single carrier signals (5.4.3-5.4.4). From the results of the SISO system, the SC-FDE signal performs the best performance. Therefore, the MIMO system is demonstrated with the SC-FDE signal (5.4.5-5.4.6).

5.4.1 Experimental Setup for SISO System

Fig. 5-6 depicts the experimental setup of the electrical I/Q up-conversion RoF system. Due to the bandwidth limitation of the arbitrary waveform generator (AWG) located at the Head-End Unit (HEU), two 3.5-GHz-wide signals (I and Q) were generated using a Matlab® program. An electrical I/Q mixer was used to up-convert the baseband OFDM signals to a 7 GHz-wide signal centered at 25 GHz as shown in inset (i) in Fig. 5-6. The resolution of the digital-to-analogue converter of the AWG was set to 8 bits. The digital to analog converter (DAC) sampling rate was 12 GSample/s. The inverse fast Fourier transform (IFFT) length was 128, resulting in a subcarrier symbol rate of 93.75 MSymbol/s. Therefore, with a total of 74 sub-carriers and bit loading modulation on each sub-carrier, the combined data rate of the 7-GHz-wide OFDM signal at the output of the electrical mixer was 40 Gb/s. The signal was then combined with a 35.5-GHz LO signal generated by a signal generator. The composite signal was then used to drive a single-electrode MZM specified for 40-Gb/s data transmission with 0-dBm driving power. The optical signal source was a distributed feedback (DFB) laser emitting +10.5 dBm optical power at 1550-nm wavelength. The continuous wave (CW) optical signal was fed into

the MZM, where it was modulated by the combined OFDM and LO signals. The MZM modulator was biased at the point of minimum transmission in order to suppress the optical carrier. Therefore, the optical signal exiting the MZM comprised a total of four sidebands-two un-modulated subcarriers at f_o±35.5 GHz and two OFDM-modulated subcarriers at f_o±25 GHz, where f_o is the optical carrier frequency, as shown in inset (ii) in Fig. 5-6.

One of the advantages of the proposed system is that the relative intensity between the un-modulated optical sidebands and the OFDM-modulated sidebands can be tuned easily by independently adjusting the amplitudes of the two input signals (RF) to optimize system performance. The optical signal was then amplified by an Erbium Doped Fiber Amplifier (EDFA) with a noise figure of 4 dB. After the EDFA, an optical band-pass filter with a 3-dB bandwidth of 3 nm was used to suppress the amplified spontaneous emission (ASE) noise. The optical signal was then transmitted to a Remote Antenna Unit (RAU) connected by standard single-mode fibers of different lengths. At the RAU, the OFDM signal at 25 GHz was up-converted to 60.5 GHz through square-law photo-detection (mixing with the remotely transmitted 35.5-GHz LO signal) in the 67-GHz photodiode. The generated electrical power is -39.3 dBm with -5-dBm receiving optical power. Therefore, the E/O and O/E conversion loss of the proposed RoF link was about 39.3 dB. Since the OFDM signal at 25 GHz was 7 GHz wide, the signal generated at the RAU was also 7 GHz wide, occupying the full spectrum at the 60-GHz band specified by the FCC (57-64 GHz). The OFDM signal was then amplified by a low noise amplifier (LNA) with 39-dB gain, and the power of the amplified OFDM signal was -0.3 dBm. After the LNA, the 60-GHz OFDM signal was fed into a

rectangular waveguide-based standard gain horn antenna with about 23-dBi gain, and transmitted over 3-m wireless distance. After transmission over the air, the 60-GHz signal was received by another standard gain horn antenna (23-dBi) with -33.1 dBm received power. Therefore, the estimated path loss of the wireless transmission is about 77.8 dB. Then, the received signals was amplified with an LNA (gain = 39 dB), and passed on to the 60-GHz down-converter. The 60-GHz down-converter consisted of a mixer driven by a 56-GHz LO, as shown in Fig. 5-6. Therefore, the received OFDM signal at 60.5 GHz was down-converted to an IF of 4.5 GHz as shown in insert (iii) of Fig. 5-6. The IF was chosen so as to maintain the 7 GHz wide spectrum of the received OFDM signal. The waveforms of the down-converted OFDM signals were captured by a real-time oscilloscope with a 40-GSample/s sampling rate and a 3-dB bandwidth of 13 GHz for off-line signal processing and analysis. An off-line Matlab® digital signal processing program was employed to demodulate the OFDM signal. The demodulation process included I/Q down-conversion, synchronization, fast Fourier transform (FFT) calculation, one-tap equalization, and BER estimation.

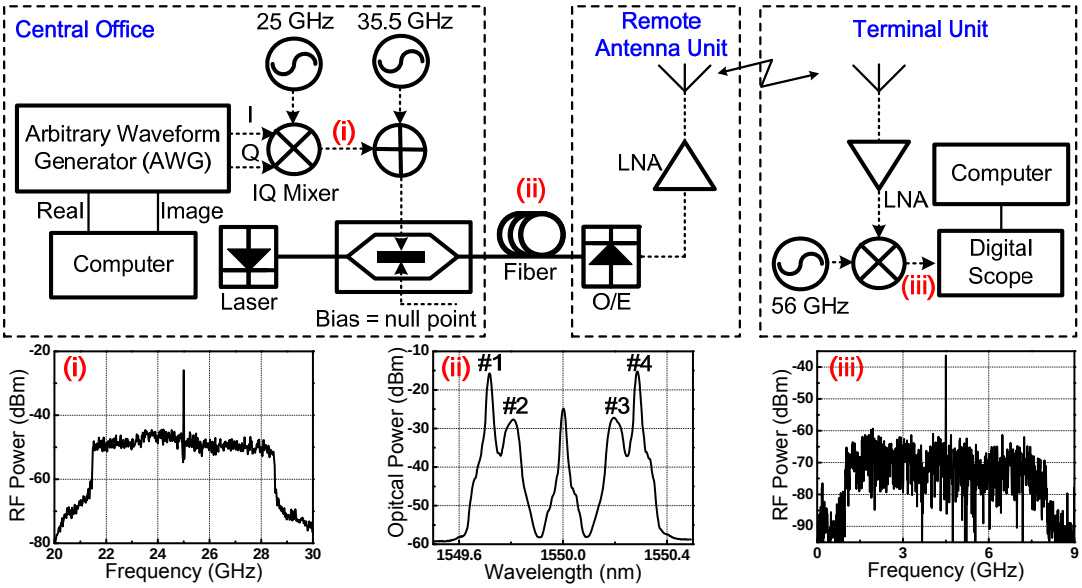

Figure 5-6 Experimental setup of the proposed RoF system.

5.4.2 Results and Discussions for OFDM Signal

First, we measured the performance of the system using OFDM signal with QPSK modulation formats for each subcarrier. To avoid the effects of I/Q imbalance, the system use a 3.5GHz-wide OFDM signal and one electrical double balance mixer to generate 7GHz-wide OFDM signal. The 3.5-GHz-wide OFDM signal that was generated using Matlab® program had 37 sub-carriers. It was then up-convert to 25 GHz using an electrical mixer. Both sidebands of the up-converted OFDM signal were retained for transmission in order to emulate a 7-GHz-wide OFDM signal. Since the OFDM subcarriers were transmitted independently (un-correlated), and demodulated independently at the receiver, the total bit-rate of the 7-GHz-wide OFDM signal was double that of the baseband OFDM signal generated by the AWG. The wireless transmission distance is fix in 3m. Fig. 5-7 shows the bit error rate (BER) curves for the received 13.875-Gb/s QPSK OFDM signal. The BER was

estimated from the measured error vector magnitude (EVM), which is defined as:

$$\text{EVM} = \sqrt{\sum|S_{Ideal} - S_{Measure}|^2 / \sum|S_{Ideal}|^2} \times 100\% \qquad (5.14)$$

where S_{Ideal} and $S_{Measure}$ are the ideal and the measured constellation points, respectively. For QPSK signal, the BER is related to EVM by

$$\text{BER} = \text{Q}[1/\text{EVM}] \qquad (5.15)$$

where Q[.] is the Gaussian co-error function. Generally, this function assumes that the noise is Additive White Gaussian Noise (AWGN).

Figure 5-7 shows that as fiber transmission length increased, the system sensitivity decreased. For back-to-back (BTB), 500-m, and 1-km transmission distances, the sensitivity was the same and equals to -13 dBm for a BER of $1x10^{-3}$. After 2 km and 3 km of fiber transmission, there was a small penalty of about 1 dB and 1.5 dB, respectively, at the BER of $1x10^{-3}$. However, after 5 km of fiber transmission, the signal was severely corrupted with the BER greater than $1x10^{-3}$. Fig. 5-8 shows the electrical spectrum of the down-converted OFDM signal. It can be seen from the figure that the bandwidth of the down-converted OFDM signal was 7-GHz wide. The spectrum also shows a peak at 4.5 GHz, which is the residual signal from the 25-GHz LO used to up-convert the baseband OFDM signal to 25 GHz back at the HEU. The progression of the chromatic-dispersion-induced fading as the fiber transmission distance becomes larger can also be seen in Fig. 5-8. It was observed that lower frequency components faded quicker and deeper, just as predicted by the theoretical analysis presented in 5.3.2. The reason for the quicker/greater fading at the lower frequency components is because the lower frequency components are generated by larger frequency differences of the two

electrical input signals at the HEU, as shown in Fig. 5-9. For the DSB modulation schemes, the result is different from the proposed system, as shown in Fig. 5-10. It was observed that higher frequency components faded quicker and deeper for the DSB modulation. The reason is that the fading issue is proportional to frequency for DSB modulation. The proposed system has 1dB power penalty with -2dBr normalize power at 57 GHz after 2 km fiber transmission. Compared with the DSB modulation scheme, the DSB system has -2dBr normalize power at 64 GHz after 400 m fiber transmission. Fig. 5-11 shows the constellation diagrams of the demodulated OFDM signals for different fiber transmission lengths with the wireless transmission distance fixed at 3 m. Very clear constellation diagrams were observed until the fiber length exceeded 3 km. The total data rate of the signal was 13.875 Gb/s. The detected optical power corresponding to the constellation diagrams was -10 dBm. For the BTB case, the calculated EVM was 17.7 %. However, lower EVM values up to 16 % were obtained at higher received optical powers. The clean constellation diagram in Fig. 5-11 (a) confirms the excellent performance of the RoF system in generating and transmitting high quality wideband OFDM signals at 60 GHz both over optical fiber and wireless distance. It also shows the potential of the system for operating at a bit-rate higher than 13.875 Gb/s by using modulation formats of higher order than QPSK (e.g. 8-QAM).

To further investigate the impact of RF fading on signal quality, the SNR of each of the 74 sub-carriers making up the OFDM signal was calculated for different fiber transmission distances, using

$$\mathrm{SNR} = -20 \cdot \log(\mathrm{EVM}/100\%). \tag{5.16}$$

The result is shown in Fig. 5-12. The higher subcarrier number corresponds

to higher subcarrier frequency (i.e. sub-carrier number 74 is around 64 GHz before down-conversion). It was observed that the SNR of the individual sub-carriers remained the same for BTB, 0.5 km, and 1 km of fiber transmission distances. However, for fiber spans longer than 1 km, a drop in the SNR of the sub-carriers at the lower end of the spectrum was observed. For example, after 3 km of fiber transmission, the SNR of the 1st and the 74th subcarriers dropped by 4 dB and 1 dB, respectively, with respect to their respective BTB SNRs. This result is consistent with the theoretical analysis presented in 5.3.2, which showed that sub-carriers at the lower frequencies suffered worse RF fading leading to a reduced average SNR.

To investigate the performance of the RoF system without wireless transmission, the OFDM signal generated at the RAU was immediately down-converted to the same IF frequency as before (i.e. 4.5 GHz). Just like before, the optical signal was transmitted over different lengths of standard single-mode fiber. The result is given in Fig. 5-13, where the estimated BER is plotted against the optical signal power. Once again, the performance of the RoF system with BTB, 500 m and 1 km of fiber transmission remained the same. This means that, just like in the case with wireless transmission, the system suffered no penalty due to fiber chromatic dispersion up to 1-km fiber transmission. For fiber transmission distances of 2 km and 3 km, there was a penalty of 1 dB, and 1.5 dB, respectively at a BERs equal to $1x10^{-3}$. A larger penalty was observed after transmission over 4 km of standard single-mode fiber. These results are similar to the ones obtained in the case of the system with wireless transmission discussed above. The difference in the sensitivities of the two systems (with and without wireless transmission, i.e. Fig. 5-7 and

Fig. 5-13, respectively) is about 1 dB. This is attributed to the presence of an extra LNA amplifier required in the wireless receiver (i.e. in the case of the system with wireless transmission).

Figure 5-12 also shows that the SNR performance depends on the location of subcarrier. The reasons are because the 60-GHz components have uneven frequency response and different frequency has different fading issue. Therefore, the dynamic bit loading is proposed to mitigate the chromatic-induced penalties. Moreover, since the 60-GHz components have uneven frequency response, the performance of the OFDM-modulated RoF system is dominated by the subcarriers with poorest error performance (i.e., having the lowest SNR). The adaptive power and bit allocation for each subcarrier is a good solution to increase the overall system performance and data rate with the same signal performance.

Note that the system use a 3.5GHz-wide OFDM signal and one electrical double balance mixer to generate 7GHz-wide OFDM signal. However, the system can only emulate the signal that both sidebands are symmetrical signal. In order to realize adaptive loading algorithm in proposed system, the experimental setup needs an electrical I/Q mixer.

Since I and Q data go through different paths, the amplitude and phase need to optimal in this experimental setup. Because each subcarrier has different optimal condition, the system would get very different constellation when optimized at different frequency. Figure 5-14 shows the SNR versus subcarrier number with different optimal frequency. These three lines are optimized at 0.56, 1.5, and 3.5 GHz, respectively. The result shows the wideband system has serious I/Q imbalance issue. Therefore, the I/Q imbalance

correction algorithm is needed in the proposed system. Figure 5-15 shows the QPSK signal with I/Q compensation. After I/Q compensation, these three lines which are optimized at different frequency have almost the same SNR curve.

Figure 5-16 shows the experimental result for adaptive loading algorithm without I/Q imbalance compensation. The experimental setup is optimized at 3.5 GHz. 8-QAM, 16-QAM, and 32-QAM formats were utilized based on the corresponding SNR of each subcarrier. By using adaptive loading algorithm, the experiment demonstrates OFDM signal generation and transmission with 31.4 Gbps within 7-GHz license-free spectrum at 60 GHz band. The BER is 3.7 $x10^{-4}$, which is below the FEC error-free transmission threshold.

Figure 5-17 shows the optical receiver sensitivity for the 41.4 Gb/s OFDM signal recovered after transmission over various fiber spans and 3 m wireless transmission distance. For the back-to-back (BTB), and 1 km fiber transmission cases, a received optical power of at least −2 dBm was needed to achieve a maximum BER of $9x10^{-4}$, which is below the forward-error-correction (FEC) error-free transmission threshold. Note that bit-loading and I/Q imbalance parameters were optimized during the BTB case (received optical power = −1.5 dBm), and kept constant during all the sensitivity measurements.

Figure 5-18 presents the BER as a function of the received RF power (after wireless transmission) for different wireless transmission distances and a bit rate of 40 Gb/s. The system was optimized at −37 dBm received RF power for 10 m case. As seen in Fig. 5-18, the received RF power of −38 dBm was enough to achieve the FEC error-free transmission for all the investigated wireless transmission distances.

Figure 5-19 the maximum achievable bit rate as a function of fiber transmission distance. The received optical and RF power were fixed at −1.5 and -2 dBm, respectively. The wireless transmission distance is fixed at 3 m. For the case with 5km fiber transmission, a significant number of subcarriers have power fading of more than 15 dB and could not meet the FEC limit (even for QPSK format). As a result, the overall system BER exceeded the FEC limit with adaptive loading OFDM signal. The data-rate of 19.69 Gbps was achieved after 5km fiber transmission.

Fig. 5-20 shows the maximum achievable bit rate as a function of received RF power for the optical BTB case. The received optical power was fixed at −1.5 dBm and wireless transmission distance at 3 m. For each received RF power, bit-loading and I/Q imbalance compensation parameters were optimized to achieve the maximum data rate. More than 40 Gb/s data rate was achieved when the received RF power was larger than −41 dBm, allowing a considerably large margin for extending the wireless transmission distance. In Fig. 5-21, the maximum achievable bit rate at each wireless transmission distance is shown. It was observed that the maximum bit rate ranged from 41.4 Gb/s at 2 wireless distance to 40 Gb/s at 10 m. In this measurement, the received optical power and received RF power were fixed at −1.5 dBm and −37 dBm, respectively. Figure 5-22 shows the impact of I/Q imbalance compensation on the performance of the RoF system. A significant improvement in the SNR of the OFDM sub-carriers to the left of Fig. 5-22 (lower frequency), as a result of I/Q imbalance compensation can clearly be seen. It is this improvement in sub-carrier SNR that leads to the significant increase in data capacity observed.

Finally, Fig. 5-23 shows the constellation diagrams of the demodulated signal at 40 Gb/s after 10 m wireless signal transmission, with the received RF and optical powers set at −37 dBm and −1.5 dBm, respectively. Clear separation of constellation points confirms excellent signal transmission quality.

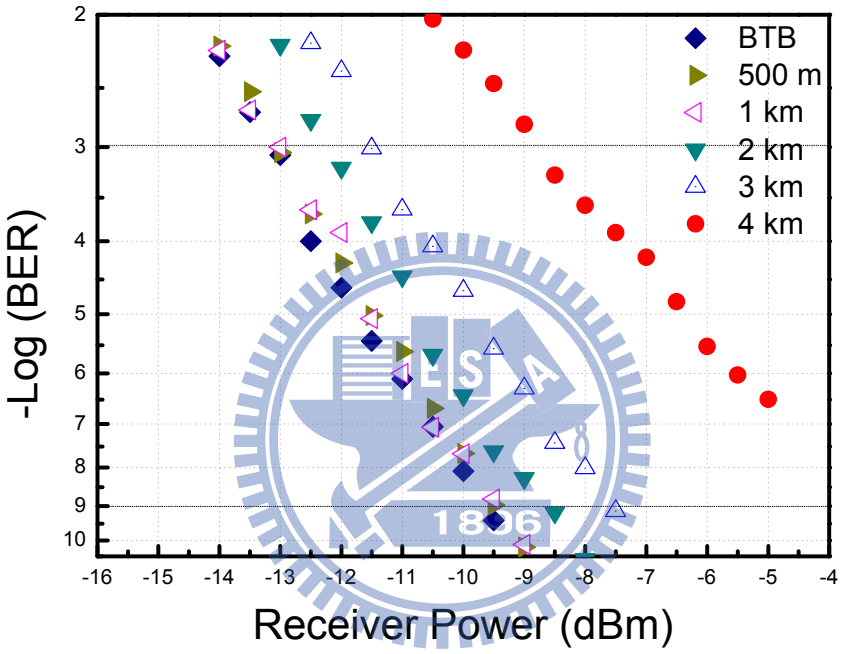

Figure 5-7 BER curves of 13.875-Gb/s QPSK OFDM signal after transmission over the RoF system including 3 m wireless distance.

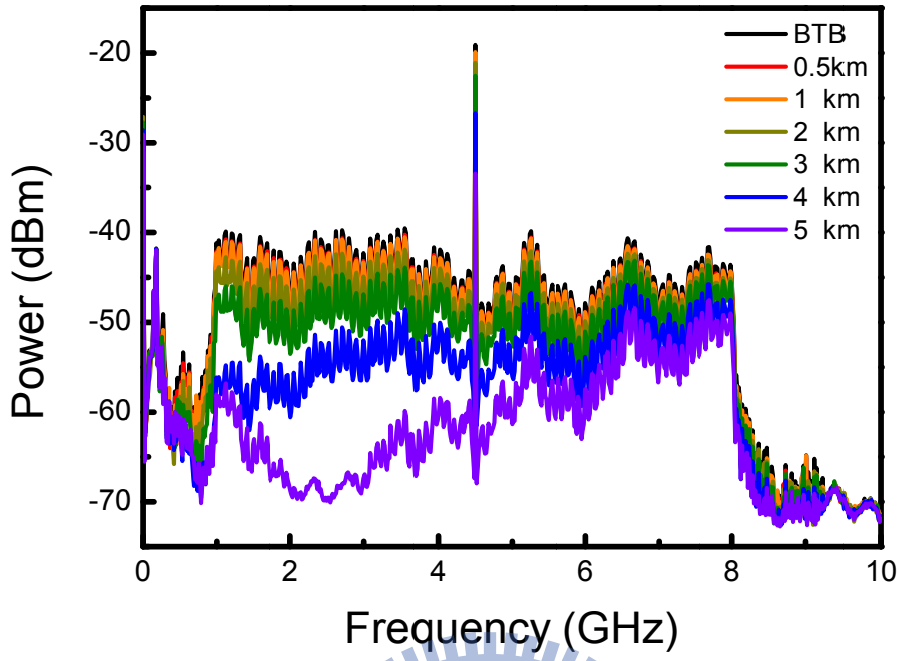

Figure 5-8 The down-convert electrical spectrums for different standard single-mode fiber transmission length.

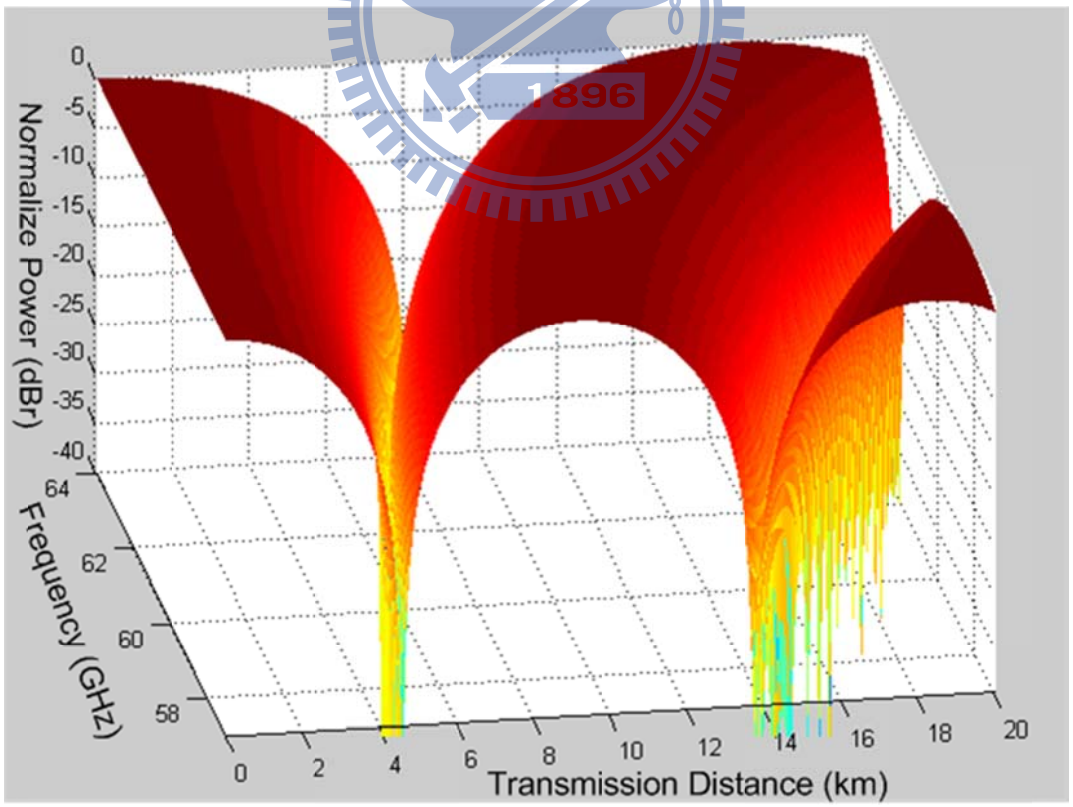

Figure 5-9 Simulations results of RF fading with DSB system.

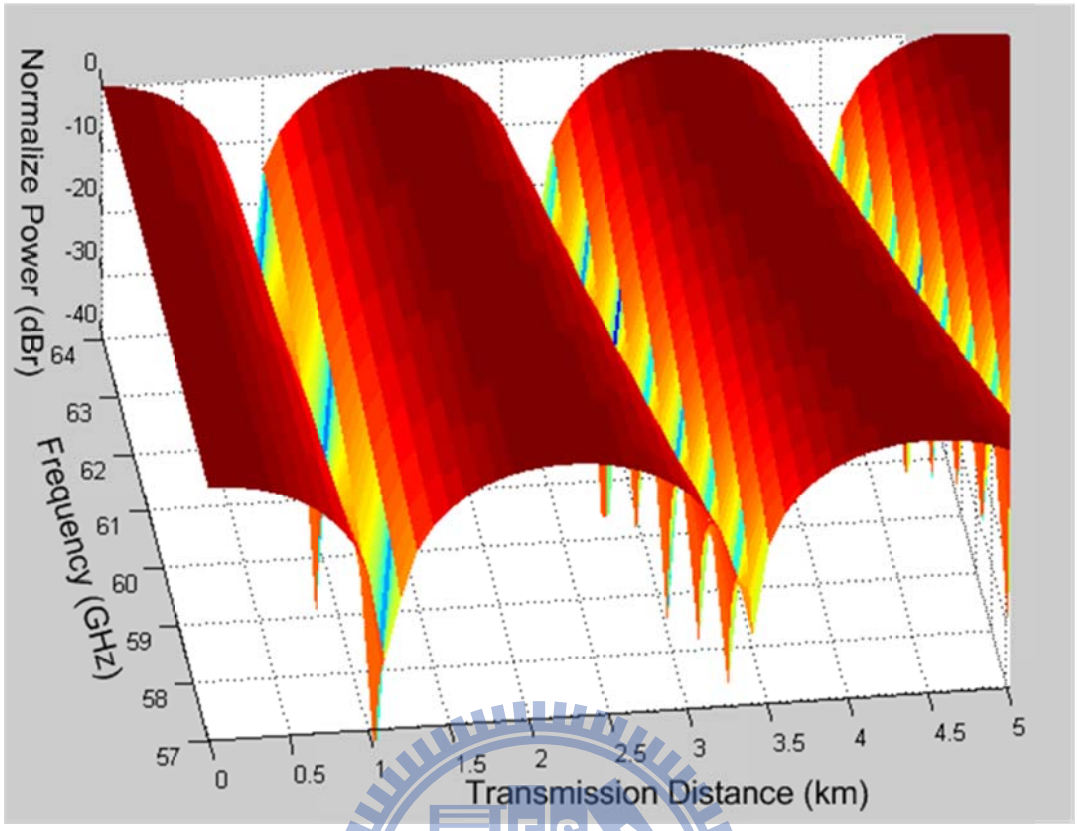

Figure 5-10 Simulations results of RF fading with proposed system.

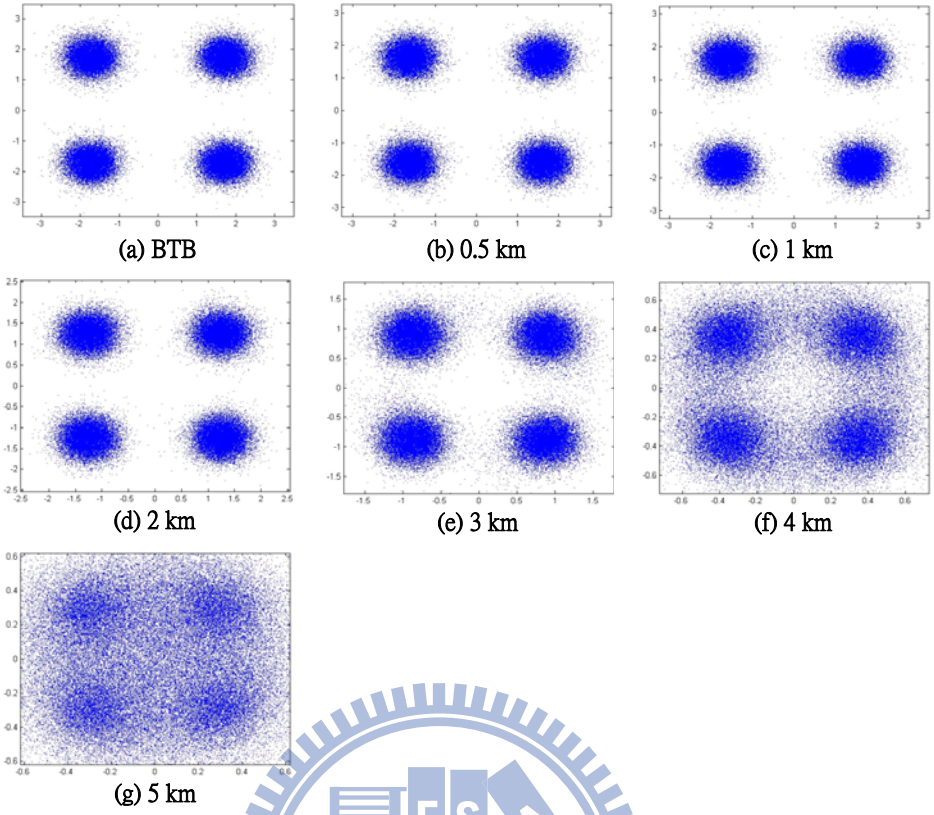

Figure 5-11 Constellations of QPSK OFDM signals.

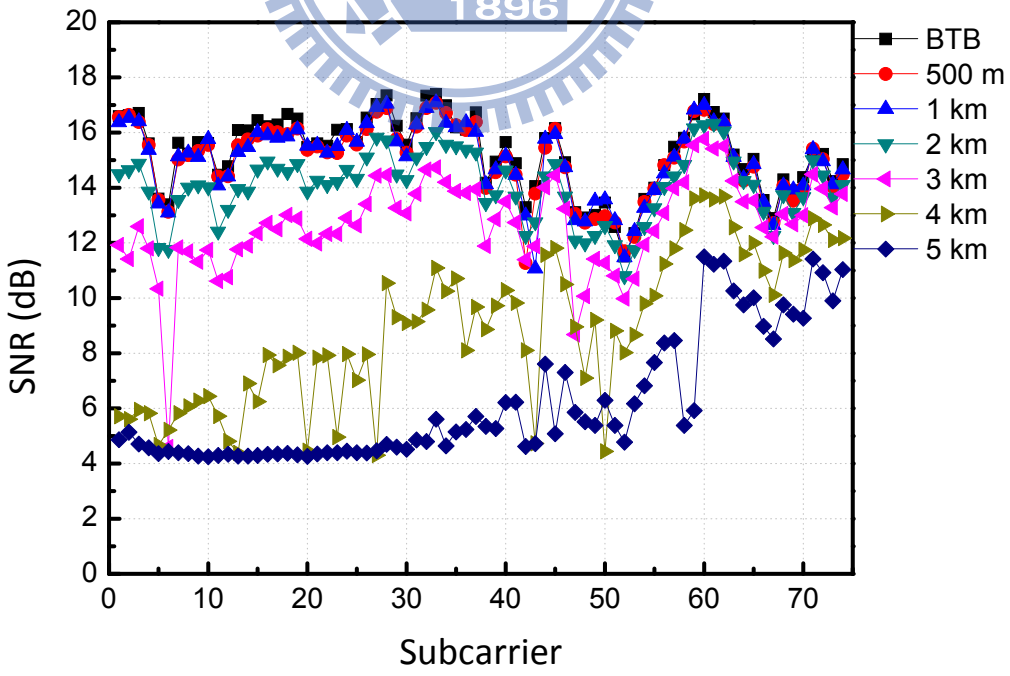

Figure 5-12 SNR versus different subcarrier for different standard single-mode fiber transmission length.

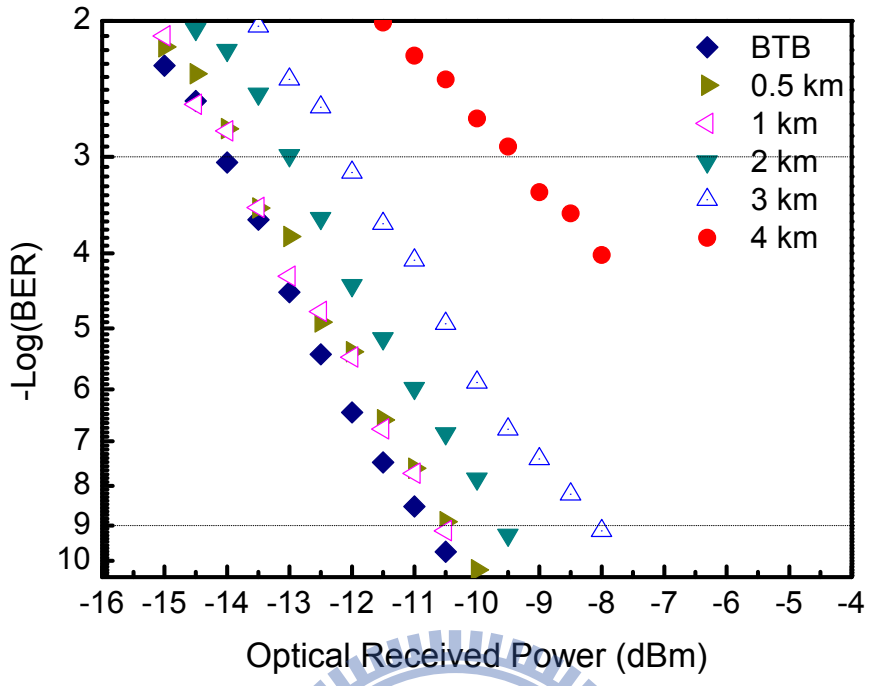

Figure 5-13 BER curves of 13.875-Gb/s QPSK OFDM signal without wireless transmission.

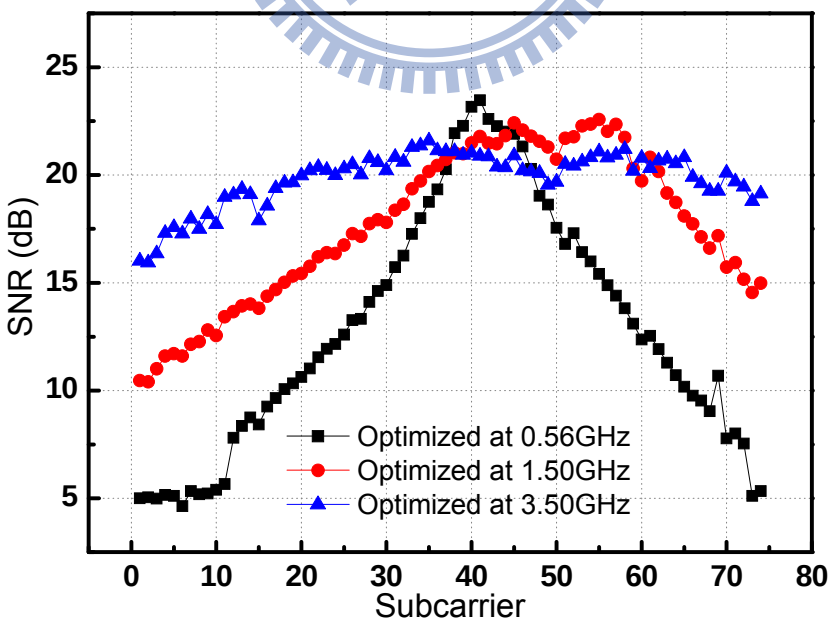

Figure 5-14 SNR versus different subcarrier for different optimized frequency.

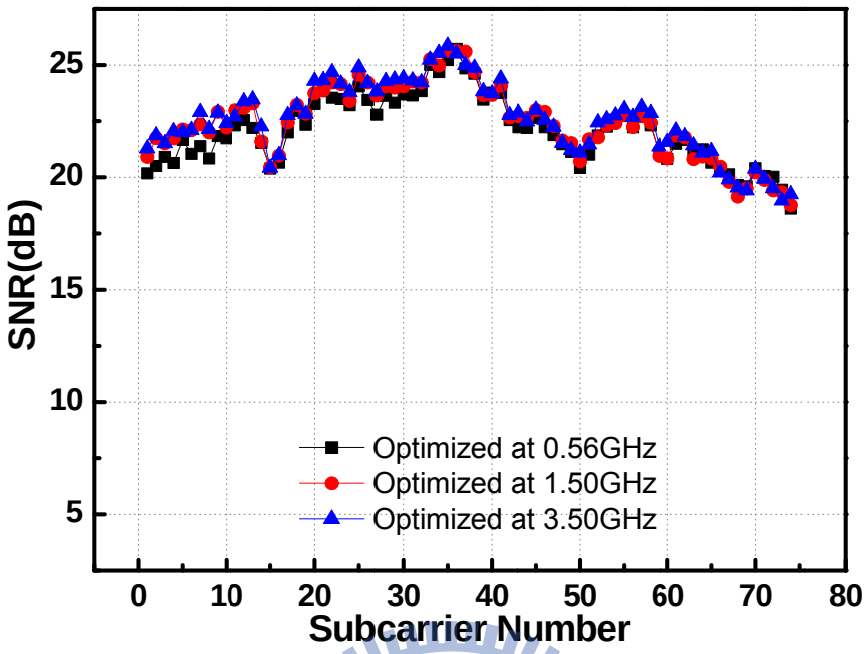

Figure 5-15 SNR versus different subcarrier with I/Q imbalance compensation.

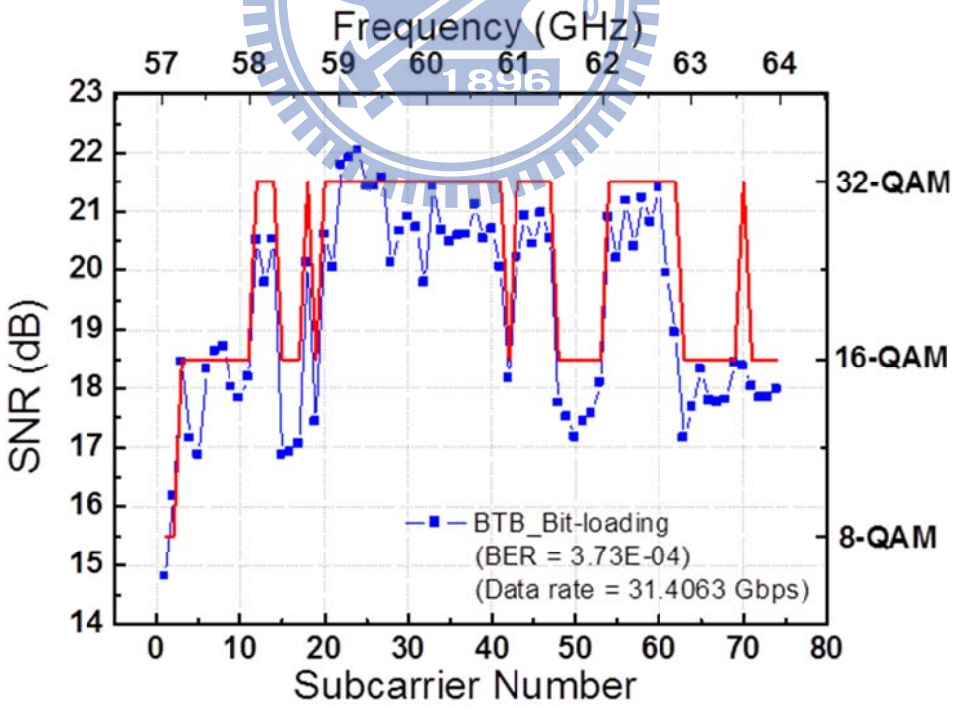

Figure 5-16 SNR and data format versus different subcarrier with adaptive bit-loading algorithm.

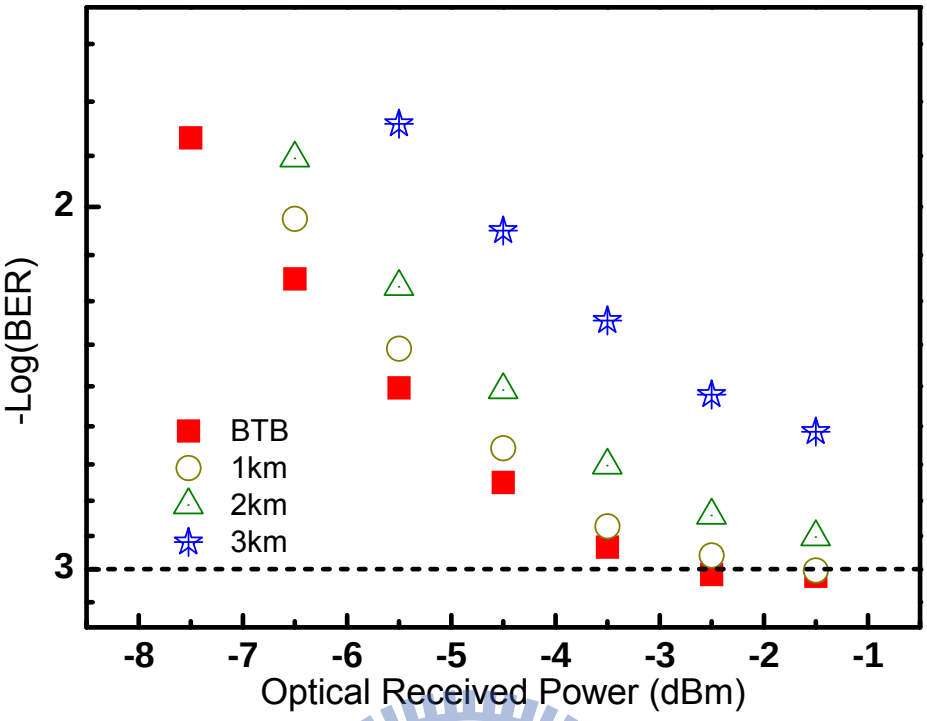

Figure 5-17 BER as functions of received optical power

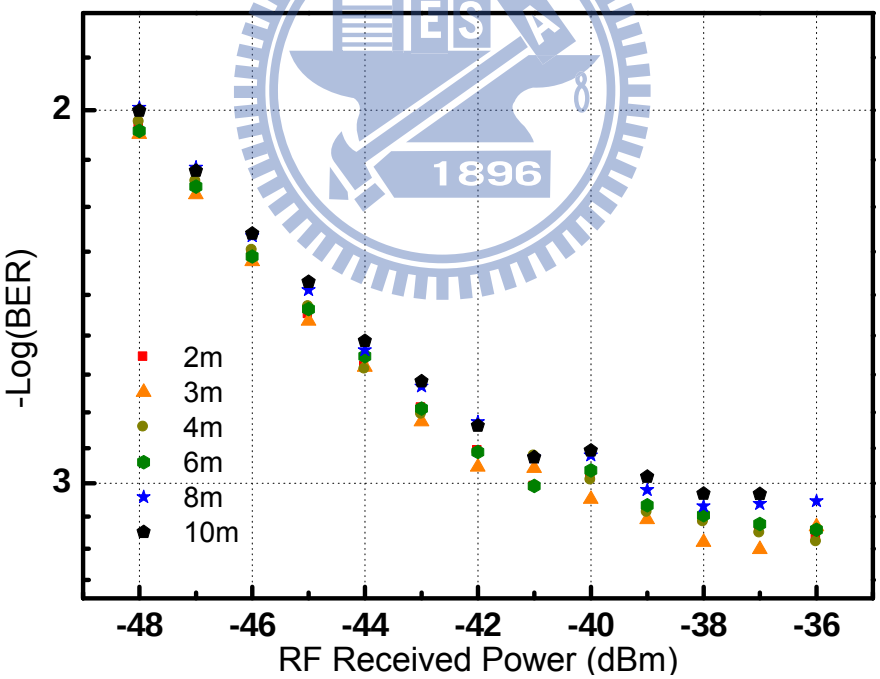

Figure 5-18 BER as functions of RF received power

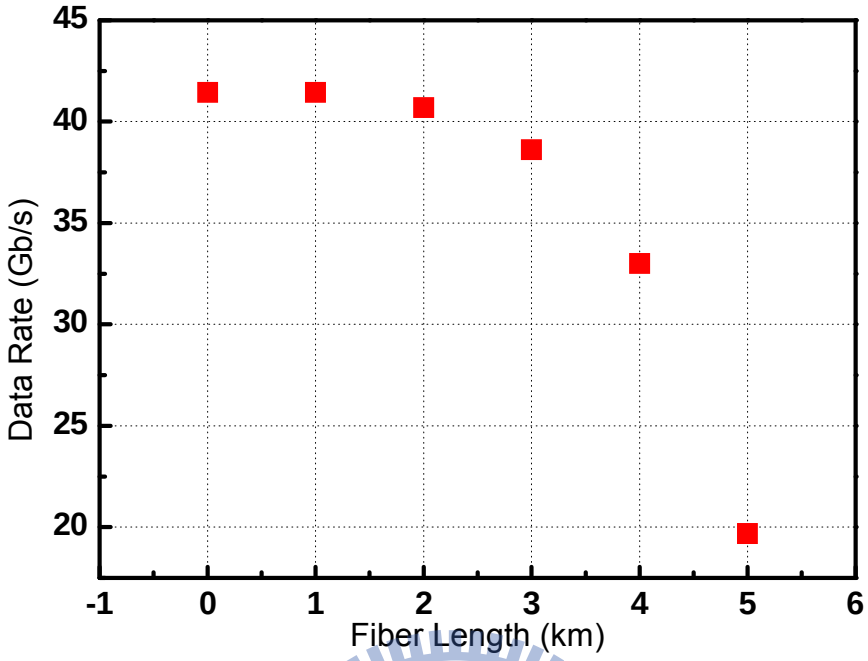

Figure 5-19 Data rate as function of optical fiber transmission distance.

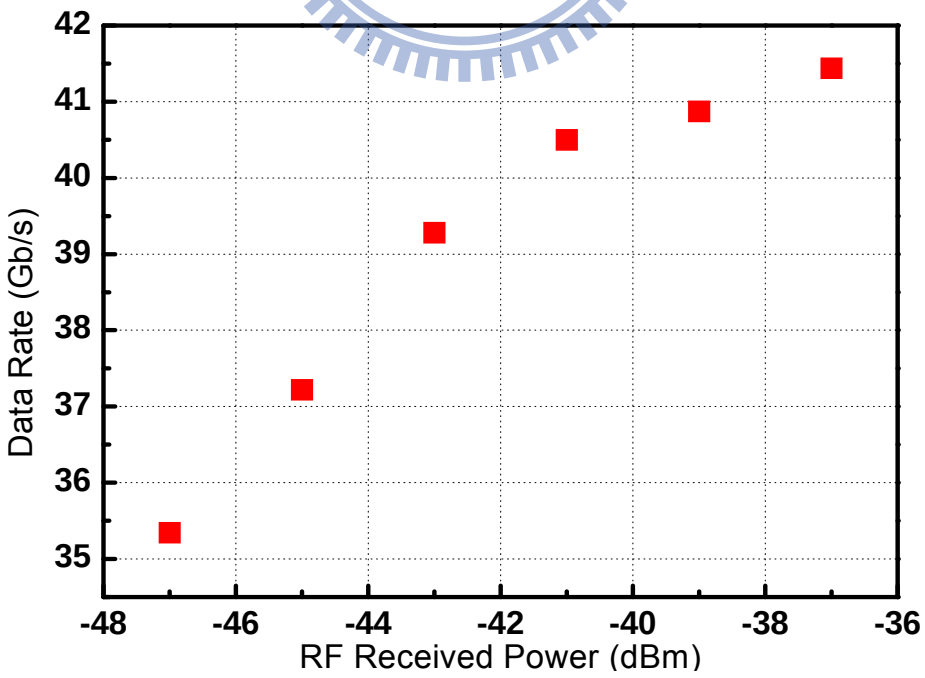

Figure 5-20 Data rate as function of RF received power.

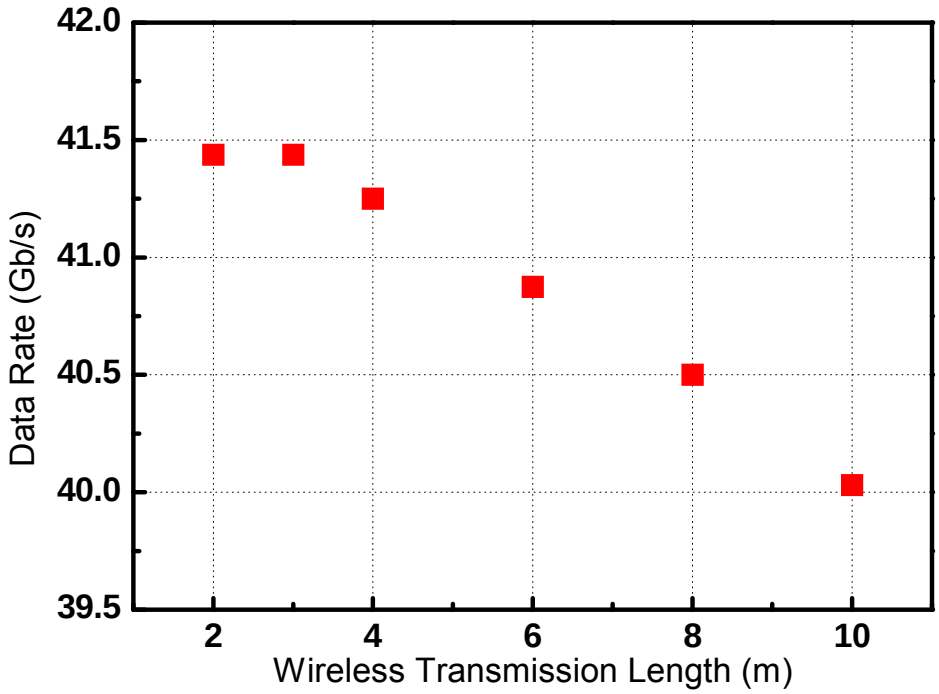

Figure 5-21 Data rate as functions of wireless distance.

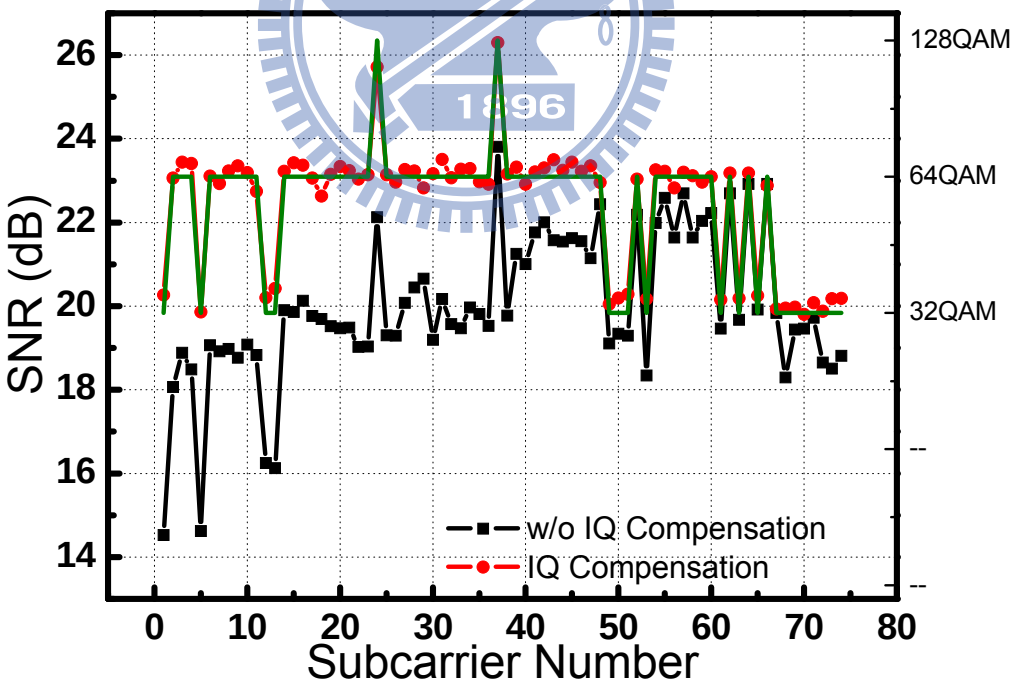

Figure 5-22 Effect of I/Q imbalance compensation.

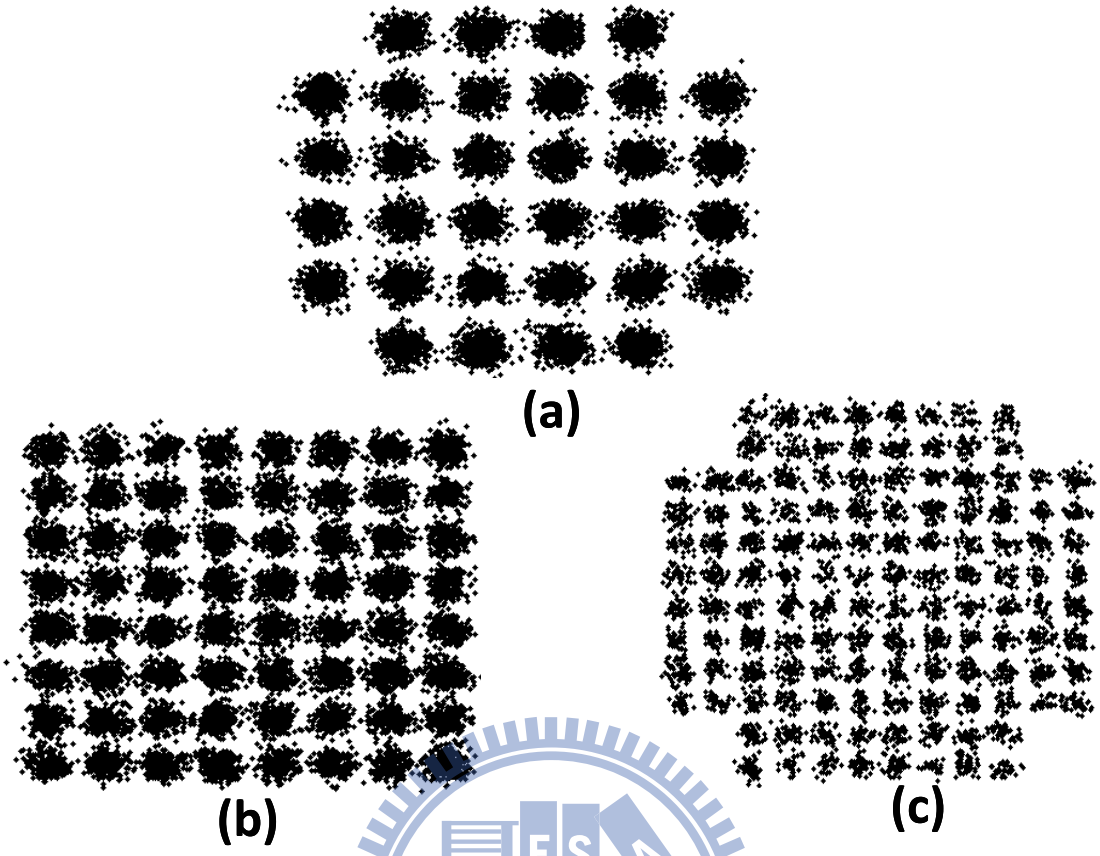

Figure 5-23 Demodulated signal at 40 Gb/s for different subcarriers (a) 67 – 71 (b) 6 – 10, and (c) 24 and 37.

5.4.3 Experimental Setup for SC-FDM Signal

The experimental setup for the SC-FDM signal is almost the same as the setup for the OFDM signal. The main differences are the Matlab® program and the transmitted signal power. For the SC-FDM signal, the sampling rate in Matlab® program equals to the wanted signal bandwidth. Due to the limited bandwidth of 60GHz signal, the sampling rate was 6.9375 GSample/s in Matlab® program. The Roll-off factor and wireless transmission distance are fixed to 0.05 and 4m in this experiment, respectively. Two subcarrier mapping methods will be investigated with different number of groups. The experiment also investigates the impact of I/Q imbalance, IFFT length, fiber transmission distance, and modulation format for each group.

5.4.4 Results and Discussions for SC-FDM Signal

Figures 5-24 plot the transmission BER curves of the 64-QAM SC-FDM signal with one group and 512 IFFT size. The I/Q imbalance compensation in frequency domain is used in SC-FDM signal. The results verify the I/Q imbalance compensation in frequency domain greatly improves system performance. The I/Q imbalance leads an oblique constellation depicted in Fig. 5-24 (a). After I/Q imbalance compensation, the constellation diagram has no obvious distortion as shown in Fig. 5-24 (b).

The number of modulation symbols in one SC-FDM block equals to the number of points of IFFT. If the system has longer IFFT size, the system will have better frequency resolution. The benefit of SC-FDM signal is the PAPR not change too much with different IFFT size, as shown in Fig. 5-25. The PAPR ($Pr(PAPR>PAPR_0) = 0.1$) of the 64-QAM SC-FDM signal with one group and 512 IFFT size is the same as 128 IFFT size. Therefore, the long IFFT size could provide better signal quality. Figure 5-26 shows the experimental result with different IFFT size of 64QAM SC-FDM signals with one group. Each block inserts 20 symbols referred to as CP in order to prevent inter-block interference (IBI). The result shows that the longer IFFT size has better performance. However, the long IFFT size has higher complexity of computation. This phenomenon is the same as the OFDM signal. Therefore, the IFFT size is set to 512 in future experiment.

Figure 5-27 shows the electrical spectrums of down-converted SC-FDM signal with different fiber transmission distance. The signal bandwidth is 7 GHz and the center frequency of down-converted signal is 4.5 GHz. The signal has no significant fading issue of up to 2km fiber transmission. The fading

issue can be observed when the fiber distance is longer than 3 km. For the 5km fiber transmission distance, the electrical power is very weak at 2.5GHz.

Figure 5-28 illustrates the BER curves of 16QAM SC-LFDM signals with different number of groups in optical BTB and 4m wireless transmission distance. As shown in Fig. 5-29, the PAPR ($Pr(PAPR>PAPR_o) = 0.1$) for 1, 8, 64, and 512 groups are 6.1, 7.5, 7.8, and 7.8dB, respectively. The signal has high PAPR when the signal has more groups. The results show the lower PAPR signal has higher system performance. Between 1 group and 512 groups, the wireless power penalty at 10^{-3} is 2dB. Results also show that higher PAPR signal is easily saturation compared with low PAPR signal. When the signal has one group, the saturation power is -38dBm. When the signal has 512 groups, the saturation power is -35dBm. Because the PAPR of the signal with 512 groups is 2.7dB higher than one group, the saturation power has 3dB difference. Figure 5-30 shows the data throughput of proposed system versus number of groups without fiber transmission. To reduce the impact of uneven channel response, the adaptive loading algorithm was used to adjust the power and the format of each group. The system with more groups has more ability to adapt fading channel, but it also suffers from higher PAPR. The target BER for adaptive bit-loading algorithm is lower than 10^{-3}. The results show that more groups also get worse system performance. There reason is the same as pervious result. When the system has no fiber transmission, the adaptive bit-loading could not provide enough benefits to resist the PAPR induced performance degradation.

Figure 5-31 illustrates the BER curves of 16QAM SC-LFDM signals with different number of groups in 5km fiber and 4m wireless transmission distance.

The electrical spectrum (see Fig. 5-27) of 5km fiber transmission distance shows the signal has serious fading issue at 2.5 GHz. The BER curves for different groups are much worse than FEC limit. This signal quality cannot be used in communication systems. Therefore, the adaptive bit-loading algorithm can reduce the impact of dispersion induced performance fading issue. The data throughput of adaptive bit-loading algorithm employ in SC-LFDM signal with 5km fiber transmission show in Fig. 5-32. The signal with one group has 7Gbps data throughput. The signal with 8 or 64 groups has 21Gbps data throughput. When the signal has 512 groups, the data throughput is decrease to 19.8Gbps. The optimal number of groups has different result with optical BTB. This results show that more groups will be more robust to fading but higher suffer from PAPR. The optimal condition depends on the situation of system. If the system has serious uneven frequency response but provide good linearity, more group can be utilized in the system. Otherwise, the system needs fewer groups.

Different mapping methods also induce different system performance. As shown in Fig. 5-33 (a), the receiver sensitivity at 10^{-3} of 16-QAM SC-IFDM signal is 1 dB better than 16-QAM SC-LFDM when both signals have 8 groups. The signals with 64 groups have the same result as shown in Fig. 5-33 (b). Figure 5-34 shows that the PAPR ($Pr(PAPR>PAPR_o) = 0.1$) of the SC-LFDM signal with 8 groups is 0.1dB higher than the SC-IFDM signal with 8 groups. The experimental results show that the PAPR will degrade system performance. After the system use adaptive bit-loading algorithm, the SC-LDFM signal has higher data throughput as shown in Fig. 5-35. The result shows the bit-loading algorithm can provide more benefit to the SC-LFDM signal.

Figure 5-36 shows the data throughput for the SC-FDM and OFDM signal. The SC-FDM signals have better system performance than the OFDM signals. Due to the main impact of the system performance with shorter fiber transmission distance is the PAPR, the SC-FDM system should have better performance with shorter fiber transmission distance. However, the optimal groups for the SC-FDM signal less than 3km fiber transmission is one. Therefore, the system is hard to balance the performance between data format and BER. The BER for OFDM and SC-FDM signal are 9.5×10^{-4} and 3.3×10^{-4} without fiber transmission, respectively. The result shows the SC-FDM signal still has opportunity to enhance data throughput.

In optical BTB, the 64QAM SC-FDM with one group which is the same as SC-FDE has the best performance. The next high order modulation format for the 64QAM (42Gbps) is 128 QAM (49Gbps). Figure 5-37 shows BER curve for the 128QAM SC-FDM signal with 1 group. Minimum BER is 3.8×10^{-3} which is higher than FEC limit. If the system use other coding that has higher coding gain, the signal could use in wireless communication system.

Given the small dispersion penalty observed for fiber spans up to 2 km, the proposed RoF system is well suited to system applications characterized by short fiber spans, but where minimal system complexity is critical. A good example is in-building applications, where in most instances fiber spans of less than 500 m are sufficient. However, if required, the fading-limited maximum fiber transmission distance may be extended by, for example, using a filter such as a wavelength interleaver to remove any one of the four sidebands (LO or vector signal) from the modulated optical signal at the HEU prior to transmission. Filtering out one of the sidebands results in the generation of only

one copy of the desired mm-wave signal at the RAU, and eliminat the possibility of fading. However, the filter makes the RoF system more complex, which as stated earlier should be avoided in short-range RoF applications.

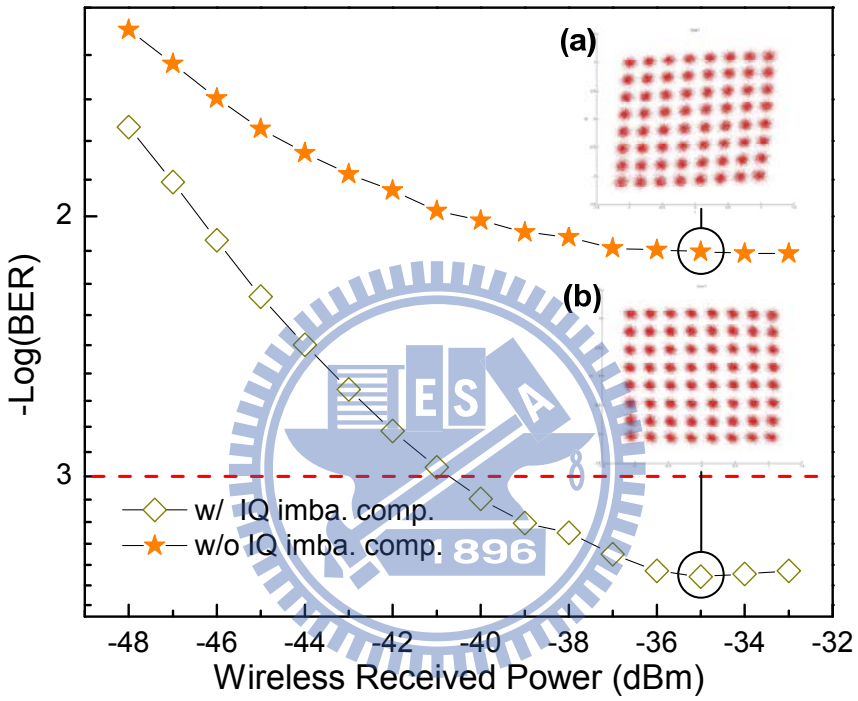

Figure 5-24 BER curves of the 64-QAM SC-FDM signal with one group and 512 IFFT size, (a) without I/Q imbalance compensation, (b) with I/Q imbalance compensation.

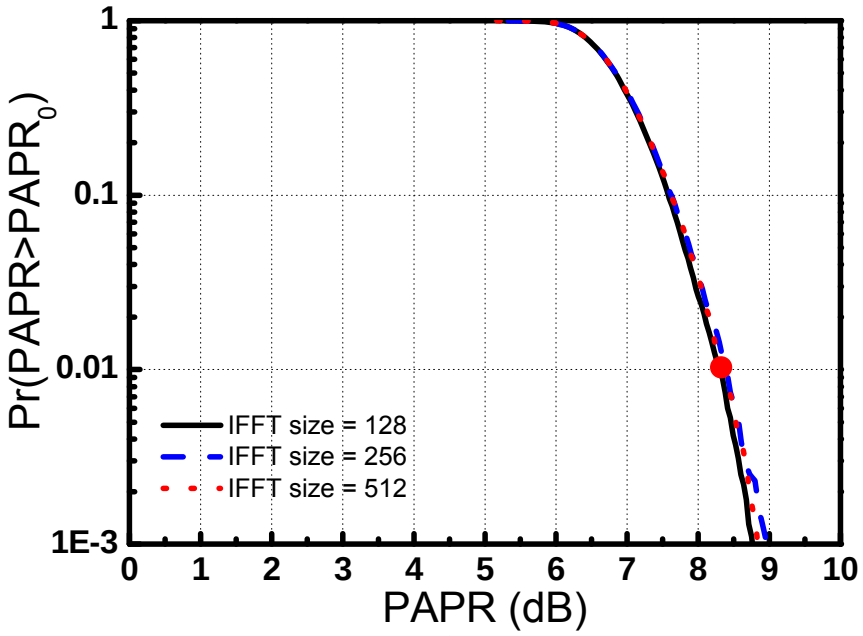

Figure 5-25 Simulations results of PAPR versus different IFFT size.

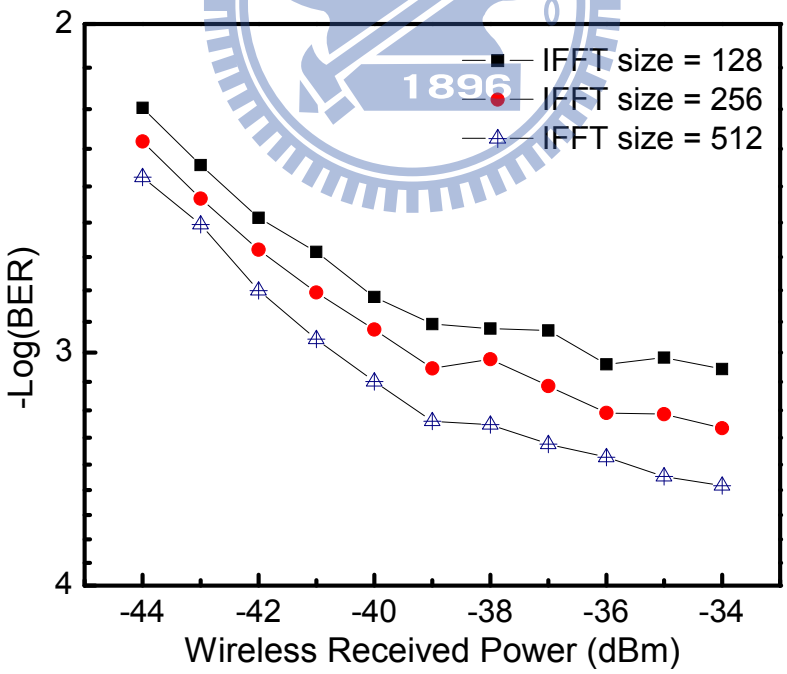

Figure 5-26 BER curves of the 64-QAM SC-FDM signal with different IFFT size.

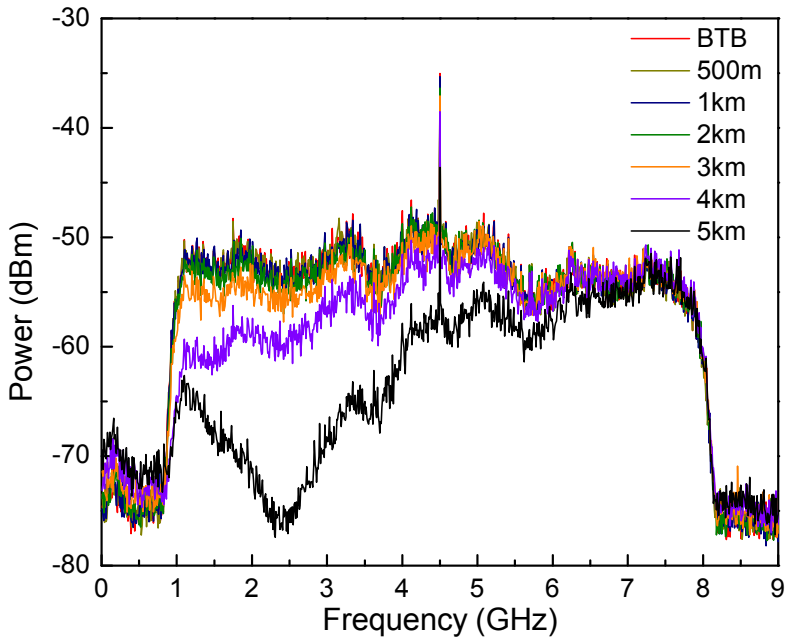

Figure 5-27 The down-convert electrical spectrums of the SC-FDM signal for different standard single-mode fiber transmission length.

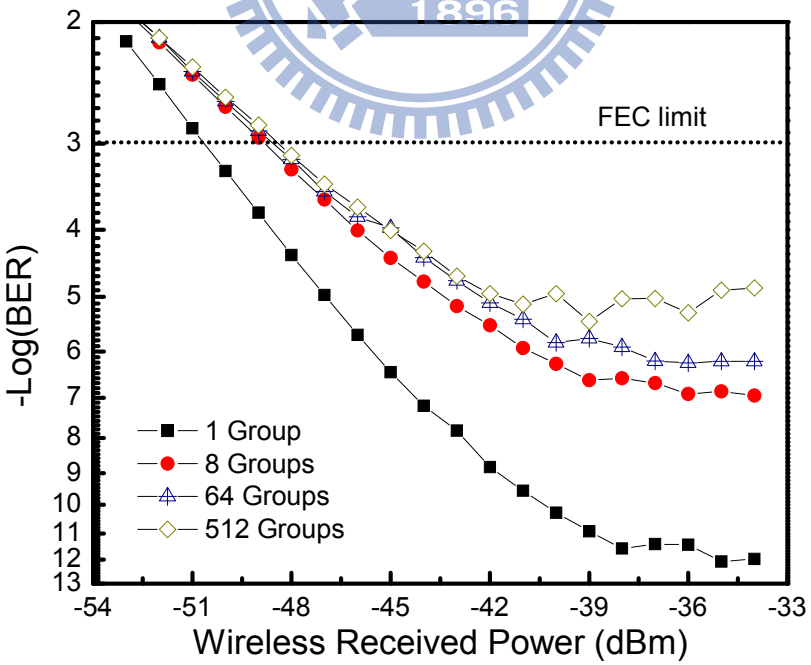

Figure 5-28 BER curves with different number of groups for BTB case.

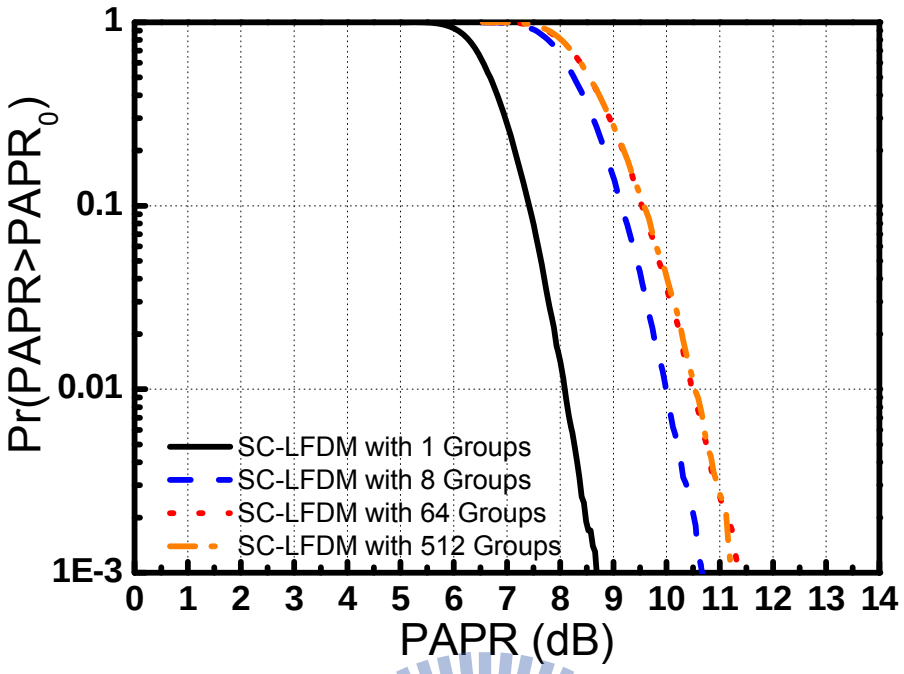

Figure 5-29 Simulations results of PAPR versus different number of groups.

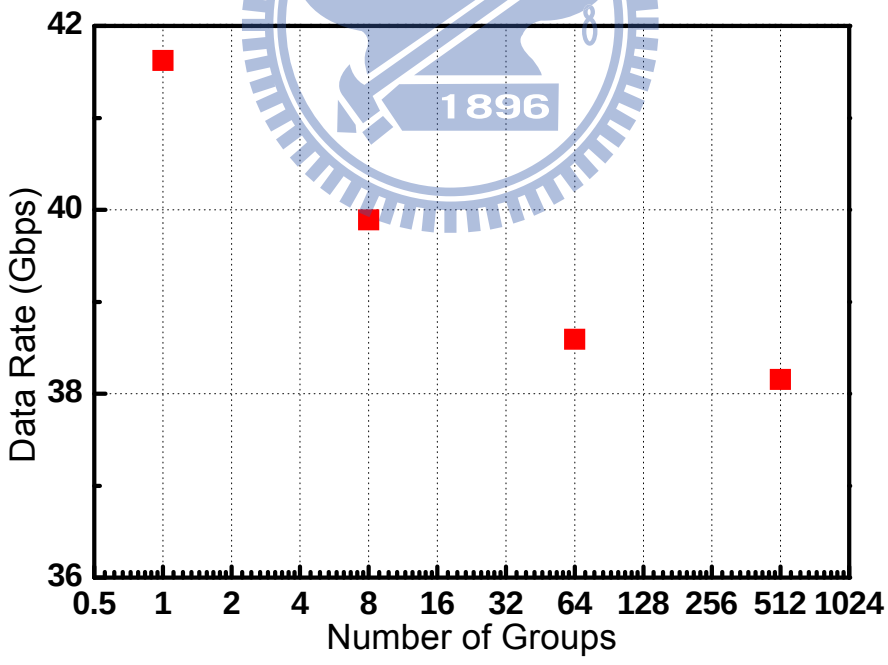

Figure 5-30 Data rate as function of number of groups for BTB case.

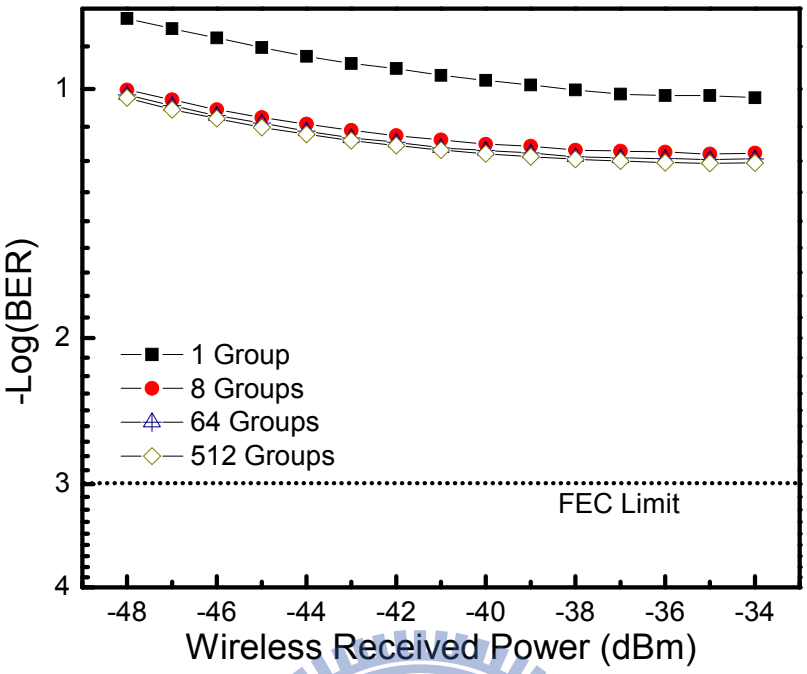

Figure 5-31 BER curves with different number of groups after 5km fiber transmission.

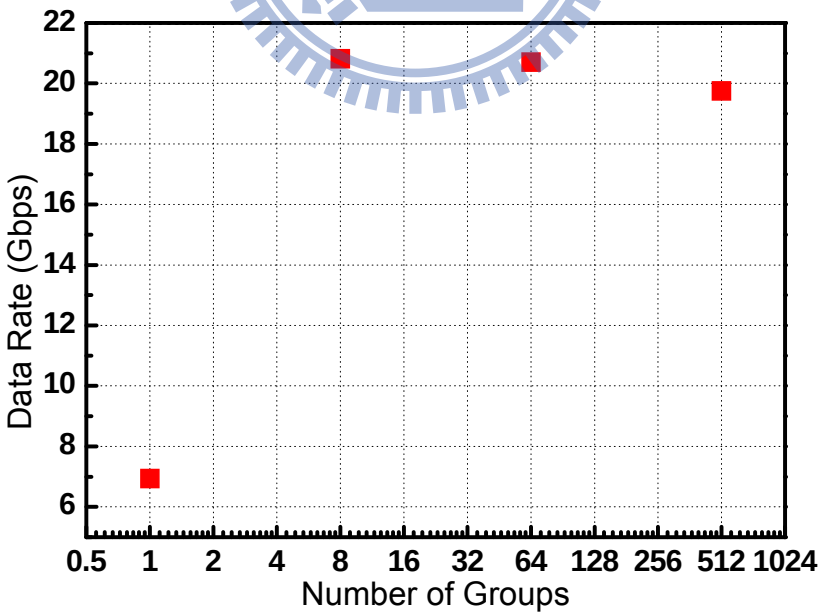

Figure 5-32 Data rate as function of number of groups after 5km fiber transmission.

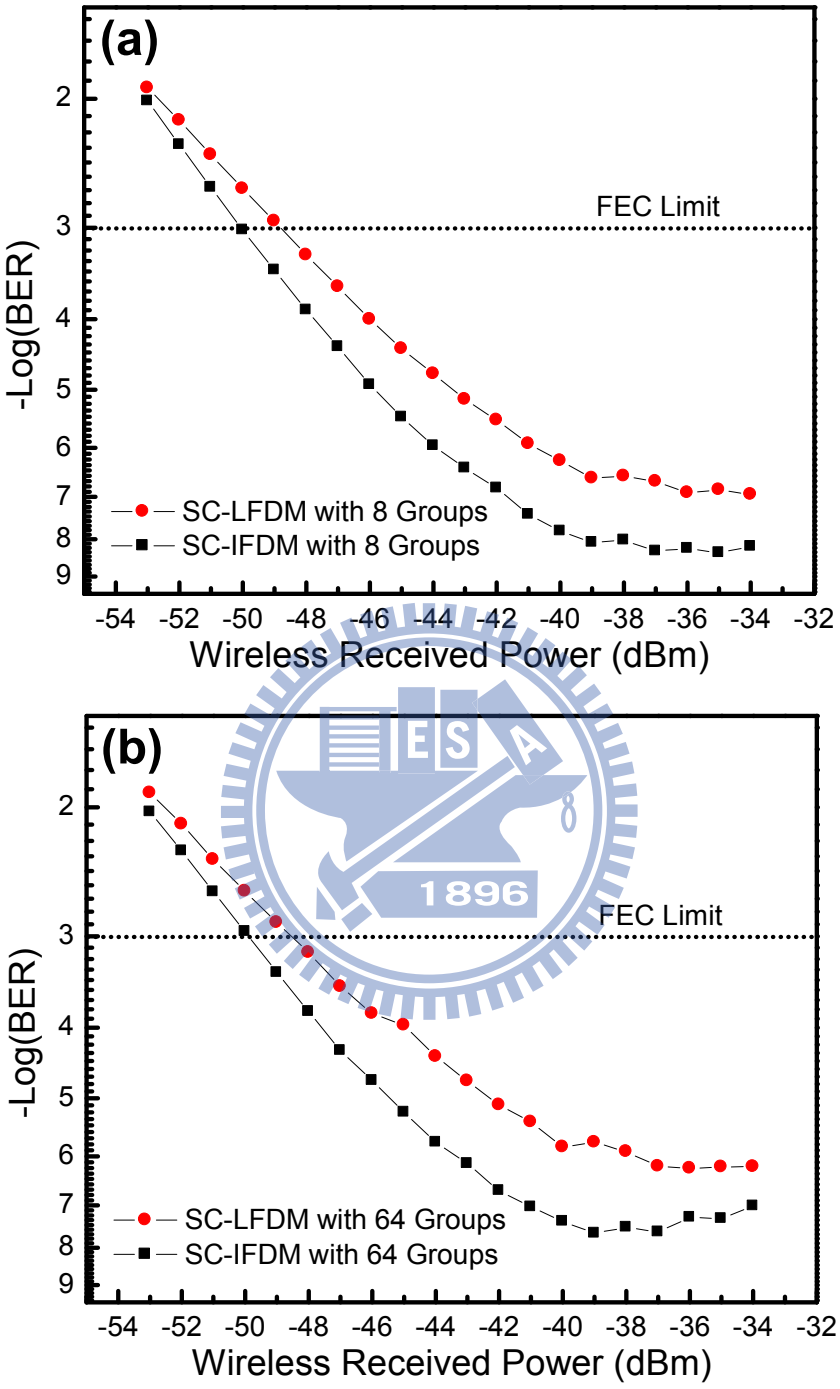

Figure 5-33 BER curves of SC-LFDM and SC-IFDM signal, (a) with 8 groups, (b) with 64 groups.

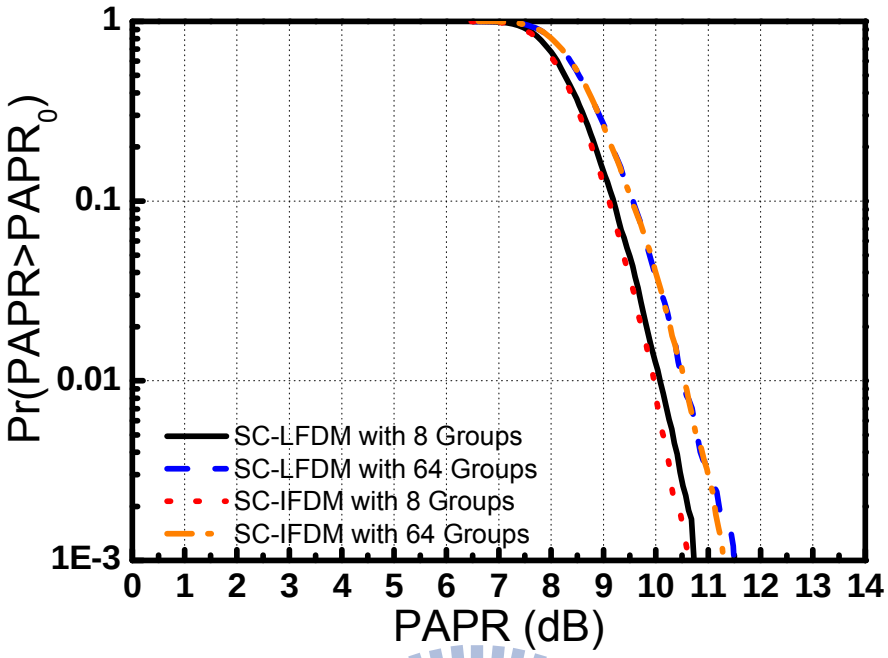

Figure 5-34 Simulations results of PAPR for SC-LFDM and SC-IFDM signal.

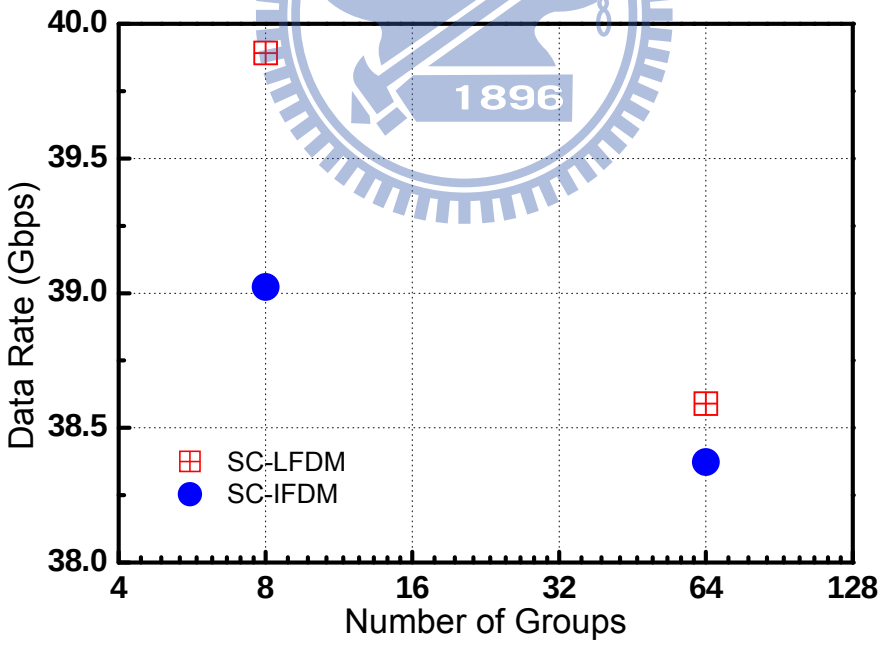

Figure 5-35 Experimental results of data rate for SC-LFDM and SC-IFDM signal.

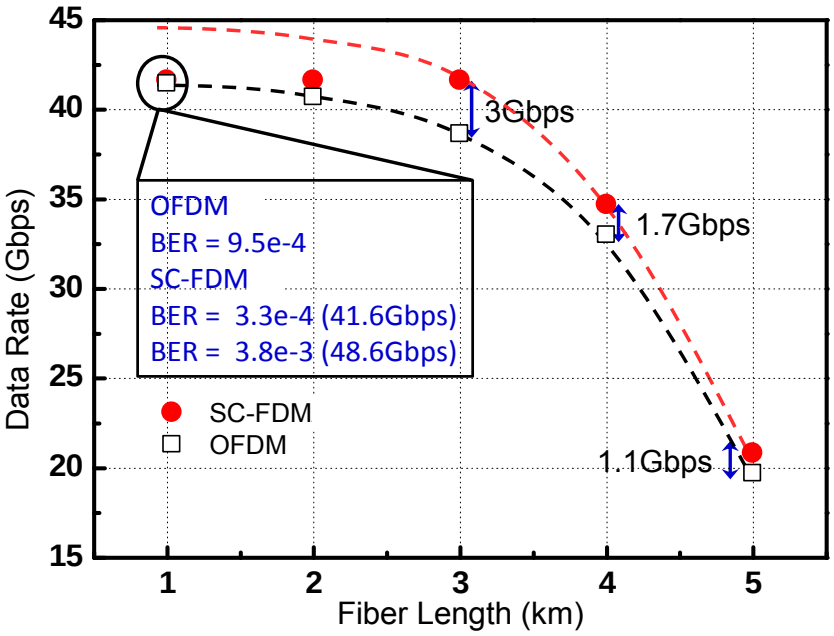

Figure 5-36 Experimental results of data rate for SC-FDM and OFDM signal.

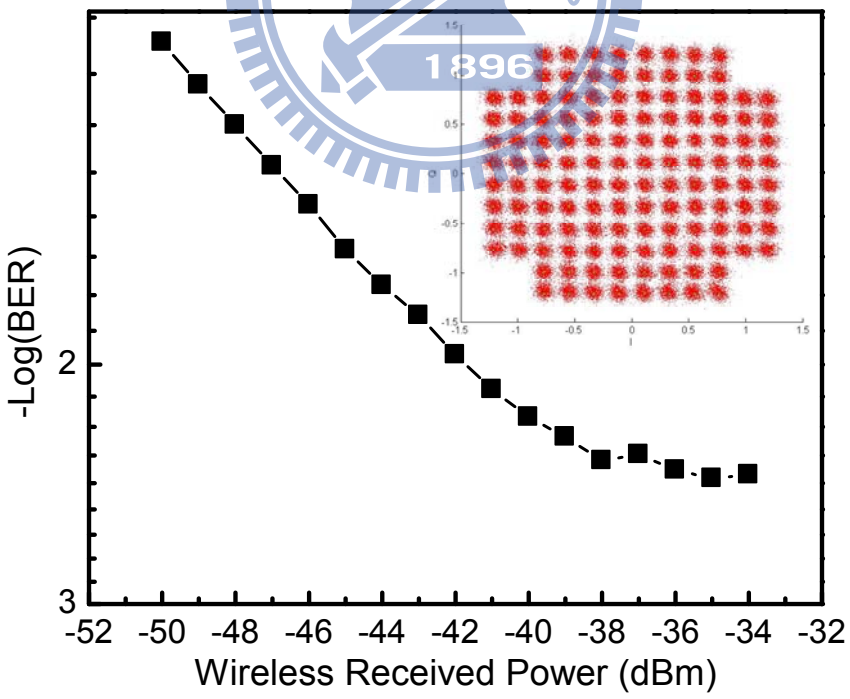

Figure 5-37 BER curves of the 128-QAM SC-FDM signal with one group and 512 IFFT size.

5.4.5 Experimental Setup for MIMO System

Figure 5-38 schematically depicts the experimental setup of the proposed 60-GHz RoF system using the 2×2 MIMO scheme. Based on previous experimental results, the 41.6-Gbps SC-FDM signal with one group (SC-FDE) provides the best system performance in optical BTB. Therefore, the SC-FDE signal is used to realize the 2x2 MIMO generation and transmission. Due to the limited equipment, two baseband SC-FDE signals for MIMO system were generated using an arbitrary waveform generator and sent into the optical modulator in serial. In order to realize RoF system, the signals transmit in optical fiber after optical transmitter. At receiver side, the optical signal was evenly split using 50:50 coupler. To imitate the MIMO system, one of the optical signals was delayed using 2 km fiber to generate parallel SC-FDE signals for MIMO system, as shown in Fig. 5-39. The fiber distance here is related to the signal time period. Since the system use 2 km fiber to delay signal, the data length of 1×10^{-5} second could be used in this demonstration. Both optical data stream were sent into individual photo detector for the generation of the 83-Gbps MIMO-SC-FDE signal at 60GHz.

After photo detectors, the electrical signals were amplified by low noise amplifiers and fed into standard horn antennas with 23-dBi gain for wireless transmission. Since the gain of two wireless transmitters cannot be exactly the same, the optical powers into photo detector were -2dBm and -2.5dBm to ensure that the wireless transmission powers are the same. The two transmit signals were separately transmitted over wireless channels and received by horn antennas. Since the 2x2 MIMO system is used, both receiver antennas would receive mixed signals from both transmitter antennas. Both the received

60.5 GHz signals were down-converted to 4.5GHz using electrical mixers and 56GHz sinusoidal signals. A digital sampling scope was used to capture the signals for offline digital signal processing.

The measurements were performed in a typical laboratory with dimensions of 7.5 m x 6.88 m (W x L). The plan of the laboratory and identifying ray-tracing paths for the 2x2 MIMO system is shown in Fig. 5-40. The transmitters and receivers were placed on tripods at the height 1.3 m above the floor. The separation distance of two receiver antennas was 5 cm which is much more than λ/2 to prevent the effects of coupling-induced correlation [88]. Both transmitter antennas always face to the center of two receiver antennas. The wireless transmission distance is fixed at 4m.

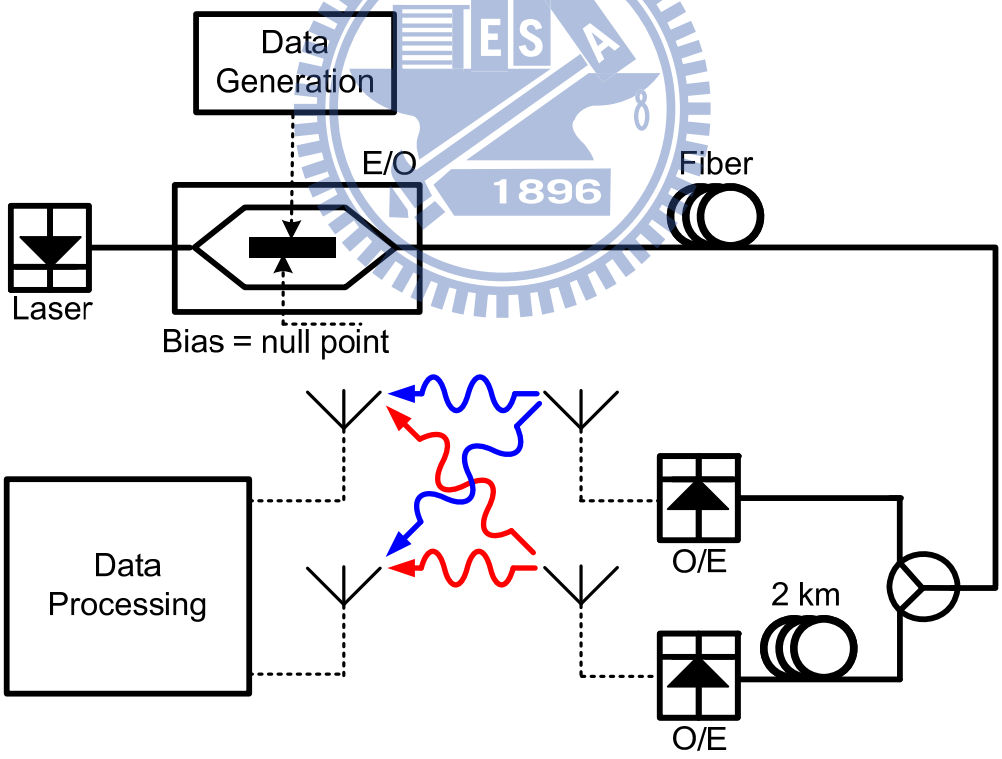

Figure 5-38 Experimental setup of 2x2 MIMO system.

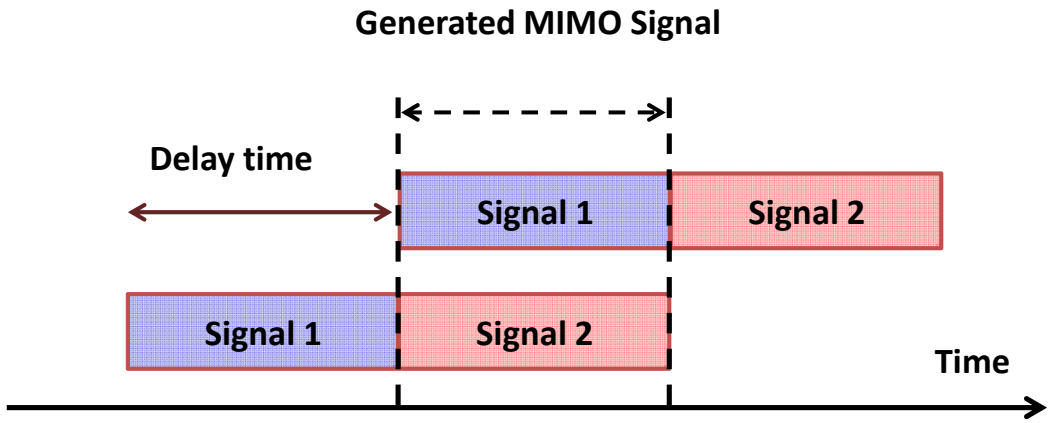

Figure 5-39 The principle diagram of the signal design of 2x2 MIMO system.

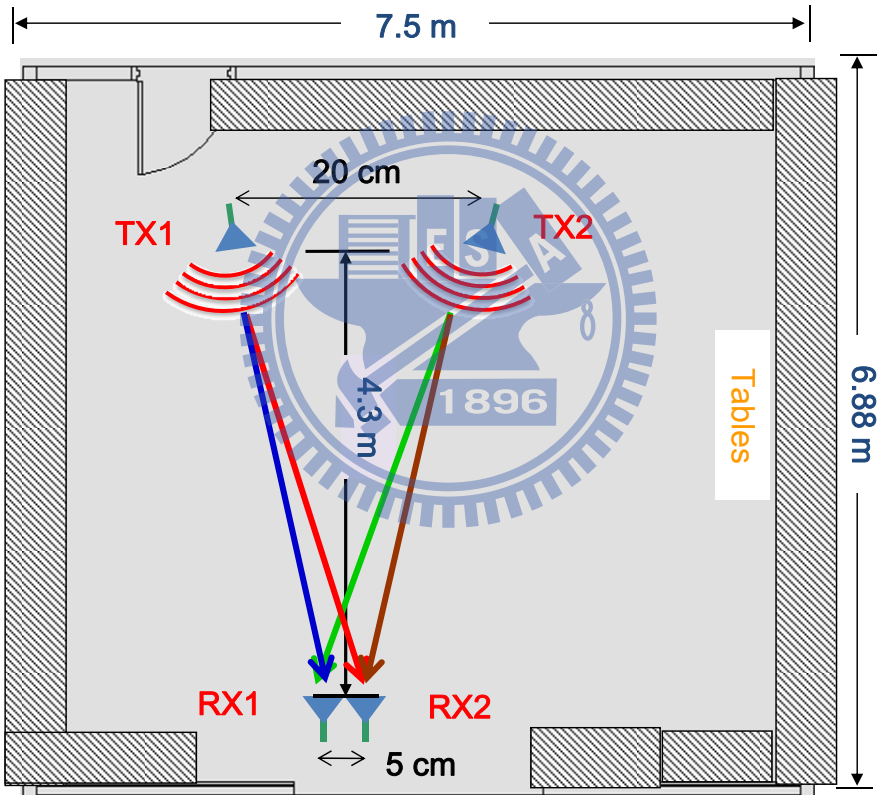

Figure 5-40 Spatial arrangements for 2x2 MIMO RoF systems.

5.4.6 Results and Discussions for MIMO System

To demonstrate the spatial multiplexing, a separation was introduced between the two transmitter antennas. The separation of the transmitter antennas is parallel to the separation of receiver antennas, and the centers of the

separations were aligned to each other. A lowest condition number (1.4) were achieved with 20-cm of transmitter antenna separation.

Figure 5-41 displays the relation of bit error rate (BER) versus wireless received power with 4m wireless transmission distance using 83-Gbps 2x2 MIMO-SC-FDE signals. From the results, 1 dB power penalty was observed between optical BTB and with 500m fiber transmission. In addition, -39 dBm wireless received power was enough to achieve FEC limit for both optical transmission distances. Since the BER of SC-FDE signal is much lower than FEC limit, 83-Gb/s data rate was achieved in the 2x2 MIMO-SC-FDE system with 7-GHz bandwidth, 64-QAM modulation format, 500m fiber, and 4m wireless transmission distances.

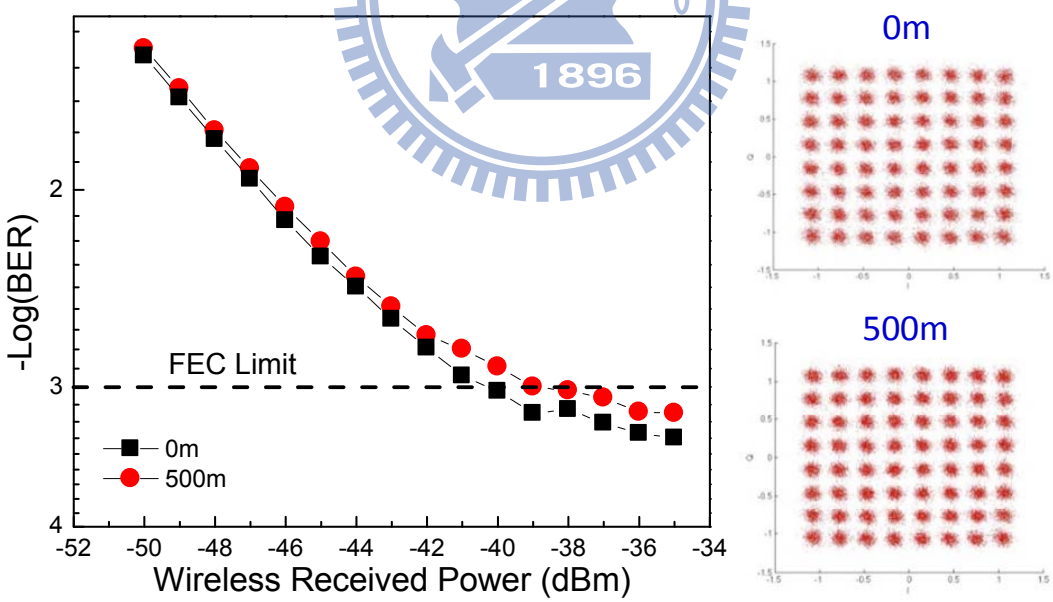

Figure 5-41 BER performance as function of wireless received power with different fiber transmission distance.

5.5 Summary

In this Chapter, we have theoretically and experimentally investigated the performance of a simple RoF system for transporting and generating multi-Gbps wireless signals at 60 GHz. The RoF system employs a single-electrode MZM and uses no linearization techniques. Theoretical analysis of the proposed system shows that by choosing appropriate input signal frequencies, the system can achieve fiber transmission distances exceeding 3 km without any chromatic dispersion compensation. The theoretical analysis was confirmed by experimental results.

This experiment employs a novel RoF system in combination with OFDM or SC-FDM modulation format. Adaptive bit-loading and I/Q imbalance compensation algorithm successfully circumvent multiple system impairments, and improve the system performance significantly. The RoF system was successfully demonstrated to transport a record of 40-Gb/s OFDM and SC-FDM signals at 60 GHz over more than 1 km of standard single-mode fiber and 4-m wireless distance. Fiber links of 1 km are sufficient for most short-range RoF applications such as in-building systems, where low system complexity is very critical. Performance of a 2x2 spatially multiplexed MIMO wireless link at 60 GHz is also evaluated. A record wireless speed of 83 Gb/s with a wireless distance of 3 m was achieved in 7 GHz bandwidth with very high spectral efficiency of ~ 12 b/s/Hz. These results demonstrate the feasibility of using MIMO at 60 GHz for increasing the capacity.

Chapter 6

HYBRID ACCESS NETWORK

6.1 Preface

Since the capacity requirement for wireless communications continues to increase, high spectral efficiency modulation and a high carrier frequency are required for the next generation of ultra-high capacity wireless systems [82]. Many standards have been proposed concerning the delivery multi-gigabit-per-second services for 60GHz wireless system in the 7GHz license-free band. They include IEEE 802.15.3c, ECMA TC48, wireless HD/HDMI, WiGig and IEEE 802.11 VHT. High path loss and high attenuation through walls allow [36] 60GHz wireless signals to be used only over a relatively short distances (< 10m). The Radio-over-Fiber (RoF) approach technique is an effective means of extending the coverage of 60GHz wireless signals.

Because of the required high bandwidth, high flexibility, high mobility, and low cost in the next generation access networks, an optical distributed infrastructure that hosts both fiber to the x (FTTx) and RoF systems is greatly desired. Recently, the simultaneous generation and transmission of FTTx and RoF systems that use a single wavelength have attracted significant interest because of sharing the same distributed infrastructure [24, 89, 90]. However, the bandwidth of a typical commercially available $LiNbO_3$ modulator is limited to 40GHz, and electrical components and equipment with an operation frequency range of up to 60 GHz are very expensive. Additionally, since the available wireless spectrum is limited, high spectral efficiency modulation

formats are very desirable for wireless systems. Therefore, the development of a cost-effective optical 60GHz vector signal generation approach that integrates FTTx service is of great interest [93, 94].

In this chapter, two novel multi-service hybrid access network systems for 60GHz wireless and wireline applications using a frequency multiplication technique will be presented. One of architecture use single-electrode MZM with frequency doubling technology. The other architecture use dual parallel MZM with frequency quadrupling technology. These two schemes employ a novel pre-coded method that is based on the digital signal processing. The proposed systems does not suffer from RF fading and needs no narrow-band optical filter at the remote node to separate the RF and baseband signals. A frequency multiplication method for RoF link is realized to reduce the bandwidth requirement of the transmitter.

6.2 Hybrid Access Network System with Frequency Doubling

6.2.1 Concept and Theoretical Analysis of Proposed System

Figure 6-1 shows the concept of the proposed optical vector signal generation system based on a DSB-CS scheme. The optical field at the input of the single electrode MZM is given by $E_{in}(t) = E_o \cos(\omega_o t)$, where E_o and ω_o are the amplitude and angular frequency of the optical field, respectively. The electrical driving signal sent into the MZM is $V(t) = V_{RF}(t) \cdot \cos\left[\omega_{RF} t + \theta(t)\right] + V_{BB}(t)$, where $V_{RF}(t)$ and $\theta(t)$ are amplitude and phase information of the RF driving signal, respectively, ω_{RF} is the angular frequency of the RF carrier signal, and $V_{BB}(t)$ is the amplitude of the

BB driving signal. When the MZM is biased at null point, the generated optical signals can be expressed as

$$E_{out}(t) = -E_o J_0[m_{RF}(t)]\sin[m_{BB}(t)]\cdot\cos[\omega_o t] + E_o J_1[m_{RF}(t)]\cos[m_{BB}(t)]\cdot\cos[(\omega_o \pm \omega_{RF})t \pm \theta(t)] \quad (6\text{-}1)$$

where $m_{RF}(t) \triangleq \pi V_{RF}(t)/2V_\pi$ and $m_{BB}(t) \triangleq \pi V_{BB}(t)/2V_\pi$ are modulation index (MI) of RF and BB signals, respectively. The J_n is the Bessel function of the first kind with order n. Notably, optical sidebands with the order of higher than J_1 can be ignored due to weak modulation condition. After square-law detection using a photodiode (PD), the desired BB and RF signals are obtained and can be written as

$$i_{BB}(t) = 1/2\, RE_0^2 J_0^2[m_{RF}(t)]\sin^2[m_{BB}(t)] + RE_0^2 J_1^2[m_{RF}(t)]\cos^2[m_{BB}(t)] \quad (6\text{-}2)$$

$$i_{RF}(t) = 1/2\, RE_0^2 J_1^2[m_{RF}(t)]\cos^2[m_{BB}(t)]\cdot\cos[2\omega_{RF}t + 2\theta] \quad (6\text{-}3)$$

where R is the PD responsivity. The frequency of the generated RF vector signal ($2\omega_{RF}$) is two times that of the driving signal (ω_{RF}). Note that the amplitude and phase information of the generated RF vector signal are $J_1^2[m_{RF}(t)]$ and $2\theta(t)$, respectively. Therefore, the amplitude ($V_{RF}(t)$) and phase information ($\theta(t)$) of the driving signal needs to be pre-coded to achieve the desired RF vector signals after square-law photo detection. By properly pre-coded of driving signals, the proposed scheme can support various kinds of modulation formats, including amplitude-shift keying (ASK), phase-shift keying (PSK), and quadrature-amplitude- modulation (QAM) signals. No optical filter is needed to separate BB and RF signals if M-ary PSK signals are utilized for RF signals [91], which is compatible with the current optical

passive optical network (PON). Therefore, the BB and RF signals can be rewritten as

$$i_{BB}(t) = RE_o^{\,2}[J_0^{\,2}(m_{RF})/2 - J_1^{\,2}(m_{RF})]\sin^2[m_{BB}(t)] + RE_o^{\,2}J_1^{\,2}(m_{RF}) \tag{6-4}$$

$$i_{RF}(t) = 1/2\, RE_o^2 J_1^{\,2}(m_{RF}) \cdot \{1 - \sin^2[m_{BB}(t)]\} \cdot \cos[2\omega_{RF}t + 2\theta(t)] \tag{6-5}$$

where m_{RF}, i.e. $m_{RF}(t)=m_{RF}$, is constant if M-ary PSK signals are utilized. Hence, for BB signals, the $RE_o^{\,2}J_1^{\,2}(m_{RF})$ term can be easily removed by using an electrical DC block. From (4), the BB signal power and the interference power induced by RF signals are proportional to $1/4J_0^{\,4}(m_{RF})\sin^4[m_{BB}(t)]$ and $J_1^{\,4}(m_{RF})\sin^4[m_{BB}(t)]$, respectively. Therefore, the BB signal-to-interference ratio (SIRBB) can be defined as

$$\mathrm{SIR_{BB}} = J_0^{\,4}(m_{RF})/4J_1^{\,4}(m_{RF}) \tag{6-6}$$

For the RF signal, the desired RF signal power and the interference power induced by the BB signal are proportional to $1/4 \cdot J_1^{\,4}(m_{RF})$ and $1/4J_1^{\,4}(m_{RF})\sin^4[m_{BB}(t)]$, respectively. We can define the RF signal-to-interference ratio (SIRRF) as

$$\mathrm{SIR_{RF}} = sin^{-4}[m_{BB}(t)] \tag{6-7}$$

Figure 6-2 shows $\mathrm{SIR_{BB}}$ versus m_{RF} and $\mathrm{SIR_{RF}}$ versus $m_{BB}(t)$. Since the interference is in-band, it cannot be removed by electrical filters. As m_{RF} and $m_{BB}(t)$ are less than 0.25, both $\mathrm{SIR_{RF}}$ and $\mathrm{SIR_{BB}}$ are more than 20 dB. In the following experiment, both m_{RF} and $m_{BB}(t)$ are confined to 0.07 to keep both $\mathrm{SIR_{BB}}$ and $\mathrm{SIR_{RF}}$ above 40 dB. Therefore, the system impairments are

dominated by the uneven frequency response and high noise of 60-GHz components, instead of interference between BB and RF signals at large m_{RF} and $m_{BB}(t)$.

In this work, 60-GHz QPSK signal is experimentally demonstrated. Figure 6-3 shows the principle of pre-coded scheme of the QPSK format. The phases information of the pre-coded QPSK signals ($\theta(t)$) which constellations are situated in the first and second quadrant are half of those of the generated QPSK signals ($2\theta(t)$). After square-law photo detection via the DSB-CS modulation, the standard QPSK signal with frequency doubling is achieved.

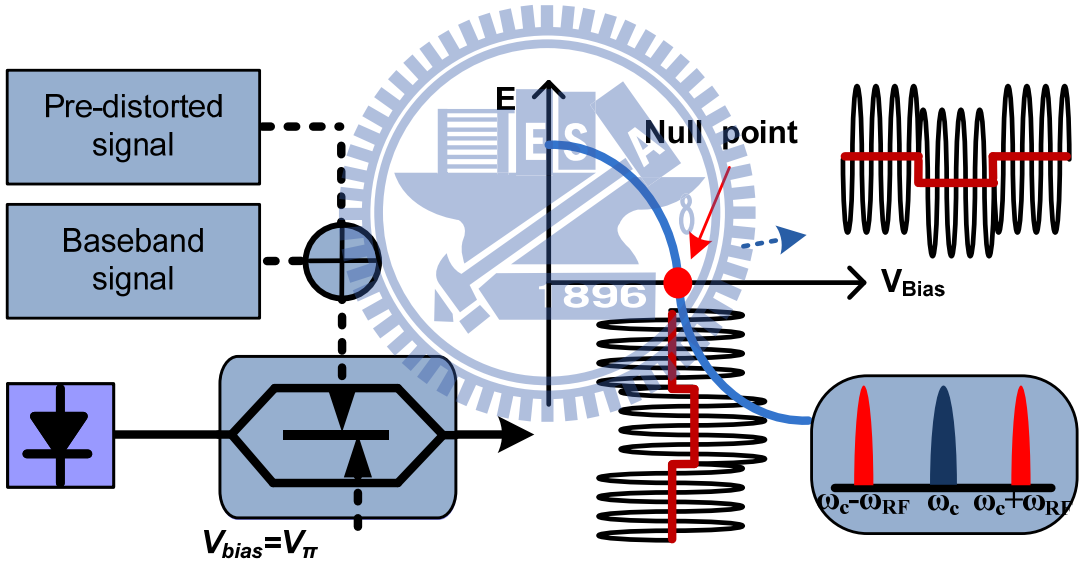

Figure 6-1 The concept of proposed hybrid access network with frequency doubling.

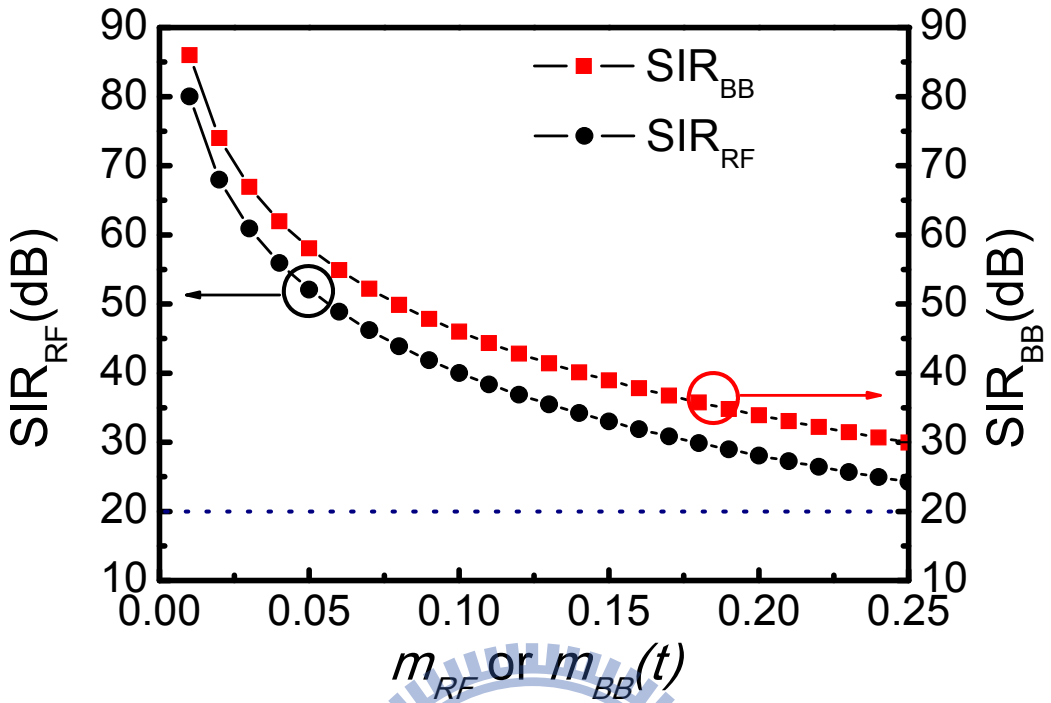

Figure 6-2 SIR_{RF} and SIR_{BB} versus modulation index of BB and RF, respectively.

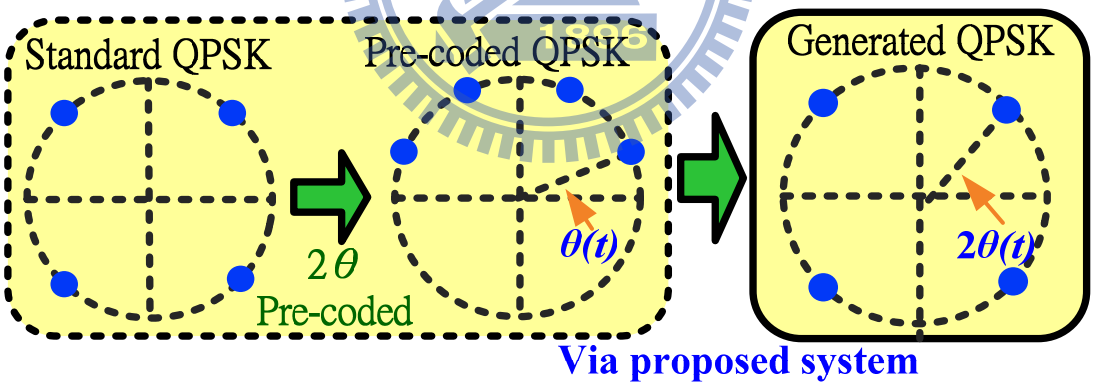

Figure 6-3 The principle of pre-coded scheme of the QPSK format with frequency doubling system. (QPSK: quadruple phase-shift keying)

6.2.2 Experimental Demonstration of Proposed System

Figure 6-4 shows the experimental setup to verify the feasibility of the proposed system. A 2.5-Gbps pre-coded QPSK signal with a 2.5-GHz center

frequency is generated by an arbitrary waveform generator (AWG, Tektronix® AWG7102) with a Matlab® program. After the AWG, the pre-coded QPSK signal is up-converted to 30 GHz using an electrical mixer. The 30-GHz pre-coded QPSK signal is combined with a BB 1.25-Gbps OOK signal and sent into a single-electrode MZM. Before the transmission of 25-km standard single-mode fiber, the generated optical signal is amplified using an erbium-doped fiber amplifier (EDFA) and then passes through an optical band-pass filter to remove the amplifier spontaneous emission (ASE) noise. At the receiver side, an optical coupler is employed to separate the optical power of the hybrid signal for different applications. For wireless applications, a standard QPSK signal with center frequency at 60 GHz is generated after square-law PD detection. To realize QPSK demodulation, the received QPSK signal is down-converted to 5 GHz and captured by digital oscilloscope (Tektronix® DPO 71254). An offline program using a Matlab® program is used to demodulate and analyze the QPSK signal. The demodulated process includes synchronization and the bit error rate (BER) estimation. For wireline applications, the BB OOK signal is directly detected using a commercial 1.25-Gbps photo receiver and sent into a BER tester. A 60-GHz DSB-CS optical spectrum with carrier suppression is observed while the BB OOK signal is turned off as shown in Fig. 6-5 (a). Only 30-GHz transmitter bandwidth is required in this experimental setup. While the BB OOK signal is turned on and combined with the pre-coded QPSK signal, a double-side-band optical spectrum with OOK-modulated carrier is obtained as shown in Fig. 6-5 (b).

Due to the power limitation of available electrical RF amplifier in our laboratory, only m_{RF}=0.07 can be achieved in this experiment. Therefore, both

m_{RF} and $m_{BB}(t)$ of 0.07 are used to verify the concept of the proposed system. According to the theoretical analysis, the mutual interference effects can be ignored. Figure 6-6 shows the BER curves and constellations of QPSK signal. For the RF QPSK signal, the BER performance is calculated from the measured error vector magnitude (EVM). The constellation diagrams of the recovered QPSK signal at BTB and after transmission are shown in the inset (i) and (ii) of Fig. 6-6. After transmission of 25-km standard single-mode fiber, 4-dB receiver power penalty is observed at a BER of 10^{-5}. The RF receiver power penalty comes from timing walk-off between the two optical sidebands with different optical frequencies [92].

Figure 6-7 shows the BER curves and eye diagrams of BB OOK signal. For the BB OOK signal, the receiver sensitivity at a BER of 10^{-9} is -19 dBm for BTB case. After 25-km standard single-mode fiber transmission, the power penalty at a BER of 10^{-9} can be ignored.

Simultaneous generation and transmission of 60-GHz 2.5-Gbps QPSK and BB 1.25-Gbps OOK signals using a single-electrode MZM was experimentally demonstrated in this study. Frequency doubling and multi-level modulation format was achieved using DSB-CS modulation scheme with a novel signal pre-coded method. No narrow-band optical filter was required at remote node to separate the BB OOK signal and RF QPSK signal for different applications, which is compatible with the current PON system. After transmission of 25-km standard single-mode fiber, 4-dB receiver power penalty which came from the timing walk-off between two optical sidebands was observed in the 60-GHz QPSK signal while a negligible receiver power penalty was observed in the BB OOK signal.

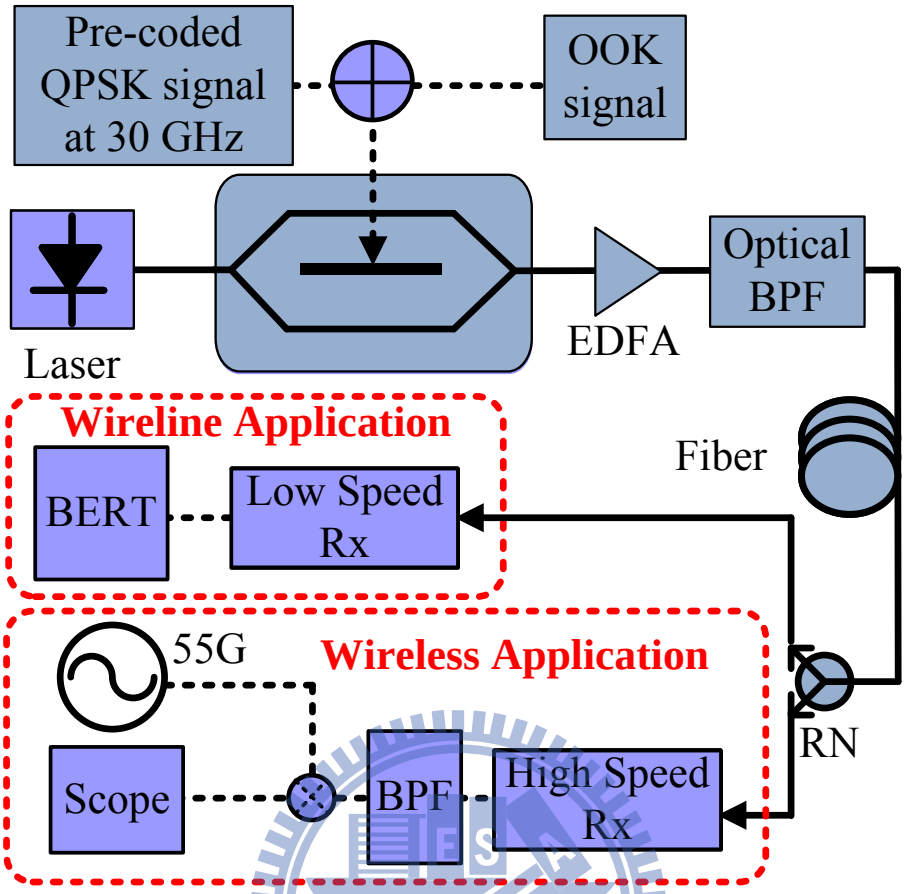

Figure 6-4 Experimental setup of the proposed system. (OOK: on-off-keying; EDFA: erbium doped fiber amplifier; BPF: band pass filter; RN: remote node; BERT: bit error rate tester.)

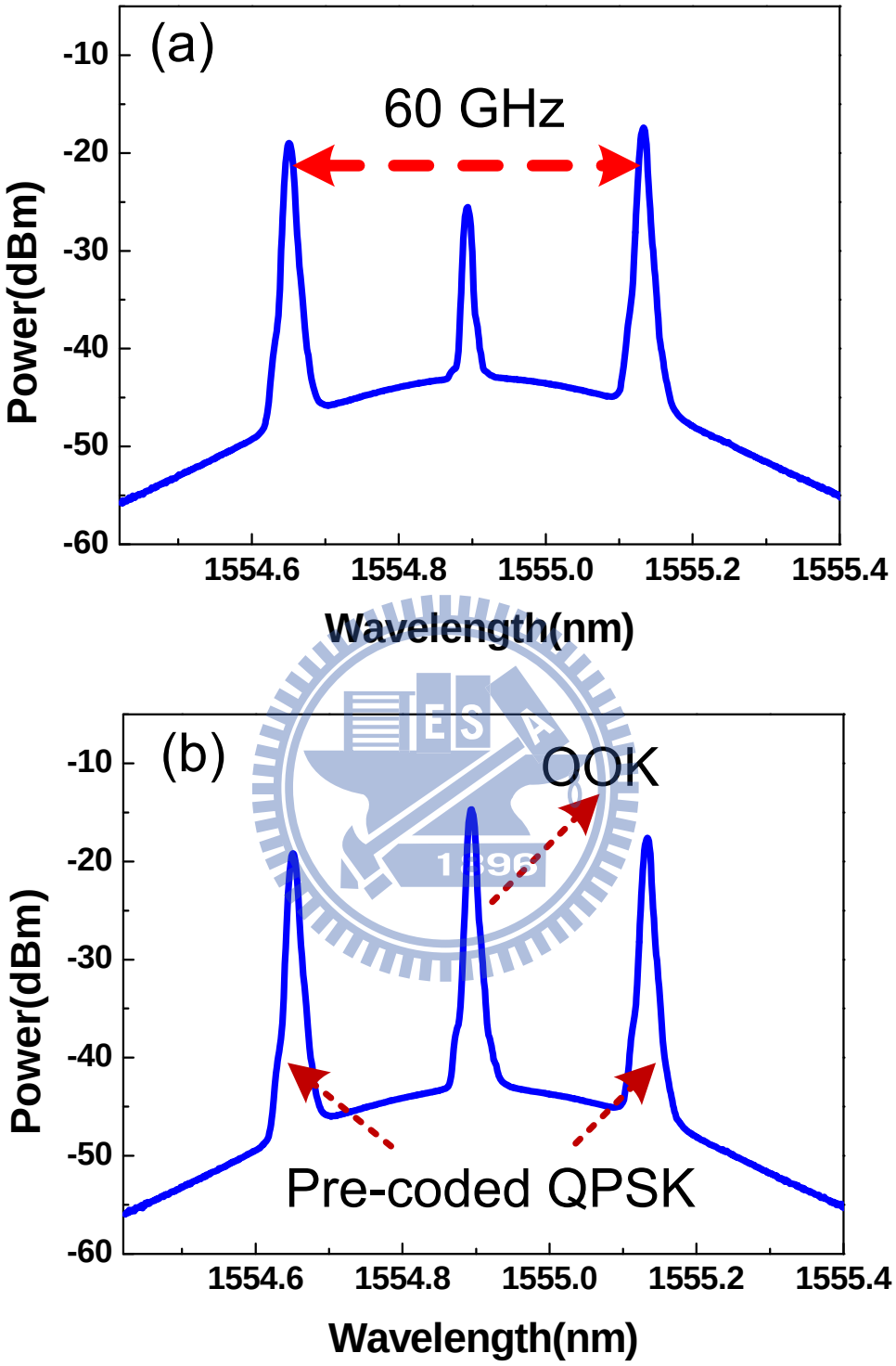

Figure 6-5 Optical spectra (a) without OOK signal (b) with OOK signal.

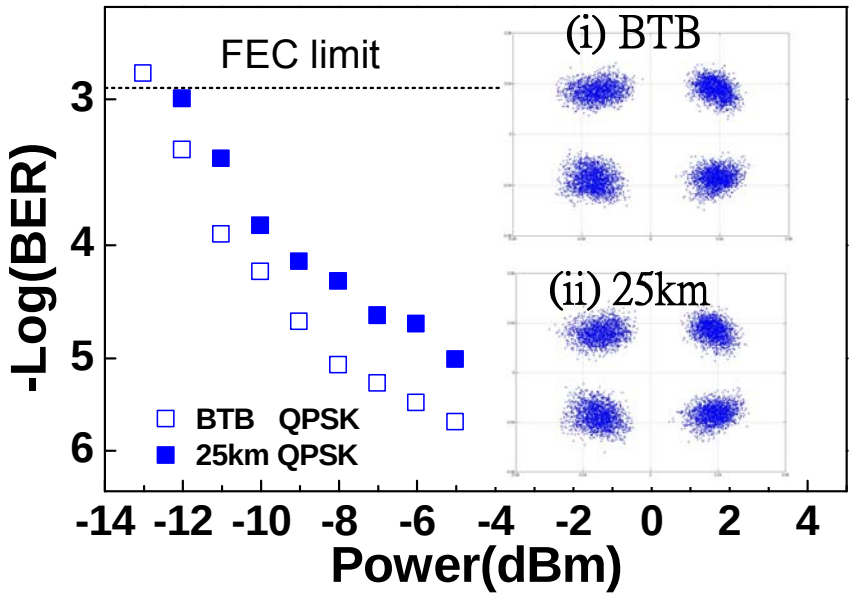

Figure 6-6 BER curves of RF QPSK signal. (FEC: forward error correction)

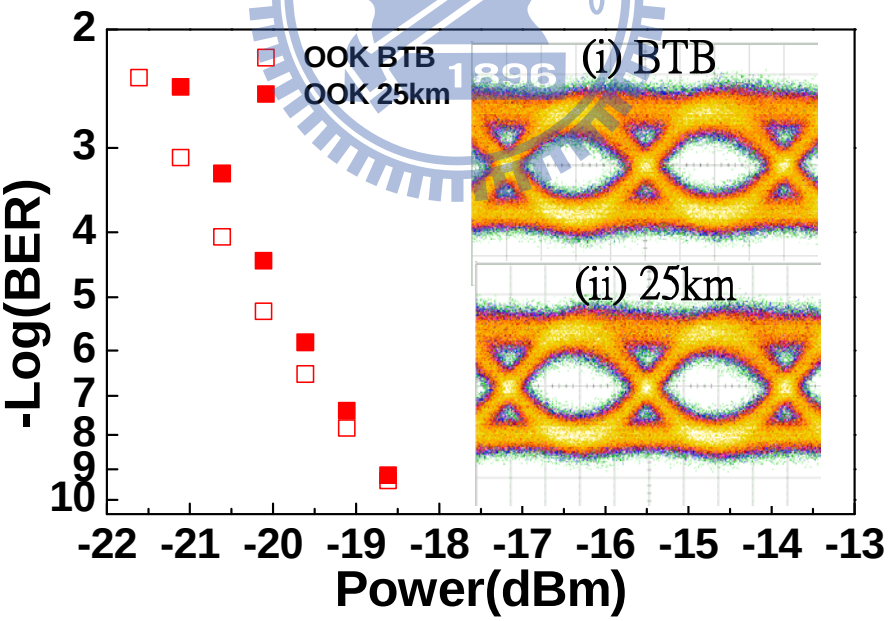

Figure 6-7 BER curves of BB OOK signal.

6.3 Hybrid Access Network with Frequency Quadrupling

6.3.1 Concept of Frequency Quadrupling System

Figure 6-8 shows a conceptual diagram of optical carrier-suppressed millimeter-wave signal generation using a frequency quadrupling technique without any optical filter. An external dual-parallel modulator that consists of three sub-MZMs is key to generating optical millimeter-wave signals. One sub-MZM (MZ-a or MZ-b) is embedded in each arm of the main modulator (MZ-c). The optical field at the input of the dual-parallel modulator is defined as $E_{in}(t) = E_o \cos(\omega_o t)$, where E_o is the amplitude of the optical field and ω_o is the angular frequency of the optical carrier. MZ-a is biased at the maximum transmission point. The electrical driving modulation signal sent into MZ-a is $V_a(t) = V_{ma} \cos(\omega_{RF} t)$, where V_{ma} and ω_{RF} are the amplitude and the angular frequency of the driving signals, respectively. Therefore, the optical field at the output of the MZ-a can be expressed as

$$E_{MZ-a}(t) = \frac{E_0}{\sqrt{2}} \cdot \{J_o(m_a)\cos(\omega_o t) + \sum_{n=1}^{\infty} J_{2n}(m_a)\cos[(\omega_o \pm 2n\omega_{RF})t + n\pi]\} \quad (6\text{-}8)$$

where J_n is the Bessel function of the first kind of order n, and m_a is defined as $\pi V_{ma} / 2V_\pi$. When the MZ-b is biased V_{bias-b}, optical field at the output of the MZ-b is $E_{MZ-b}(t) = E_o / \sqrt{2} \cdot \cos(m_b) \cdot \cos(\omega_o t)$, where the m_b is $\pi V_{bias-b} / 2V_\pi$. If $\cos(m_b) = J_0(m_a)$ and another π phase difference between MZ-a and MZ-b after MZ-c, optical field at the output of the dual-parallel modulator, after destructive interference, can be expressed as

$$E_{out}(t) = E_o / 2 \cdot \{\sum_{n=1}^{\infty} J_{2n}(m_a) \cdot \cos[(\omega_o \pm 2n\omega_{RF})t + n\pi]\} \quad (6\text{-}9)$$

The optical carrier can be easily suppressed by adjusted the biased of MZ-b. As modulation index of MZ-a ($MI_a=V_{ma}/2V_\pi=m_a/\pi$) approaches 0.5, the signal (J_2) to higher orders subcarriers (J_4, J_6, J_8, etc.) power ratio can achieve 58 dB. Therefore, it is reasonable to ignore optical sidebands with order higher than J_4 without causing significant errors, and the optical field can be further simplified to

$$E_{out}(t) = -E_o/2 \cdot \{J_2(m_a)\cos[(\omega_o \pm 2\omega_{RF})t] - J_4(m_a)\cos[(\omega_o \pm 4\omega_{RF})t]\} \quad (6\text{-}10)$$

After square-law detection using a photodiode (PD), the photocurrent can be obtained from $i(t) = R \cdot |E(t)|^2$, where R is the photo detector's responsively. The cross terms of Eq. (3) will generate the desired millimeter-wave signal and its harmonic distortion signals. These millimeter-wave signal terms are

$$\begin{cases} i_{2\omega_{\mathrm{RF}}} = R/4 \cdot E_o^{\,2} \cdot [2 \cdot J_2(m_a) \cdot J_4(m_a)] \cdot \cos(2\omega_{\mathrm{RF}} t) \\ i_{4\omega_{\mathrm{RF}}} = R/4 \cdot E_o^{\,2} \cdot [J_2(m_a) \cdot J_2(m_a)] \cdot \cos(4\omega_{\mathrm{RF}} t) \\ i_{6\omega_{\mathrm{RF}}} = R/4 \cdot E_o^{\,2} \cdot [2 \cdot J_2(m_a) \cdot J_4(m_a)] \cdot \cos(6\omega_{\mathrm{RF}} t) \end{cases} \quad (6\text{-}11)$$

A strong millimeter-wave with frequency quadrupling ($4\omega_{\mathrm{RF}}$) can be achieved.

Compared with previous works [93], synchronization between two electrical paths is unnecessary because only one RF driving signal is required to drive one of the sub-MZM. In addition, active trimming by controlling the sub-MZM DC bias can be utilized to improve the harmonic suppression ratio. Moreover, high modulation index (MI) is required in the previous work (MI=1.6). With the increasing of RF driving signal frequency (e.g. 40 GHz and beyond), high power driving signal is uneasy to obtain. The required MI in the proposed system is about 0.3. Therefore, costly high frequency power amplifiers are not required in the proposed system. However, the fourth order optical sideband cannot be suppressed inherently. In the previous work, only

sixth order optical sidebands are observed beside the second order optical sidebands. The sixth order optical sidebands are much smaller than the fourth ones because of the properties of the Bessel function. Therefore, the harmonic suppression of the current system is not as good as the previous work and there is about 10 dB suppression ratio difference between these two systems. Nonetheless, reasonable suppression ratio of 28 dB and 24 dB can be obtained at 40 GHz and 60 GHz RoF systems, respectively.

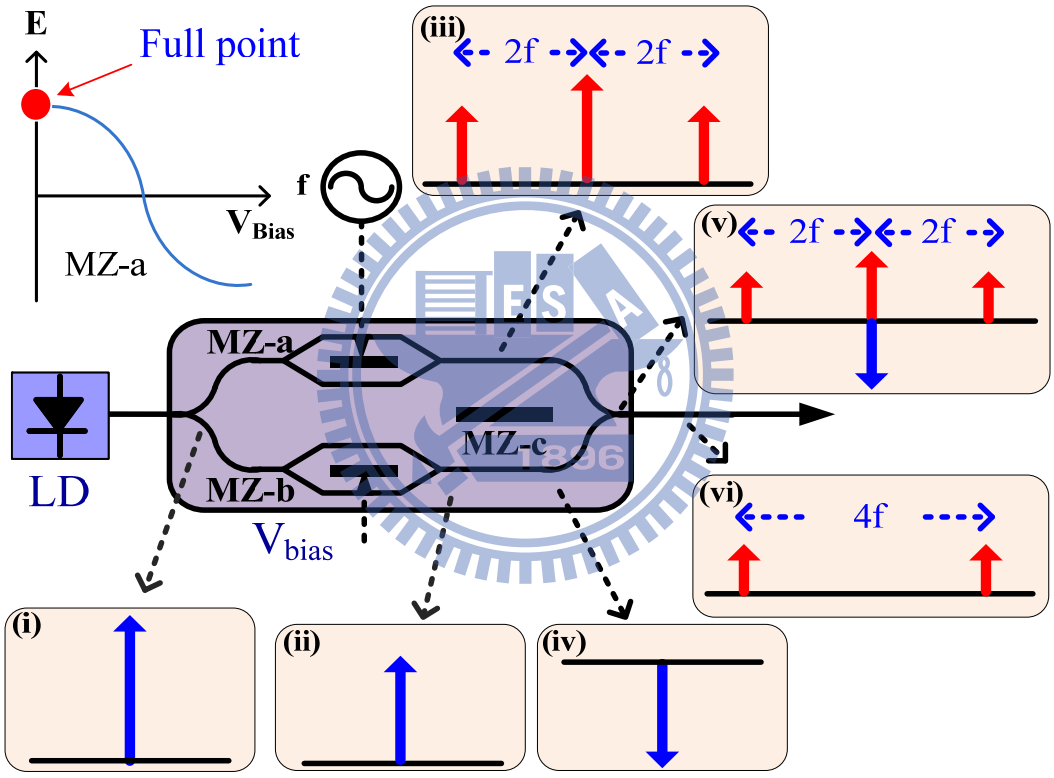

Figure 6-8 The concept of optical frequency quadrupling millimeter-wave generation. (LD: laser diode)

6.3.2 Experimental Demonstration of Frequency Quadrupling

Figure 6-9 (a) shows the measured spectrum of the optical 40-GHz millimeter-wave signal using a 10-GHz driving signal and a dual-parallel modulator with 12-GHz bandwidth. The optical carrier is effectively

suppressed, and the power of the two second-order sidebands can be converted into 40-GHz electrical millimeter-wave signal after PD detection. In addition to the second and fourth order sidebands, the other harmonic sidebands are observed due to the imbalance y-junction splitting ratio of MZM. However, the suppression of the undesired harmonic sidebands can achieve more than 28.5 dB and induces a negligible influence on the performance of the optical millimeter-wave signal. Figure 6-9 (b) shows the waveform of the optical millimeter-wave signal with 50% duty cycle due to high optical carrier and harmonic distortion suppression ratio. The optical 60-GHz millimeter-wave signal is also demonstrated using a 15-GHz driving signal. Figures 6-10 (a) and (b) show that the optical power of the two second sidebands is 24 dB higher than that of the other sideband, which is good enough for most practical applications. The different suppression ratios of 40-GHz and 60-GHz millimeter signals are caused by the limited modulator bandwidth (12 GHz).

Figure 6-11 illustrates the experimental setup of the frequency quadrupled WDM up-conversion system. 4 × 1.25-Gbps optical carrier suppressed WDM signals are generated and up-converted to 20 GHz using only one external modulator and 5-GHz electrical driving signals. Four distributed feedback (DFB) lasers are used to achieve 4 wavelength signals from 1544.53 nm to 1546.92 nm with 100-GHz channel spacing. A 1x4 optical coupler is used to combine these four DFB lasers. After the optical coupler, the lightwaves are modulated via a single electrode MZM driven by 1.25-Gbps pseudo random bit sequence (PRBS) electrical signal with a word length of 2^{31}-1.

All WDM signals are then up-converted by using proposed method. At the remote node, a tunable optical filter with 0.3 nm bandwidth is utilized to select

the desired channel. The baseband (BB) OOK wireline signal can be recovered by low speed photo receiver, and the RF OOK wireless signal is detected by high speed photo receiver. The BB OOK signal is then sent to bit-error-rate (BER) tester, and the RF OOK signal is down-converted to BB using an electrical mixer before sent into BER tester. Figure 6-12 (a) shows the optical spectrum of the four WDM channels. After frequency quadrupling, two sidebands are separated by 20 GHz as shown in Fig. 6-12 (b).

Figure 6-13 shows receiver sensitivities at BER of 10^{-9} versus different sub-MZM bias voltage drift deviation ratios. The bias voltage drift deviation ratio is defined as $(\Delta V/V_{\pi})\times 100\%$. As the bias drift deviation ratio of each sub-MZM is 15%, the receiver sensitivity penalty of the 20-GHz RF OOK signal is about 1.5 dB. With all three sub-MZM biases drift together, the penalty is less than 2 dB when drift deviation ratio is 10%.

Figure 6-14 plots the BER curves and eye diagrams of the received 1.25-Gbps BB and RF OOK signals at 0-km and 50-km standard single-mode fiber transmission. The power penalty of BB and RF signals of four channels after 50-km standard single-mode fiber transmission are less than 1.5 dB. Notably, the cross point of the eye diagram of the RF OOK signal changes after 50-km standard single-mode fiber transmission. This is because fiber chromatic dispersion causes different group velocities of optical upper and lower sidebands of RF OOK signals [92].

In this thesis, a novel filterless frequency quadrupling technique for optical millimeter-wave generation using a dual-parallel modulator is proposed. Frequency tunability can be easily achieved because no driving signal synchronization is needed. The optical carrier and harmonic distortion

suppression ratio of generated optical millimeter-wave signals can reach more than 24 dB. We also demonstrate four-channel up-conversion in RoF systems with 1.5-dB penalty after 50-km standard single-mode fiber transmission.

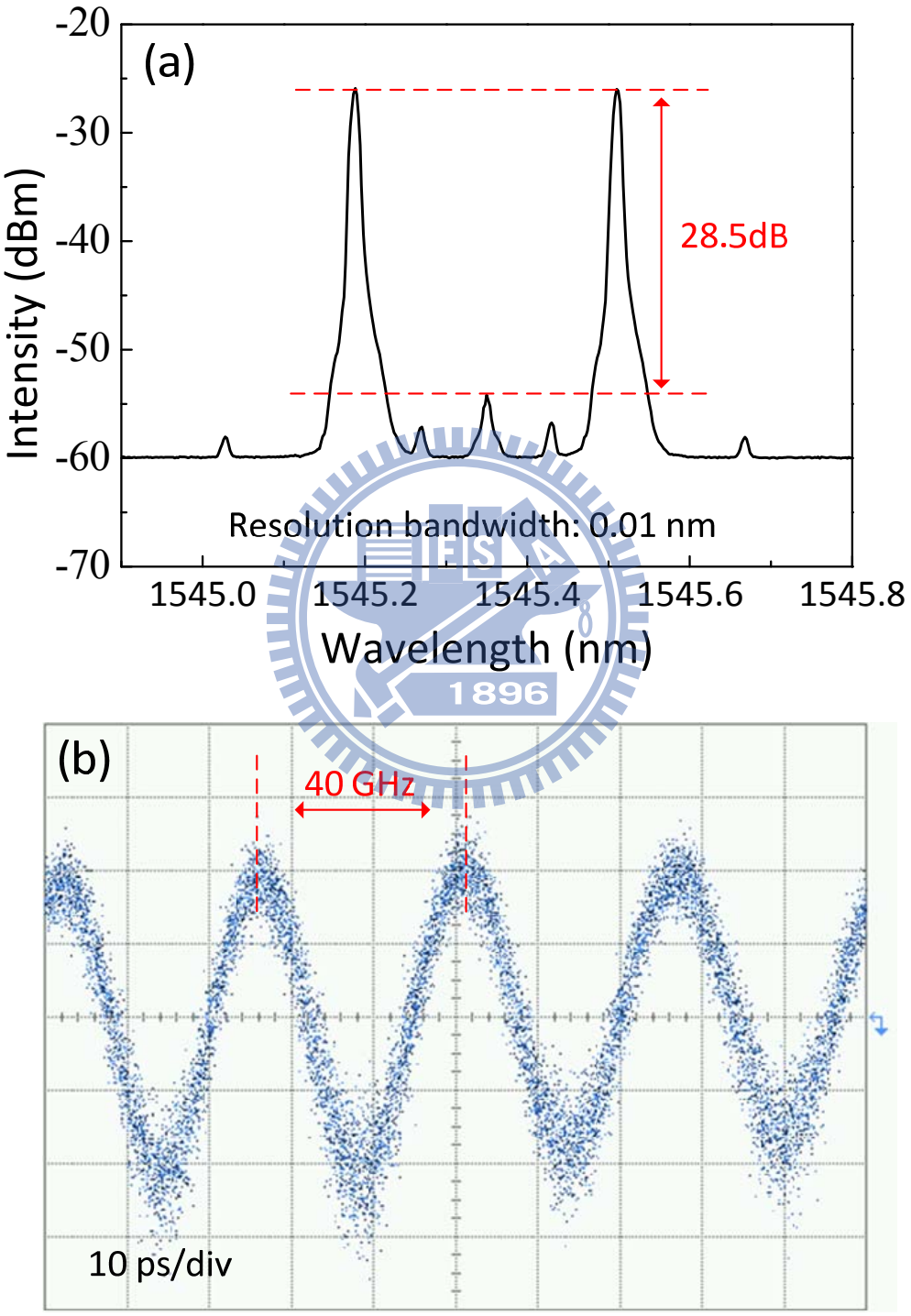

Figure 6-9 Experimental results of the 40-GHz optical spectrum and electrical waveform.

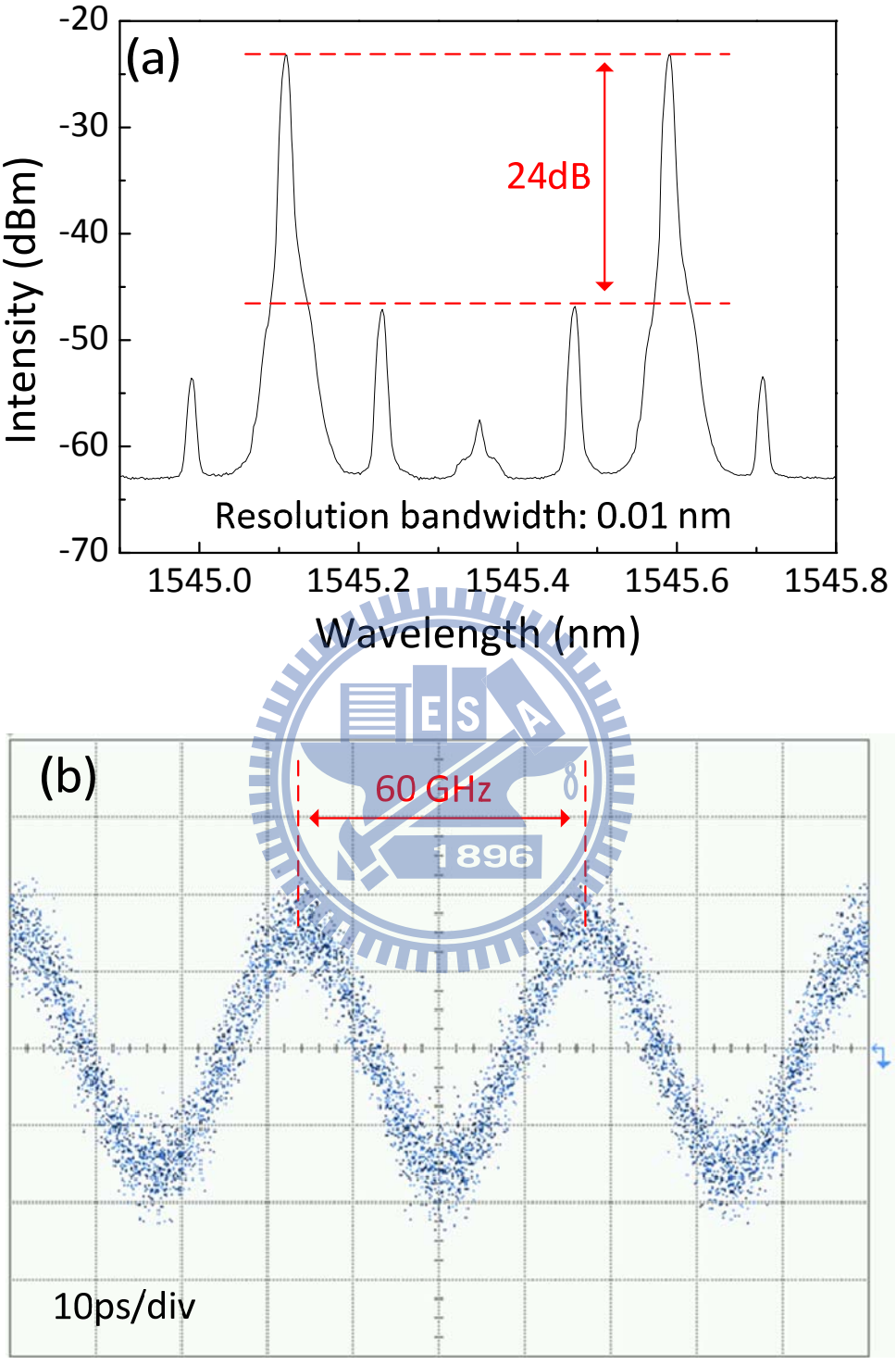

Figure 6-10 Experimental results of the 60-GHz optical spectrum and electrical waveform.

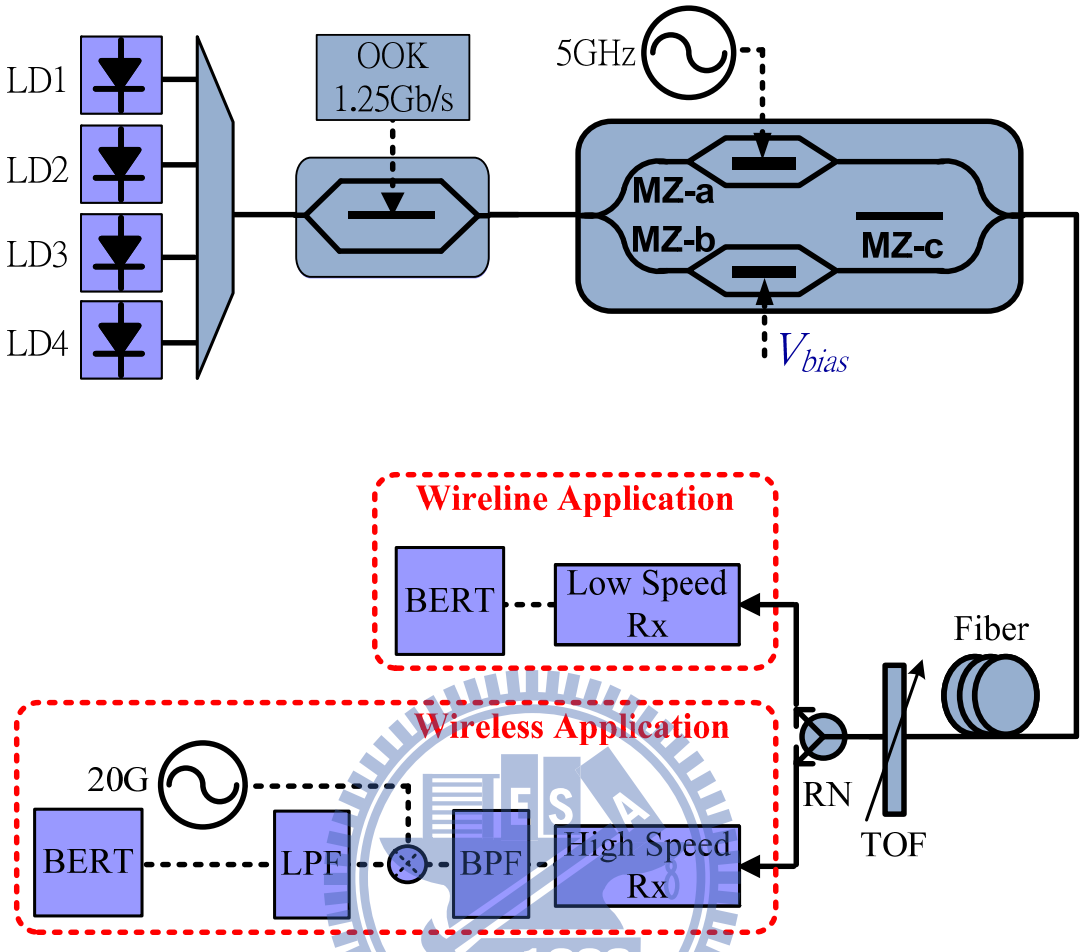

Figure 6-11 Experimental setup of the WDM up-conversion system using frequency quadrupling technique with four channels 1.25-Gbps OOK signal. (TOF: tunable optical filter; LPF: lowpass filter.)

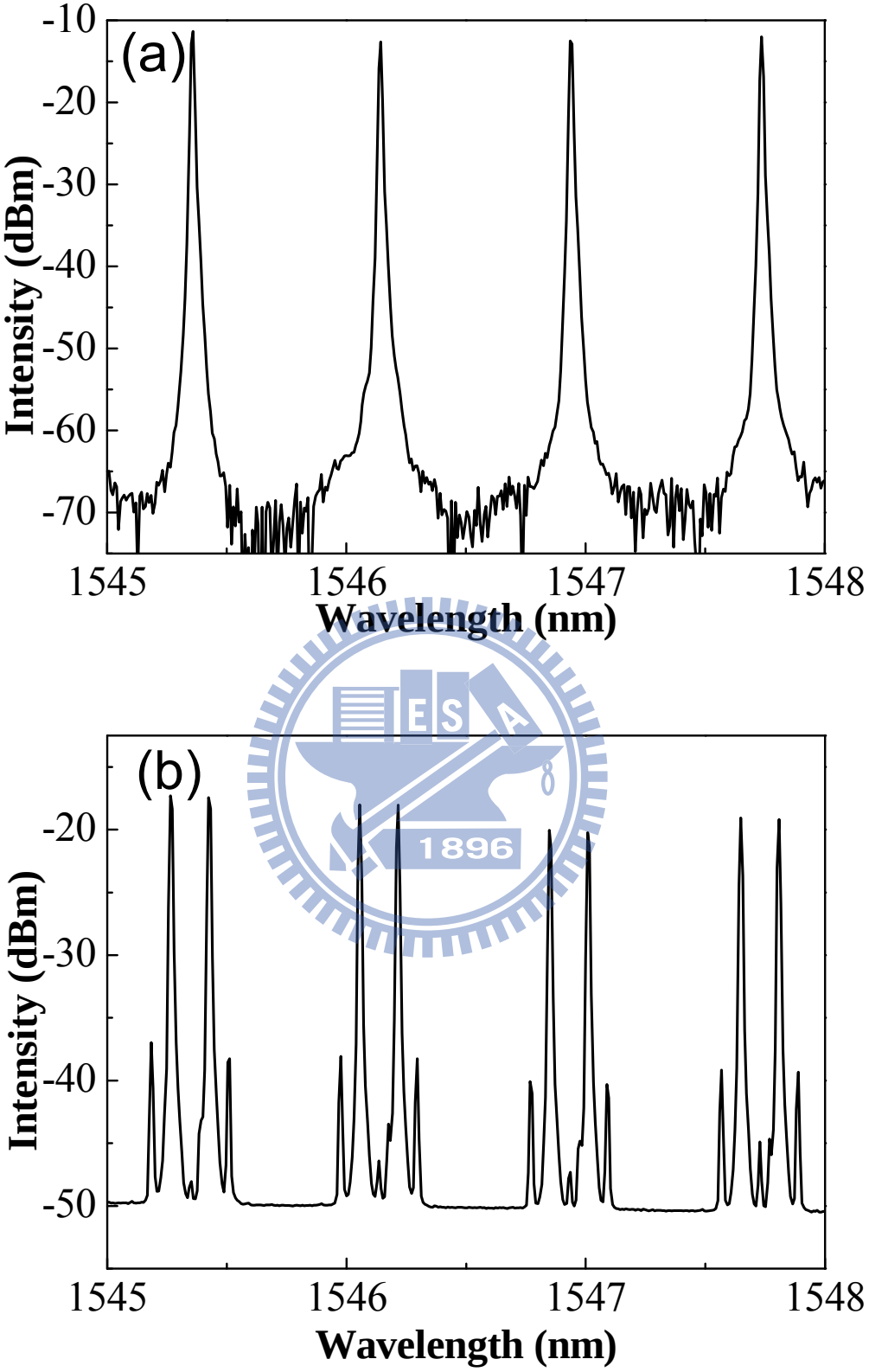

Figure 6-12 The optical spectra (a) without up-conversion (b) with up-conversion.

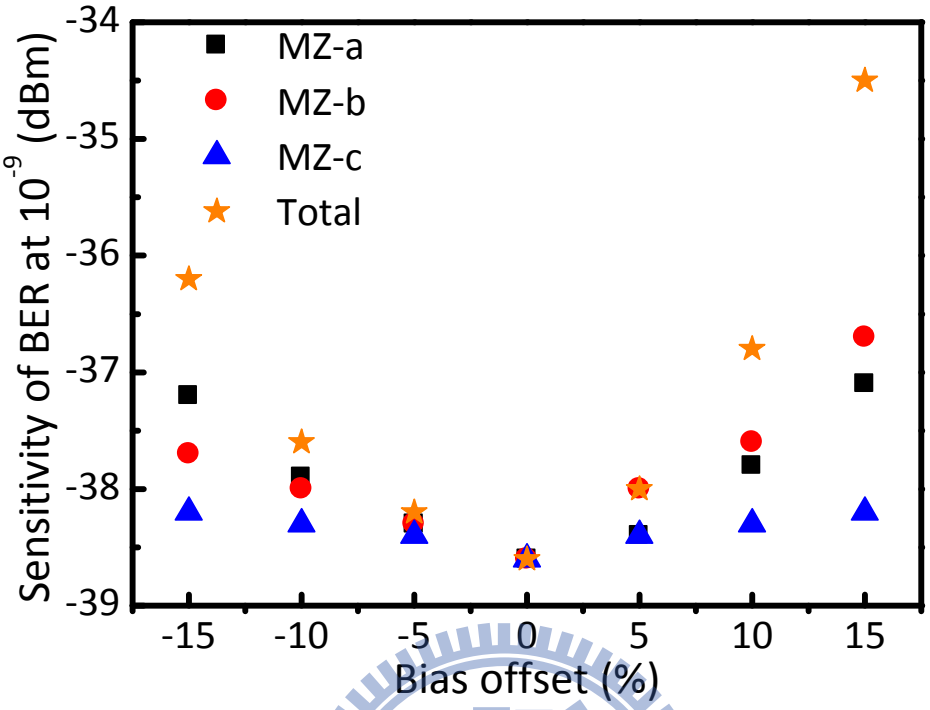

Figure 6-13 Receiver sensitivities versus different sub-MZM bias drift.

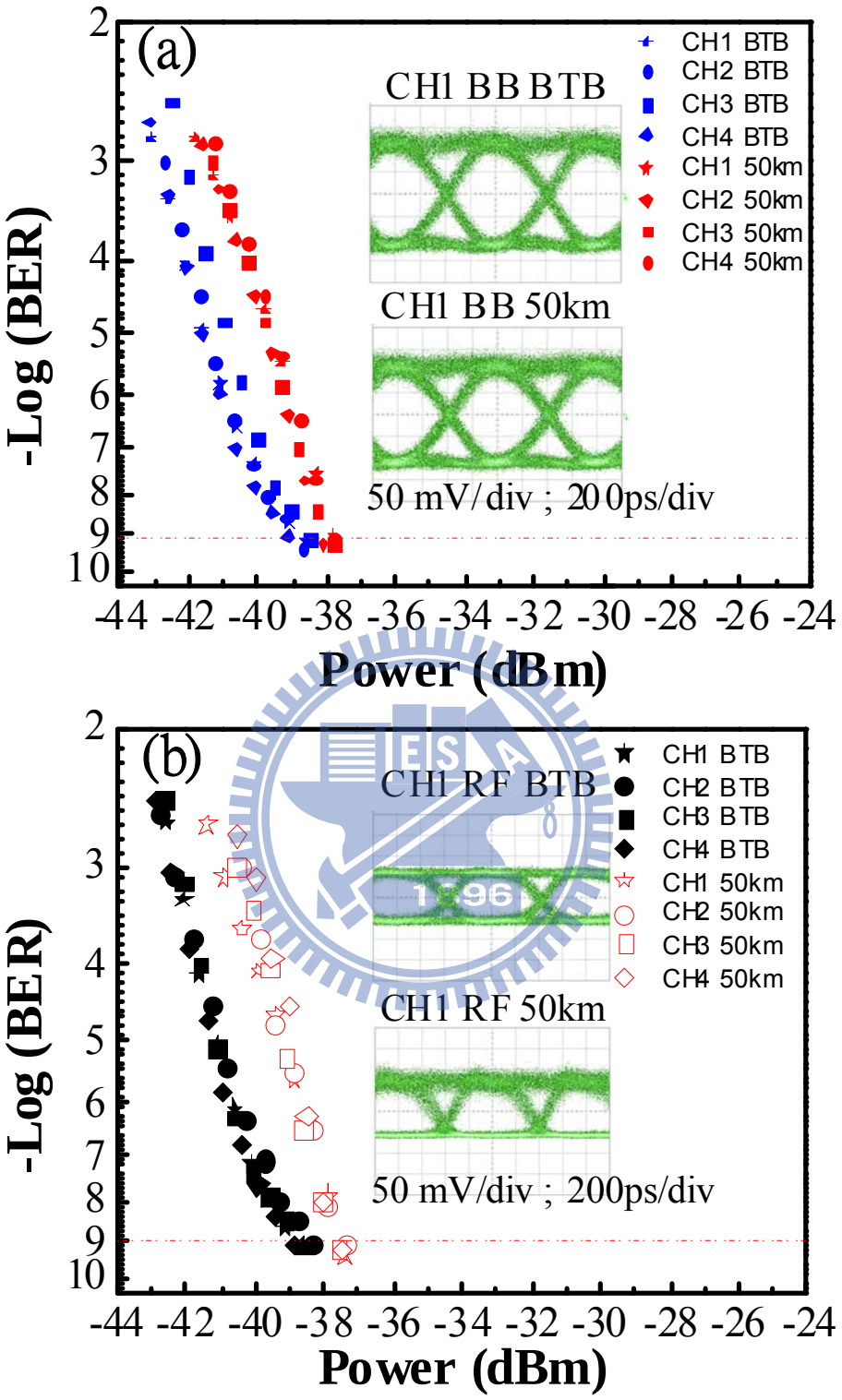

Figure 6-14 The BER curves and eye diagrams for BTB and after 50-km standard single-mode fiber transmission. (a) BB wireline signals; (b) RF OOK wireless signals.

6.3.3 Concept of Pre-coded Technique

Figure 6-15 schematically depicts the concept of the millimeter-wave generation using single-electrode MZM. The single drive Mach-Zehnder modulator (MZM) used to modulate optical field. The optical field at the input of MZM is given by $E_{in}(t) = E_o \cos(\omega_o t)$, where E_o and ω_o are the amplitude and angular frequency of the optical field, respectively. The driving signal $V(t)$ consisting a DC biased voltage and RF signal at frequency ω_{RF} is $V(t) = V_{bias} + V_m(t)\cos(\omega_{RF} t + \theta(t))$, where V_{bias} is the dc biased voltage, $V_m(t)$ and $\theta(t)$ are the amplitude and phase information of RF signal, respectively. The optical field at the output of the MZM is then given by

$$E_{out}(t) = E_o \cos\left[\frac{\pi}{2}\left(\frac{V_{\text{bias}}}{V_\pi} + \frac{V_m(t)}{V_\pi}\cos\left[\omega_{RF} t + \theta(t)\right]\right)\right]\cos\left[\omega_o t\right]$$

$$= E_o \left\{\cos \text{b} \cdot \cos\left[m(t)\cos\left[\omega_{RF} t + \theta(t)\right]\right] - \sin \text{b} \cdot \sin\left[m(t)\cos\left[\omega_{RF} t + \theta(t)\right]\right]\right\} \cdot \cos\left[\omega_o t\right] \quad (6\text{-}12)$$

where b is $\frac{\pi V_{\text{bias}}}{2V_\pi}$, and $m(t)$ is $\frac{\pi V_m(t)}{2V_\pi}$. Using Bessel function expansion, the output optical field at the output of the MZM can be rewritten as

$$\begin{aligned} E_{out}(t) = {} & E_0 \cos \text{b}\left[J_0(m(t))\cos(\omega_c t)\right. \\ & \left. + \sum_{n=1}^{\infty} J_{2n}(m(t))\cos(\omega_c t \pm 2n(\omega_{RF} t + \theta(t)) \mp n\pi)\right] \\ & + E_0 \sin \text{b}\left[\sum_{n=1}^{\infty} J_{2n-1}(m(t))\cos(\omega_c t \pm (2n-1)(\omega_{RF} t + \theta(t)) \mp n\pi)\right] \end{aligned} \quad (6\text{-}13)$$

Due to the power of optical sidebands with the order of higher than J_2 are smaller than J_2 term and the generated optical signal would filter by optical band pass filter, the high order optical sidebands can be neglected with

significant errors. The output optical can be further simplified to

$$E_{out}(t) = E_0 \cos b\left[J_0(m(t))\cos(\omega_c t)\right.$$

$$\left.+J_2(m(t))\cos(\omega_c t \pm 2\omega_{RF} t \pm 2\theta(t))\right]$$

$$-E_0 \sin b\left[J_1(m(t))\cos(\omega_c t \pm \omega_{RF} t \pm \theta(t))\right] \quad (6\text{-}14)$$

If MZM is biased at the null point (V_{bias} = V_π), the output field at the output of the MZM is become as

$$E_{out}(t) = -E_0\left[J_1(m(t))\cos(\omega_c t \pm \omega_{RF} t \pm \theta(t))\right] \quad (6\text{-}15)$$

After square-law photo detection the photocurrent of the generated RF signal can be express as

$$i_{4\omega_{RF}}(t) = \frac{1}{2}\cdot R \cdot J_1^2[m(t)]\cdot\cos[2\omega_{RF} t + 2\theta(t)], \quad (6\text{-}16)$$

where R is the responsivity of photodiode. This result is proposed frequency doubling system, the phase information of signal need pre-coded form $2\theta(t)$ to $\theta(t)$. Because the frequency doubling system is less arrange type can choose. In this work, the frequency quadrupling system is used to analysis pre-code method.

If the MZM is biased at the full point (V_{bias} = 0), the output field at the output of the MZM is become

$$E_{out}(t) = E_o \cdot\left\{J_0(m(t))\cdot\cos(\omega_o t) - J_2(m(t))\cdot\cos(\omega_o t \pm 2\omega_{RF} t \pm 2\theta(t))\right\}, \quad (6\text{-}17)$$

where $m(t)$ is the modulation index defined as $V_m(t)\pi/2V_\pi$, $J_n()$ is the n_{th} order. After the modulation, the strong optical carrier at ω_o would decade the signal sensitivity. Therefore, the strong optical carrier can be suppress by notch fiber bragg grating and the output optical can be further simplified to

$$E_{out}(t) = -E_o J_2(m) \cdot \cos(\omega_o t \pm 2\omega_{RF} t \pm 2\theta(t)) \quad (6\text{-}18)$$

This result is the same with previous proposed frequency quadrupling result. The amplitude and phase information of two optical sidebands at $\omega_o \pm 2\omega_{RF}$ are $J_2(m)$ and $2\theta(t)$, respectively. After square-law photo detection the photocurrent of the generated RF signal can be express as

$$i_{4\omega_{RF}}(t) = \frac{1}{2} \cdot R \cdot J_2^2[m(t)] \cdot \cos[4\omega_{RF} t + 4\theta(t)] \quad (6\text{-}19)$$

The frequency of the generated RF signal ($4\omega_{RF}$) is four times that of the driving signal (ω_{RF}). The amplitude and phase information of generated RF signal are $J_2^2[m(t)]$ and $4\theta(t)$, respectively. Since the amplitude and phase information of generated RF signal is different with driving signal, the driving signal needs to be pre-coded to achieve the desired information. By properly pre-coded driving signals, the proposed scheme can support various kinds of vector signals, including amplitude-shift keying (ASK), phase-shift keying (PSK), and quadrature amplitude modulation (QAM). The pre-coded $V_m(t)$ is related to the second order of Bessel function, and the phase information of the generated vector signal is four times of $\theta(t)$.

For the QPSK signal, since the phase information will change after the proposed system, the original signal need to pre-code. Figure 6-16 shows the standard and pre-coded QPSK signals, the standard QPSK have four constellation points at $\pi/4 + n \cdot \pi/2$, where n = 0,1,2, and 3. For every point has four different points will reach same constellation points after frequency quadrupling system. For example, the previous result use four points in first

quadrant and get standard QPSK constellation points after receiver. In fact, there are many different arrange types will get the same signal. However, the signal shows different performance with different arrange type.

In this work, we discuss pre-coded QPSK signal with twelve different arrange types and compare their performance. The twelve different arrange type shows in Table 6-1. The different arrange type that has different RF spectrum is show in Fig. 6-17. The constellation point would transfer to each other. If the constellation has centralized points, it causes constellation points have lower variation and the signal energy would centralize at the carrier frequency as show in Fig. 6-17. In other words, if the constellation points have large variation, it also needs more energy in high frequency to provide constellation point transfer. Therefore, the bandwidth of 97% of electrical power in how much symbol rate could calculate form electrical spectrum as shown in the Table 6-1. Because the electrical spectrum of generation RF signal has centralized bandwidth, the signal suffers less band limit channel effect. After frequency quadrupling system, the phase information would change to four times than original phase information. The stander QPSK signal would appear after square-law photo detection. However, the constellation transfer path would different form different arrange type, as shown in Fig. 6-18. Figure 6-18 (a) shows the constellation transfer path of first arrange type. The original four points are at $\pi/16$, $3\pi/16$, $5\pi/16$, and $7\pi/16$. After frequency quadrupling system and square-law photo detection, the four points would at $\pi/4$, $3\pi/4$, $5\pi/4$, and $7\pi/4$. Moreover, the transfer path of phase information from $\pi/16$ to $7\pi/16$ is counterclockwise. Due to the path of original driving signal, the path of generated signal is also counterclockwise. This reason cause the receive

constellation transfer path is different between with regular QPSK signal and the signal with different arrange type also have different constellation transfer path. The length of constellation transfer path could calculate form original pre-code constellation point. If we don't consider the amplitude variation, the length of constellation transfer path after system is proportion to original driving signal. Table 6-1 shows the length of constellation path that calculate from pre-code driving signal. Normally, the nearest distance between two points is the length of straight line between two points. Because the generated signal comes from different pre-code signal, the generated signal would have different transfer path. When the length of the constellation transfer path becomes more and more, this signal need more bandwidth to provide the constellation point transfer or provide more time to transfer. Therefore, the signal with large bandwidth would suffer channel response very serious. The worse channel response would cause signal performance decrease a lot especially in the signal with large bandwidth. Therefore, the complex transfer path needs more bandwidth for the constellation point transfer. If the channel bandwidth is limited, the signal would distortion after demodulator. For other arrange type, like Fig. 6-18 (b). The original four points are at π/16, 3π/16, 5π/16, and 15π/16. After frequency quadrupling system and square-law photo detection, the four points would at π/4, 3π/4, 5π/4, and 15π/4. This signal path between π/4, 3π/4, and 5π/4 are the same with pervious case. The different are points to 15π/4 point and form 15π/4 point to other points. For example, the phase information continues change from the π/16 point to 15π/16 point. After the receiver, the phase information from π/4 to 15π/4 would pass 2π and then reach 7π/4. This phase change is large fluctuations, an undesirable quality in

communication systems. This work would discuss different arrange type and compare performance each other.

For the start 8-QAM signal generation, it would include amplitude information. Due to the analysis result of the optimal condition is four points closely that have lowest bandwidth and the lowest constellation length path. Therefore, the simulation condition of star 8-QAM signal would fix inner and outside four points is closely and change the position between inner and outside as shown in Fig. 6-19. The star 8-QAM signal can be divided into eight different arrange type, as shown in Table 6-2. Figure 6-20 shows the electrical spectrum before send into MZM. The 500-Msymbol/s 8-QAM signal is used to demonstrate.

Figure 6-20 shows the electrical spectrum that inner and outside point from small to large. The figure shows that the points are centralization would have higher carrier power and lower sideband power. The 97% power in how much bandwidth is show in Table 6-2. The length of transfer path could calculate form pre-code signal, as shown in Table 6-2. In this work, we would give detail analysis and experimental demonstration of direct-direction RF QPSK and 8-QAM signals using frequency quadrupling.

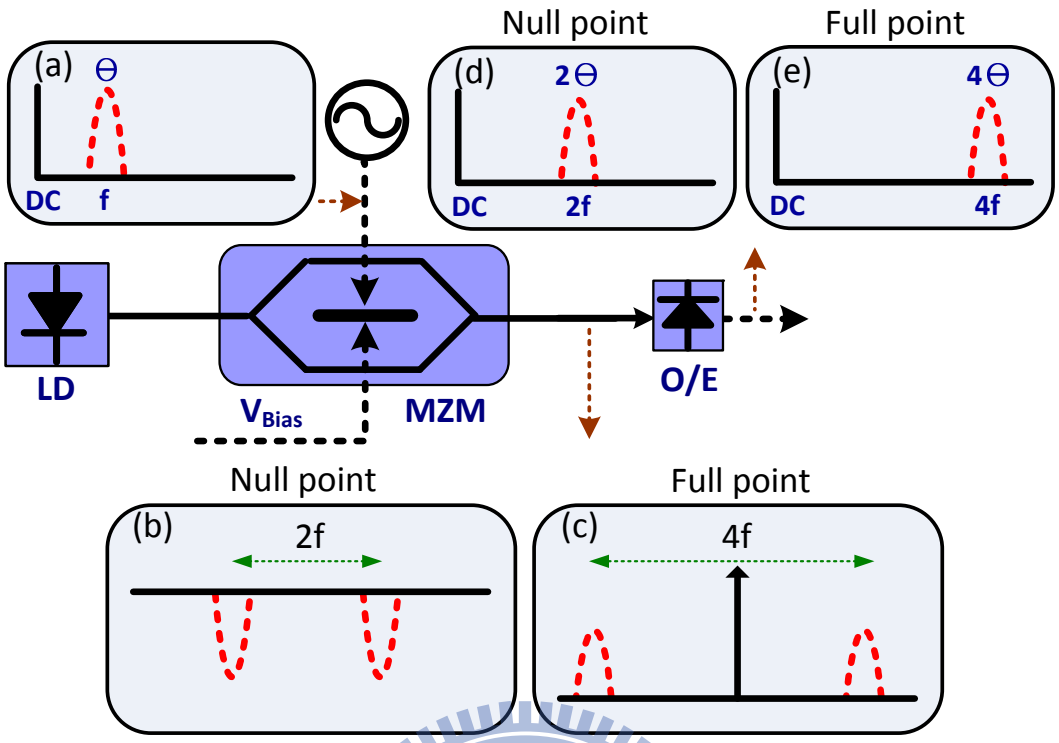

Figure 6-15 The concept of the millimeter-wave generation using single-electrode MZM.

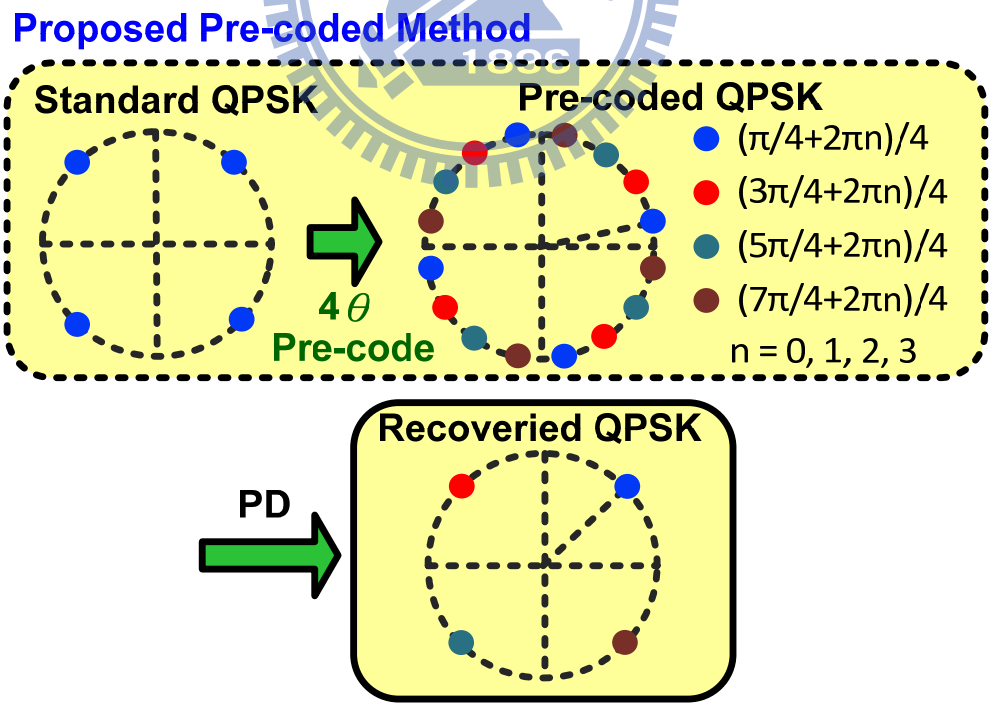

Figure 6-16 The principle of pre-coded scheme of the QPSK format with frequency quadrupling system.

Table 6-1 Comparison of 12 pre-coded QPSK signals.

Arrange type	n, $(\frac{2n+1}{16}\pi)$	Path Length	Power(97%)(Symbol rate)
1	0, 1, 2, 3	1	0.523
2	0, 1 ,2, 7	1.84084	1.379
3	0, 1, 6, 7	2.12475	1.452
4	0, 1, 3, 6	1.80687	1.259
5	0, 1, 6, 11	2.38026	1.521
6	0, 1, 3, 10	2.10828	1.457
7	0, 1, 7, 10	2.39219	1.536
8	0, 1, 3 ,14	1.52295	0.752
9	0, 2, 5, 7	2.07987	1.391
10	0, 2, 5, 11	2.36379	1.503
11	0, 5, 7, 14	2.38128	1.533
12	0, 3, 6, 9	2.35823	1.489

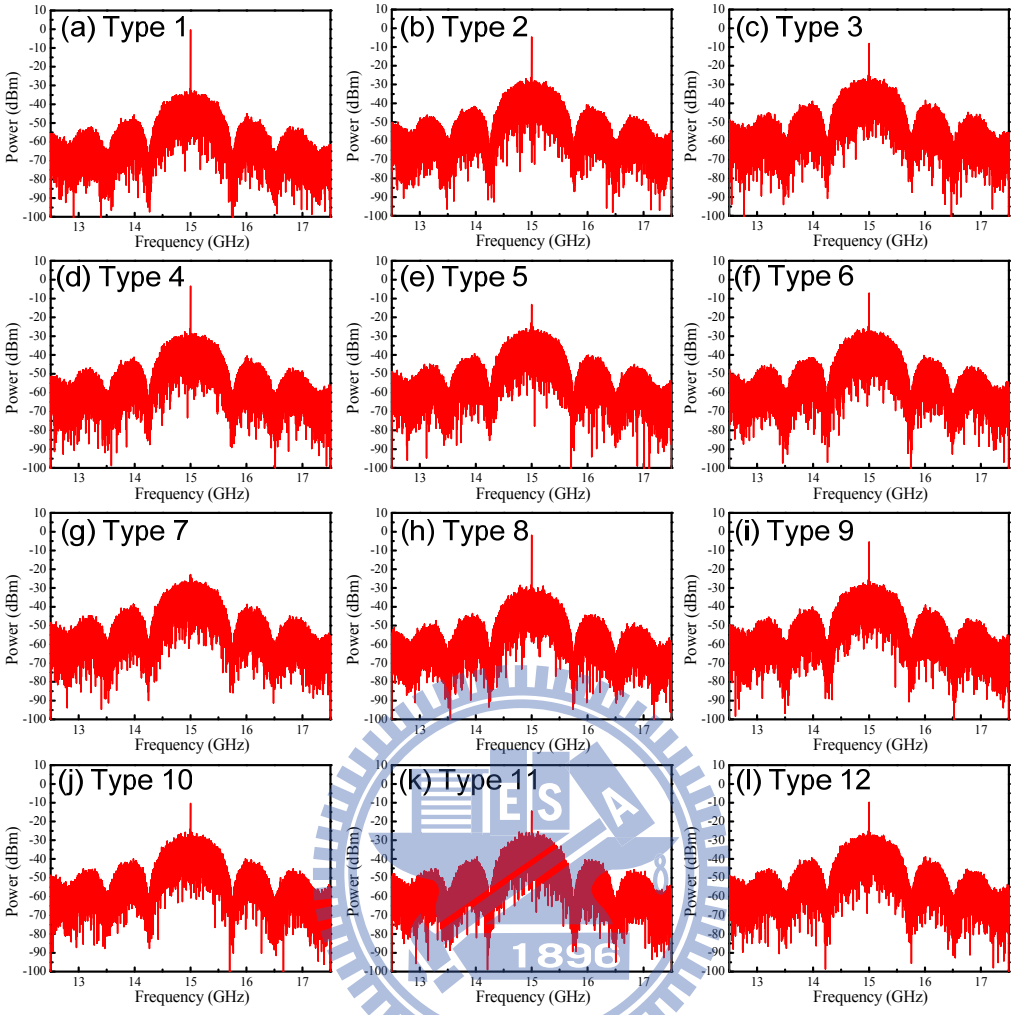

Figure 6-17 Electrical spectra of 12 pre-coded QPSK signals.

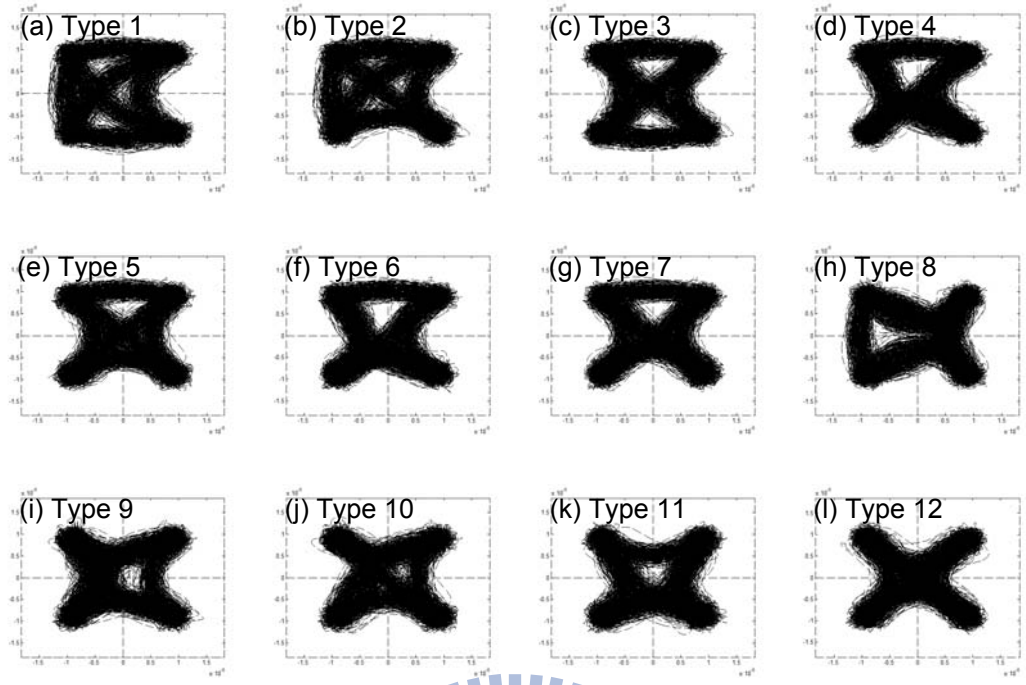

Figure 6-18 Constellation transfer path of 12 pre-coded QPSK signals.

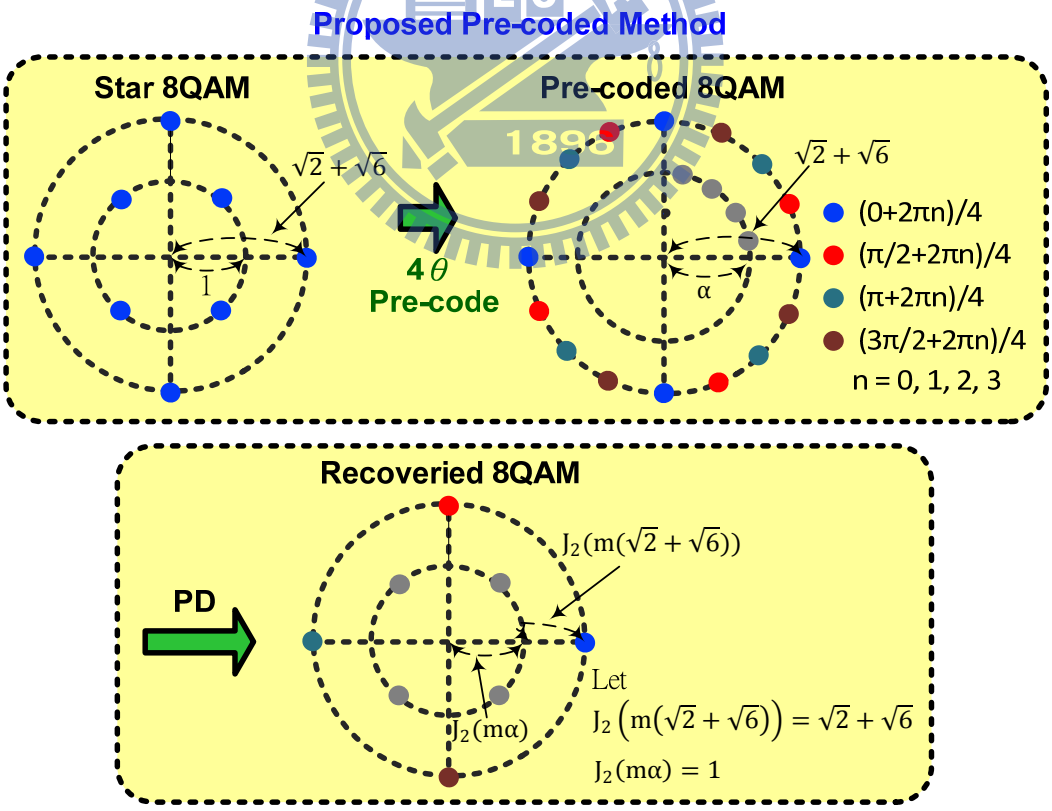

Figure 6-19 The principle of pre-coded scheme of the 8-QAM format with frequency quadrupling system.

Table 6-2 Comparison of 8 pre-coded 8-QAM signals.

Arrange type	n, $(\frac{2n+1}{16}\pi)$ n=0, 1, 2, 3 k, $(\frac{2k}{16}\pi)$	Path Length	Power(97%)(Symbol rate)
1	k=1, 2, 3, 4	1	0.556
2	k=2, 3, 4, 5	1.12157	0.610
3	k=3, 4, 5, 6	1.32592	0.698
4	k=4, 5, 6, 7	1.56471	0.866
5	k=5, 6, 7, 8	1.79024	1.340
6	k=6, 7, 8, 9	1.972	1.454
7	k=7, 8, 9, 10	2.0982	1.492
8	k=8, 9, 10,11	2.16274	1.524

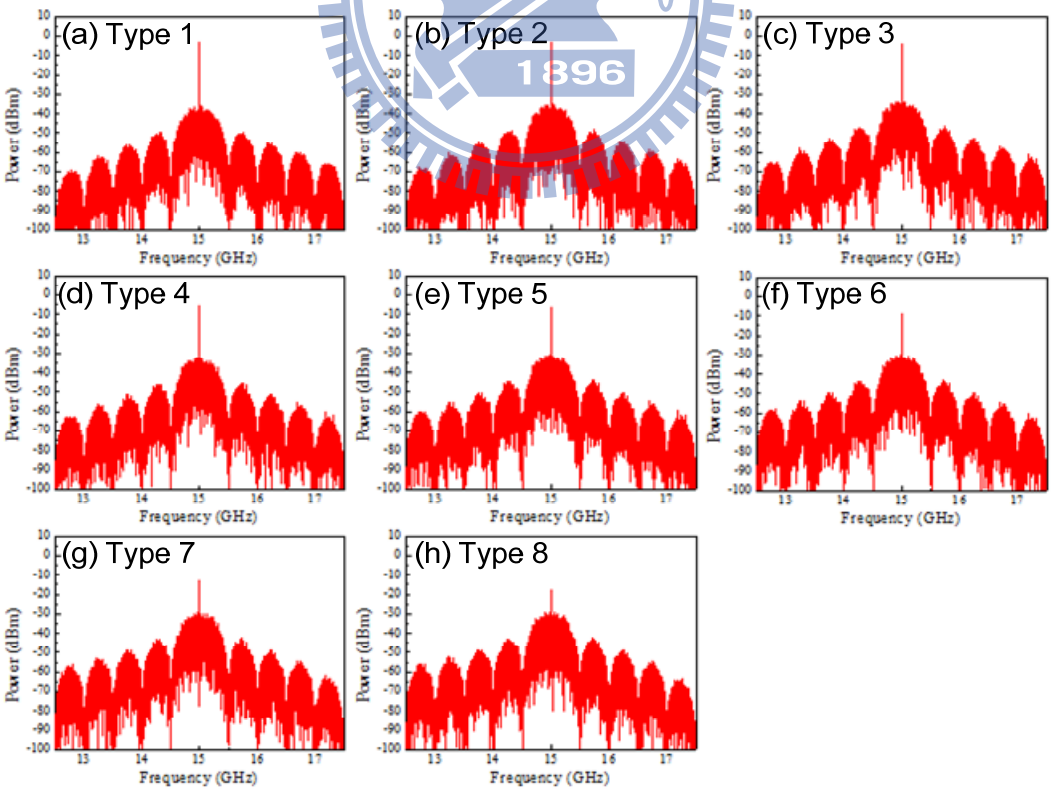

Figure 6-20 Electrical spectra of 8 pre-coded 8-QAM signals.

6.3.4 Experimental Demonstration of Pre-coded Technique

Figure 6-21 depicts the experimental setup of the pre-coded test system. In order to generate the pre-coded signal, the arbitrary waveform generator (AWG, Tektronix® AWG7102) is used. The 1.5-Gbps pre-coded QPSK and 8-QAM signal with a center frequency at 2.5 GHz is generated by an AWG using a Matlab® program, as shown in Fig. 6-22. The resolution of the digital-to-analogue converter of the AWG was set to 8 bits. The digital to analog converter (DAC) sampling rate was 20 Gsample/s. It was then up-convert to 15 GHz using an electrical mixer and 15-GHz sinusoidal signal. And then the electrical bandpass filter use to filter out image signal at 10 GHz, as shown in Fig. 6-23. The pre-coded signal was then used to drive a single-electrode $LiNbO_3$ MZM with 3-dB bandwidth of 20 GHz is employed. The optical signal source was an external-cavity laser emitting +4-dBm optical power at 1550-nm wavelength. The continuous wave (CW) optical signal was fed into the MZM, where it was modulated by the pre-coded signal. The MZM was biased at the maximum transmission point in order to generate two second-order sidebands. After the MZM, the original optical carrier is suppressed by fiber bragg grating with 28 dB suppression ratio. The optical signal was then amplified by an Erbium Doped Fiber Amplifier (EDFA) with a noise figure of 4 dB. After the EDFA, an optical band-pass filter with a 3-dB bandwidth of 0.7 nm was used to suppress the amplified spontaneous emission (ASE) noise. As shown in Fig. 6-24, two second-order sidebands are very clear. Two strong second-order sidebands are modulated with different phase information but the same amplitude information. Notably, the undesired sideband suppression ratio is more than 31 dB, which has negligible effect on

the performance of the optical vector signal. Before being sent into receiver side, the optical signal transmits 25-km standard single-mode fiber. At the receiver, the electrical signal generate at 60 GHz through square-law photo-detection (beating term for two second-order sidebands) in the 67-GHz photodiode. Since the amplitude and phase information of generated RF signal are different with original driving signal, the standard vector signal is generated by pre-coded signal. The RF signal was then amplified by a low noise amplifier (LNA) with 40-dB gain, and down-converted to 5 GHz as shown in Fig. 6-25. The time domain waveforms of the down-converted signals were captured by digital oscilloscope with a 50-Gsample/s and a 3-dB bandwidth of 12.5 GHz for off-line signal processing and analysis. An off-line processing using a Matlab® program includes synchronization and BER estimation.

First, we measured the performance of the 1.5-Gbps QPSK signal. Figure 6-26 shows the signal-to-noise (SNR) of constellation versus different arrange type. The SNR of constellation is defined as

$$\text{SNR} = -20 \log (\text{EVM}/100\%). \quad (6\text{-}20)$$

Figure 6-26 also shows the transmission distance between constellations points increased, the signal performance decreased. For the arrange type one, the signal performance is best due to short transmission distance. The signal quality is depend on the different arrange type. As the path length becomes two times of arrange type one, the SNR of signal would decrease 3dB. The reason is complex transfer constellation points, the large variation need large bandwidth. Due to the bandwidth is limited and the channel response is not perfect, the channel would induce ISI. When the signal has complex transfer constellation points, the signal would have more ISI. Figure 6-27 shows the

BER curves for QPSK signal with three different arrange type. This figure shows 1, 8 and 12 arrange type. For lower optical receiver power have almost the same sensitivity, it means the signal performance domain by noise. For higher optical receiver power, the sensitivity are different for different arrange type. Figure 6-27 also shows the BER curves with BTB and 25-km fiber transmission. If the path length becomes more, the signal need more transfer speed or timing. The transfer speed becomes more means that the signal needs more bandwidth. The transfer timing becomes longer means that the receiver need more precision decision point. Due the signal transmission of optical fiber would suffer dispersion induce walk-off effect, fiber chromatic dispersion causes different group velocities of optical upper and lower sidebands, would cause the eye opening becomes small. Due to the distance between constellation point would need higher bandwidth or lower eye opening, lower eye opening would suffer higher penalty after fiber transmission. As shown in the Fig. 6-27, the complex arranged signal after 25-km standard single-mode fiber transmission would has more power penalty. For the arrange 1, the power penalty is about 0dB after 25-km fiber transmission. For the arrange 8 and 12, the power penalty are 0.5 and 1.5 dB, respectively.

Figure 6-28 has additionally information about 8-QAM signal, the pre-coded method not only can carrier phase information but also amplitude information. Figure 6-28 also shows that the different arrange type would have different performance. When the length of constellation transfer path is increased, the signal SNR would decrease. The result is the same with QPSK signal, the SNR decrease 3dB with the distance of transfer path becomes two times. Moreover, the complex type has higher penalty after 25-km standard

single-mode fiber transmission as shown in Fig. 6-29. The results is the same with QPSK signal.

This work use frequency quadrupling technique and pre-code method to generate 1.5-Gbps QPSK and 8-QAM signal at 60GHz. The results show different pre-code method would generate different bandwidth, path length, and signal quality. The signal has closely constellation points would have better performance and minimum bandwidth. After 25-km standard single-mode fiber transmission, closely constellation points have lowest power penalty.

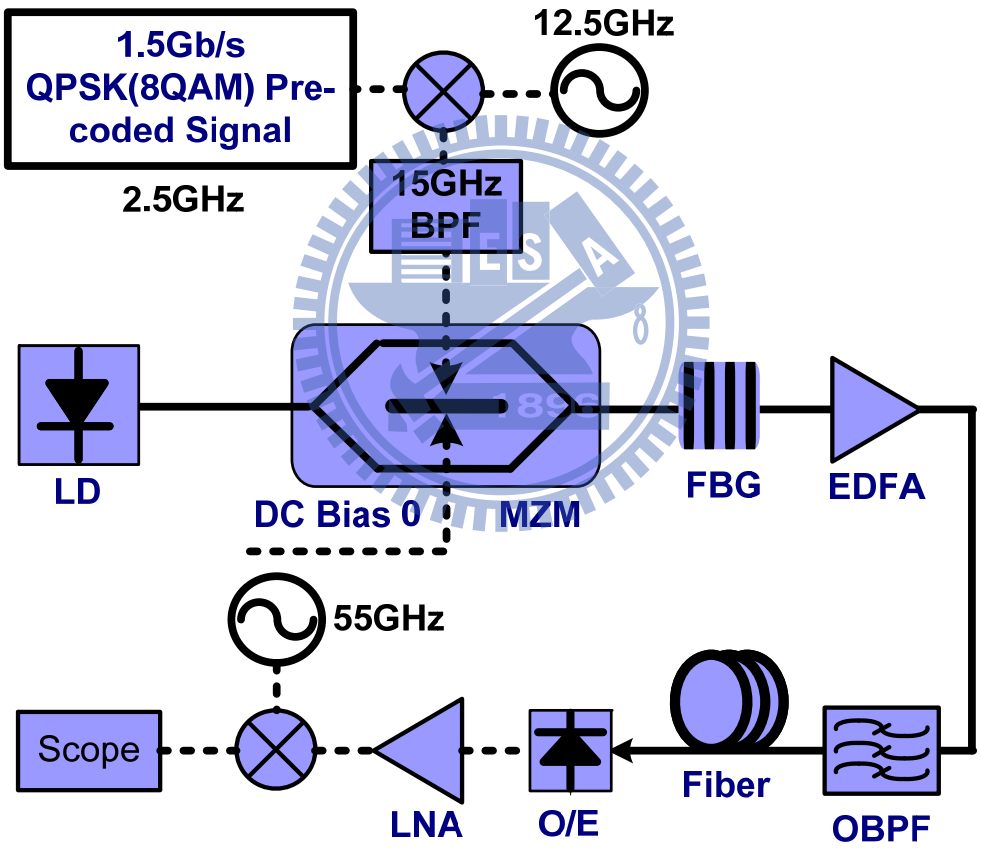

Figure 6-21 Experimental setup of pre-coded test system.

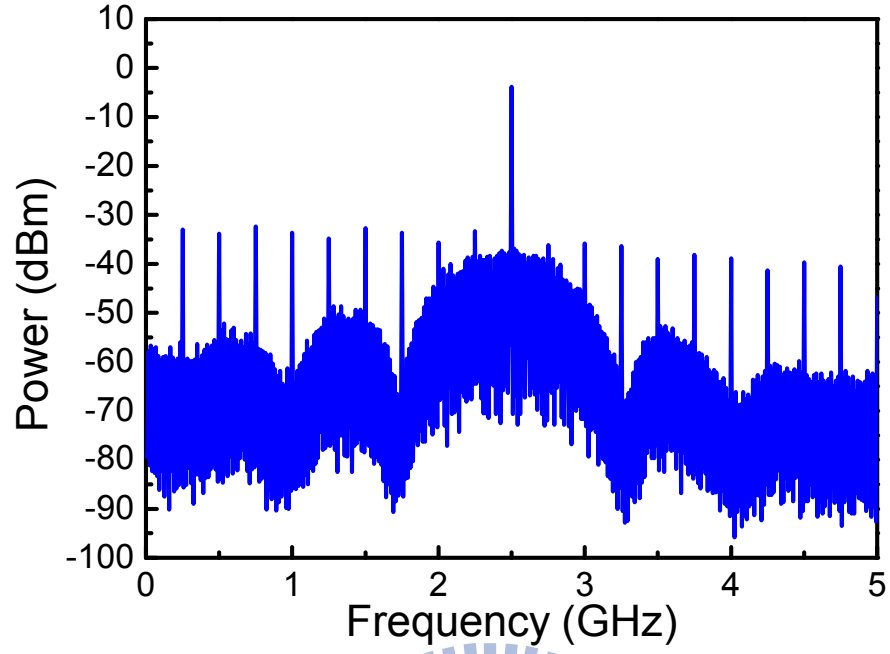

Figure 6-22 Electrical spectrum after arbitrary waveform generator.

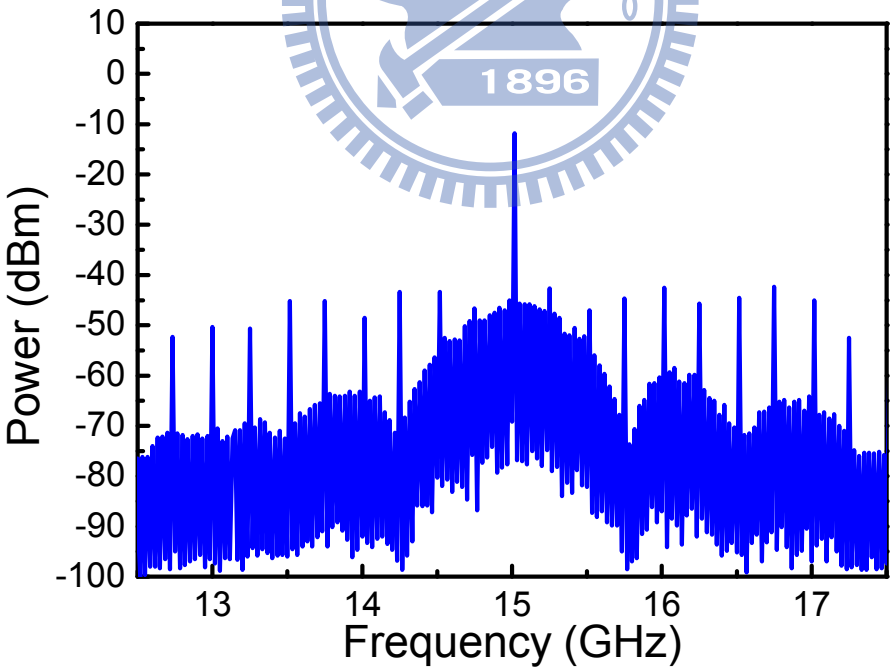

Figure 6-23 Electrical spectrum after up-conversion.

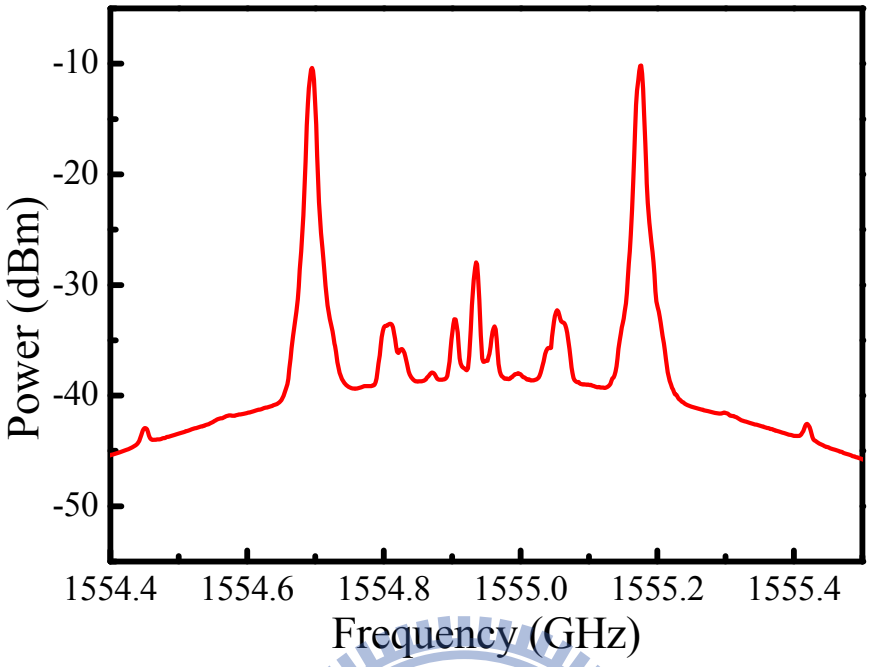

Figure 6-24 Optical spectrum after MZM modulation.

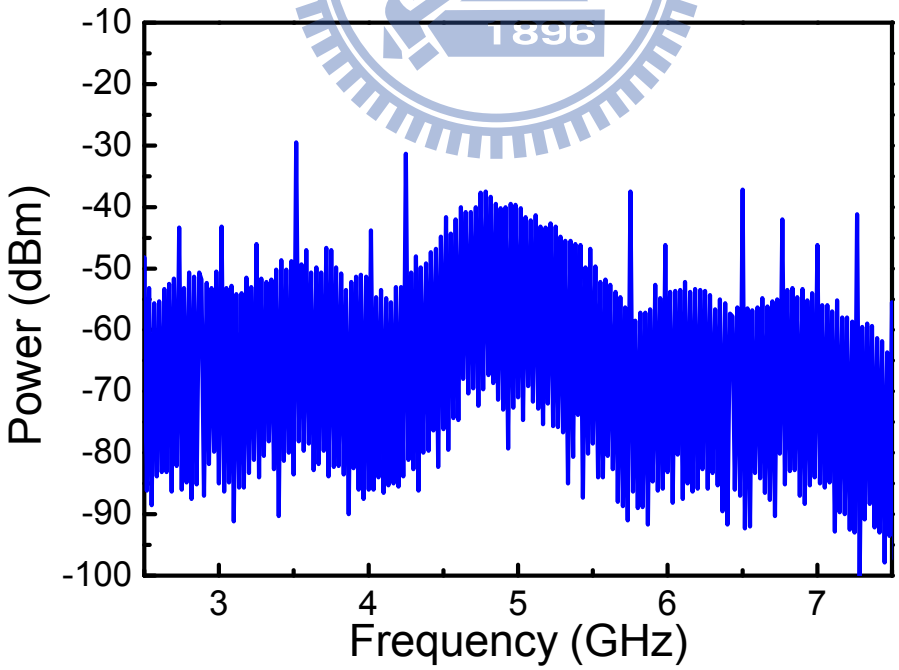

Figure 6-25 Electrical spectrum after down-conversion.

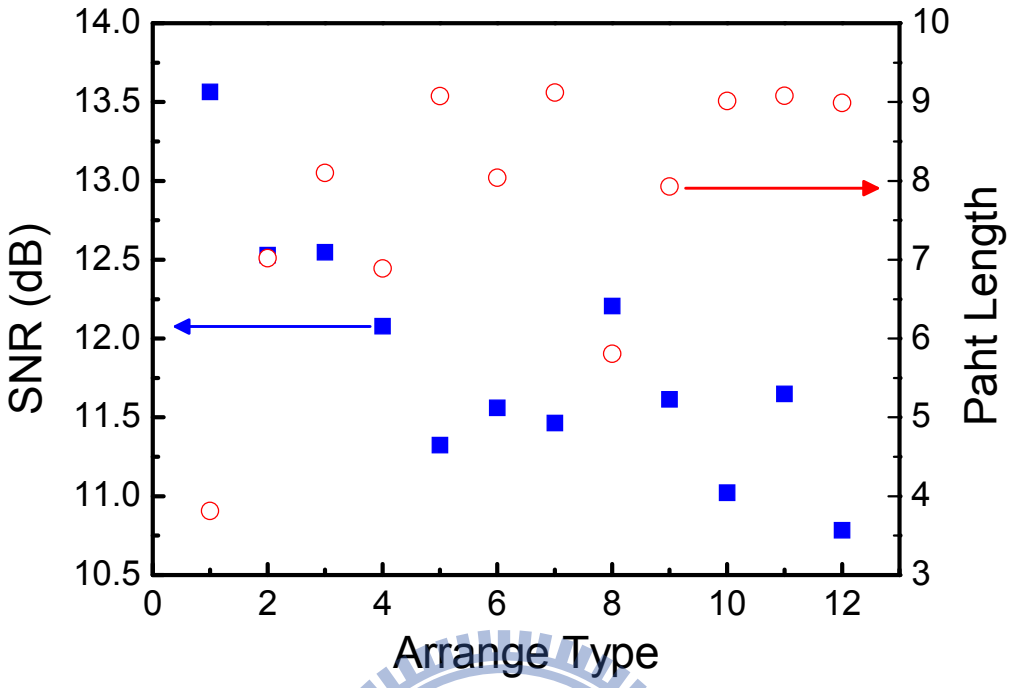

Figure 6-26 SNR and path length versus different QPSK signals.

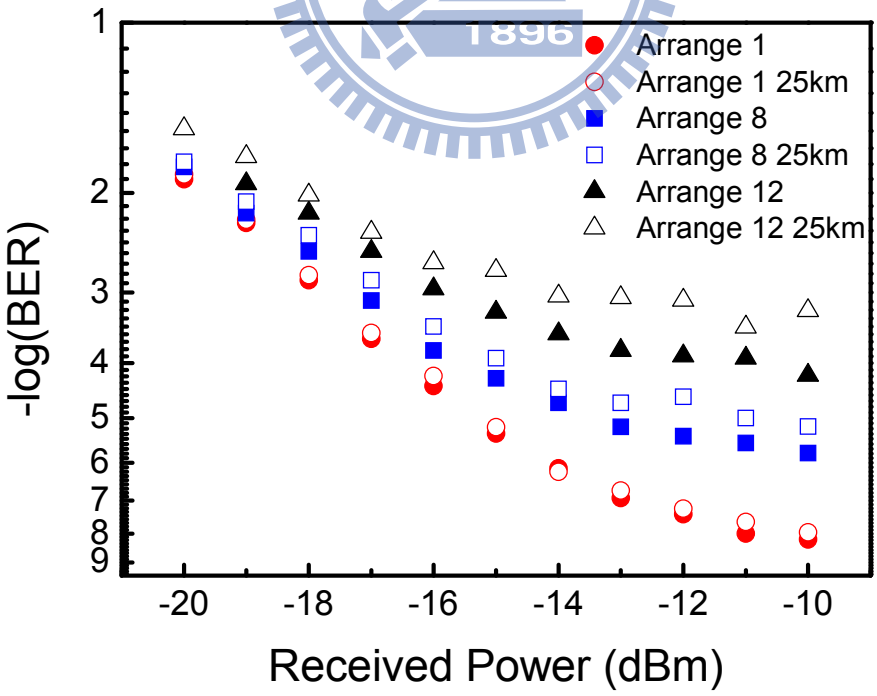

Figure 6-27 The BER curves for QPSK signals with different arrange type.

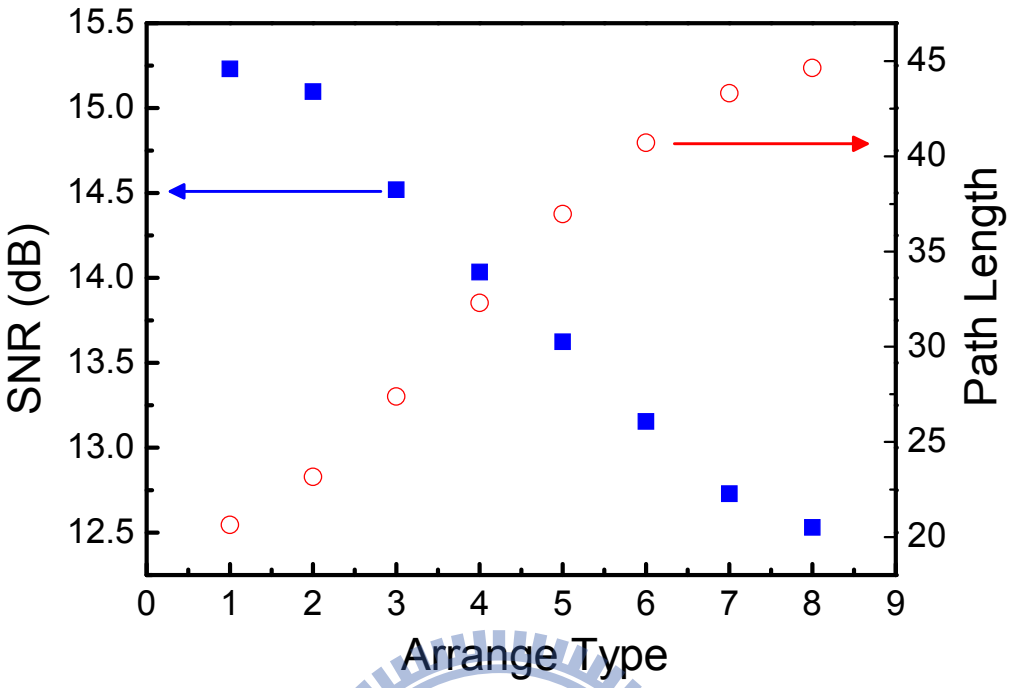

Figure 6-28 SNR and path length versus different 8-QAM signals.

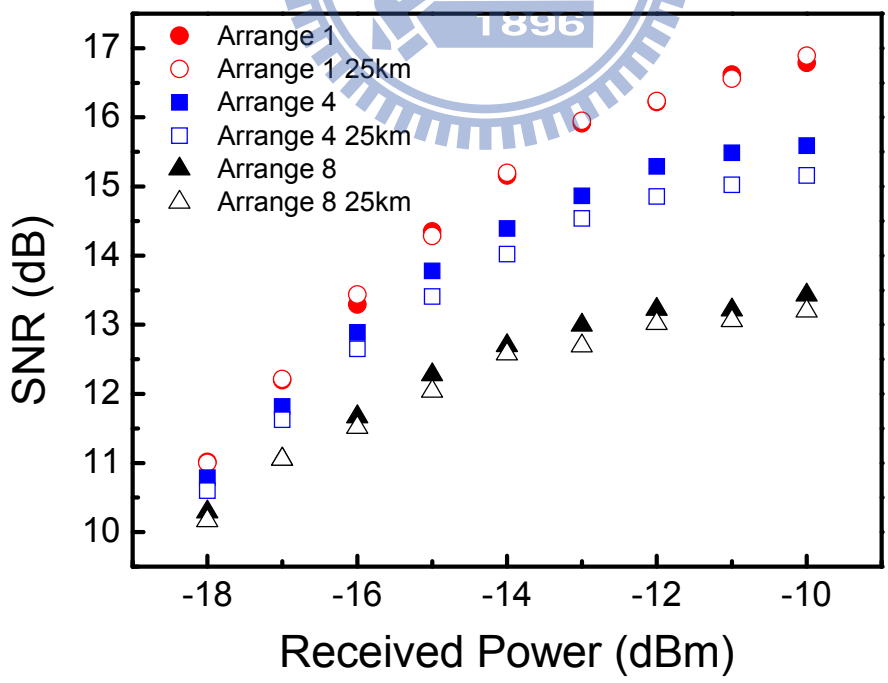

Figure 6-29 The BER curves for 8-QAM signals with different arrange type.

6.3.5 Concept of Hybrid Access Network

Figure 6-30 schematically depicts a proposed hybrid access network system that uses a dual parallel MZM. The MZ-a driving signal is a RF PSK signal with a frequency of *f* for wireless application. When the MZ-a is biased at full point, only even-order optical subcarriers are generated, as presented in inset (i) in Fig. 6-30. The original optical carrier can be completely suppressed by adjusting the bias point of MZ-b and introducing a 180 degrees phase shift between MZ-a and MZ-b, indicating that the output optical carrier field of MZ-a, $J_0[m_a]$, equals the output carrier field of MZ-b, $\cos[m_b]$, where m_a and m_b are $\pi V_a / 2V_\pi$ and $\pi V_b / 2V_\pi$, respectively. However, when an OOK signal is sent to MZ-b in a wireline applications, $J_0[m_a]$ does not always equal $\cos[m_b]$. The optical carrier re-appears, as presented in the insets (ii)-(iv) in Fig. 6-30. This phenomenon implies that an RF signal with a frequency of 2*f* will appear at the receiver, but this signal can be easily filtered out by an electrical band-pass filter that is centered at 4*f*. Inset (v) in Fig. 6-30 presents the generated optical spectrum, which includes two optical sidebands and optical carrier at the output of the modulator. After square-law photo detection, the beating terms of the two optical sidebands generate the desired electrical RF PSK signal, as presented in Fig. 6-31. Since the amount of frequency and phase information for the generated RF signal is four times that in the original electrical RF signal, pre-coded data are needed to ensure that the generated RF signal is regular PSK [95]. For FTTx applications, the square terms of the optical sidebands and optical carrier contribute to the BB signal. When the pre-coded data represent a pre-coded PSK signal, the square terms of the optical sidebands contribute only DC term to the BB signals, causing only

negligibly interfering with the BB OOK signal after being suppressed by an electrical DC block. Therefore, the BB OOK signal can be easily recovered using a typical low-speed receiver, whereas the RF PSK signal can be recovered using a high-speed receiver with no interference from the BB signals. Therefore, no optical filter is required to separate the BB and RF signals. Since no additional narrow-band optical filter is required, the proposed structure is compatible with the existing wavelength division multiplexing passive optical network (WDM-PON).

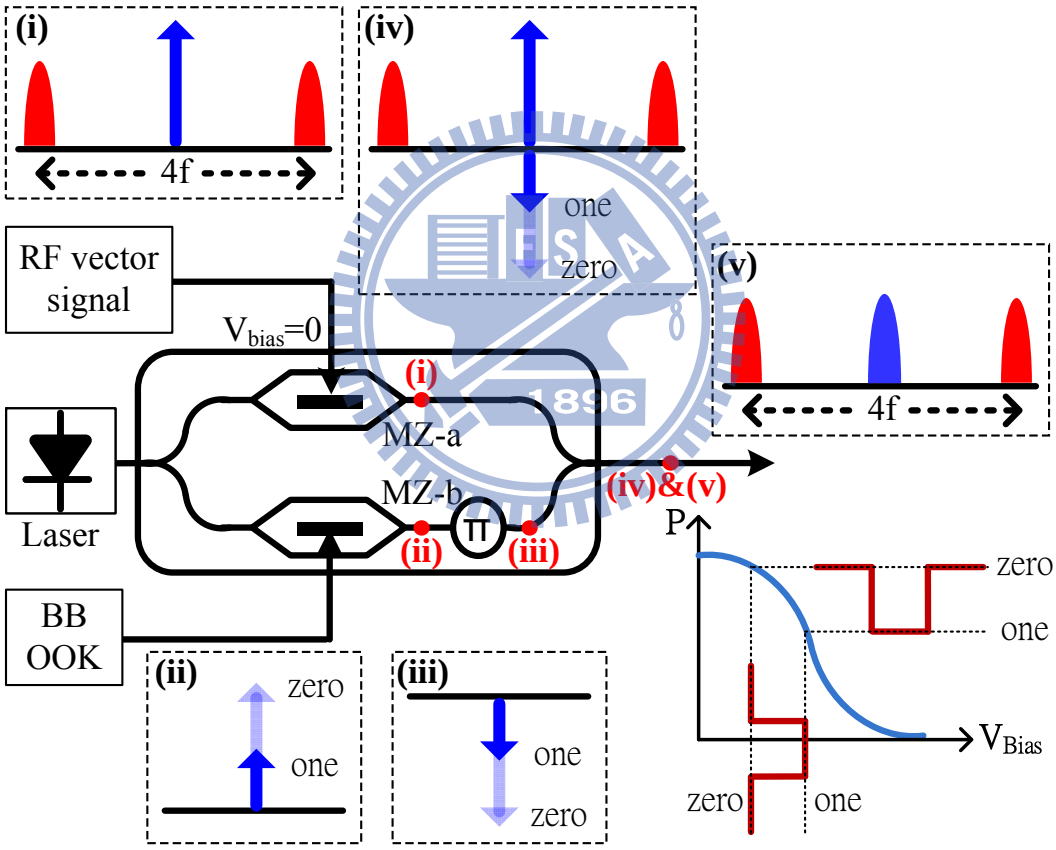

Figure 6-30 Concept of proposed hybrid access network system with frequency quadrupling.

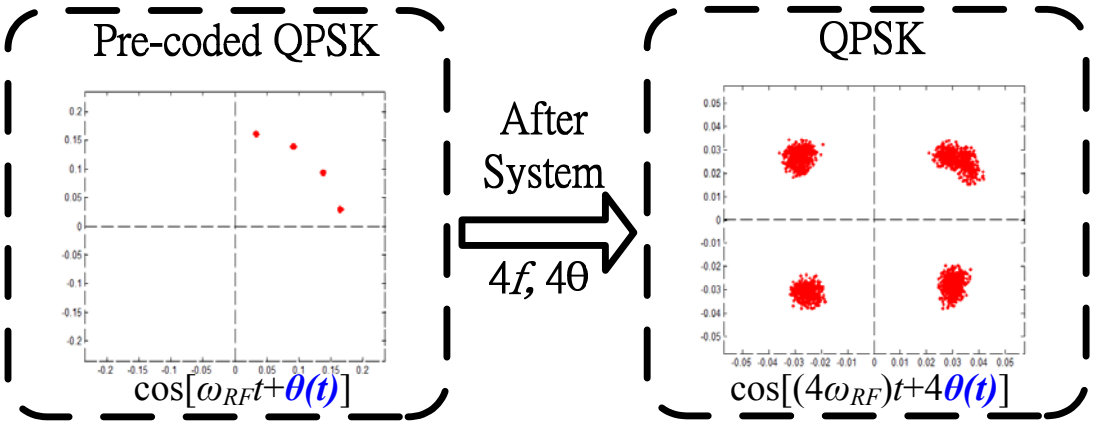

Figure 6-31 Concept of pre-coded method with frequency quadrupling.

6.3.6 Experimental Demonstration of Hybrid Access Network

Figure 6-32 depicts the experimental setup to verify the feasibility of the proposed hybrid access network system. A tunable laser with linewidth of 10kHz is utilized as the optical source. The laser output power is 3.8dBm center at 1550nm. The pre-coded 1.2Gbps 8PSK and 1.25Gbps QPSK signals at 2.5GHz are generated using a Tektronix® AWG7102 arbitrary waveform generator (AWG) with a Matlab® program. The sampling rate and digital-to-analog converter resolution of the AWG are 10GS/s and 8bits, respectively. After the signal from the AWG, the signal is up-converted to 15GHz using an electrical mixer with a 12.5GHz local oscillator signal and an electrical band pass filter that is centered at 15GHz with a 4GHz passband, as presented in Fig. 6-33. The generated RF signal is then applied to the MZ-a with bias at the full point. The modulation index (MI≜$V_{p\text{-}p}/2V_{\pi}$) is set at one to maximize the undesired sideband suppression ratios. The generation of optical carrier is suppressed by adjusting the bias voltage of the MZ-b.

Figure 6-34 shows the optimal optical spectrum, and the optical powers of the two desired second-order sidebands are 24dB higher than those of the other sidebands. The BB OOK signal is a 1.25Gbps pseudorandom binary sequence

(PRBS) signal with a word length of 2^{11}-1. Figure 6-34 also plots the optical spectra of the OOK signal. Second-order sidebands and optical carrier are clearly shown. Since the losses of the dual parallel MZM and 25km standard single-mode fiber are about 14dB and 5dB, respectively, the generated optical signal is amplified using an erbium-doped fiber amplifier (EDFA) to compensate for this loss. At the receiver end, an optical coupler is adopted to separate the optical power to deliver it to various applications. For wireless applications, the 60GHz 8PSK or QPSK signal is generated by square-law photo-detection (beating term of two second order sidebands) and down-converted to 5GHz using a 55GHz sinusoidal signal, as shown in Fig. 6-35. Five thousands symbols of 8PSK (QPSK) waveforms are captured using a digital scope at a 50GHz sampling rate for offline signal processing. The bit error rate (BER) is estimated from the error vector magnitude. For wireline applications, the optical signal is directly detected using a commercial 1.25-Gbps photo receiver and the performance is evaluated using a BER tester. For uplink applications, wavelength reuse is achieved via an RSOA, and a 1.25-Gbps OOK signal is directly applied to the RSOA. For the RSOA, the electrical bandwidth is 1.2GHz, the bias voltage is set at 4 Volts and the driving voltage of the OOK signal is 2 Volts. To reduce the effect of the original optical signal, the input power of the RSOA is set to -8dBm to ensure that the RSOA operates in the saturation region.

Since the wireless signal is more sensitive to the transmission environment than is the wireline signal, the system operators must be able to adjust freely the power ratio between the wireline and wireless services, according to geography. Figure 6-36 shows the optical spectrum, which indicates that the

relative intensity of the RF-modulated sidebands and BB-modulated carrier can be tuned easily by adjusting the power of the two input signals to the proposed system. The optical power ratio (OPR) is defined as

$$OPR(dB) = P_{BB}/P_{RF}, \quad (6\text{-}21)$$

where P_{BB} and P_{RF} are the power of the BB-modulated carrier and RF-modulated sidebands, respectively.

Figure 6-37 presents the sensitivity of the 1.2-Gbps 8PSK signal at -20dBm and that of the 1.25-Gbps OOK signal at -10dBm with different OPRs. Insets (i)-(vi) in Fig. 6-37 present the constellations (eye diagrams) for the 8PSK (OOK) signal with different OPRs. The performance tradeoff between the 8PSK and OOK signals is clearly observed.

Figure 6-38 and Fig. 6-39 show the BER curves for the RF and BB signals for back-to-back (BTB) and a transmission length of 25km. No significant receiver power penalties are observed following the transmission. Figure 6-38 also presents the tradeoff between the spectral efficiency and the receiving power sensitivity. The 8PSK signal has 1.5 times the spectral efficiency of the QPSK signal, but it has the worse receiver sensitivity. Whether the RF signal data format is 8PSK or QPSK does not significantly affect the sensitivity of the receiver to the OOK signal. Figure 6-40 plots the BER curves for the upstream signal. After transmission over 25-km standard single-mode fiber, the sensitivity penalty at a BER of 10^{-9} is less than 0.5dB. Figure 6-38, Fig. 6-39, and Fig. 6-40 also present the constellations of the RF 8PSK signals, the eye diagrams of the downstream OOK signals, and the eye diagrams of the upstream OOK signals, respectively. Following the transmission, all of the diagrams are observed without significant distortion.

A novel hybrid access network architecture was demonstrated using one dual parallel MZM; a 60GHz RF signal, a 1.25-Gbps downstream BB signal and a 1.25-Gbps upstream signal are transmitted on a single wavelength. The 1.2-Gbps 8PSK and 1.25-Gbps QPSK signals are produced by 15-GHz RF components of the transmitter by frequency quadrupling and pre-coded. After transmission over 25-km standard single-mode fiber, the power penalties for both RF and BB signals are negligible. The proposed system exhibits no RF fading; no narrow-band optical filter is required at the remote node to separate the RF and BB signals; uplink services are provided, and vector signals are carried. In summary, the proposed system provides a simple and cost-effective solution for hybrid access networks.

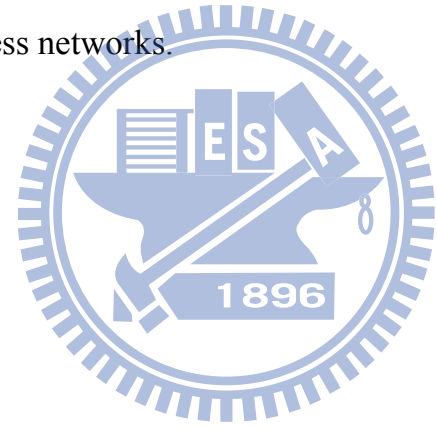

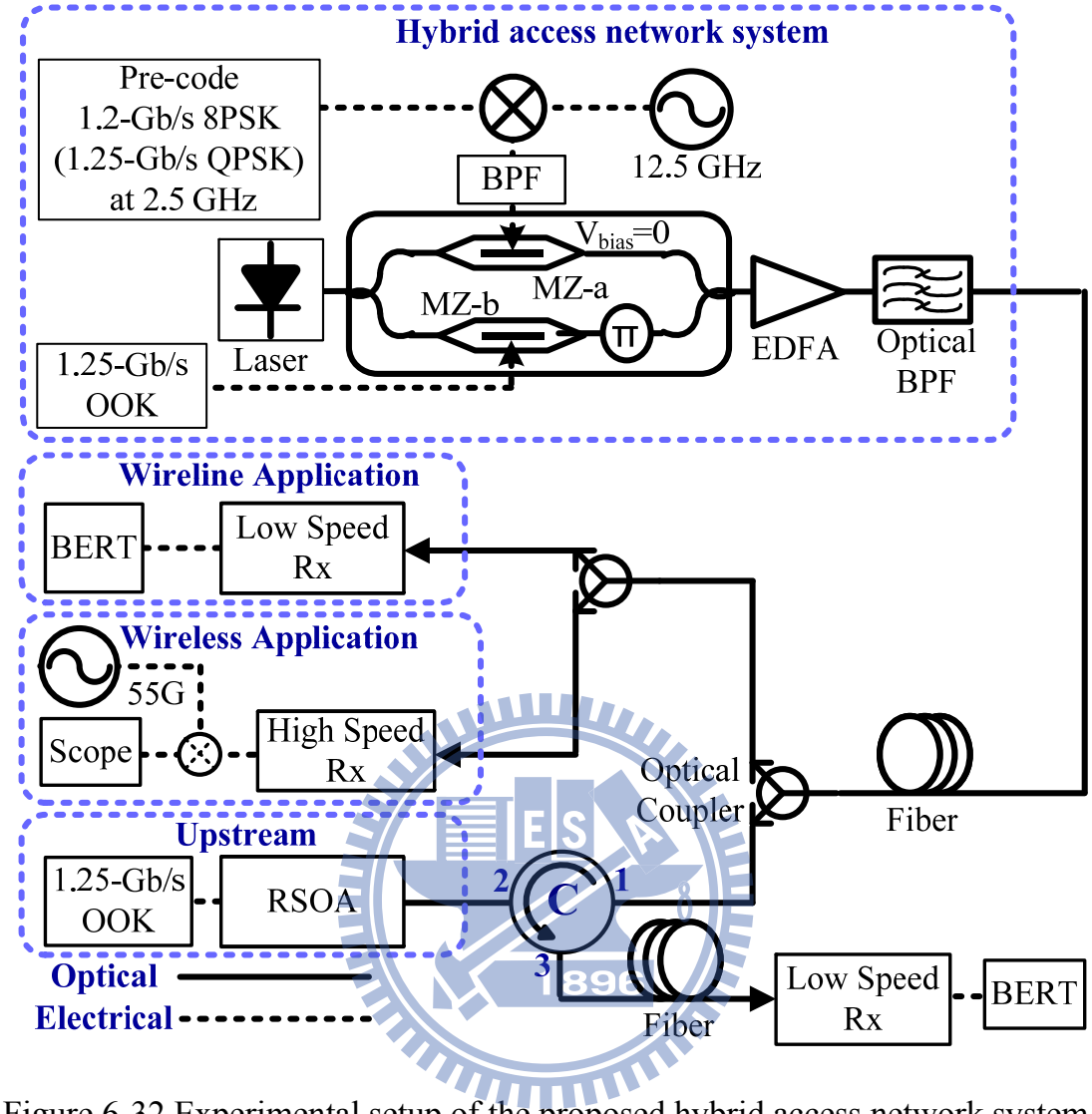

Figure 6-32 Experimental setup of the proposed hybrid access network system with frequency quadrupling. (RSOA: reflective semiconductor optical amplifier.)

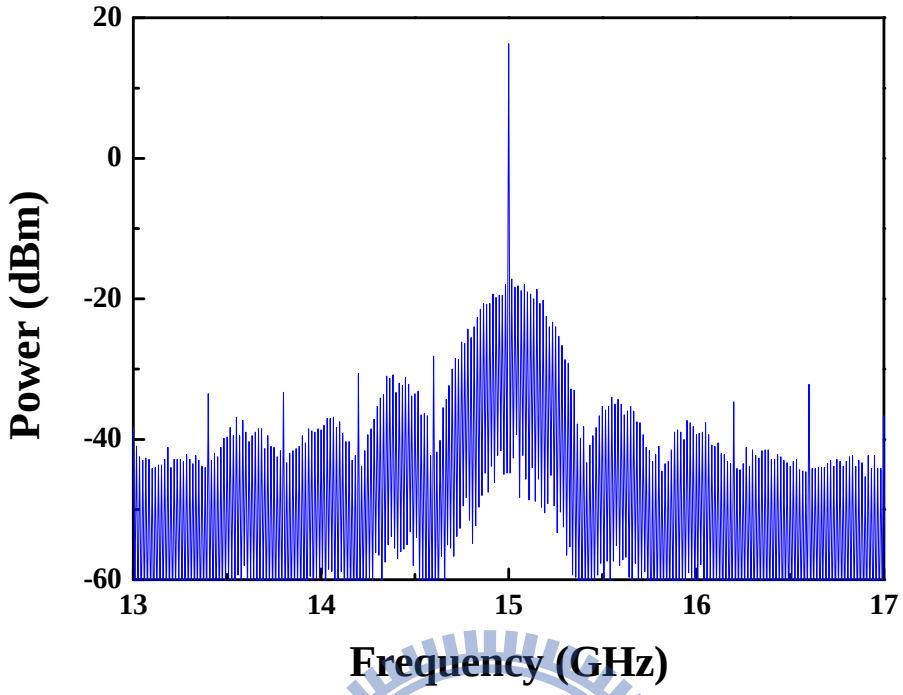

Figure 6-33 Electrical spectrum after up-conversion.

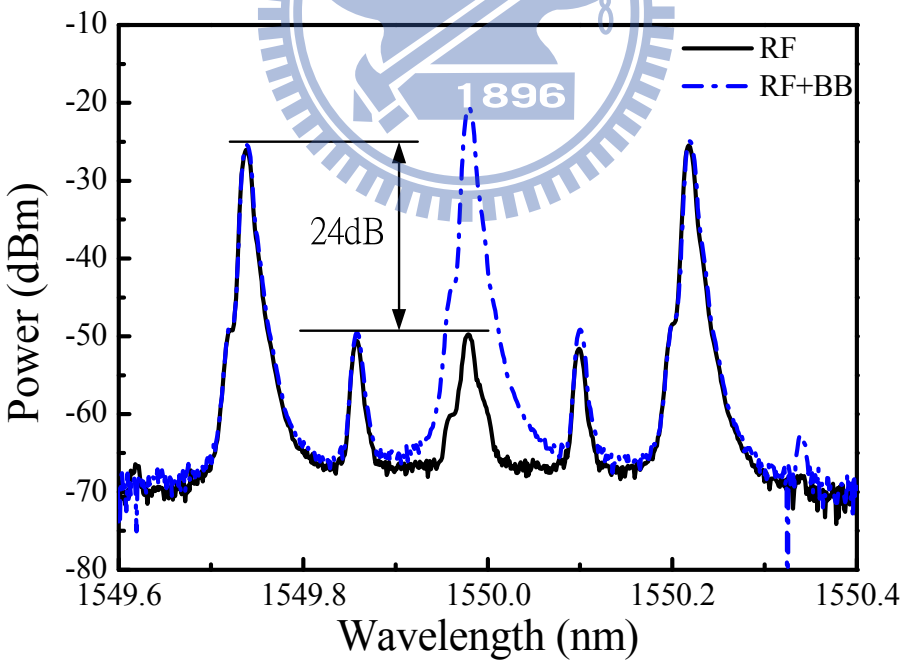

Figure 6-34 Optical spectra of the RF signal before and after combing.

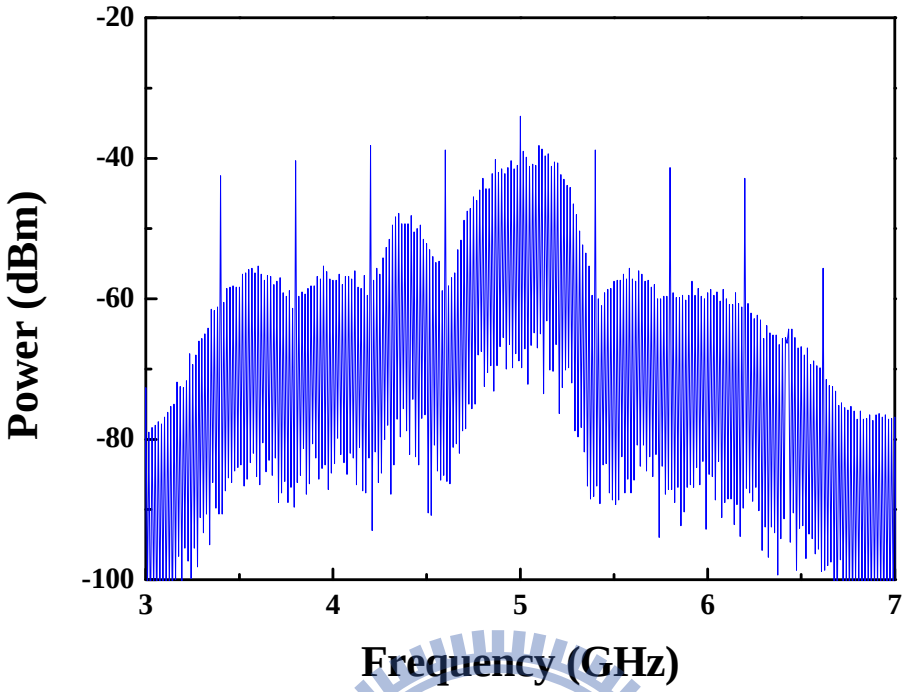

Figure 6-35 Electrical spectrum after down-conversion.

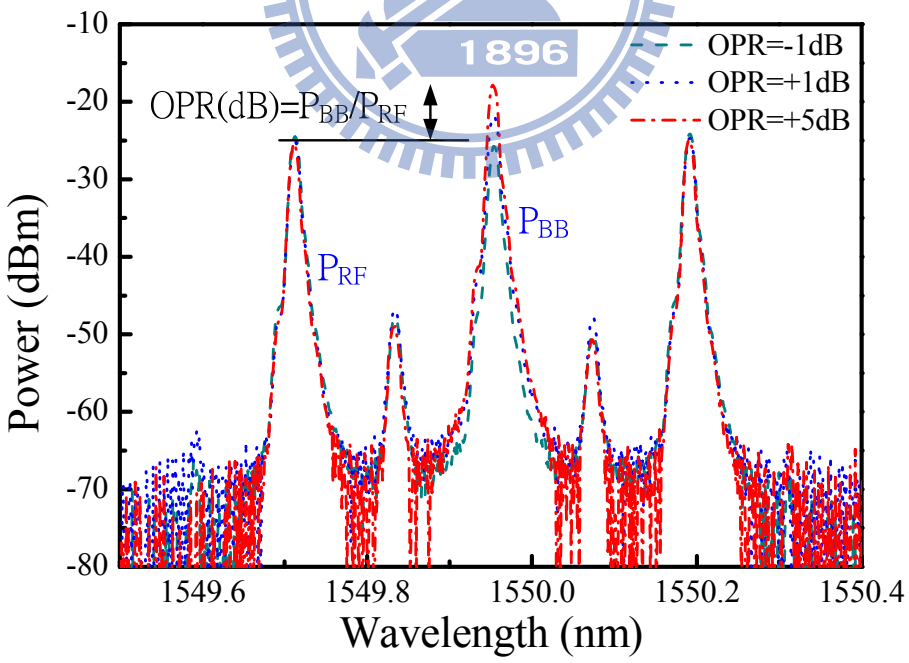

Figure 6-36 Optical spectra of different OPRs.

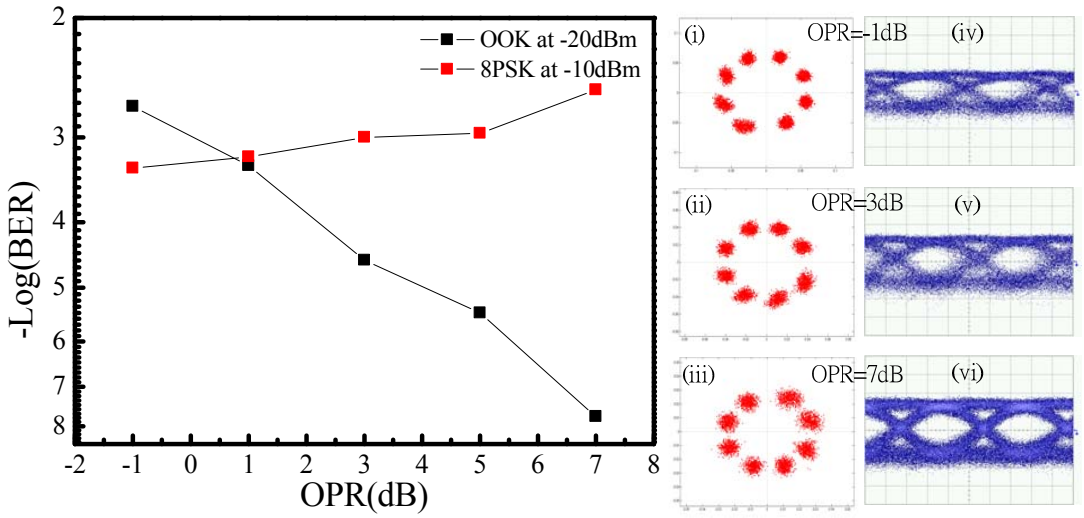

Figure 6-37 BB OOK and RF 8-PSK sensitivities with different OPRs.

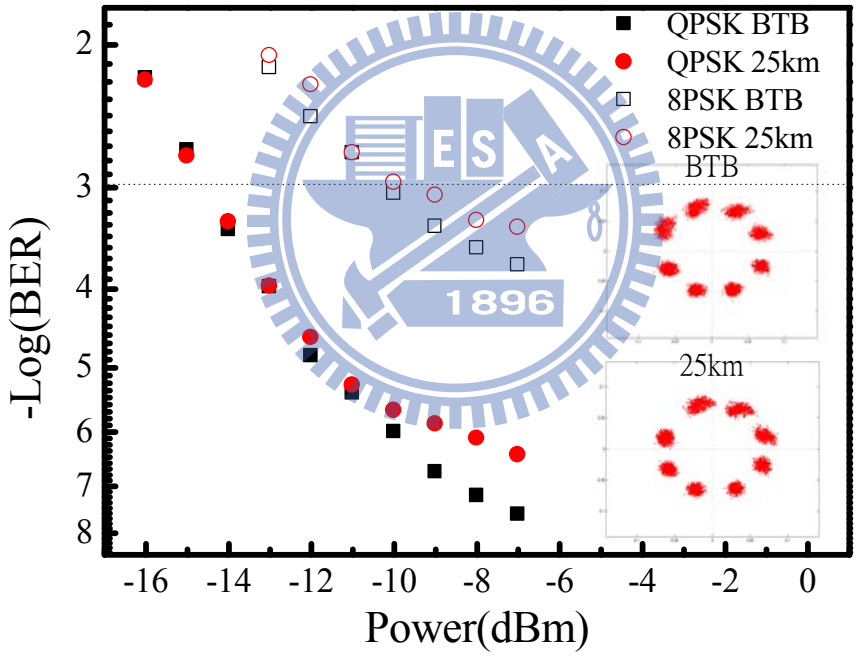

Figure 6-38 BER curves of RF PSK signal.

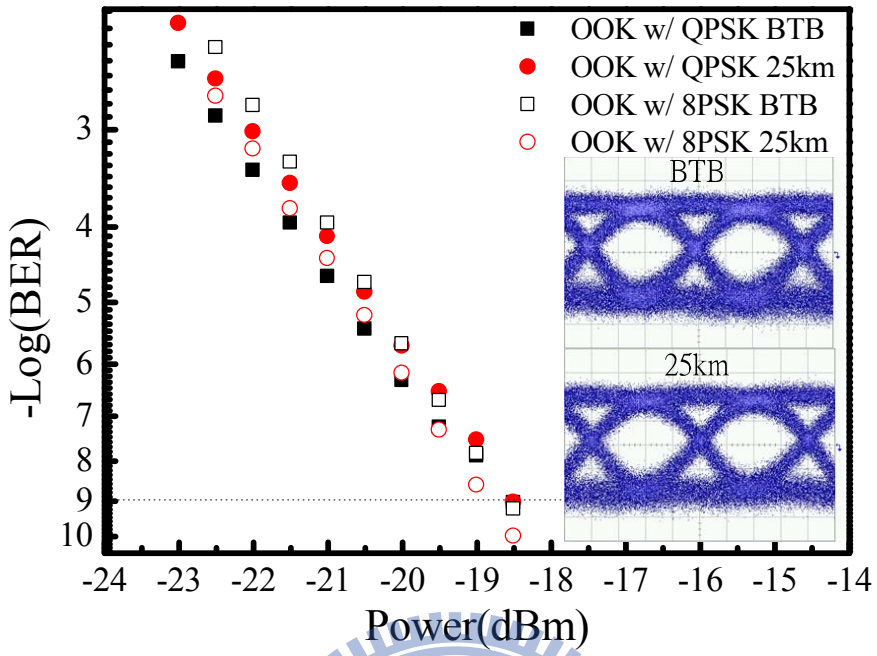

Figure 6-39 BER curves of BB OOK signal.

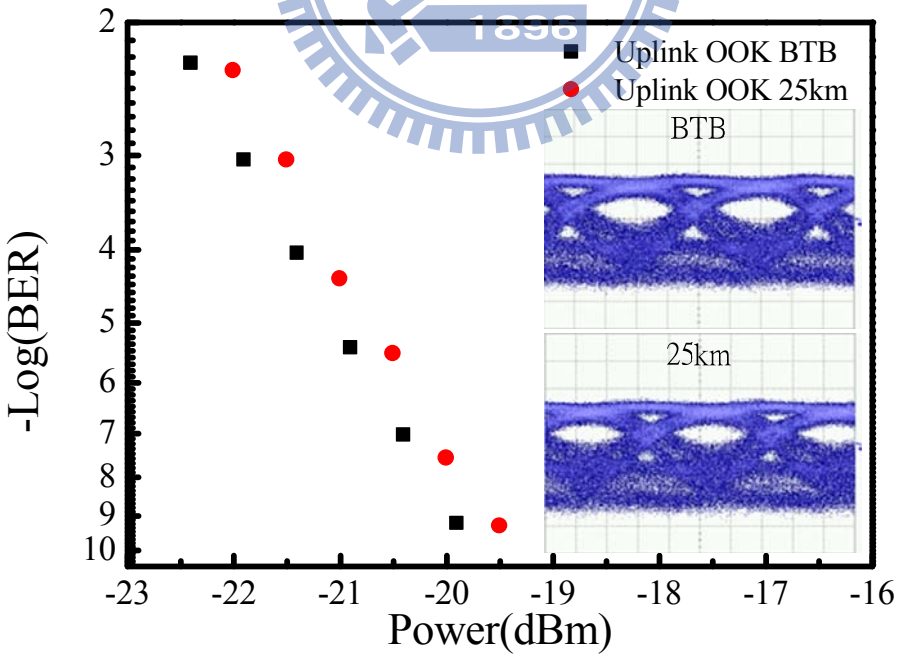

Figure 6-40 BER curves of uplink OOK signal.

6.4 Summary

The hybrid access network systems with frequency doubling and frequency quadrupling are proposed. For the system with frequency doubling technique, simultaneous generation and transmission of 60-GHz 2.5-Gbps QPSK and BB 1.25-Gbps OOK signals using a single-electrode MZM was experimentally demonstrated in this study. Frequency doubling and multi-level modulation format was achieved using DSB-CS modulation scheme with a novel signal pre-coded method. After transmission of 25-km standard single-mode fiber, 4-dB receiver power penalty which came from the timing walk-off between two optical sidebands was observed in the 60-GHz QPSK signal while a negligible receiver power penalty was observed in the BB OOK signal.

For the system with frequency quadrupling technique, the system was demonstrated using one dual parallel MZM; a 60GHz RF signal, a 1.25Gbps downstream BB signal and a 1.25Gbps upstream signal are transmitted on a single wavelength. The 1.2Gbps 8PSK and 1.25Gbps QPSK signals are produced by 15-GHz RF components of the transmitter by frequency quadrupling and pre-coded. After transmission over 25-km standard single-mode fiber, the power penalties for both RF and BB signals are negligible. Furthermore, wavelength reuse for uplink data transmission via a RSOA is also demonstrated with a penalty of less than 0.5 dB.

Two proposed systems exhibit no RF fading; no narrow-band optical filter is required at the remote node to separate the RF and BB signals, and vector signals are carried. Therefore, the proposed systems are compatible with the current PON system. In summary, the proposed systems provide a simple and

cost-effective solution for hybrid access networks.

Chapter 7

CONCLUSION

Four novel RoF systems for transporting and generating wideband signals at 60 GHz have discussed in this thesis. The first architecture demonstrates the feasibility of the generation of an RF direct-detection vector signal using optical I/Q up-conversion. The second system demonstrates a short-range RoF system employing a single-electrode MZM. Both systems transmit single-carrier and multi-carrier signal and employ several digital signal processing. The third and fourth systems present two simple hybrid access network architectures for generating and transmitting a 60GHz radio frequency (RF) phase-shift keying (PSK) signal with a baseband (BB) on-off keying (OOK) signal simultaneously.

Chapter 1 provides the review of wireless systems and the advantages of 60 GHz technology. The challenges of the transmission of the 60 GHz signal were discussed. Therefore, the 60 GHz RoF systems with digital signal processing attract great interests for future applications. Chapter 2 describes the basic ideas of 60 GHz RoF systems using external modulator. RoF system can be separated into an optical system and a wireless system. Optical system includes the optical transmitter, the optical channel and the optical receiver. The optical doubul-sideband (DSB) and DSB with carrier suppression (DSB-CS) modulation schemes were discussed. The properties of 60 GHz components and 60 GHz wireless channel were discussed. The impairments of 60 GHz RoF systems were also investigated in Chapter 2. The properties of digital signal modulation formats and digital signal processing were discussed in Chapter 3. The signal carrier, orthogonal frequency-division multiplexing

(OFDM), single-carrier frequency domain equalization (SC-FDE) and single-carrier frequency division multiple access (SC-FDMA) modulation formats were discussed. The digital signal processing for system impairments and concept of Multiple-Input Multiple-Output (MIMO) were also discussed.

A novel optical I/Q up-conversion RoF system for 60 GHz wireless applications was proposed in Chapter 4. The advantage of the proposed transmitter is that no electrical mixer is needed to generate RF signals. Therefore, I/Q data of RF signals are processed at baseband at the transmitter, which is independent of the carrier frequency of the generated RF signal. Theoretical analysis and experimental demonstration of this system were performed. The impact of the I/Q imbalance was also discussed. In order to achieve multi-standard operation, signal carrier and OFDM signals are utilized in the proposed system. The I/Q imbalance correction and adaptive loading algorithm are used to improve system performance. After employing adaptive bit-loading and I/Q imbalance compensation algorithm, a 32.38 Gb/s RoF signal at 60 GHz band signal is demonstrated. After transmission over 25-km standard single-mode fiber, negligible penalty is achieved without any dispersion compensation.

In Chapter 5, a simple 60GHz RoF system employing a single-electrode MZM was demonstrated. This system uses only one single-electrode Mach-Zehnder modulator (MZM) with bandwidth less than 35.5-GHz bandwidth. The impact of fiber chromatic dispersion and beat-noise on the performance of the RoF system are investigated by theoretical analysis and experimental demonstration. OFDM, SC-FDE and SC-FDMA signals generation and modulation techniques were developed. The RoF system was

successfully used to transport 40-Gb/s OFDM and SC-FDM signals at 60 GHz over more than 1 km of standard single-mode fiber and 4-m wireless distance. 2 x 2 MIMO technologies were also investigated to increase the data throughput within the 7 GHz band. A record wireless speed of 83 Gb/s with a wireless distance of 3 m was achieved in 7 GHz bandwidth with very high spectral efficiency of ~ 12 b/s/Hz. These results demonstrate the feasibility of using MIMO at 60 GHz for increasing the capacity.

The proposed optical and electrical up-conversion systems could achieve high-capacity. Both systems could support vector signal generation that helps compatible with wireless standard. The optical up-conversion system does not suffer RF-fading problem but complex system is needed for signal generation. Therefore, the optical up-conversion system is not suitable for short range RoF communication. The electrical up-conversion system is much simple than optical up-conversion system that would much suitable for short range RoF communication but system would suffer RF-fading problem that hard to support long range RoF communication. By the way, the optical I/Q modulator has much large bandwidth than electrical I/Q mixer. The optical up-conversion system suffers less I/Q imbalance issue than electrical system. The experimental results show that the total data throughput is improved 1Gbps for optical up-conversion system and 10Gbps for electrical up-conversion system. Therefore, the optical up-conversion system has much potential for large bandwidth communication in the future.

In Chapter 6, two novel multi-service hybrid access network systems for 60GHz wireless and wireline applications using frequency multiplication techniques were presented. One of architecture uses single-electrode MZM

with frequency doubling technology. The other architecture uses a dual-parallel MZM with frequency quadrupling technology. These two schemes employ a novel pre-coded method that is based on the digital signal processing. The proposed systems does not suffer from RF fading and needs no narrow-band optical filter at the remote node to separate the RF and baseband signals. A frequency multiplication method for RoF link is realized to reduce the bandwidth requirement of the transmitter. For the system with frequency doubling technique, simultaneous generation and transmission of 60-GHz 2.5-Gbps QPSK and BB 1.25-Gbps OOK signals using a single-electrode MZM was experimentally demonstrated in this study. After transmission of 25-km standard single-mode fiber, 4-dB receiver power penalty which came from the timing walk-off between two optical sidebands was observed in the 60-GHz QPSK signal while a negligible receiver power penalty was observed in the BB OOK signal. For the system with frequency quadrupling technique, the system was demonstrated using one dual-parallel MZM; a 60GHz RF signal, a 1.25Gbps downstream BB signal and a 1.25Gbps upstream signal were transmitted on a single wavelength. The 1.2Gbps 8PSK and 1.25Gbps QPSK signals are produced by 15-GHz RF components of the transmitter by frequency quadrupling and pre-coded. After transmission over 25-km standard single-mode fiber, the power penalties for both RF and BB signals are negligible. Furthermore, wavelength reuse for uplink data transmission via a RSOA is also demonstrated. Two proposed hybrid access network systems exhibit no RF fading; no narrow-band optical filter is required at the remote node to separate the RF and BB signals, and vector signals are carried. Therefore, the proposed systems are compatible with the current PON system.

REFERENCES

[1] H. H. Chen, J. F. Yeh, and N. Suehiro, "A multicarrier CDMA architecture based on orthogonal complementary codes for new generations of wideband wireless communications," *IEEE Communications Magazine,* vol. 39, pp. 126-135, Oct 2001.

[2] A. Ghosh, R. Ratasuk, B. Mondal, N. Mangalvedhe, and T. Thomas, "LTE-ADVANCED: NEXT-GENERATION WIRELESS BROADBAND TECHNOLOGY," *IEEE Wireless Communications,* vol. 17, pp. 10-22, Jun 2010.

[3] J. Kim, T. Daim, and T. Anderson, "A look into the future of wireless mobile communication technologies," *Technology Analysis & Strategic Management,* vol. 22, pp. 925-943, 2010.

[4] Q. H. Li, G. J. Li, W. Lee, M. I. Lee, D. Mazzarese, B. Clerckx, and Z. X. Li, "MIMO Techniques in WiMAX and LTE: A Feature Overview," *IEEE Communications Magazine,* vol. 48, pp. 86-92, May 2010.

[5] P. Mogensen, W. Na, I. Z. Kovacs, F. Frederiksen, A. Pokhariyal, K. I. Pedersen, T. Kolding, K. Hugl, and M. Kuusela, "LTE capacity compared to the Shannon bound," in *2007 IEEE 65th Vehicular Technology Conference, Vols 1-6*, ed, 2007, pp. 1234-1238.

[6] D. Tilson and K. Lyytinen, "The 3G transition: Changes in the US wireless industry," *Telecommunications Policy,* vol. 30, pp. 569-586, Nov-Dec 2006.

[7] International Telecommunication Union, “About Mobile Technology and IMT-2000,” http://www.itu.int/osg/spu/imt-2000/technology.html.

[8] J. Wells, “Faster than fiber: the future of multi-Gb/s wireless,” *IEEE Microwave Magn. New York*, vol. 10, pp. 104 – 112, May 2009.

[9] J. Wells, “Faster than fiber: The future of multi-G/s wireless”, *IEEE Microw. Magazine*, vol. 10, no. 3, pp. 104-122, 2009.

[10] J. Lee, M. C. Liu, and H. D. Wang, "A 75-GHz phase-locked loop in 90-nm CMOS technology," *IEEE Journal of Solid-State Circuits*, vol. 43, pp. 1414-1426, Jun 2008.

[11] S. K. Yong and C. C. Chong, "An overview of multigigabit wireless through millimeter wave technology: Potentials and technical challenges," *Eurasip Journal on Wireless Communications and Networking*, 2007.

[12] S. K. Yong, P. Xia, and A. Valdes Garcia, *60GHz Technology for Gbps WLAN and WPAN: From Theory to Practice*, John Wiley & Sons, 2011.

[13] P. F. M. Smulders, “60 GHZ radio: Prospects and future directions,” in Proc. *IEEE Benelux Chapter on Communications and Vehicular Technology*, Eindhoven, The Netherlands, 2003, pp. 1–8.

[14] R. Emrick, S. Franson, J. Holmes, B. Bosco, and S. Rockwell, “Technology for emerging commercial applications at millimeter-wave frequencies,” *in Proc. IEEE/ACES Int. Conf. Wireless Communications and Applied Computational Electromagnetics*, 2005, pp. 425–429.

[15] B. Razavi, “Gadgets gab at 60 GHZ,” *IEEE Spectrum*, vol. 45, no. 2, pp. 46-58, Feb 2008.

[16] C. Park, and T. S. Rappaport, “Short-range wireless communications for Next-Generation Networks: UWB, 60 GHZ millimeter-wave WPAN, and ZigBee,” *IEEE Wireless Communications*, vol. 14, no.4, pp. 70-78, 2007.

[17] P. Smulders, “Exploiting the 60 GHZ band for local wireless multimedia access: prospects and future directions,” *IEEE Comm. Magn.*, vol. 40, no. 1, pp. 140-146, 2002.

[18] Y. X. Guo, B. Luo, C.S. Park, L. C. Ong, M.-T. Zhou, and S. Kato, “60

GHz radio-over-fiber for Gbps transmission," *in Proc. Global Symposium on Millimeter Waves (GSMM)*, Invited paper, 2008.

[19] C. S. Park, Y. X. Guo, L. C. Ong, Y. K. Yeo, Y. X. Wang, M. T. Zhou, and H. Harada, "Application of an electroabsorption modulator in radio-over-fiber networks Invited," *J. of Optical Networking*, vol. 8, pp. 146-155, Feb 2009.

[20] T. Taniguchi, N. Sakurai, K. Kumozaki, and T. Imai, "Full-Duplex 1.0 Gbit/s Data Transmission Over 60 GHz Radio-on-Fiber Access System Based on the Loop-Back Optical Heterodyne Technique," *IEEE J. Lightw. Technol.*, vol. 26, pp. 1765-1776, Jul-Aug 2008.

[21] J. H. Seo, C. S. Choi, Y. S. Kang, Y. D. Chung, J. Kim, and W. Y. Choi, "SOA-EAM frequency up/down-converters for 60-GHz bi-directional radio-on-fiber systems," *IEEE Trans. on Microw. Theory and Tech.*, vol. 54, pp. 959-966, Feb 2006.

[22] P. T. Shih, A. Ng'oma, C-T. Lin, F. Annunziata, J. Chen, J. George, M. Sauer, and S. Chi, "2×21 Gbps Symmetrical Full-Duplex Transmission of OFDM Wireless Signals over a Bidirectional IMDD Radio-over-Fiber System at 60 GHz," 36nd European Conference on Optical Communication (ECOC 2010), Th.9.B.4, Torino, Italy, September 19-23, 2010.

[23] M. Weiß, M. Huchard, A. Stöhr, B. Charbonnier, S. Fedderwitz, and D. S. Jäger, "60-GHz photonic millimeter-wave link for short- to medium-range wireless transmission up to 12.5 Gb/s," *IEEE J. Lightw. Technol.*, vol. 26, no. 15, pp. 2424-2429, Aug. 1, 2008.

[24] J. J. V. Olmos, T. Kuri, T. Sono, K. Tamura, H. Toda, and K. Kitayama, "Reconfigurable 2.5-Gb/s baseband and 60-GHz (155-Mb/s) millimeter-waveband radio-over-fiber access network," *IEEE J. Lightw. Technol.*, vol. 26, no. 15, pp. 2506-2512, Aug. 1, 2008.

[25] M. Huchard, M. Weiß, A. Pizzinat, S. Meyer, P. Guignard, and B.

Charbonnier, “Ultra-broadband wireless home network based on 60-GHz WPAN cells interconnected via RoF,” *IEEE J. Lightw. Technol.*, vol. 26, no. 15, pp. 2364-2372, Aug. 1, 2008.

[26] G. H. Nguyen, B. Cabon, and Y. Le Guennec, "Generation of 60-GHz MB-OFDM Signal-Over-Fiber by Up-Conversion Using Cascaded External Modulators," *IEEE J. Lightw. Technol.*, vol. 27, pp. 1496-1502, Jun 2009.

[27] W. K. Kim, S. W. Kwon, W. J. Jeong, G. S. Son, K. H. Lee, W. Y. Choi, W. S. Yang, H. M. Lee, and H. Y. Lee, "Integrated optical modulator for signal up-conversion over radio-on-fiber link," *Opt. Express*, vol. 17, pp. 2638-2645, Feb 2009.

[28] C. S. Park, Y. Guo, Y. K. Yeo, Y. Wang, L. C. Ong, and S. Kato, "Fiber-optic 60-GHz wireless downlink using cross-absorption modulation in an EAM," *IEEE Photon. Technol. Lett.*, vol. 20, pp. 557-559, Mar-Apr 2008.

[29] A. Ng'oma, M. Sauer, D. Thelen, and J. George, "Data Throughput Tripling by Feed-Forward Equalization and Photonic QPSK in a 7 Gbps Single-Carrier RoF Link at 60 GHz," *IEEE in International Topical Meeting on Microwave Photonics/2008 Asia-Pacific Microwave Photonics Conference*, Gold Coast, AUSTRALIA, 2008, pp. 213-216.

[30] M. Mohamed, X. P. Zhang, B. Hraimel, and K. Wu, "Frequency sixupler for millimeter-wave over fiber systems," *Opt. Express*, vol. 16, pp. 10141-10151, Jul 2008.

[31] Y. Le Guennec, G. Maury, J. P. Yao, and B. Cabon, "New optical microwave up-conversion solution in radio-over-fiber networks for 60-GHz wireless applications," *IEEE J. Lightw. Technol.*, vol. 24, pp. 1277-1282, Mar 2006.

[32] A. Ng’oma, M. Sauer, F. Annunziata, W. J. Jiang, C. T. Lin, J. Chen, P. T. Shi, and S. Chi, “14 Gbps 60 GHz RoF Link Employing a Simple

System Architecture and OFDM Modulation," *in Proc of IEEE MWP 2009 Conf. 2009*, Valencia, Spain, Oct. 2009.

[33] P. T. Shih, C. T. Lin, W. J. Jiang, Y. H. Chen, J. Chen, and S. Chi, "Full duplex 60-GHz RoF link employing tandem single sideband modulation scheme and high spectral efficiency modulation format," *Opt. Express*, vol. 17, no.22, pp. 19501-19508, Oct. 26, 2009.

[34] P. T. Shih, C. T. Lin , H. S. Huang, W. J. Jiang, J. Chen, A. Ng'oma, M. Sauer, and S. Chi, "13.75-Gb/s OFDM Signal Generation for 60-GHz RoF System within 7-GHz License-Free Band via Frequency Sextupling," *in Proc. European Conf. on Optical Communication., (ECOC 2009)*, paper 4.5.4, Sep., 2009.

[35] C. T. Lin, E. Z. Wong, W. J. Jiang, P. T. Shih, J. Chen, and S. Chi, "28-Gb/s 16-QAM OFDM Radio-over-Fiber System within 7-GHz License-Free Band at 60 GHz Employing All-Optical Up-Conversion" *in Proc. Conf. on Lasers and Electro-Optics (CLEO 2009)*, paper CPDA8, May. 31, 2009.

[36] H. Xu, V. Kukshya and T. S. Rappaport, "Spatial and temporal characteristics of 60 GHz indoor channels," *IEEE J. Select. Areas Commun.*, vol. 20, no. 3, pp. 620-630, Apr., 2002.

[37] A. M. J. Koonen, and M. García Larrodé, "Radio-Over-MMF Techniques—Part II: Microwave to Millimeter-Wave Systems," *J. Lightw. Technol.*, vol. 26, no. 15, pp. 2396–2408, Aug. 1, 2008.

[38] M. Sauer, A. Kobyakov, J. George, "Radio over fiber for picocellular network architectures," *J. Lightw. Technol.*, vol. 25, no. 11, pp. 3301-3320, 2007.

[39] M. Weiß, M. Huchard, A. Stöhr, B. Charbonnier, S. Fedderwitz, and D. S. Jäger, "60 GHZ photonic millimeter-wave link for short- to mediumrange wireless transmission up to 12.5 Gb/s," *J. Lightw. Technol.*, vol. 26, no. 15, pp. 2424–2429, Aug. 1, 2008.

[40] P. Lombard, Y. L. Guennec, G. Maury, E. Novakov, and B. Cabon, “Optical Distribution and Upconversion of MB-OFDM in Ultrawide-Band-Over-Fiber Systems,” *J. Lightw. Technol.*, vol. 27, no. 9, pp. 1072-1078, May 2009.

[41] F. Xiong, *Digital Modulation Techniques,* 2nd ed. London: Artech House, INC., 2006.

[42] J. Yu, Z. Jia, L. Yi, G. K. Chang, and T. Wang, “Optical millimeter wave generation or up-conversion using external modulators,” *IEEE Photon. Technol. Lett.*, vol. 18, pp. 265–267, 2006.

[43] Saleh Bahaa, E. A., and Teich, M. C. *Fundamentals of Photonics, Second Edition.* John Wiley and Sons, Inc., Hoboken, New Jersey, 2007.

[44] Wooten, E. L., Kissa, K. M., Yi-Yan, A., et al. A Review of Lithium Niobate Modulators for Fiber-Optic Communications Systems. *IEEE Journal of Selected Topics in Quantum Electronics*, Vol. 6, Issue 1, pp. 69-82, January/February, 2000.

[45] Kaminow, I. P., and Koch, T. L. *Optical Fiber Telecommunications, IIIB*. Academic Press, 1997.

[46] Korenev, B. G. *Bessel Functions and their Applications*. Taylor & Francis, 2002.

[47] Agrawal, G. P. *Fiber-Optic Communication Systems Third Edition.* John Wiley& Sons, Inc., 2002.

[48] Hyung G. Myung and David J. Goodman *Single Carrier FDMA: A New Air Interface for Long Term Evolution.* John Wiley& Sons, Inc., 2008.

[49] Agilent 8 Hints for Making and Interpreting EVM Measurements, Agilent Technologies, May 2005 [Online]. Available: http://cp.literature.agilent.com/litweb/pdf/5989-3144EN.pdf

[50] J. Wang and J. M. Kahn, "Performance of electrical equalizers in

optically amplified OOK and DPSK systems," *IEEE Photonics Technology Letters*, vol. 16, pp. 1397-1399, May 2004.

[51] C. M. Xia and W. Rosenkranz, "Nonlinear electrical equalization for different modulation formats with optical filtering," *IEEE Journal of Lightwave Technology*, vol. 25, pp. 996-1001, Apr 2007.

[52] M. Bohn and C. M. Xia, "Electrical and optical equalization strategies in direct detected high-speed transmission systems," *International Journal of Electronics and Communications*, vol. 63, pp. 526-532, 2009.

[53] A. J. Lowery, L. B. Du, and J. Armstrong, "Performance of optical OFDM in ultralong-haul WDM lightwave systems," *IEEE J. Lightw. Technol.*, vol. 25, no. 1, pp. 131-138, Jan, 2007.

[54] S. L. Jansen, I. Morita, T. C. W. Schenk, and H. Tanaka, "121.9-Gb/s PDM-OFDM Transmission With 2-b/s/Hz Spectral Efficiency Over 1000 km of SSMF," *IEEE J. Lightw. Technol.*, vol. 27, pp. 177-188, Jan-Feb 2009.

[55] Q. Yang, Y. Tang, Y. Ma, and William Shieh, "Experimental demonstration and numerical simulation of 107-Gb/s high spectral efficiency coherent optical OFDM," *IEEE J. Lightw. Technol.*, vol. 27, no. 3, pp. 168-176, Feb. 1, 2009.

[56] W. Shieh, "High spectral efficiency coherent optical OFDM for 1 Tb/s ethernet transport," *in Proc. Optical Fiber Communication Conf. (OFC 2009)*, OWW1, Mar., 2009.

[57] D. Falconer, S. L. Ariyavisitakul, A. Benyamin-Seeyar, and B. Eidson, " Frequency domain equalization for single-carrier broadband wireless systems," *IEEE Comm. Magn.*, vol. 40, pp. 58–66, 2002.

[58] Andreas Czylwik, "Comparison between adaptive OFDM and single carrier modulation with frequency domain equalization," *Proc. Vehicular Technology Conference*, pp. 865–869, 1997.

[59] S. Beyme and C. Leung, "Efficient computation of DFT of Zadoff-Chu sequences," *Electron. Lett.*, pp. 461–463, 2009.

[60] Balachandran, K., Calin, D., Cheng, F-C., et al., "Design and Analysis of an IEEE 802.16e-based OFDMA Communication System," *Bell Labs Tech. Jour.*, vol. 11, no. 4, Mar. 2007, pp. 53–73.

[61] S. Srikanth, V. Kumaran, C. Manikandan et al., "Orthogonal Frequency Division Multiple Access: is it the multiple access system of the future?," *AU-KBC Research Center*, Anna University, India.

[62] Das, S., Li, S., Monogioudis, P., et al., "EV-DO Revision C: Evolution of the cdma2000 Data Optimized System to Higher Spectral Efficiencies and Enhanced Services," *Bell Labs Tech. Jour.*, vol. 11, no. 4, Mar. 2007, pp. 5–24.

[63] Sorger, U., De Broeck, I., and Schnell, M., "Interleaved FDMA - A New Spread-Spectrum Multiple-Access Scheme," *Proc. IEEE ICC '98, Atlanta*, GA, Jun. 1998, pp. 1013–1017.

[64] Frank, T., Klein, A., and Costa, E., "IFDMA: A Scheme Combining the Advantages of OFDMA and CDMA," *IEEE Wireless Commun.*, vol. 14, no. 3, June 2007, pp. 9–17.

[65] S. Daumont, B. Rihawi, and Y. Lout, "Root-raised cosine filter influences on PAPR distribution of single-carrier signals," *in Proc. IEEE ISCCSP'08*, pp. 841-845, Mar. 2008.

[66] H. G. Myung, J. Lim, and D. J. Goodman, "Peak-to-average power ratio of single carrier FDMA signals with pulse shaping," *in Proc. IEEE PIMRC'06*, Sept. 2006.

[67] J. Campello et al., "Optimal discrete bit loading for multicarrier modulation systems," *in Proc. ISIT'98*, pp. 193, 1998.

[68] T. N. Duong, N. Genay, M. Ouzzif, J. Le Masson, B. Charbonnier, P. Chanclou, and J. C. Simon, "Adaptive Loading Algorithm Implemented

in AMOOFDM for NG-PON System Integrating Cost-Effective and Low-Bandwidth Optical Devices," *IEEE Photonics Technology Letters*, vol. 21, pp. 790-792, May-Jun 2009.

[69] A. Garcia-Armada, "SNR gap approximation for M-PSK-based bit loading," *IEEE Transactions on Wireless Communications*, vol. 5, pp. 57-60, Jan 2006.

[70] I. Fatadin, S. J. Savory, and D. Ives, "Compensation of Quadrature Imbalance in an Optical QPSK Coherent Receiver," *IEEE Photonics Technology Letters*, vol. 20, pp. 1733-1735, Sep-Oct 2008.

[71] A. Tarighat, R. Bagheri, and A. H. Sayed, "Compensation schemes and performance analysis of IQ imbalances in OFDM receivers," *IEEE Transactions on Signal Processing*, vol. 53, pp. 3257-3268, Aug 2005.

[72] A. Tarighat and A. H. Sayed, "MIMO OFDM receivers for systems with IQ imbalances," *IEEE Transactions on Signal Processing*, vol. 53, pp. 3583-3596, Sep 2005.

[73] F. Yan, W. P. Zhu, and M. O. Ahmad, "Carrier frequency offset estimation and I/Q imbalance compensation for OFDM systems," *Eurasip Journal on Advances in Signal Processing*, 2007.

[74] H. Lin and K. Yamashita, "Subcarrier Allocation Based Compensation for Carrier Frequency Offset and I/Q Imbalances in OFDM Systems," *IEEE Transactions on Wireless Communications*, vol. 8, pp. 18-23, Jan 2009.

[75] W. R. Peng, B. Zhang, X. X. Wu, K. M. Feng, A. E. Willner, and S. Chi, "Compensation for I/Q Imbalances and Bias Deviation of the Mach-Zehnder Modulators in Direct-Detected Optical OFDM Systems," *IEEE Photonics Technology Letters*, vol. 21, pp. 103-105, Jan-Feb 2009.

[76] Q. H. Spencer, A. Lee Swindlehurst and Martin Haardt, “Zero-Forcing Methods for Downlink Spatial Multiplexing in Multiuser MIMO Channels,” *in IEEE Trans. Sig. Proc.*, vol. 52, no. 2, pp. 461-471, 2004.

[77] G. G. Raleigh and J. M. Cioffi, “Spatio-temporal coding for wireless communication," *IEEE Trans. Comm.*, vol. 46, no. 3, pp. 357-366, 1998.

[78] C. K. Weng, Y. M. Lin, and W. I. Way, “Radio-over-fiber 16-QAM, 100-km transmission at 5 Gb/s using DSB-SC transmitter and remote heterodyne detection,” *IEEE J. Lightw. Technol.*, vol. 26, pp. 643-653, 2008.

[79] P. Candelas, “Optically generated electrical-modulation formats in digital-microwave link applications,” *IEEE J. Lightw. Technol.*, vol. 21, pp. 496-499, 2003.

[80] T. Ye, C. Yan, Q. Chang, and Y. Su, “An optical (Q)PSK-RF-signal transmitter based on two cascaded Mach-Zehnder modulators,” *Optics Communications*, vol. 18, pp. 4648-4652, 2008.

[81] Y. Zhang, K. Xu, J. Li, J. Wu, X. Hong, and J. Lin, “Photonic DPASK/QAM signal generation at microwave/millimeter-wave band based on an electro-optic phase modulator,” *Opt. Lett.*, vol. 33, pp. 2332-2334, 2008.

[82] R. Sambaraju, V. Polo, J. Luis Corral, and J. Marti, “Ten gigabits per second 16-level quadrature amplitude modulated millimeter-wave carrier generation using dual-drive Mach-Zehnder modulators incorporated photonic-vector modulator,” *Opt. Lett.*, vol. 33, pp. 1833-1835, 2008.

[83] Y. Zhang, K. Xu, R. Zhu, J. Q. Li, J. Wu, X. B. Hong, and J. T. Lin, “Photonic Generation of M-QAM/M-ASK Signals at Microwave/Millimeter-Wave Band Using Dual-Drive Mach-Zehnder Modulators With Unequal Amplitudes,” *IEEE J. Lightw. Technol.*, vol. 26, pp. 2604-2610, 2008.

[84] C. T. Lin, Y. M. Lin, J. Chen, S. P. Dai, P. T. Shih, P. C. Peng, and S. Chi, “Optical direct-detection OFDM signal generation for radio-over-fiber link using frequency doubling scheme with carrier suppression,” *OSA Opt. Express*, vol. 16, no.9, pp. 6056-6063, Apr. 28, 2008.

[85] C. T. Lin, P. T. Shih, J. Chen, W. Q. Xue, P. C. Peng, and S. Chi, “Optical millimeter-wave signal generation using frequency quadrupling technique and no optical filtering,” IEEE Photon. Technol. Lett., vol. 20, no. 12, pp. 1027-1029, Jun. 15, 2008.

[86] C. Lim, M. Attygalle, A. Nirmalathas, D. Novak, and R. Waterhouse, “Analysis of optical carrier-to-sideband ratio for improving transmission performance in fiber-radio links,” IEEE Trans. on Microw. Theory and Tech., vol. 54, no. 5, pp. 2181-2187, May, 2006.

[87] A. Flatman, "*In-premises optical fibre installed base analysis to 2007*.", IEEE 802.3 Gigabit Ethernet over FDDI-Grade Fiber Study group, Orlando, FL, USA, 2004.

[88] M. Jiang, G. Yue, and S. Rangarajan, “ MIMO transmission with rank adaptation for multi-gigabit 60 GHz wireless,” *in Proc. GLOBECOM 2010, IEEE Global Telecommunications Conf.*, pp. 1-5, Dec. 2010.

[89] S. H. Fan, H. C. Chien, Y. T. Hsueh, A. Chowdhury, J. Yu, and G. K. Chang, “Simultaneous Transmission of Wireless and Wireline Services Using a Single 60-GHz Radio-Over-Fiber Channel by Coherent Subcarrier Modulation,” *IEEE Photon. Technol. Lett.*, vol. 21, no. 16, pp. 1127 – 1129, Aug. 15, 2009.

[90] Q. J. Chang, H. Y. Fu, and Y. K. Su, "Simultaneous generation and transmission of downstream multiband signals and upstream data in a bidirectional radio-over-fiber system," *IEEE Photonics Technology Letters*, vol. 20, pp. 181-183, Jan-Feb 2008.

[91] P. T. Shih, C. T. Lin, W. J. Jiang, Y. H. Chen, Y. H. Chen, J. Chen, and S. Chi, “Hybrid access network integrated with wireless multi-level vector and wired baseband signals using frequency doubling and no optical filtering,” *IEEE Photon. Technol. Lett.*, vol. 21, no. 13, pp. 857 – 859, Jul. 1, 2009.

[92] J. Ma, J. Yu, C. Yu, X. Xin, J. Zeng, and L. Chen, “Fiber dispersion influence on transmission of the optical millimeter-waves generated using LN-MZM intensity modulation,” *IEEE J. Lightw. Technol.*, vol. 25, no. 11, pp. 3244–3256, Nov. 2007.

[93] C. T. Lin, P. T. Shih, J. Chen, W. J. Jiang, S. P. Dai, P. C. Peng, Y. L. Ho, and S. Chi, "Optical Millimeter-Wave Up-Conversion Employing Frequency Quadrupling Without Optical Filtering," *IEEE Transactions on Microwave Theory and Techniques*, vol. 57, pp. 2084-2092, Aug 2009.

[94] M. Mohamed, X. P. Zhang, B. Hraimel, and K. Wu, "Analysis of frequency quadrupling using a single Mach-Zehnder modulator for millimeter-wave generation and distribution over fiber systems," Optics Express, vol. 16, pp. 10786-10802, Jul 2008.

[95] C. T. Lin, P. T. Shih, W. J. Jiang, E. Z. Wong, J. Chen, and S. Chi, “Photonic Vector Signal Generation at Microwave/Millimeter-wave Bands Employing Optical Frequency Quadrupling Scheme,” *Opt. Lett.*, vol. 34, no. 14, pp. 2171–2173, Jul. 15, 2009.

[96] *Forward Error Correction for High Bit Rate DWDM Submarine Systems*, Telecommunication Standardization Sector, International Telecommunication Union, G. 975.1, Feb. 2004

CURRICULUM VITAE

Wen-Jr Jiang

Institute of Electro-Optical Engineering and Department of Photonics,
National Chiao-Tung University,
1001 Ta Hsueh Rd., Hsin-Chu, Taiwan, 300
Phone: 886-3-5712121 ext: 52992
E-mail: jiang.eo97g@nctu.edu.tw

Education

- Ph.D., Electro-Optical Engineering, National Chiao Tung University, Taiwan.
  (Aug. 2008 ~ July 2012)
  Advisors: **Prof. Jason (Jyehong) Chen and Assistant Prof. Chun-Ting Lin**

- M.S., Display Institute, National Chiao Tung University, Taiwan.
  (Sept. 2006 ~ July 2008)
  Advisor: **Prof. Jason (Jyehong) Chen**

- B.S., Department of Electrophysics, National Chiao Tung University, Taiwan.
  (Sept. 2002 ~ Jun. 2006)

Professional Skills

- Radio-over-fiber communication system
- 60-GHz wireless communication
- Digital modulation format
- Digital signal processing
- Optical millimeter-wave signal generation
- Photonic vector signal generation
- Hybrid access networks

PUBLICATION LIST

International Journals (SCI Journal Paper)

1. ***W. J. Jiang***, C. T. Lin, C. H. Ho, C. C. Wei, P. T. Shih, J. Chen, and S. Chi, "Photonic Vector Signal Generation Employing an Novel Optical Direct-Detection I/Q Up-Conversion," ***OSA Optics Letters***, vol.35, No. 23, pp. 4069-4071, Dec. 1, 2010.

2. ***W. J. Jiang***, C. T. Lin, A. Ng'oma, P. T. Shih, J. Chen, M. Sauer, F. Annunziata, and S. Chi, "Simple 14 Gbps Short-Range Radio-over-Fiber System Employing a Single-Electrode MZM for 60 GHz Wireless Applications," ***IEEE/OSA Journal of Lightwave Technology***, vol. 28, No. 16, pp. 2238-2246, August 15, 2010. **(Invited Paper)**

3. ***W. J. Jiang***, C. T. Lin, P. T. Shih, L. Y. Wang He, J. Chen, and S. Chi, "Simultaneous Generation and Transmission of 60GHz Wireless and Baseband Wireline Signals with Uplink Transmission using an RSOA," ***IEEE Photonics Technology Letters***, vol. 22, No. 15, pp. 1099-1101, August 1, 2010.

4. ***W. J. Jiang***, C. T. Lin, P. T. Shih, Y. H. Chen, J. Chen, and S. Chi, "Transmission of Wireless and Wired Services Employing a Simple System Architecture," ***IEEE Photonics Technology Letters***, vol. 22, No. 8, pp. 532-534, April 15, 2010.

5. ***W. J. Jiang***, C. T. Lin, P. T. Shih, J. Chen, P. C. Peng, and S. Chi, "A Full duplex radio-over-fiber link with Multi-level OFDM signal via a single-electrode MZM and wavelength reuse with a RSOA," ***OSA Optics Express***, vol. 18, pp. 2710-2718, 1 February, 2010.

6. C. T. Lin, A. Ng'oma, W. Y. Lee, C. C. Wei, C. Y. Wang, T. H. Lu, J. Chen, ***W. J. Jiang***, C. H. Ho, "2 x 2 MIMO radio-over-fiber system at 60 GHz employing frequency domain equalization," ***OSA Optics Express***, vol. 20,

pp. 562-567, 2 January, 2012.

7. C. C. Wei, C. T. Lin, M. I. Chao, and ***W. J. Jiang***, "Adaptively Modulated OFDM RoF Signals at 60 GHz Over Long-Reach 100-km Transmission Systems Employing Phase Noise Suppression," ***IEEE Photonics Technology Letters***, vol. 24, No. 1, pp. 49-50, January 1, 2012.

8. P. T. Shih, J. Chen, C. T. Lin, ***W. J. Jiang***, H. S. Huang, P. C. Peng, and S. Chi, "Optical millimeter-wave signal generation via frequency 12-tupling," ***IEEE/OSA Journal of Lightwave Technology***, vol. 28, No. 1, pp. 71-78, January 1, 2010.

9. C. T. Lin, J. Chen, P. T. Shih, ***W. J. Jiang***, and S. Chi, " Ultra-high Data-rate 60 GHz Radio-over-Fiber Systems Employing Optical Frequency Multiplication and OFDM Formats," ***IEEE/OSA Journal of Lightwave Technology***, vol. 28, No. 16, pp. 2296-2306, August 15, 2010. (Invited Paper)

10. P. T. Shih, C. T. Lin, ***W. J. Jiang***, H. S. Huang, J. Chen, A. Ng'oma, M. Sauer, and S. Chi, "Transmission of 20-Gb/s OFDM signals occupying 7-GHz license-free band at 60 GHz using a RoF system employing frequency sextupling optical up-conversion," ***OSA Optics Express***, vol. 18, pp. 12748-12755, 7 June, 2010.

11. C. T. Lin, P. T. Shih, ***W. J. Jiang***, J. Chen, and S. Chi, "A continuously tunable and filterless optical millimeter-wave generation via frequency octupling," ***OSA Optics Express***, vol. 17, pp. 19749-19756, 26 October, 2009.

12. P. T. Shih, C. T. Lin, ***W. J. Jiang***, Y. H. Chen, J. Chen, and S. Chi, "Full Duplex 60-GHz RoF Link Employing Tandem Single Sideband Modulation Scheme and High Spectral Efficiency Modulation Format," ***OSA Optics Express***, vol. 17, pp. 19501-19508, 26 October, 2009.

13. F. M. Kuo, J. W. Shi, S. N. Wang, N. W. Chen, P. T. Shih, C. T. Lin, ***W. J. Jiang***, E. Z. Wong, J. Chen, and S. Chi, "W-Band Wireless Data

Transmission by the Integration of a Near-Ballistic Uni-Traveling-Carrier Photodiode (NBUTC-PD) with a Horn Antenna Fed by a Quasi-Yagi Radiator," ***IEEE Electron Device Letters***, vol. 30, No. 11, pp. 1167-1169, Nov. 2009.

14. C. T. Lin, P. T. Shih, J. Chen, ***W. J. Jiang***, S. P. Dai, P. C. Peng, Y. L. Ho, and S. Chi, "Optical millimeter-wave up-conversion employing frequency quadrupling without optical filtering," ***IEEE Transactions on Microwave Theory and Techniques***, vol. 57, No. 8, pp. 2084-2092, August 1, 2009.

15. J. W. Shi, F. M. Kuo, Y. S. Wu, N. W. Chen, P. T. Shih, C. T. Lin, ***W. J. Jiang***, E. Z. Wong, J. Chen, and S. Chi, "A W-Band Photonic Transmitter-Mixer Based on High-Power Near-Ballistic Uni-Traveling-Carrier Photodiodes for BPSK and QPSK Data Transmission Under Bias Modulation," ***IEEE Photonics Technology Letters***, vol. 21, No. 15, pp. 1039-1041, August 1, 2009.

16. C. T. Lin, P. T. Shih, ***W. J. Jiang***, E. Z. Wong, J. Chen, and S. Chi, "Photonic Vector Signal Generation at Microwave/Millimeter-wave Band Employing Optical Frequency Quadrupling Scheme," ***OSA Optics Letters***, vol.34, No. 14, pp. 2171-2173, July 15, 2009.

17. P. T. Shih, C. T. Lin, ***W. J. Jiang***, Y. H. Chen, J. Chen, and S. Chi, "Hybrid Access Network Integrated with Wireless Multi-level Vector and Wired Baseband Signals Using Frequency Doubling and No Optical Filtering," ***IEEE Photonics Technology Letters***, vol. 21, No. 13, pp. 857-859, July 1, 2009.

18. P. C. Peng, F. M. Wu, ***W. J. Jiang***, R. L. Lan, C. T. Lin, J. Chen, P. T. Shih, G. R. Lin, and S. Chi, "RF Phase Shifter using a Distributed Feedback Laser in Microwave Transport Systems," ***OSA Optics Express***, vol. 17, pp. 7609-7614, 27 April, 2009.

19. J. Chen, C. T. Lin, P. T. Shih, ***W. J. Jiang***, S. P. Dai, Y. M. Lin, P. C. Peng, and S. Chi, "Generation of Optical Millimeter-wave Signals and

Vector Formats Using an Integrated Optical I/Q Modulator," ***OSA Journal of Optical Networking***, vol. 8, No. 2, pp. 188-200, Feb 2009. **(Invited Paper)**

20. P. T. Shih, C. T. Lin, ***W. J. Jiang***, J. Chen, H. S. Huang, Y. H. Chen, P. C. Peng, and S. Chi, "WDM up-conversion employing frequency quadrupling in optical modulator," ***OSA Optics Express***, vol. 17, pp. 1726-1733, 2 Feb 2009.

21. C. T. Lin, ***W. J. Jiang***, J. Chen, P. T. Shih, P. C. Peng, E. Z. Wong, and S. Chi, "Novel Optical Vector Signal Generation with Carrier Suppression and Frequency Multiplication Based on Single-Electrode Mach-Zehnder Modulator," ***IEEE Photonics Technology Letters***, vol. 20, issue 24, pp. 2060-2062, Dec. 15, 2008.

22. C. T. Lin, P. T. Shih, J. Chen, P. C. Peng, S. P. Dai, ***W. J. Jiang***, W. Q. Xue, and S. Chi, "Cost-Effective Multi-Services Hybrid Access Networks with no Optical Filter at Remote Nodes," ***IEEE Photonics Technology Letters***, vol. 20, issue 10, pp. 812-814, May 15, 2008.

23. P. C. Peng, C. T. Lin, ***W. J. Jiang***, J. Chen, F. M. Wu, P. T. Shih, and S. Chi, "Improvement of Transmission in Fiber Wireless System Using Semiconductor Laser Amplifier," ***IEE Electronics Letters***, vol. 44, no. 4, pp. 298-299, Feb 2008.

24. P. C. Peng, F. M. Wu, C. T. Lin, J. H. Chen, W. C. Kao, P. T. Shih, ***W. J. Jiang***, H. C. Kuo, and S. Chi, "40 GHz Phase Shifter based on Semiconductor Laser," ***IEE Electronics Letters***, vol. 44, no. 8, pp. 520-521, Apr 2008.

International Conferences

1. ***W. J. Jiang***, H. Yang, Y. M. Yang, C. T. Lin, and A. Ng'oma, "40 Gb/s RoF Signal Transmission with 10 M Wireless Distance at 60 GHz," ***2012 Optical Fiber Communication Conference (OFC 2012)***, OTu2H.1, Los Angeles, California, March 4-8, 2012.

2. ***W. J. Jiang***, C. T. Lin, L. Y. Wang He, C. C. Wei, C. H. Ho, Y. M. Yang, P. T. Shih, J. Chen, and S. Chi, "32.65-Gbps OFDM RoF Signal Generation at 60GHz Employing an Adaptive I/Q Imbalance Correction," ***36nd European Conference on Optical Communication (ECOC 2010)***, Th.9.B.5, Torino, Italy, September 19-23, 2010.

3. ***W. J. Jiang***, C. T. Lin, E. Z. Wong, P. T. Shih, J. Chen, and S. Chi, "A Novel Optical Direct-Detection I/Q Up-Conversion with I/Q Imbalance Compensation via Gram-Schmidt Orthogonalization Procedure," ***35nd European Conference on Optical Communication (ECOC 2009)***, Paper 10.4.2, Vienna, Austria, September 20-24, 2009.

4. ***W. J. Jiang***, C. T. Lin, Y. H. Chen, P. T. Shih, D. Z. Hsu, J. Chen, and S. Chi, "Simultaneous Generation and Transmission of 60-GHz RF and Baseband Signals Employing Only a Simple Single Electrode MZM," ***35nd European Conference on Optical Communication (ECOC 2009)***, 4.5.2, Vienna, Austria, September 20-24, 2009.

5. ***W. J. Jiang***, C. T. Lin, Han-Sheng Huang, Po-Tsung Shih, Jason(Jyehong) Chen, and S. Chi, "60-GHz Photonic Vector Signal Generation Employing Frequency Quadrupling Scheme for Radio-over-Fiber Link," *Submitted to* ***2009 Optical Fiber Communication Conference (OFC 2009)***, OWF1, San Diego, California, Mar. 24-26, 2009.

6. ***W. J. Jiang***, C. T. Lin, Han-Sheng Huang, Po-Tsung Shih, Jason(Jyehong) Chen, and S. Chi, "Experimental demonstration of a novel filterless frequency quadrupling technique for colorless WDM millimeter-wave up-conversion systems," ***2009 Optical Fiber Communication Conference (OFC 2009)***, JWA75, San Diego, California, Mar. 24-26, 2009.

7. C. H. Ho, R. Sambaraju, ***W. J. Jiang***, T. H. Lu, C. Y. Wang, H. Yang, W. Y. Lee, C. T. Lin, C. C. Wei, A. Ng'oma, and S. Chi, "50-Gb/s Radio-Over-Fiber System Employing MIMO and OFDM Modulation at 60 GHz," ***2012 Optical Fiber Communication Conference (OFC 2012)***, OM2B.3, Los Angeles, California, March 4-8, 2012.

8. C. T. Lin, S. Y. Jian, Anthony Ng'oma, C. H. Ho, ***W. J. Jiang***, C. C. Wei, and J. Chen, "35-Gb/s 32-QAM Radio-over-Fiber System Employing Single-Sideband Single-Carrier Modulation at 60 GHz," ***2011 IEEE International Topical Meeting on Microwave Photonics (MWP 2011)***, 2143, Singapore, October 18-21, 2011.

9. C. T. Lin, Anthony Ng'oma, W. Y. Lee, C. Y. Wang, T. H. Lu, ***W. J. Jiang***, C. H. Ho, C. C. Wei, J. Chen, and S. Chi, "MIMO-Enhanced Radio-over-Fiber System at 60 GHz," ***36th European Conference on Optical Communication (ECOC 2011)***, We.10.P1.120, Geneva, Switzerland, September 18-22, 2011.

10. C. C. Wei, C. T. Lin, M. I. Chao, ***W. J. Jiang***, and C. H. Ho, "Long-Reach 26.54-Gbps OFDM RoF System at 60 GHz over 100-km Fiber and 3-m Wireless Transmission Employing Phase Noise Compensation and Bit-Loading Algorithms," ***36th European Conference on Optical Communication (ECOC 2011)***, We.7.C.5, Geneva, Switzerland, September 18-22, 2011.

11. C. H. Ho, C. T. Lin, ***W. J. Jiang***, Y. L. Ho, C. C. Wei, J. Chen, S. Y. Jian, W. E. Chen, and S. Chi, "4-Gb/s QPSK radio-over-fiber system at 60 GHz employing single sideband modulation," ***16th Opto-Electronics and Communications Conference (OECC 2011)***, 12220055, Kaohsiung, Taiwan, July 4-8, 2011.

12. C. T. Lin, J. Chen, ***W. J. Jiang***, L. Y. Wang He, P. T. Shih, C. H. Ho, and S. Chi, "Ultra-High Data-Rate 60 GHz Radio-over-Fiber Systems Employing Optical Frequency Multiplication and Adaptive OFDM Formats," ***2011 Optical Fiber Communication Conference (OFC 2011)***, OThJ6, Los Angeles, California, March 6-10, 2011. (**Invited Talk**)

13. A. Ng'oma, C. T. Lin, L. Y. Wang He, ***W. J. Jiang***, F. Annunziata, J. Chen, P .T Shih, and S. Chi, "31 Gbps RoF System Employing Adaptive Bit-Loading OFDM Modulation at 60 GHz," ***2011 Optical Fiber***

Communication Conference (OFC 2011), OWT7, Los Angeles, California, March 6-10, 2011.

14. F. M. Kuo, Y. K. Ho, J. W. Shi, N. W. Chen, ***W. J. Jiang***, C. T. Lin, J. Chen, C. L. Pan, and S. Chi, "12.5-Gb/s Wireless Data Transmission by Using Bias Modulation of NBUTC-PD Based W-Band Photonic Transmitter-Mixer," ***2010 Optical Fiber Communication Conference (OFC 2010)***, OThF7, San Diego, California, Mar. 21-25, 2010.

15. A. Ng'oma, P. T. Shih, J. George1, F. Annunziata1, M. Sauer1, C. T. Lin, ***W. J. Jiang***, J. Chen, and S. Chi, "21 Gbps OFDM Wireless Signal Transmission at 60 GHz Using a Simple IMDD Radio-over-Fiber System," ***2010 Optical Fiber Communication Conference (OFC 2010)***, OTuF4, San Diego, California, Mar. 21-25, 2010.

16. A. Ng'oma, M. Sauer, F. Annunziata, ***W. J. Jiang***, P. T. Shih, C. T. Lin, J. Chen, and S. Chi "14 Gbps 60 GHz RoF Link Employing a Simple System Architecture and OFDM Modulation," ***2009 IEEE International Topical Meeting on Microwave Photonics (MWP 2009)***, Fr1.3, Valencia, Spain, October 14-16, 2009.

17. P. T. Shih, C. T. Lin, H. S. Huang, ***W. J. Jiang***, J. Chen, A. Ng'oma, M. Sauer, and S. Chi, "13.75-Gb/s OFDM Signal Generation for 60-GHz RoF System within 7-GHz License-Free Band via Frequency Sextupling," ***35nd European Conference on Optical Communication (ECOC 2009)***, 4.5.4, Vienna, Austria, September 20-24, 2009.

18. P. T. Shih, C. T. Lin, H. S. Huang, ***W. J. Jiang***, D. Z. Hsu, J. Chen, F. M. Kuo, N. W. Chen, J. W. Shi, and S. Chi, "W-band 3.75-Gb/s 8PSK Wireless Signal Generation and Transmission via Optical Frequency Octupling and Bias Modulation of NBUTC-PD with Feed-Forward Equalizer," ***35nd European Conference on Optical Communication (ECOC 2009)***, P3.14, Vienna, Austria, Sep. 20-24, 2009.

19. C. T. Lin, E. Z. Wong, ***W. J. Jiang***, P. T. Shih, J. Chen, S. Chi, "28-Gb/s 16-QAM OFDM Radio-over-Fiber System within 7-GHz License-Free Band at 60 GHz Employing All-Optical Up-Conversion," ***IEEE/OSA Conference on Lasers and Electro-Optics (CLEO/QELS 2009)***, CPDA8, Maryland, Baltimore, May 31-June 5, 2009. **(Post-deadline Paper)**

20. C. T. Lin, ***W. J. Jiang***, Jason(Jyehong) Chen, Er-Zih Wong, Sheng-Peng Dai, Yu-Min Lin, P. T. Shih, P. C. Peng, and S. Chi,"Experimental Demonstration of Optical 5-Gb/s 16-QAM OFDM Signal Generation and Wavelength Reuse for 1.25-Gbit/s Uplink Signal" ***34nd European Conference and Exhibition on Optical Communication Conference (ECOC 2008)***, We.1.F.3, Brussels, Belgium, Sep. 21-25, 2008.

21. C. T. Lin, S. P. Dai, ***W. J. Jiang***, J. Chen, Y. M. Lin, P. T. Shih, P. C. Peng, and S. Chi, "Experimental Demonstration of Optical Colorless Direct-Detection OFDM Signals with 16- and 64-QAM Formats beyond 15 Gb/s" ***34nd European Conference and Exhibition on Optical Communication Conference (ECOC 2008)***, Mo.3.E.1, Brussels, Belgium, Sep. 21-25, 2008.

22. C. T. Lin, ***W. J. Jiang***, E. Z. Wong, J. Chen, P. T. Shih, P. C. Peng, and S. Chi, "Optical Vector Signal Generation Using Double Sideband with Carrier Suppression and Frequency Multiplication," ***IEEE/OSA Conference on Lasers and Electro-Optics (CLEO/QELS 2008)***, CThR5, San Jose, California, May 4-9, 2008.

23. P. C. Peng, F. M. Wu, C. T. Lin, J. Chen, P. T. Shih, W. C. Kao, ***W. J. Jiang***, H. C. Kuo, and S. Chi, "Tunable Slow Light in Quantum Well Vertical-Cavity Surface-Emitting Laser at 40 GHz," ***IEEE/OSA Conference on Lasers and Electro-Optics (CLEO/QELS 2008)***, JThA2, San Jose, California, May 4-9, 2008.

24. P. C. Peng, C. T. Lin, ***W. J. Jiang***, J. Chen, P. T. Shih, F. M. Wu, and S. Chi, "Transmission Improvement in Fiber Radio Links Using

Semiconductor Laser," ***2008 Optical Fiber Communication Conference (OFC 2008)***, JThA68, San Diego, California, Feb. 24-28, 2008.

25. P. C. Peng, F. M. Wu, ***W. J. Jiang***, C. T. Lin, J. H. Chen, P. T. Shih, W. C. Kao, S.Chi, "Slow Light in Distributed Feedback Laser for All-Optical Inverter" ***OSA Slow and Fast Light Topical Meeting***, Paper no. 08-C-225-SL, 2008.

26. Po-Tsung Shih, C. T. Lin, ***W. J. Jiang,*** Er-Zih Wong, J. Chen, S. Chi, Y.-S. Wu, F.-M. Kuo, Nan-Wei Chen, and J.-W. Shi, "W-Band Vector Signal Generation via Optical Millimeter-wave Generation and Direct Modulation of NBUTC-PD," ***2009 Optical Fiber Communication Conference (OFC 2009)***, OWP4, San Diego, California, Mar. 24-26, 2009.

27. Y.-S. Wu, F.-M. Kuo, Nan-Wei Chen, J.-W. Shi, P. T. Shih, C. T. Lin, ***W. J. Jiang***, Er-Zih Wong, and Jason(Jyehong) Chen "A W-Band Photonic Transmitter-Mixer Based on High-Power Near-Ballistic Uni-Traveling-Carrier Photodiode (NBUTC-PD) for 1.25-Gb/s BPSK Data Transmission under Bias Modulation," ***2009 Optical Fiber Communication Conference (OFC 2009)***, OWX3, San Diego, California, Mar. 24-26, 2009.

28. Po-Tsung Shih, C. T. Lin, Yu-Hung Chen, ***W. J. Jiang***, Jason(Jyehong) Chen and S. Chi "Hybrid Access Network Integrated with Multi-level RF Vector Signal and Baseband Signal without Optical Filtering," ***2009 Optical Fiber Communication Conference (OFC 2009)***, OTuB5, San Diego, California, Mar. 24-26, 2009.

29. Po-Tsung Shih, C. T. Lin, Yu-Hung Chen, ***W. J. Jiang***, Jason(Jyehong) Chen and S. Chi "Experimental Demonstration of 10-Gb/s OFDM-QPSK Signal at 60 GHz Using Frequency-Doubling and Tandem SSB Modulation," ***2009 Optical Fiber Communication Conference (OFC 2009)***, OMV7, San Diego, California, Mar. 24-26, 2009.

30. Anthony Ng'oma, Michael Sauer, Frank Annunziata, ***W. J. Jiang***, C. T. Lin, Jyehong Chen, Po-Tsung Shi and S. Chi "Simple Multi-Gbps 60 GHz Radio-over-Fiber Links Employing Optical and Electrical Data Up-conversion and Feed-Forward Equalization," ***2009 Optical Fiber Communication Conference (OFC 2009)***, OWF2, San Diego, California, Mar. 24-26, 2009.

31. P. C. Peng, S. K. Ye, F. M. Wu, J. Chen, C. T. Lin, ***W. J. Jiang***, P. T. Shih, H. C. Kuo, and S. Chi "Tunable Photonic Microwave Filter using Slow Light in Vertical Cavity Surface Emitting Laser," ***2009 Optical Fiber Communication Conference (OFC 2009)***, JWA58, San Diego, California, Mar. 24-26, 2009.

Domestic Conferences

1. ***W. J. Jiang***, C. T. Lin, C. H. Ho, Y. M. Yang, L. Y. Wang He, J. Chen, and S. Chi, " A Record 32.65-Gb/s OFDM Radio-over-Fiber Signal at 60GHz Employing an I/Q Imbalance Correction ," ***Optics and Photonics in Taiwan (OPT'10).***

2. ***W. J. Jiang***, C. T. Lin, P. T. Shih, J. Chen, and S. Chi, "Simultaneous Transmission of 60-GHz Uncompression wireless HDTV and Wired Signals Employing a Simple System Architecture," ***Optics and Photonics in Taiwan (OPT'09).*** **(2009年光電科技研討會學生論文獎/Student paper award)**

3. ***W. J. Jiang***, C. T. Lin, D. Z Hsu, P. T. Shih, J. Chen, and S Chi, "Laser Linewidth Impact on Beyond 10 Gb/s Optical OFDM Transmission in 60-GHz RoF System within 7-GHz License-Free Band," ***Optics and Photonics in Taiwan (OPT'09).***

4. ***W. J. Jiang***, C. T. Lin, P. T. Shih, J. Chen, and S. Chi, and P. C. Peng, "Experimental Demonstration of Optical Direct-Detection 20-Gb/s 16-QAM and 15-Gb/s 64-QAM OFDM Signals Generation for Radio-over-Fiber Link ", ***International Conference on Optics and Photonics in Taiwan (OPT'08).***

5. ***W. J. Jiang***, P. C. Peng, C. T. Lin, J. Chen, P. T. Shih, F. M. Wu, S. Chi, "Performance Improvement In Radio-over-Fiber System by Using Semiconductor Laser Amplifer," BO-043, presented at ***OPT2007 (Optics and Photonics Taiwan)***, Nov. 30-Dec.1, 2007, Taichung, Taiwan.

6. ***W. J. Jiang***, C. W. Chen , and C. L. Pan, "Pulse Reconstruction From Frequency-Resolved Optical Gating Measurement By Use Of Population-Split Genetic Algorithm (PSGA)," PC-FR2-05, presented at ***OPT2005 (Optics and Photonics Taiwan***), Dec. 9-10, 2005, Tainan, Taiwan.

7. C. H. Ho, C. T. Lin, ***W. J. Jiang***, P. T. Shih, L. Y. Wang He, J. Chen, and Sien Chi, "Simultaneous 60GHz Wireless and Wired Signals Transmission Employing a Simple System Architecture," ***Optics and Photonics in Taiwan (OPT'10).***

8. L. Y. Wang-He, C. T. Lin, ***W. J. Jiang***, P. T. Shih, J. Chen, and S. Chi, "All Optical I/Q Up-conversion for 28-Gb/s 16-QAM OFDM Signal Generation at 60-GHz Band," ***Optics and Photonics in Taiwan (OPT'09).*** **(2009年光電科技研討會學生論文獎/Student paper award)**

9. S. Y. Jian, C. T. Lin, ***W. J. Jiang***, P. T. Shih, J. Chen, and S. Chi, "8-QAM RF Signal Generation at 60 GHz with Optical Frequency Quadrupling Technology," ***Optics and Photonics in Taiwan (OPT'09).***

10. W. Y. Li, C. T. Lin, ***W. J. Jiang***, P. T. Shih, J. Chen, and S. Chi, "A Noval I/Q Imbalance Compensation for Optical I/Q Up-Conversion," ***Optics and Photonics in Taiwan (OPT'09).***

11. Y. M. Yang, C. T. Lin, ***W. J. Jiang***, P. T. Shih, J. Chen, and S. Chi, "Colorless WDM millimeter-wave up-conversion Systems With Novel Filterless Frequency Quadrupling Technique," ***Optics and Photonics in Taiwan (OPT'09).***

12. G. Y. Huang, C. T. Lin, P. T. Shih, ***W. J. Jiang***, J. Chen, and S.

Chi, ”Hybrid Optical Access Network Integrating with Wireless 8-PSK Signal and Wireline OOK Signal,” ***Optics and Photonics in Taiwan (OPT'09).***

13. M. I. Chao, C. T. Lin, P. T. Shih, ***W. J. Jiang***, J. Chen, and S .Chi, ”13.75-Gb/s OFDM Signal Generation in the 60-GHz Band Based on Frequency Sextupling Technology,” ***Optics and Photonics in Taiwan (OPT'09).***

14. Y. L. Ho, C. T. Lin, P. T. Shih, ***W. J. Jiang***, J. Chen , F. M. Kuo, N. W. Chen, J. W. Shi, and S. Chi, ”Generate and Transmiss W-band 3.75-Gb/s 8PSK Wireless Signal via Optical Frequency Octupling and Bias Modulation of NBUTC-PD with Feed-Forward Equalizer,” ***Optics and Photonics in Taiwan (OPT'09).***

15. F. M. Kuo, J. W. Shi, S. N. Wang, N. W. Chen, P. T. Shih, C. T. Lin, ***W. J. Jiang***, E. Z. Wong, J. Chen, and S. Chi, ”W-Band Wireless Data Transmission by use of the Integration of a Near-Ballistic Uni-Traveling-Carrier Photodiode (NBUTC-PD) with a Horn Antenna Fed by a Quasi-Yagi Radiator,” ***Optics and Photonics in Taiwan (OPT'09).***

16. H. S. Huang, P. T. Shih, C. T. Lin, ***W. J. Jiang***, J. Chen, P. C. Peng, and S. Chi , “WDM Optical Colorless Millimeter-wave Up-Conversion Using Frequency Quadrupling”, ***International Conference on Optics and Photonics in Taiwan (OPT'08).*** **(2008年光電科技研討會學生論文獎/Student paper award)**

17. E. Z. Wong, C. T. Lin, ***W. J. Jiang***, P. T. Shih, J. Chen , and S. Chi , “Optical I/Q Up-conversion for Direct-Detection OFDM System”, ***International Conference on Optics and Photonics in Taiwan (OPT'08).***

18. Y. H. Chen, C. T. Lin, ***W. J. Jiang***, J. Chen, E. Z. Wong, S. P. Dai, P. T. Shih, P. C. Peng, and S. Chi , “Experimental Demonstration of Optical 5-Gb/s 16-QAM OFDM Signal Generation and Wavelength Reuse for 1.25-Gbit/s Uplink Signal” ***International Conference on Optics and***

Photonics in Taiwan (OPT'08).

19. P. T. Shih, C. T. Lin, ***W. J. Jiang***, E. Z. Wong, J. Chen, S. Chi, Y. S. Wu, F. M. Kuo, N. W Chen, and J. W. Shi," W-Band Vector Signal Generation via Optical Millimeter-Wave Generation and Direct Modulation of NBUTC-PD " ***International Conference on Optics and Photonics in Taiwan (OPT'08).***

20. S. K. Yeh, J. Chen, F. M. Wu, C. T. Lin, ***W. J. Jiang***, P. T. Shih, H. C. Kuo, P. C. Peng, and S. Chi, "Tunable Notch Filter Using Slow Light in Semiconductor Laser " ***International Conference on Optics and Photonics in Taiwan (OPT'08).*** **(2008年光電科技研討會學生論文獎/Student paper award)**

21. C. W. Chen, ***W. J. Jiang*** and C. L. Pan, "Phase Retrieval Of Ultrafast Optical Pulses From Interferometric Autocorrelation Measurement By Population-Split Genetic Algorithm (PSGA) ," C-FR-V2-7, presented at ***OPT2005 (Optics and Photonics Taiwan)***, Dec. 9-10, 2005, Tainan, Taiwan.**(2005年光電科技研討會學生論文獎/Student paper award)**

Patents

1. "光調變裝置 (Optical Modulation Device) ," US Patent (pending) and ROC Patent (公開編號: 201017245).

2. "訊號傳送系統及方法 (System and Method for Transmitting Signals) ," US and ROC Patent (pending).

3. "升頻系統及方法 (Frequency Up-Conversion System and Method for The Same) ," US and ROC Patent (pending).

Others

1. ***W. J. Jiang***, "High Spectrum Efficiency OFDM Generation for Radio-over-fiber System with Frequency Multiplication," Master thesis, 2008. **(中華民國光學工程學會97年度學生論文獎/Master thesis award)**

2. ***W. J. Jiang***, “高頻譜效率之正交分頻多工技術應用於倍頻光纖擷取系統,”光學工程, 第105期, pp. 31-36, Apr. 2009.